



FACULTY OF
MECHANICAL ENGINEERING

On the dynamic modelling of automatic ball balancers applied to laboratory centrifuges

Dissertation

zur Erlangung des akademischen Grades

**Doktoringenieur
(Dr.-Ing.)**

von M.Sc. Lars Spannan
geb. am 19.06.1990 in Lippstadt

genehmigt durch die Fakultät für Maschinenbau
der Otto-von-Guericke-Universität Magdeburg

Gutachter:

Jun.-Prof. Dr.-Ing. Elmar Woschke
Prof. Dipl.-Ing. Dr. techn. Horst Ecker

Promotionskolloquium am 18.08.2021

Contents

1. Introduction	1
1.1. Current state of research	3
1.2. Dissertation objective	6
1.3. Overview	7
2. Application	9
2.1. Challenges in the design of automatic ball balancers	12
2.2. Constructional variations and improvements	15
3. Navier-Stokes equations in cylindrical domains	19
4. Translational oscillator model	28
4.1. Equations of motion	28
4.2. Influences on the ABB operation	49
4.3. Extension to spatial rotordynamic models	59
5. ABB Multibody system force element	60
5.1. Modelling contact, friction, rolling resistance and adherence	63
5.2. Modelling drag forces	70
6. Model validation with centrifuge test rigs	80
6.1. Discoidal rotor	83
6.2. CFRP centrifuge rotor	116
7. Summary	125
7.1. Outlook	126

Contents

A. Derivations of equations	130
A.1. Approximation of border frequencies of non-synchronous vibrations	130
A.2. Incompressible flow in cylindrical domains	133
A.3. Vorticity-stream function formulation in axisymmetric cylindrical domains	143
B. Test rig details	147
B.1. Discoidal rotor	147
B.2. CFRP rotor	151
C. Useful dimensions of ball bearings for automatic balancing	153
References	I
List of figures	XVIII
List of tables	XXIII

Symbols

Notation	Unit	Description
A	m	Vibration amplitude
a	m	Normal force offset distance
\bar{A}	m ²	Ball cross-sectional area
$\underline{\underline{A}}$	specific	Eigenvalue problem matrix
a_r	-	Mesh staggering factor in radial direction
a_z	-	Mesh staggering factor in axial direction
B	m	Vibration amplitude
b	N s m ⁻¹	Linear damping parameter
$B1, B2$	-	Automatic balancing plane
$\underline{\underline{B}}$	specific	Eigenvalue problem matrix
c_d	-	Drag coefficient
$c_{d,cor}$	-	Slipstream corrected drag coefficient
c_{vm}	-	Coefficient of virtual mass
D	-	Damping ratio
d_b	m	Balancing ball diameter
d_{bore}	m	Radial ball bearing bore diameter
d_{outer}	m	Radial ball bearing outer diameter
E	m	Raceway eccentricity
\underline{e}	-	Unit vector
F_{adh}	N	Adherence force
F_b	N	Damping force
F_{Drag}	N	Drag force
F_N	N	Normal force
F_T	N	Tangential force
F_{vm}	N	Force of virtual mass

Symbols

Notation	Unit	Description
g	N kg^{-1}	Gravitational constant
\underline{g}	m s^{-2}	Body forces vector
H	m	Annulus height
h	m	Mesh grid spacing
\underline{h}_a	specific	Vector of outer loads
\underline{h}_ω	specific	Vector of inertial effects in the moving reference system
J	kg m^2	Moment of inertia
k	N m^{-1}	Linear stiffness parameter
L	J	Lagrangian function
l	m	Slipstream ball distance
$\underline{\underline{M}}$	specific	Multibody system mass matrix
M	kg	Total rotor mass
M_0	N m	Driving Torque
m_0	kg	Primary unbalance mass
m_b	kg	Balancing ball mass
$M_{\beta 0}$	N m	External damping torque
M_D	N m	Damping moment
m_{eff}	kg	Effective balancing mass
N	-	Number of balancing units
n	-	Number of balancing balls
n_{max}	-	Amount of balls for maximum balancing capability
n_r	-	Number of grid points in radial direction
n_z	-	Number of grid points in axial direction
\mathcal{O}_G	-	Centre of raceway geometry
\mathcal{O}_M	-	Centre of mass
\mathcal{O}_R	-	Centre of rotation
p	N m^{-2}	Pressure
q	specific	Generalized coordinate
R	m	Vibration amplitude
r	m	Radial coordinate, radius

Symbols

Notation	Unit	Description
Re	-	(Particle) Reynolds number
r_{groove}	m	Raceway groove radius
\underline{r}	m	Position vector
$s\nu_{\text{adh}}$	m	State variable of adherence
T	J	Kinetic energy
t	s	Time
u	m s^{-1}	Velocity
$U1, U2$	-	Plane of primary unbalance
u^*	m s^{-1}	Regularisation parameters
U_b	kg m	Balancing capability of one ball
u_{flow}	m s^{-1}	Fluid flow velocity
U_{max}	kg m	Maximum balancing capability
u_{orb}	m s^{-1}	Orbit velocity
u_{rel}	m s^{-1}	Undisturbed flow velocity relative to the ball
u_t	m s^{-1}	Tangential relative velocity
u_{thresh}	m s^{-1}	Threshold velocity
V	J	Potential energy
\underline{v}	specific	Eigenvector
W	m	Annulus width
W_1, W_2	m	Annulus width dimensions
W_{diss}	J	Dissipative Work
x	m	Spatial coordinate
\underline{y}	specific	Vector of degrees of freedom
y	m	Spatial coordinate
z	m	Axial coordinate
<i>Greek letters</i>		
α	rad	Half of sector occupied by one ball
α_{tot}	rad	Total occupied sector
β	N m s	Linear viscous drag damping coefficient
Γ	$\text{m}^2 \text{s}^{-1}$	Angular Momentum

Symbols

Notation	Unit	Description
γ	rad	Raceway eccentricity orientation
δ	-	Infinitesimal entity
δ_c	m	Contact indentation
ε	m	Orbit radius
ε_0	m	Primary unbalance radius
ζ	s^{-1}	Axial vorticity component
η	s^{-1}	Azimuthal vorticity component
θ	rad	Azimuthal coordinate
$\dot{\theta}_{\text{target}}$	rad s^{-1}	Rated rotor speed
ϑ	$^{\circ}\text{C}$	Temperature
κ	rad	Ball rotation angle
λ	specific	Eigenvalue
μ	-	Friction coefficient
μ_{adh}	-	Adherence coefficient
μ_{kin}	-	Kinetic friction coefficient
μ_R	-	Rolling resistance coefficient
ν	$\text{m}^2 \text{s}^{-1}$	Kinematic viscosity
ζ	s^{-1}	Radial vorticity component
ρ_b	kg m^{-3}	Balancing ball density
ρ_{fl}	kg m^{-3}	Fluid density
$\underline{\underline{\sigma}}$	N m^{-2}	Stress tensor
ζ	rad	Equilibrium angle / inclination angle
$\underline{\underline{\tau}}$	N m^{-2}	Shear stress tensor
ϕ_x	-	Argument of complex amplitude
ϕ_y	-	Argument of complex amplitude
φ	rad	Orbital position w.r.t. the primary unbalance
Ψ	rad	Phase angle
ψ	$\text{m}^3 \text{s}^{-1}$	Stokes stream function
Ω	rad s^{-1}	Rotor angular velocity
ω_{crit}	rad s^{-1}	Critical angular velocity
ω_x	rad s^{-1}	Critical speed in orthotropic bearings

Symbols

Notation	Unit	Description
ω_y	rad s^{-1}	Critical speed in orthotropic bearings
Ω_{bo}	rad s^{-1}	Instability border angular frequency

Subscripts

adh		Adherence
b		Balancing ball
bw		Backward whirl
c		Contact point
fl		Fluid
fw		Forward whirl
max		Maximum value
min		Minimum value
NSE		Navier Stokes equations solution
ODE		Multibody motion solution
or		Outer ring / raceway
R		Rotor-fixed system
r		Radial direction / component
x		In direction of x
y		In direction of y
z		Axial direction / component
θ		Azimuthal direction / component
$\underline{\circ}$		Vector
$\underline{\underline{\circ}}$		Matrix

Superscripts

*		Intermediate solution
$\dot{\circ}$		Temporal derivative
$\tilde{\circ}$		Substitute coordinate
$\hat{\circ}$		Amplitude
k		Time step

Acronyms

Notation	Description
ABB	Automatic ball balancer
ABU	Automatic balancing unit
CFD	Computational fluid dynamics
CFL	Courant-Friedrichs-Lewy (number)
CFRP	Carbon fibre reinforced polymer
EVP	Eigenvalue problem
fps	Frames per second
KBM	Krylov-Bogoliubov-Mitropolsky
LDV	Laser Doppler vibrometer
LTS	Laser triangulation sensor
ODE	Ordinary differential equation
PDE	Partial differential equation
RANS	Reynolds-averaged Navier–Stokes
RMS	Root mean square
rpm	Rotations per minute
VTC	Viscosity-temperature coefficient

Abstract

This thesis deals with the balancing of unbalanced rotor systems and the resulting reduction of vibration. In particular, calculations and experiments utilizing so-called automatic balancing units with spherical balancing masses considering the use case in laboratory centrifuges are described. The specified modelling approaches for describing the fluid flow and friction effects acting on the balancing masses aim towards a more differentiated examination of the influence of geometry and manufacturing tolerances when designing automatic balancing units. For this purpose, the investigated centrifuges are modelled by multibody systems in which the kinematic and dynamic coupling of the balancing masses with the rotor system is realized by a special force element. In addition to the results on the rotor deflection, which is relevant from an operational point of view, the comparison of the transient balancing mass positions relative to the rotor in experiment and simulation is presented.

Kurzfassung

In der vorliegenden Arbeit wird der Ausgleich von Unwuchten in Rotorsystemen und der resultierenden Schwingungsreduktion behandelt. Im Speziellen wird die Verwendung von sogenannten selbsttätigen Auswuchteinheiten mit kugelförmigen Ausgleichsmassen für Laborzentrifugen beschrieben. Die hierin dargelegten Modellierungsansätze zur Beschreibung der auf die Ausgleichsmassen wirkenden Strömungs- und Reibungseinflüsse sollen einen Beitrag dazu leisten, bei der Gestaltung von selbsttätigen Auswuchteinheiten unter anderem den Einfluss von Geometrie und Fertigungstoleranzen differenzierter betrachten zu können. Hierzu werden die untersuchten Zentrifugen durch Mehrkörpersysteme abgebildet, in denen die kinematische und dynamische Kopplung der Ausgleichsmassen mit dem Rotorsystem durch ein spezielles Kraffelement realisiert wird. Neben den Ergebnissen zur betriebstechnisch äußerst relevanten Rotorauslenkung wird auch der experimentelle Abgleich der transienten Ausgleichsmassenpositionen relativ zum Rotor dargelegt.

1. Introduction

To ensure the safe and efficient operation of rotating machinery, the elimination of rotor imbalance is the ‘most important and fundamental procedure to reduce unfavorable vibrations’ ([Ish12]) and conventional static and dynamic balancing is the main problem for the majority of rotors [Gas06]. Excessive translational and rotational vibrations lead to large stresses, noise emission and a reduction in the service life of bearing components. Therefore, rotor imbalances caused by manufacturing and assembly tolerances are identified before commissioning and compensated by mass correction. However, for a variety of rotor systems the conventional balancing approach may not be economically feasible or not applicable at all, due to the functional principle of the machinery, e.g., a variable mass distribution during operation. In these cases, automatic balancing units (ABU) can be attached to the rotor and compensate for variable imbalances during operation by an additional redistribution of inherent masses. Since the ongoing technological advancement strives towards more lightweight systems with higher power density and, where applicable, health and operational safety regulations are intensified regarding the accelerations inflicted to the operator, methods to mitigate imbalance induced rotor vibrations will retain their significance and ABUs will likely also be considered in the future as a supporting measure in systems that are currently only balanced conventionally.

The automatic ball balancer (ABB) is the focus of this work and a type of ABU where two or more spherical compensation masses are located inside an annulus concentric to the rotor axis of rotation, see fig. 1.1 for an example with two ABBs to compensate the dynamic imbalance of a rigid rotor in two planes. The working principle of ABBs can be understood by examining the rotor deflection in the balancing plane. As is well known, the lag angle of the deflection regarding the unbalance excitation changes when the rotor speed

1. Introduction

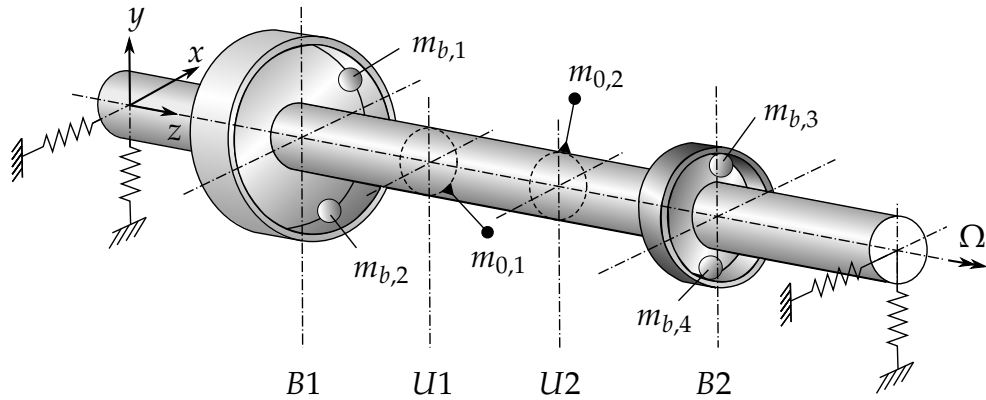


Figure 1.1.: Example of a dynamically unbalanced Jeffcott rotor with primary imbalance masses $m_{0,1}$ and $m_{0,2}$ in the planes U1 and U2, respectively and equipped with two ball-type automatic balancers in the balancing planes B1 and B2. The illustration is based on a graphic in [Spe+02].

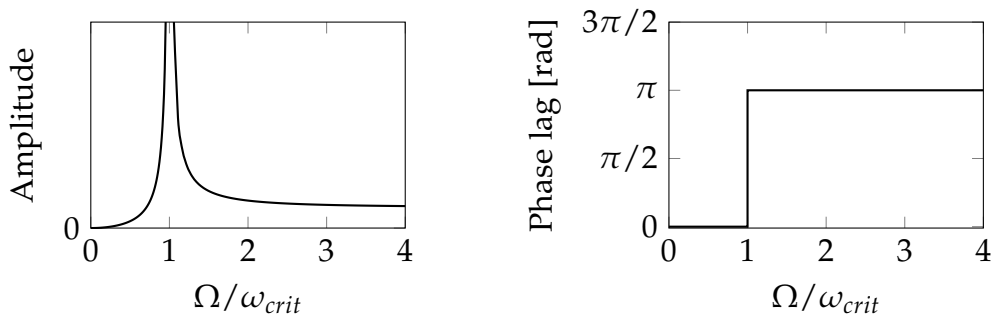


Figure 1.2.: Imbalance-excited vibration response of an undamped oscillator as a function of the circular frequency of excitation relative to the critical speed.

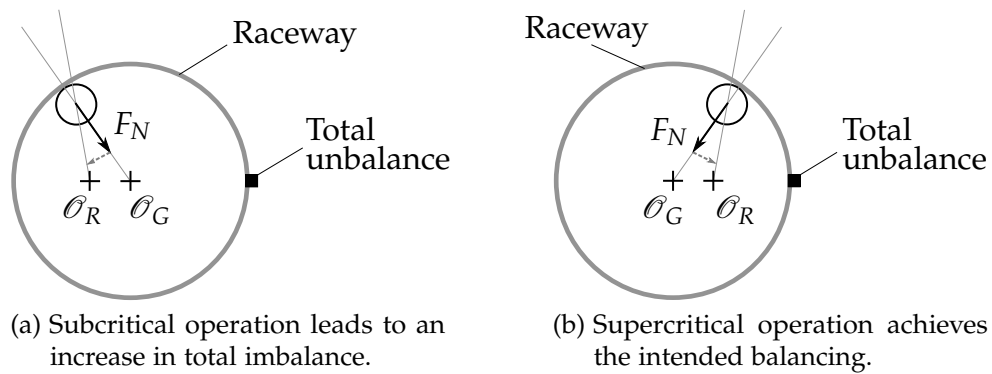


Figure 1.3.: Working principle of the ABB. Lacking a force in orbital direction, indicated by the dashed vector, results in movement of the ball along the orbit in the opposite direction.

1.1. Current state of research

Ω exceeds the critical angular frequency ω_{crit} . For rotors without external damping, it steps from 0 to π . If the rotor is operated exactly at the critical angular frequency, the angle of lag is $\pi/2$, see fig. 1.2. Thus, in the balancing plane, the centre of rotation \mathcal{O}_R , the geometric centre of the ABB raceway \mathcal{O}_G and the position of the total imbalance in this plane are collinear, as shown in fig. 1.3. For all operating speeds, the normal force F_N acting on a balancing ball due to contact with the raceway points in the direction of \mathcal{O}_G and with the neglect of friction, no forces act in the direction tangential to the ball orbit. However, for the ball to maintain its orbital position regarding the raceway, such a force would have to be present as indicated by the dashed vector in fig. 1.3a and fig. 1.3b, so that in sum the required centripetal force directed towards \mathcal{O}_R is applied. Since this condition is not fulfilled, the inertia thus causes the ball to move in the opposite orbital direction. The balancing balls therefore consistently move to the position on the raceway that experiences the greatest deflection from the centre of rotation. Hence, it is evident that an ABB in subcritical operation amplifies the unbalance excitation and only in supercritical operation, due to the phase lag, the intended automatic balancing occurs when the imbalance vectors of the balancing balls cancel out the initial rotor imbalance in the specific plane. To allow for the ideal balancing of variable initial unbalances, an ABB must therefore be equipped with at least two balls.

1.1. Current state of research

In order to access and optimize the dynamic behaviour of systems equipped with ABBs, several researchers have taken on the problem and over the years have published modelling approaches of increasing depth and successfully applied them to concrete applications. For a classification of the modelling aspects and solution methods, these are presented below, whereby a compilation of application-related research is omitted at this point and can be found in chapter 2.

The first publication of an automatic balancing unit with spherical balancing masses was by Thearle and Schenectady in [TS32] which was followed

1. Introduction

by further experimental investigations, see [The50]. The early calculation approaches consider a planar oscillator with an ABB, assuming a no-slip condition between the balls and the raceway. In addition, a linear viscous modelling of the damping effect of the fluid on the ball motion is followed. One of the first descriptions of the movements by differential equation systems can be found in [Ble64], where the stability of the balanced state is investigated.

Further stability investigations on a similar basis are described in [IAM67], the results of which were also validated experimentally. In [Sha75] the system of differential equations is transformed into an eigenvalue problem through perturbation analysis. With numerical procedures, the stability is checked, i.e., the real parts of the eigenvalues are checked to be negative, and a sensitivity analysis regarding the ABB properties was conducted. In the research of [Nes84] as well as [AB85] an orthotropic mount of the oscillator is analysed showing that two separate rotor speed ranges with stable balancing exist in these cases.

In [BH86], the multiple scales method was used to show that stable balancing is also possible with non-planar ABBs. On the other hand, eccentricities of the raceway have a disadvantageous effect, as investigated by [AB86] and [Maj88]. It was found that complete balancing is not possible and a residual vibration remains. The extension to three-dimensional rotors equipped with two ABBs to compensate for the moment and force due to imbalance was investigated by [SMD00]. The transient motions of the rotor and the balancing balls were investigated by numerical time integration of the equations of motion. In the investigation by [Ryz+01], using the method of direct separation of motion, an approximate solution was derived that allows for a determination of the operating range of stable balancing in the form of an explicit equation. However, this is limited to the planar case with isotropic bearing. In a subsequent study, see [RSD03], the same authors discussed the use of transient numerical simulations to identify an ideal viscous parameter for the fluid inside an ABB which optimizes both the subcritical and supercritical vibration response. Still, the authors lack indications on how to correlate the viscous

1.1. Current state of research

parameter with the physical properties of the fluid, namely density and viscosity.

Another aspect of the growing modelling depth is the implementation of rolling friction effects. In [Kan+01], an implementation of rolling friction is discussed, but a no-slip condition is still assumed in the raceway contact of the balls. A more detailed model 'based on Hertzian contact mechanics and hysteresis loss is established' in [CSL05], which is used to analyse ball mispositioning near their ideal balancing locations. This is done through the method of multiple scales as well as numerical simulations. Also in [Bol10] numerical simulations are utilized to examine the influence of different levels of rolling friction and adherence on the transient movement as well as the final resting positions of the balancing balls. This was followed by investigations striving for a better replication of the dissipative effects of ball collision in ABBs, as seen in [Ded16].

Only in more recent publications has the modelling depth of the damping effect on the balancing balls resulting from the relative motion in the fluid been increased. Huang et al. proposed a non-linear model based on the drag force with constant drag coefficients which are to be determined based on the 'ball size, shape, surface roughness and dynamic viscosity' ([Hua+02]), but without stating implementation details. In [SDW17] this approach was pursued further and a velocity-dependent formulation for determining the drag coefficient was presented. Another implementation of this approach was done in [Hai18], but in which the inertial effects of the fluid in the acceleration phase are still neglected.

In addition to the semi-analytical solutions, which can describe the basic behaviour and the stability properties of the planar oscillator with an ABB, numerical simulation is the common method used to capture the additional non-linear effects of friction and damping and to make statements about the transient behaviour.

1.2. Dissertation objective

The initial research project, which finally led to the objectives of this thesis, envisaged the design of an ABU for laboratory centrifuge rotors, which are not made of aluminium, as is usually the case, but of carbon fibre reinforced polymer (CFRP). By choosing this material, a weight reduction of more than 50% can be achieved [KSG13], which reduces the kinetic energy at operating speed and increases the safety of the containment in the event of an accident. In addition, this facilitates the handling of the rotors if a modular centrifuge with exchangeable rotors is used. However, the weight reduction has a disadvantageous effect on the imbalance-induced vibrations, since the expected imbalance remains unchanged and thus the vibration amplitude increases.

To simulatively optimize the configuration of the ABB, a multibody simulation approach is pursued. Since it can be assumed that the run-up process of laboratory centrifuges remains unchanged, special attention is devoted to the selection of the fluid in the annulus, since the density and viscosity significantly influence the transient positioning of the balancing masses. Finally, with knowledge of the ABB geometry and the operating parameters, it is intended to identify suitable fluid properties so that the transient vibration amplitudes are not significantly increased in the subcritical speed range and at the same time a rapid stable positioning of the balancing masses is achieved as soon as the supercritical speed range is reached.

In contrast to the previously listed models from the literature, the dissipative effect of the fluid on the balancing masses is represented by a non-linear calculation instead of a linear viscous one. Since the velocity of the balancing balls relative to the raceway and the mean fluid velocity is assumed to be significantly different in the run-up period compared to the balanced state at stationary supercritical operation, a corresponding significant difference in flow resistances is expected. This deviation is further increased by neglecting the fluid inertia in the annulus. Hence, this dependence on the flow regime defies linear modelling and the expected divergence rises with increasing rotor acceleration during run-up. In addition, the available sources with linear

1.3. Overview

viscous modelling lack a discussion on how the quantitative identification of the viscous damping coefficient should be achieved.

Nevertheless, certain boundaries and limits to the conducted research are set. As mentioned at the beginning of this section, only a basic ABB design, i.e., balls in an annulus filled with a Newtonian fluid, is considered. To mitigate the increase in vibration response at subcritical speeds, several design enhancements are proposed in the literature. A selection of which will be presented shortly in section 2.2 without discussing possible implementation details. Accordingly, active automatic balancing units in which sensors and actuators are used to identify and compensate for imbalances, see [ZLZ18; Jun20; JKJ20] for example, are also not discussed in the work at hand. The conducted experiments and simulations only consider either one or two balancing balls in order to maximize the possible distance between them and reduce the possibility of slipstream effects to be significant. In addition, the uncertainty in the initial conditions of every additional ball will likely increase the deviations between measurements and simulated results. Also, only one ABB is considered in each of the prototype rotors, resulting in a single balancing plane.

To summarize, the intent of this thesis is to present a multibody simulation implementation of the basic ABB design which is accessible to sensitivity analyses of the geometric parameters and the fluid properties, leaving only the coefficients of friction and rolling resistance for the lubricated contacts to be determined from experience or measurements.

1.3. Overview

In the following chapter 2 a compilation of use cases of ABBs in technical systems and products is given together with related research publications. Furthermore, the basic decision-making process in the design of ABBs and the trade-offs to be made are discussed. Finally, for completeness, proposed constructive modifications of the ABB are discussed but without going into specifics of the implementation or computational analysis.

1. Introduction

Chapter 3 covers the flow of Newtonian fluids, which form the basis for the simulation model investigated in this thesis for representing ABBs integrated in laboratory centrifuges.

Since the basic dynamic characteristics of ABBs can easily be shown on the model of the planar oscillator, in chapter 4 the differential equation system according to the Lagrangian method is derived and analysed, addressing the influences of the system parameters on the dynamic behaviour. In addition, a novel explicit equation for the determination of the stability in the isotropic case is presented, which is capable of replacing the numerical analysis of the eigenvalue problem.

In chapter 5 the implementation details for the developed multibody force element incorporating ABBs to transient analyses are given with a focus on the modelling approaches towards the drag and friction effects.

Chapter 6 accommodates studies on two rotor test rigs with ABBs comprising assemblies from laboratory centrifuges. The measurement results are utilized to look at the modelling of the flow effects in more detail and to validate the results of the multi-body simulations regarding stability as well as transient rotor deflection and positioning of the balancing masses. From the insights of the advanced drag modelling for the multibody simulation, a recommendation for the quantitative determination of the linear viscous damping coefficient is also derived.

Chapter 7 concludes the thesis with a summarized evaluation of the presented modelling approach and gives an outlook on further studies on the problem of automatic balancing units.

2. Application

Automatic balancing can support or even replace the conventional balancing of rotors, which are prone to unbalance excitation. The motivation for implementing an automatic compensation of unbalances can be different. Firstly, automatic balancers can be implemented in rotating machines which are produced in bulk, such as small ventilation fans [Cha93; BWo1; Oli+17; Fil+19], where an individual balancing of each rotor is not efficient from an economic point of view.

Secondly, automatic balancing devices adapt to changing states in unbalance during operation. Therefore, changes in the mass distribution of the rotor, which can be caused by wear or temperature dependent deformation for example, can be counteracted without the need to shut down the machine for a conventional rebalancing. This is especially beneficial for aircraft engines, gas turbine engines or agricultural machines [Fil+17]. Similarly, the accumulation and sudden detachment of ice on rotor blades under cold weather conditions can be counteracted, if the drive shaft is operated super-critically [HP16; Hai18]. Furthermore, consumer products which suffer from varying unbalance states during usage are not needed to be maintained for rebalancing. A good example are hand held power tools like angle grinders, see [Aga76], [Lin96], and [RR98]. In the general case of hand-operated rotating machinery, the implementation of ABUs is beneficial to reduce the imbalance induced accelerations to the user, where effective values are one of the major characteristics for occupational health and safety regulations. As the technology advances, these are also intensified, resulting in stricter requirements to the products. It is worth mentioning that in the case of hand-operated machines, the above-mentioned supercritical operation refers to the oscillating system including the operator, which therefore has a low first critical speed due to the comparatively high compliance of the hand guidance.

2. Application

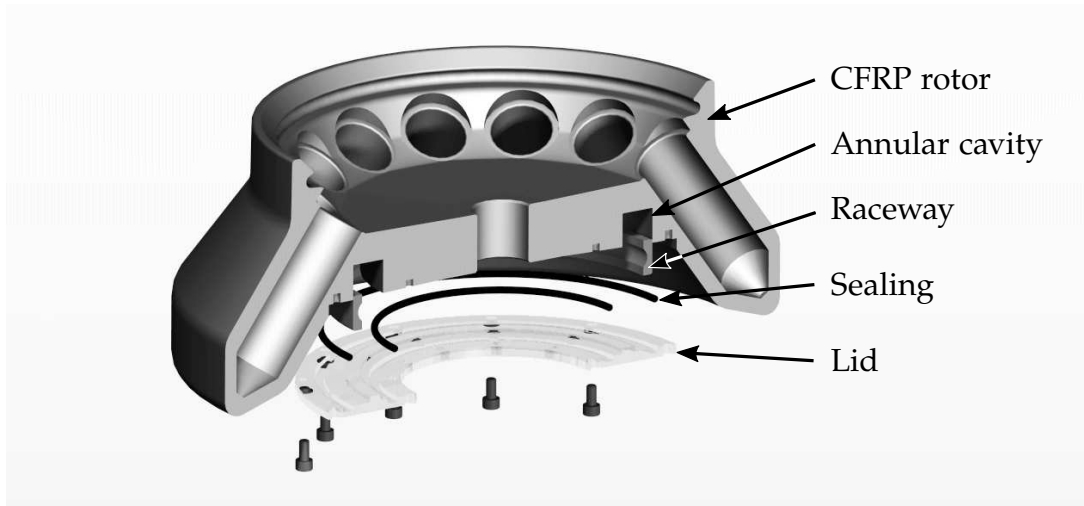


Figure 2.1.: Concept design of a tabletop centrifuge rotor with an integrated ABB.

Thirdly, a large group of rotating systems which can benefit from automatic balancers deal with variable unbalances due to their operating process, e.g., washing machines, samples centrifuges and optical disc drives. The clothes in washing machines are rearranged randomly during the washing cycle and can cause significant unbalance excitations during the spin cycle, which results in unpleasant noise levels or even the inability to pass the critical speed of the washing drum. The applicability of automatic balancers in laundry machines was examined by [Con94; CZW15; CJK14] and others. One essential problem is the subcritical operation during the washing cycles, where the automatic balancer has a negative effect on the unbalance state. Constructional improvements, see section 2.2, and customized run-up profiles [FA18] are therefore considered overcoming this problem.

Tabletop centrifuges, frequently used in the medical or chemical industry and research sectors, are used to separate liquid samples. To prevent excessive excitation, the operators are advised to weight the samples and distribute them symmetrically, which takes a non-negligible amount of set-up time. With a view to current efforts in producing lightweight CFRP centrifuge rotors, see [KSG13] for example, the use of automatic balancers helps to reduce the vibration and noise levels as well as the operating times while increasing the lifespan of the centrifuge bearings.

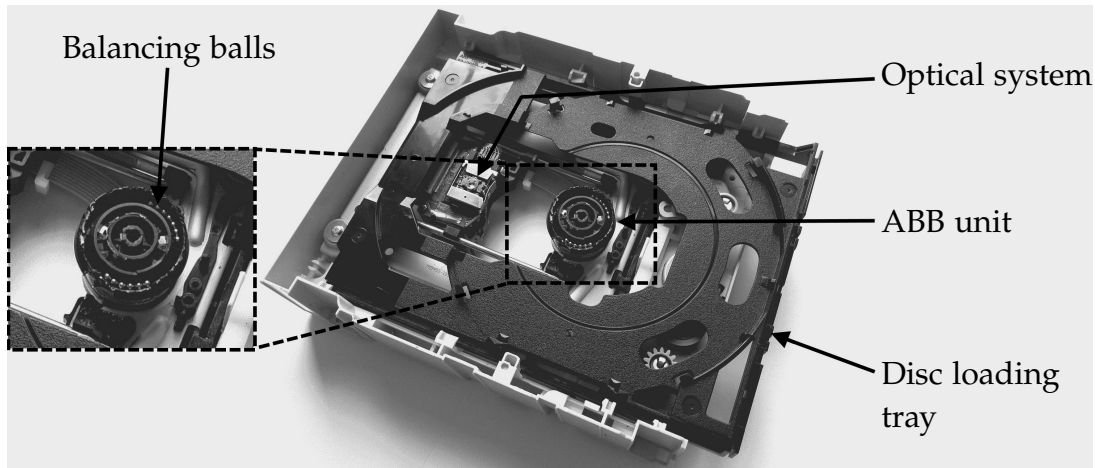


Figure 2.2.: Partially disassembled HP SH-216 DVD Writer Drive with ABB unit (pried open) to counterbalance variable disc unbalances.

Although the prevalence of optical drives is declining in favour of solid-state storage media today, ABB units are still found in many households in the form of DVD and Blu-ray drives, see fig. 2.2. As the rotor mass is mainly characterized by the mass-produced data carriers, which are not balanced individually, the ABB units are used to achieve high speeds and the associated data transfer rates [Hua+02; CSL05; Yan+05; LWH09].

Also influenced by change in unbalance but rather impulsively and at a higher rate are centrifugal crushers and centrifugal juicers, for example, with the latter being examined in [Gon+17b].

In contrast to the most use-cases of vibration reduction, the ball-balancer mechanism is also used to induce multi frequent vibrations to applicable systems [Yat+18; Fil+20; Yat20; Yat+20]. As will be shown in section 4.2, a speed range above the critical frequency exists where the balancing masses circulate with the critical frequency while the rotor rotates together with the primary unbalance at a higher speed. Therefore, the system is excited by unbalance forces of two different frequencies whose difference can be tuned by the balancer design parameters. Such excitations are desired in the operation of screen boxes, vibrating sieves and separators where the lower frequency is performing the main technical process and the higher frequency is exploited

2. Application

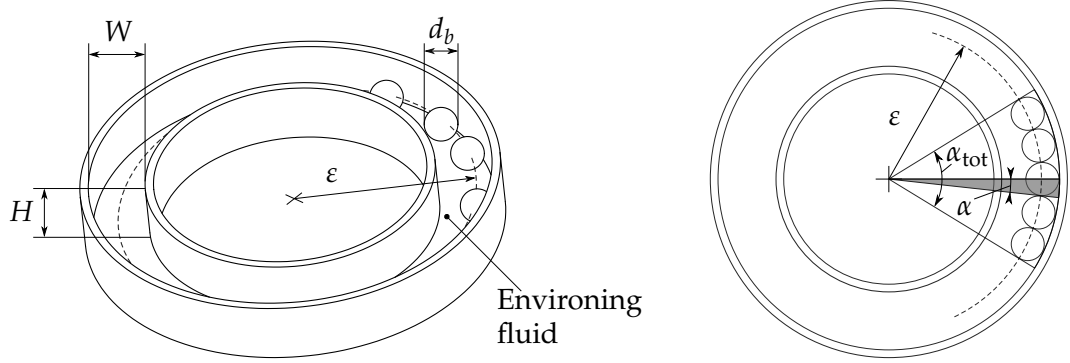


Figure 2.3.: Basic design parameters of an automatic ball balancer. Oblique perspective (left) and top view (right).

for the self-cleaning process of the machine. In [Yat+17] an experimental investigation on a screen box equipped with a ball-balancer was conducted.

2.1. Challenges in the design of automatic ball balancers

The initial question raised in the design of ABBs is the expected unbalance to be compensated. With the choice of the number of balancing balls n , the orbit radius ε , the ball diameter d_b and ball material density ρ_b the maximum balancing potential can be determined. Since the available design space to accommodate the annular ABB assembly, roughly defined by the height H and width W of the cavity as well as the orbit radius, is often limited, the expectable potential is directly affected. The balancing capability U_b of one ball is determined with

$$U_b = \frac{1}{6} \pi d_b^3 (\rho_b - \rho_{fl}) \varepsilon, \quad (2.1)$$

where, due to the buoyancy in the environing fluid, the effective mass is used. With

$$\alpha = \arcsin \left(\frac{d_b}{2\varepsilon} \right) \quad (2.2)$$

2.1. Challenges in the design of automatic ball balancers

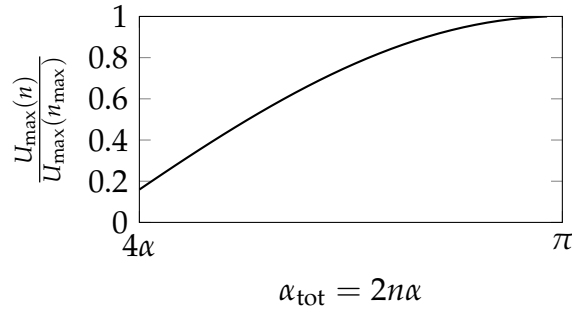


Figure 2.4.: Increase of the exploited ABB potential as a function of the sector occupied by the balls.

being half of the sector occupied by one ball, see fig. 2.3, the total occupied sector is $\alpha_{\text{tot}} = 2n\alpha$ and the maximum balancing capability is reached when half of the annulus is filled, i.e., $\alpha_{\text{tot}} \approx \pi$ and $n = n_{\max} = \lfloor \frac{\pi}{2\alpha} \rfloor$. This results in a total maximum balancing capability U_{\max} of a one track balancing device with n balls of

$$\frac{U_{\max}(n)}{U_b} = \text{mod}(n, 2) \left[1 + \sum_{j=2}^n 2 \cos((j-1)\alpha) \text{mod}(j, 2) \right] + \text{mod}(n-1, 2) \sum_{j=2}^n 2 \cos((j-1)\alpha) \text{mod}(j-1, 2) \quad \forall n \leq \lfloor \frac{\pi}{2\alpha} \rfloor, \quad (2.3)$$

where the term in brackets disappears for an even number of balls n and the remaining term disappears if n is uneven. Through trigonometry, leading to the cosine terms in eq. (2.3), it can be seen that as the total number of balls increases, the individual contribution to the total capability decreases, as shown in fig. 2.4. Although adding further balls, exceeding n_{\max} , lowers the balancing capability again, this has the advantage of reduced response time when the rotor imbalance changes, since the individual balls have less distance to travel along the orbit. The latter configuration may be considered for use cases with impulsive imbalance changes in which the additional mass of the ABB unit is incidental to the design.

Even though rotational symmetry of the balancing masses along its axis parallel to the rotation axis is sufficient, and therefore cylinders and rollers are

2. Application

possible, the contact area with the outer wall is reduced to a minimum for spherical geometries leading to less friction. As will be discussed throughout this thesis, the reduction of friction is a central point in increasing efficiency, since it causes non-ideal positioning of the balls and therefore residual imbalance. Despite the better volume exploitation through cylindrical geometries in the annular cavity, the disadvantage of increased friction predominates in many cases. Therefore, only spherical balancing masses are considered in the following. However, regarding the presented equations and modelling approaches, a transfer to cylindrical geometries of the compensating masses is often possible with minor adjustments. To minimize friction, it is advised to use incompressible and surface finished balls and raceways. The outer ring and balls of a radial ball bearing are particularly well-suited as discussed in [Lin96] and readily available in an abundant number of dimensions. For regular deep groove ball bearings [SKF18] the ratio $d_b / (2\epsilon)$ ranges from 0.05 to 0.27 and for thin section bearings [Sch14] it ranges from 0.012 to 0.065. Since the ball diameter and orbit radii are usually not explicitly stated in catalogues, a table for common bearings is given in appendix C. If the rotor system in question has wide margins regarding the permissible ABB dimensions and the balancing capacity is stipulated, the diameter of the balls can be optimized, as investigated in [IMZ12] and [Gon+17a].

Contrary to the previously mentioned aspects, which are subject to minimization or maximization, the selection of the fluid surrounding the balancing balls in the annulus requires a more differentiated examination. Fluids of low viscosity exert correspondingly less damping on the balls, so that long periods of time are required until the velocity difference to the rotor is diminished, and the balls have positioned themselves optimally. In the opposite case of too high viscosity, the damping forces may cause synchronization with the rotor frequency to occur quickly, but the subsequent positioning due to the inertial effects is subject to high resistance. To prevent the fluid from leaking out of the ABB, suitable seals or encapsulation of the entire unit must also be planned. This is correspondingly less complicated with fluids of higher viscosity and surface tension.

2.2. *Constructional variations and improvements*

The general conflicts of technical and economic objectives in the design thus lie in

- maximizing the balancing potential
- adhering to the space limitations
- reducing the overall mass contributed by the ABB
- reducing form and position tolerances of the raceway
- choosing a suitable fluid to optimize the transient behaviour.

2.2. Constructional variations and improvements

In addition to the basic design depicted in fig. 2.3 on page 12 various alternative designs and improvements have been proposed and investigated in the literature. Due to the resulting increase in unbalance when an automatic balancer is operated below the critical speed of the rotor for a significant amount of time, additional mechanisms to prevent or reduce sub-critical excitation have been proposed. One method to avoid the increase in imbalance at subcritical speeds is to block the balancing masses in a neutral position until the critical speed is exceeded. Using springs aligned between the balancing masses in the circumferential direction, see fig. 2.5a, a concentration of the masses can be prevented until the critical speed is surpassed. By altering the spring stiffness, this can be adapted to the respective rotor system [KN13]. Unfortunately, the forces acting in the circumferential direction that load the springs depend on the eccentricity of the rotor. When the ABB reaches a balanced state and thus diminishing the eccentricity, the balls are moved from their ideal resting position. As a result, the modification with circumferential springs is not able to balance the rotor completely.

A different enhancement with passive components is presented in [CJ17] in the application of washing machines. With the use of permanent magnets, the balls will be held at a neutral position on the inner wall of the annulus as long as the magnetic forces provide the necessary centripetal force to prevent detachment, see fig. 2.5b.

2. Application

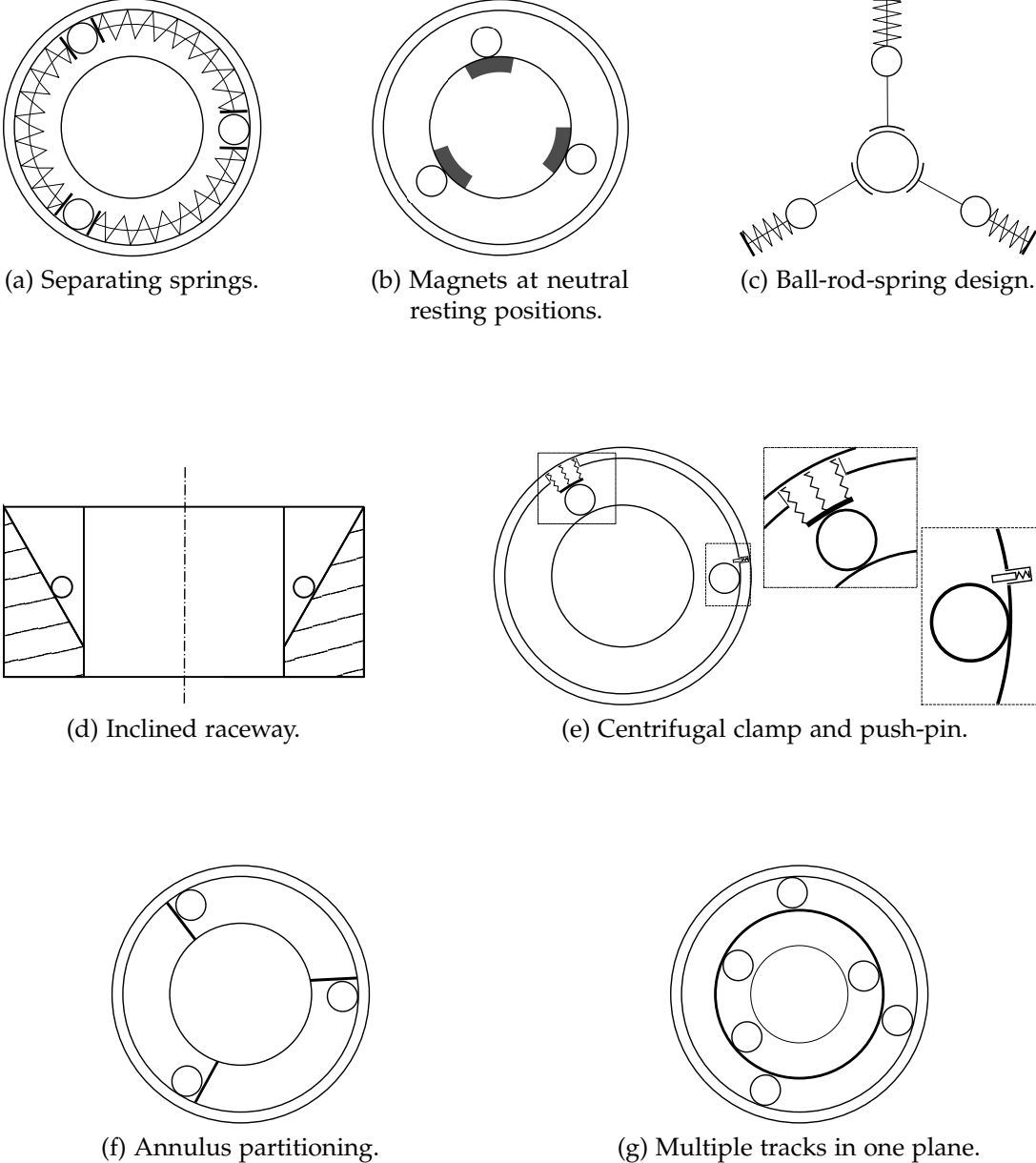


Figure 2.5.: Ball-balancer modifications to reduce unbalance increase at sub-critical speeds.

2.2. *Constructional variations and improvements*

By using springs in the radial direction and guiding the balls on rods, which can rotate independently, fig. 2.5c, the unbalance radii of the masses are increasing with the rotor speed, hence leading to a smaller impact during subcritical speeds and maximum balancing effect at supercritical speeds, see [LW11] and [RF15]. Due to the structure, however, this variant is more related to pendulum balancers since the spherical shape of the masses is not mandatory.

In [Kel87] an inclined outer raceway is proposed, causing the balls to have increased orbit radii at higher speeds, see fig. 2.5d. However, this approach requires gravity parallel to the rotor axis and considerable axial installation space.

Spring-loaded components such as push-pins and clamping plates can be added to the raceway to block the ball movement, see fig. 2.5e. At sufficient speeds, the springs are compressed to such an extent that the obstructing components recess into the raceway and an unhindered movement of the balls is achieved. Experimental studies on a radial clamping mechanism are presented in [CCA16] and a numerical simulation model is implemented in [Hai18].

In [IMZ12] different enhancements to the ABB are discussed. In particular, the partitioning of the annulus is proposed to limit the imbalance increase at subcritical speeds, as shown in fig. 2.5f. While this modification also reduces the maximum balancing capacity, this method is suitable if the expected rotor imbalance is low enough and the available freedom of movement in each sector is sufficient.

Finally, as shown in [HC99], the radial juxtaposition of several raceways is proposed. Hereby the mutual contact between the balls is reduced and two balls in different raceways can occupy the same angular position, see fig. 2.5g. Additionally, as mentioned in [CJ17], the assembly of several sealed annuli allows the utilization of different fluids so that the damping effects can differ significantly. As a result, the balancing balls of different tracks experience unequal acceleration and therefore the transient excitation is lower on average due to the partial neutralization of each other. At steady supercritical opera-

2. *Application*

tion, the different fluid damping of the tracks has no negative influence on the automatic balancing of the rotor.

The presented modifications provide different approaches to positively influence the dynamic behaviour of ABBs. However, due to the more complex design, these are also associated with higher manufacturing costs and may cause unanticipated complications. Therefore, the focus in the conducted experiments and numerical simulations presented in this thesis lies on the conventional, one track automatic ball balancer with a constant runway radius.

3. Navier-Stokes equations in cylindrical domains

The Navier-Stokes equations represent the application of Newton's second law to fluid motion while assuming viscous flow and are evaluated to describe the fluid flow. No closed form solution exists for the non-linear partial differential equations (PDE). Due to the rectangular geometry of the fluid filled annulus in automatic ball-balancers, the Navier-Stokes equations will be presented and numerically solved in the cylindrical coordinates r, θ, z . An extensive derivation is given in appendix A.2, following the explanations provided in [Mic20].

Continuity equation

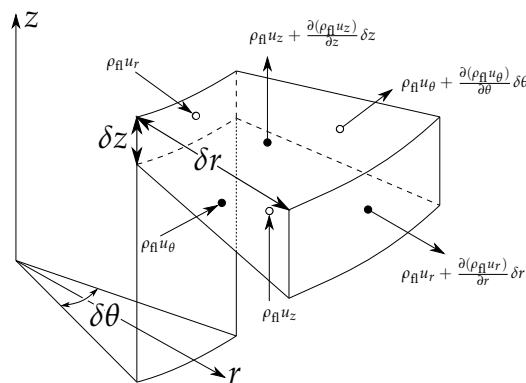


Figure 3.1.: In- and outgoing mass flows of an infinitesimal volume in cylindrical coordinates.

Let

$$\underline{u}(r, \theta, z, t) = u_r(r, \theta, z, t)\underline{e}_r + u_\theta(r, \theta, z, t)\underline{e}_\theta + u_z(r, \theta, z, t)\underline{e}_z \quad (3.1)$$

3. Navier-Stokes equations in cylindrical domains

be the velocity vector of a fluid in a cylindrical domain. Considering an infinitesimal volume in cylindrical coordinates, fig. 3.1, summing the in- and outgoing mass flows and demanding mass conservation yields, under the assumption of an incompressible fluid and therefore constant density ρ_{fl} , the continuity equation

$$0 = \frac{1}{r} \frac{\partial(ru_r)}{\partial r} + \frac{1}{r} \frac{\partial u_\theta}{\partial \theta} + \frac{\partial u_z}{\partial z}. \quad (3.2)$$

Momentum equation

The Cauchy momentum equation in convective form reads

$$\frac{D\mathbf{u}}{Dt} = \frac{1}{\rho_{fl}} \nabla \cdot \underline{\underline{\sigma}} + \underline{\underline{g}}, \quad (3.3)$$

where $\frac{D\mathbf{u}}{Dt}$ describes the total differential of the velocity field \mathbf{u} with respect to time, $\nabla \cdot \underline{\underline{\sigma}}$ is the gradient of the stress tensor $\underline{\underline{\sigma}}$ and $\underline{\underline{g}}$ describes the body forces [Ach90]. The gradient of the stress tensor can be derived by summing up the forces acting on the infinitesimal volume, fig. 3.2, referring them to the volume $r\delta r\delta\theta\delta z$ and forming the limit value with $\delta r \rightarrow 0$, $\delta\theta \rightarrow 0$, $\delta z \rightarrow 0$, reading

$$\begin{aligned} \nabla \cdot \underline{\underline{\sigma}} = & \left(\frac{\sigma_{rr}}{r} + \frac{\partial\sigma_{rr}}{\partial r} + \frac{1}{r} \frac{\partial\sigma_{r\theta}}{\partial\theta} + \frac{\partial\sigma_{rz}}{\partial z} - \frac{\sigma_{\theta\theta}}{r} \right) \mathbf{e}_r \\ & + \left(\frac{2}{r} \sigma_{r\theta} + \frac{\partial\sigma_{r\theta}}{\partial r} + \frac{1}{r} \frac{\partial\sigma_{\theta\theta}}{\partial\theta} + \frac{\partial\sigma_{\theta z}}{\partial z} \right) \mathbf{e}_\theta \\ & + \left(\frac{1}{r} \sigma_{rz} + \frac{\partial\sigma_{rz}}{\partial r} + \frac{1}{r} \frac{\partial\sigma_{\theta z}}{\partial\theta} + \frac{\partial\sigma_{zz}}{\partial z} \right) \mathbf{e}_z. \end{aligned} \quad (3.4)$$

Under the assumption of incompressibility and viscous flow, the components

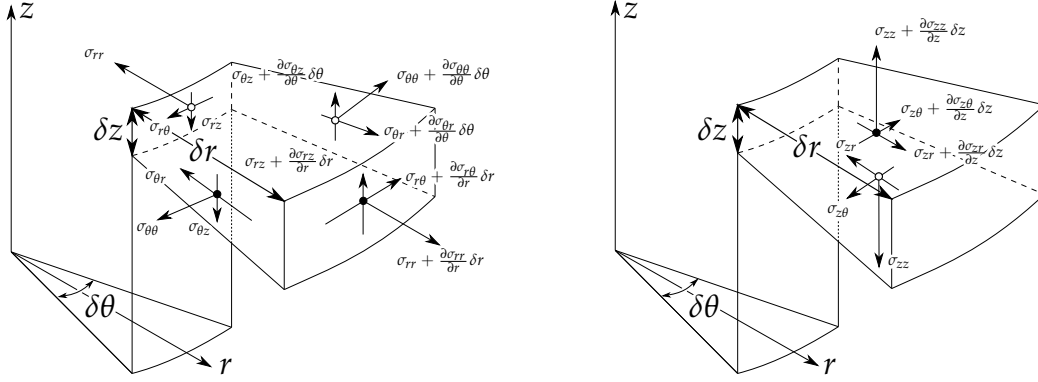


Figure 3.2.: Stresses on an infinitesimal volume in cylindrical coordinates.

of the stress tensor read

$$\begin{aligned}
 \sigma_{rr} &= -p + 2\nu\rho_{fl} \frac{\partial u_r}{\partial r}, & \sigma_{r\theta} = \sigma_{\theta r} &= \nu\rho_{fl} \left(\frac{1}{r} \frac{\partial u_r}{\partial \theta} + \frac{\partial u_\theta}{\partial r} - \frac{u_\theta}{r} \right), \\
 \sigma_{\theta\theta} &= -p + 2\nu\rho_{fl} \left(\frac{1}{r} \frac{\partial u_\theta}{\partial \theta} + \frac{u_r}{r} \right), & \sigma_{rz} = \sigma_{zr} &= \nu\rho_{fl} \left(\frac{\partial u_r}{\partial z} + \frac{\partial u_z}{\partial r} \right), \\
 \sigma_{zz} &= -p + 2\nu\rho_{fl} \frac{\partial u_z}{\partial z}, & \sigma_{\theta z} = \sigma_{z\theta} &= \nu\rho_{fl} \left(\frac{1}{r} \frac{\partial u_z}{\partial \theta} + \frac{\partial u_\theta}{\partial z} \right),
 \end{aligned} \quad (3.5)$$

where p and ν describe the isotropic pressure and the kinematic viscosity, respectively. Substituting eq. (3.4) and eq. (3.5) in eq. (3.3) the Navier-Stokes

3. Navier-Stokes equations in cylindrical domains

equations (3.6)-(3.8) in cylindrical domains are obtained

$$\begin{aligned} \rho_{fl} \left(\frac{\partial u_r}{\partial t} + u_r \frac{\partial u_r}{\partial r} + \frac{u_\theta}{r} \frac{\partial u_r}{\partial \theta} + u_z \frac{\partial u_r}{\partial z} - \frac{u_\theta^2}{r} \right) &= -\frac{\partial p}{\partial r} + \rho_{fl} g_r \\ &+ \nu \rho_{fl} \left(\frac{1}{r} \frac{\partial}{\partial r} \left(r \frac{\partial u_r}{\partial r} \right) + \frac{1}{r^2} \frac{\partial^2 u_r}{\partial \theta^2} + \frac{\partial^2 u_r}{\partial z^2} - \frac{u_r}{r^2} - \frac{2}{r^2} \frac{\partial u_\theta}{\partial \theta} \right), \end{aligned} \quad (3.6)$$

$$\begin{aligned} \rho_{fl} \left(\frac{\partial u_\theta}{\partial t} + u_r \frac{\partial u_\theta}{\partial r} + \frac{u_\theta}{r} \frac{\partial u_\theta}{\partial \theta} + u_z \frac{\partial u_\theta}{\partial z} + \frac{u_r u_\theta}{r} \right) &= -\frac{1}{r} \frac{\partial p}{\partial \theta} + \rho_{fl} g_\theta \\ &+ \nu \rho_{fl} \left(\frac{1}{r} \frac{\partial}{\partial r} \left(r \frac{\partial u_\theta}{\partial r} \right) + \frac{1}{r^2} \frac{\partial^2 u_\theta}{\partial \theta^2} + \frac{\partial^2 u_\theta}{\partial z^2} + \frac{2}{r^2} \frac{\partial u_r}{\partial \theta} - \frac{u_\theta}{r^2} \right), \end{aligned} \quad (3.7)$$

$$\begin{aligned} \rho_{fl} \left(\frac{\partial u_z}{\partial t} + u_r \frac{\partial u_z}{\partial r} + \frac{u_\theta}{r} \frac{\partial u_z}{\partial \theta} + u_z \frac{\partial u_z}{\partial z} \right) &= -\frac{\partial p}{\partial z} + \rho_{fl} g_z \\ &+ \nu \rho_{fl} \left(\frac{1}{r} \frac{\partial}{\partial r} \left(r \frac{\partial u_z}{\partial r} \right) + \frac{1}{r^2} \frac{\partial^2 u_z}{\partial \theta^2} + \frac{\partial^2 u_z}{\partial z^2} \right). \end{aligned} \quad (3.8)$$

Stream function formulation for axisymmetric flow

Assuming symmetry of the fluid flow in the annulus with respect to the azimuthal coordinate θ , all partial derivatives with respect to θ equal zero and the Navier-Stokes equations can be reduced to a two dimensional problem in the r - z -plane, see appendix A.3. By introducing the stokes stream function ψ and the angular momentum Γ according to

$$\underline{u} = -\frac{1}{r} \frac{\partial \psi}{\partial z} \underline{e}_r + \frac{1}{r} \Gamma \underline{e}_\theta + \frac{1}{r} \frac{\partial \psi}{\partial r} \underline{e}_z, \quad (3.9)$$

the continuity equation (3.2) is fulfilled automatically and the Navier-Stokes equations can be transformed to one elliptic PDE of the Poisson type in ψ and

two parabolic PDEs in η and Γ respectively, reading

$$\frac{\partial \Gamma}{\partial t} = \frac{1}{r} \frac{\partial \Gamma}{\partial r} \frac{\partial \psi}{\partial z} - \frac{1}{r} \frac{\partial \Gamma}{\partial z} \frac{\partial \psi}{\partial r} + \nu \left(\frac{\partial^2 \Gamma}{\partial r^2} - \frac{1}{r} \frac{\partial \Gamma}{\partial r} + \frac{\partial^2 \Gamma}{\partial z^2} \right), \quad (3.10)$$

$$\begin{aligned} \frac{\partial \eta}{\partial t} = & -\frac{1}{r} \frac{\partial \psi}{\partial r} \frac{\partial \eta}{\partial z} + \frac{1}{r} \frac{\partial \psi}{\partial z} \frac{\partial \eta}{\partial r} - \frac{1}{r^2} \eta \frac{\partial \psi}{\partial z} + \frac{2}{r^3} \Gamma \frac{\partial \Gamma}{\partial z} \\ & + \nu \left(\frac{\partial^2 \eta}{\partial r^2} + \frac{\partial^2 \eta}{\partial z^2} + \frac{1}{r} \frac{\partial \eta}{\partial r} - \frac{1}{r^2} \eta \right), \end{aligned} \quad (3.11)$$

$$-r\eta = \frac{\partial^2 \psi}{\partial r^2} - \frac{1}{r} \frac{\partial \psi}{\partial r} + \frac{\partial^2 \psi}{\partial z^2}, \quad (3.12)$$

with η being the vorticity component of the flow in azimuthal direction. The boundary conditions at the walls for the rotating annulus problem are of the Neumann type and are given in fig. 3.3 for the stream function ψ [LS98; PTA12]. Assuming annular geometries with inner walls and therefore $r_{\text{out}} > r_{\text{in}} > 0$, the coordinate singularity at $r = 0$ is of no concern.

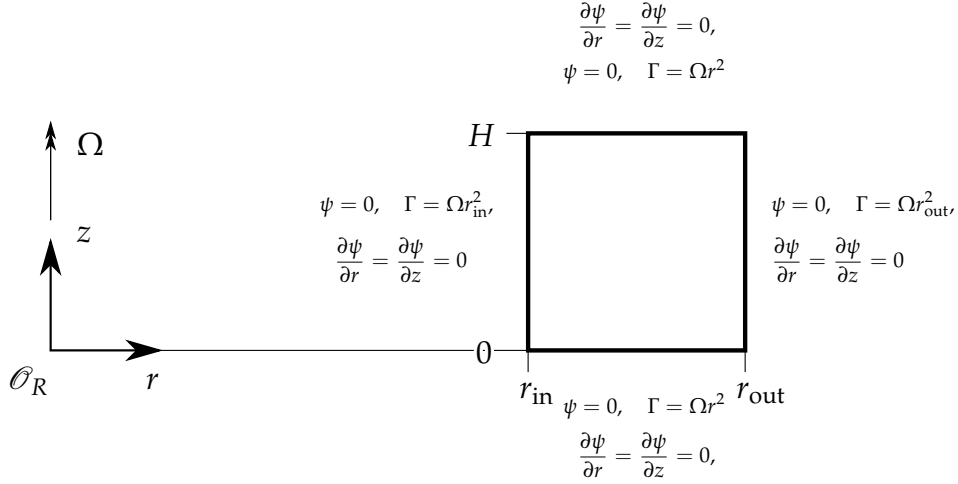


Figure 3.3.: Boundary conditions for the rotating annulus problem in the stream function formulation.

Finite difference solution

Despite spectral solution methods have been shown to be efficient in solving the presented flow problem, e.g. [LS98], the extensively used finite difference scheme is used in the present work to solve the system of equations (3.10), (3.11) and (3.12). Lacking boundary conditions for the vorticity η , an explicit time discretization is proposed in the literature [LS98], [PTA12].

Based on a second-order centered differences discretization in space on the grid points (r_i, z_j) the equations (3.10)-(3.12) result in the system

$$\frac{\partial}{\partial t} \Gamma_{ij} = G_1(\Gamma_{ij}, \eta_{ij}, \psi_{ij}), \quad (3.13)$$

$$\frac{\partial}{\partial t} \eta_{ij} = G_2(\Gamma_{ij}, \eta_{ij}, \psi_{ij}), \quad (3.14)$$

$$\frac{\partial^2 \psi_{ij}}{\partial r^2} - \frac{1}{r_i} \frac{\partial \psi_{ij}}{\partial r} + \frac{\partial^2 \psi_{ij}}{\partial z^2} = -r_i \eta_{ij}, \quad (3.15)$$

where G_1 and G_2 describe the finite difference representations of the right hand sides of equations (3.10) and (3.11), respectively. Equation (3.15), evaluated with the boundary conditions for ψ , gives

$$\eta = -\frac{1}{r} \frac{\partial^2 \psi}{\partial z^2} \quad (3.16)$$

for the walls in radial direction and

$$\eta = -\frac{1}{r} \frac{\partial^2 \psi}{\partial r^2} \quad (3.17)$$

for the walls in axial direction. The second-order predictor-corrector scheme is implemented in accordance with [LS98] as follows. The superscripts k , $*$ and $k+1$ denote the solutions of the current time step, the intermediate predictor step and the next time step, respectively.

1. Evaluate

$$\Gamma_{ij}^* = \Gamma_{ij}^k + 0.5 \Delta t_{\text{NSE}} G_1 \left(\Gamma_{ij}^k, \eta_{ij}^k, \psi_{ij}^k \right)$$

$$\eta_{ij}^* = \eta_{ij}^k + 0.5 \Delta t_{\text{NSE}} G_2 \left(\Gamma_{ij}^k, \eta_{ij}^k, \psi_{ij}^k \right)$$

on the interior grid nodes.

2. Solve the Poisson equation

$$\frac{\partial^2 \psi_{ij}^*}{\partial r^2} - \frac{1}{r_i} \frac{\partial \psi_{ij}^*}{\partial r} + \frac{\partial^2 \psi_{ij}^*}{\partial z^2} = -r_i \eta_{ij}^*,$$

3. Implement boundary conditions on Γ^* and η^*

4. Evaluate

$$\Gamma_{ij}^{k+1} = \Gamma_{ij}^k + \Delta t_{\text{NSE}} G_1 \left(\Gamma_{ij}^*, \eta_{ij}^*, \psi_{ij}^* \right)$$

$$\eta_{ij}^{k+1} = \eta_{ij}^k + \Delta t_{\text{NSE}} G_2 \left(\Gamma_{ij}^*, \eta_{ij}^*, \psi_{ij}^* \right)$$

on the interior grid nodes.

5. Solve the Poisson equation

$$\frac{\partial^2 \psi_{ij}^{k+1}}{\partial r^2} - \frac{1}{r_i} \frac{\partial \psi_{ij}^{k+1}}{\partial r} + \frac{\partial^2 \psi_{ij}^{k+1}}{\partial z^2} = -r_i \eta_{ij}^{k+1},$$

6. Implement boundary conditions on Γ^{k+1} and η^{k+1}

7. Go to the next time step.

The generalized cyclic reduction routine BLKTRI from the FISHPACK package [SS76] can solve the Poisson equations on staggered grids efficiently. The numerical convergence of a cartesian finite difference scheme is subject to the necessary Courant-Friedrichs-Lewy condition [CFL67]

$$\text{CFL} = \left(\frac{|u_x|}{\Delta x} + \frac{|u_y|}{\Delta y} \right) \Delta t_{\text{NSE}} \leq \text{CFL}_{\text{max}} = 1, \quad (3.18)$$

3. Navier-Stokes equations in cylindrical domains

with Δx and Δy being the grid spacing. For the chosen coordinates r and z in the stream function formulation, as stated in eq. (3.9), condition (3.18) reads

$$\text{CFL} = \frac{1}{r} \left(\frac{1}{\Delta r} \frac{\partial \psi}{\partial z} + \frac{1}{\Delta z} \frac{\partial \psi}{\partial r} \right) \Delta t_{\text{NSE}} \leq \text{CFL}_{\text{max}} = 1 \quad (3.19)$$

and therefore

$$\Delta t_{\text{NSE}} \leq r \left(\frac{1}{\Delta r} \frac{\partial \psi}{\partial z} + \frac{1}{\Delta z} \frac{\partial \psi}{\partial r} \right)^{-1} \text{CFL}_{\text{max}}. \quad (3.20)$$

Due to the boundary conditions specified in the flow problem under consideration, the highest gradients in ψ are encountered near the walls. Therefore, the use of a staggered grid is advised in order to avoid small time-steps. A stagger according to

$$r_i = r_{\text{out}} \left(\frac{r_{\text{in}}}{r_{\text{out}}} + \left(1 - \frac{r_{\text{in}}}{r_{\text{out}}} \right) \left(\frac{i}{n_r} - a_r \sin \left(2\pi \frac{i}{n_r} \right) \right) \right) \quad (3.21)$$

$$z_j = H \left(\frac{j}{n_z} - a_z \sin \left(2\pi \frac{j}{n_z} \right) \right) \quad (3.22)$$

with $n_r = n_z = 32$ grid points in both directions results in the mesh depicted in fig. 3.4. The stretching factors a_r and a_z are from $[0, 1[$ where a value of zero results in no staggering. The central finite difference coefficients for the derivatives on a non-uniform grid spacing, as shown in fig. 3.5, are summarized in table 3.1 for a discretisation of ψ in radial direction. The discretisation in z follows accordingly.

Table 3.1.: Finite difference coefficients for the first and second derivative on a non-uniform mesh [Lyn05].

	ψ_{i-1}	ψ_i	ψ_{i+1}
$(h_1 h_2^2 + h_2 h_1^2) \frac{\partial \psi_i}{\partial r}$	$-h_2^2$	$h_2^2 - h_1^2$	h_1^2
$(h_1 h_2^2 + h_2 h_1^2) \frac{\partial^2 \psi_i}{\partial r^2}$	$2h_2$	$-2(h_1 + h_2)$	$2h_1$

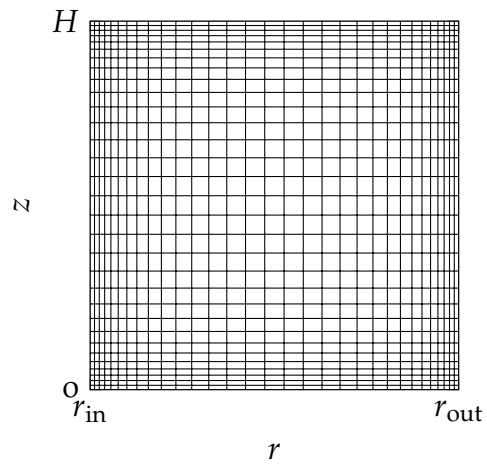


Figure 3.4.: A staggered grid with 32×32 grid points and stretching factors of $a_r = a_z = 0.1$.

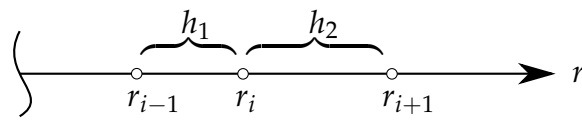


Figure 3.5.: Finite difference grid points on a non-uniform mesh given exemplarily for the radial coordinate.

4. Translational oscillator model

The planar model of an oscillator is the earliest mechanical surrogate in the field of ABBs and has been extensively studied in the literature, cf. section 1.1 of this work. Conclusions from said research on this model can be transferred to a wide range of applications making use of passive ABBs. In section 4.2 the major factors of influence on the dynamic behaviour of ABBs are compiled.

In addition to the established solutions and analyses for this model, however, a new explicit equation for determining the stability limit for the isotropic case is derived in section 4.2.2.

Contrary to the model in [Bol10], friction is not taken into account in the equations of motion, as the non-linear characteristic makes the analysis of the dynamics only accessible through numerical simulation. However, a discussion of the principal influences of friction on the ABB behaviour is given in section 4.2.3.

4.1. Equations of motion

Using Lagrange's method, the equations of motion for a translational oscillator with an automatic balancer containing n number of balls in one track can be derived from

$$\frac{d}{dt} \frac{\partial L}{\partial \dot{q}_j} - \frac{\partial L}{\partial q_j} = \frac{\partial W_{\text{diss}}}{\partial q_j}, \quad (4.1)$$

with

$$L = T - V \quad (4.2)$$

4.1. Equations of motion

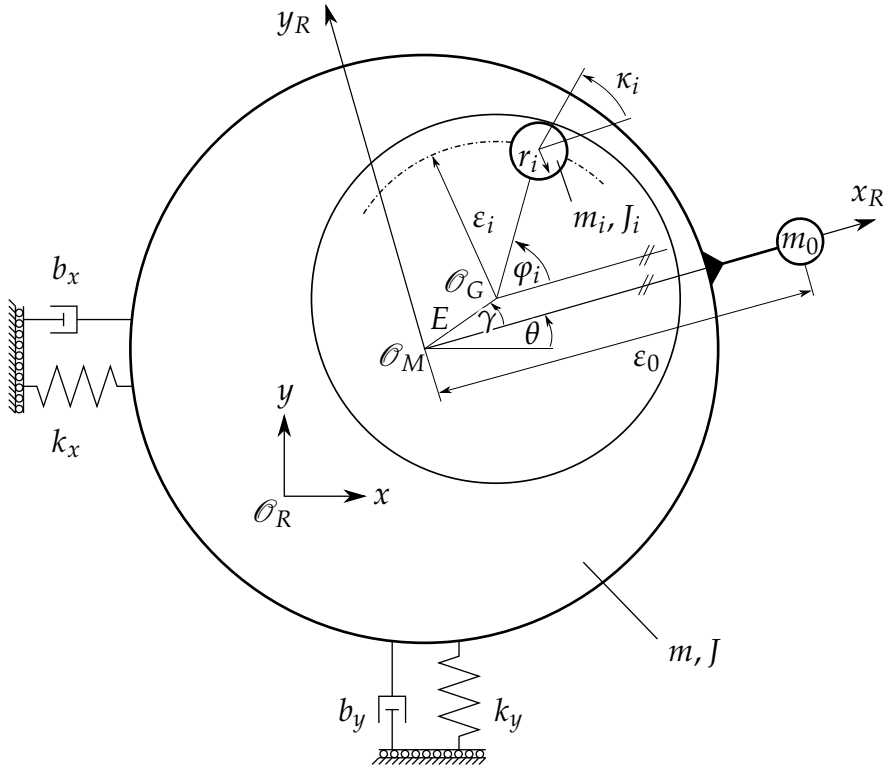


Figure 4.1.: Translational oscillator with primary unbalance and one counterbalancing mass of a balancer with an eccentricity.

being Lagrange's function and T and V being the kinetic and potential energy, respectively. W_{diss} represents the dissipative work and q_j are the j generalized coordinates.

Considering a rotor with translatory degrees of freedom perpendicular to the axis of rotation, as depicted in fig. 4.1, x and y denote the deflection of the rotors ideal centre of mass \mathcal{O}_M from the rotation axis \mathcal{O}_R . The primary imbalance of the rotor is defined by the mass m_0 located at a distance of ϵ_0 from \mathcal{O}_M . Its location is used to define the angle of rotation θ of the rotor fixed coordinate system $x_R - y_R$.

In relation to the rotor, the balancing unit has an eccentric raceway, with its centre \mathcal{O}_G being defined by the eccentricity E and the angle γ . The n balancing balls, with mass m_i , radius r_i and moment of inertia J_i are guided by the raceway on circular orbits with radius ϵ_i . The individual position of each balls

4. Translational oscillator model

centre of mass regarding the primary imbalance is denoted by the angle φ_i while κ_i describes the rotation of the ball about its central axis.

For the oscillator, orthotropically mounted in the $x - y$ plane by linear springs with spring constants k_x and k_y and linear dampers with constants b_x and b_y , follows

$$V = \frac{1}{2} (k_x x^2 + k_y y^2) . \quad (4.3)$$

The kinetic energy results in

$$T = T_R + T_0 + \sum_{i=1}^n T_i , \quad (4.4)$$

with

$$T_R = \frac{1}{2} (m (\dot{x}^2 + \dot{y}^2) + J\dot{\theta}^2) , \quad (4.5)$$

$$T_0 = \frac{1}{2} m_0 (\dot{x}_0^2 + \dot{y}_0^2) , \quad (4.6)$$

and

$$T_i = \frac{1}{2} (m_i (\dot{x}_i^2 + \dot{y}_i^2) + J_i \dot{\kappa}_i^2) \quad (4.7)$$

being the kinetic energies of the rotor itself, the primary imbalance and the n balls, respectively. Using the no-slip rolling condition

$$\varepsilon_i \varphi_i + (\kappa_i - \theta) r_i = 0 \quad (4.8)$$

and x, y, θ, φ_i as generalized coordinates, the inertial coordinates of the

4.1. Equations of motion

centres of mass can be represented as

$$\begin{aligned}
 x_0 &= x + \varepsilon_0 \cos(\theta), & x_i &= x + \varepsilon_i \cos(\theta + \varphi_i) + E \cos(\theta + \gamma), \\
 y_0 &= y + \varepsilon_0 \sin(\theta), & y_i &= y + \varepsilon_i \sin(\theta + \varphi_i) + E \sin(\theta + \gamma), \\
 \kappa_i &= \theta - \frac{\varepsilon_i}{r_i} \varphi_i.
 \end{aligned} \tag{4.9}$$

The Lagrange function follows as

$$\begin{aligned}
 L &= \frac{M}{2} (\dot{x}^2 + \dot{y}^2) - \frac{1}{2} (k_x x^2 + k_y y^2) \\
 &+ \sum_{i=1}^n m_i \varepsilon_i (\cos(\theta + \varphi_i) \dot{y} - \sin(\theta + \varphi_i) \dot{x}) \dot{\varphi}_i \\
 &+ \sum_{i=1}^n \left(\frac{J_i \varepsilon_i^2}{2r_i^2} + \frac{m_i \varepsilon_i^2}{2} \right) \dot{\varphi}_i^2 \\
 &+ \sum_{i=1}^n \left(E m_i \varepsilon_i \cos(\gamma - \varphi_i) - \frac{J_i \varepsilon_i}{r_i} + m_i \varepsilon_i^2 \right) \dot{\varphi}_i \dot{\theta} \\
 &+ \left((\cos(\theta) \dot{y} - \sin(\theta) \dot{x}) \varepsilon_0 m_0 \right. \\
 &\quad \left. + (\cos(\theta + \gamma) \dot{y} - \sin(\theta + \gamma) \dot{x}) E \sum_{i=1}^n m_i \right. \\
 &\quad \left. + \sum_{i=1}^n (\cos(\theta + \varphi_i) \dot{y} - \sin(\theta + \varphi_i) \dot{x}) \varepsilon_i m_i \right) \dot{\theta} \\
 &+ \frac{1}{2} \left(J + m_0 \varepsilon_0^2 + \sum_{i=1}^n E^2 m_i + 2E m_i \varepsilon_i \cos(\gamma - \varphi_i) + J_i + m_i \varepsilon_i^2 \right) \dot{\theta}^2
 \end{aligned} \tag{4.10}$$

with $M = m + m_0 + \sum_{i=1}^n m_i$.

4. Translational oscillator model

The viscous forces of the fluid on the balls are modelled in accordance with [Sha75; LV96; SMDoo] and several others in a simple linear manner by the torque

$$M_D = -\beta_i \dot{\varphi}_i. \quad (4.11)$$

However, no information is given in the literature on how β_i can be quantitatively determined. As will be presented in detail in section 5.2, a novel proposal for the calculation of β_i is given with

$$\beta_i = \frac{c_d \text{Re}}{4} \pi \rho_{\text{fl}} \nu r_i \varepsilon_i^2. \quad (4.12)$$

Here, ρ_{fl} and ν are the density and kinematic viscosity of the fluid inside the ABB annulus, respectively. The product of drag coefficient and particle Reynolds number $c_d \text{Re}$ is a constant for low velocities $\dot{\varphi}_i$ and depends on the annulus and ball geometry.

Furthermore, translatory damping forces

$$F_{bx} = -b_x \dot{x}, \quad F_{by} = -b_y \dot{y},$$

a driving torque M_0 and an opposing external damping torque

$$M_{\beta_0} = -\beta_0 \dot{\theta}$$

are considered, leading to the differential change of virtual work

$$\partial W_{\text{diss}} = -b_x \dot{x} \partial x - b_y \dot{y} \partial y + M_0 \partial \theta - \beta_0 \dot{\theta} \partial \theta - \sum_{i=1}^n \beta_i \dot{\varphi}_i \partial \varphi_i. \quad (4.13)$$

Evaluation of eq. (4.1) yields a system of $n + 3$ ordinary differential equa-

4.1. Equations of motion

tions

$$\begin{aligned}
 M\ddot{x} + b_x\dot{x} + k_x x = & \\
 & \left(m_0\varepsilon_0 \sin(\theta) + \sum_{i=1}^n Em_i \sin(\gamma + \theta) + m_i\varepsilon_i \sin(\theta + \varphi_i) \right) \ddot{\theta} \\
 & + \left(m_0\varepsilon_0 \cos(\theta) \dot{\theta} + \sum_{i=1}^n Em_i \cos(\gamma + \theta) \dot{\theta} + m_i\varepsilon_i (\dot{\theta} + \dot{\varphi}_i) \cos(\theta + \varphi_i) \right) \dot{\theta} \\
 & + \sum_{i=1}^n m_i\varepsilon_i \sin(\theta + \varphi_i) \ddot{\varphi}_i + m_i\varepsilon_i (\dot{\theta} + \dot{\varphi}_i) \cos(\theta + \varphi_i) \dot{\varphi}_i, \quad (4.14)
 \end{aligned}$$

$$\begin{aligned}
 M\ddot{y} + b_y\dot{y} + k_y y = & \\
 & - \left(m_0\varepsilon_0 \cos(\theta) + \sum_{i=1}^n Em_i \cos(\gamma + \theta) + m_i\varepsilon_i \cos(\theta + \varphi_i) \right) \ddot{\theta} \\
 & + \left(m_0\varepsilon_0 \sin(\theta) \dot{\theta} + \sum_{i=1}^n Em_i \sin(\gamma + \theta) \dot{\theta} + m_i\varepsilon_i (\dot{\theta} + \dot{\varphi}_i) \sin(\theta + \varphi_i) \right) \dot{\theta} \\
 & + \sum_{i=1}^n m_i\varepsilon_i (\dot{\theta} + \dot{\varphi}_i) \sin(\theta + \varphi_i) \dot{\varphi}_i - m_i\varepsilon_i \cos(\theta + \varphi_i) \ddot{\varphi}_i, \quad (4.15)
 \end{aligned}$$

4. Translational oscillator model

$$\begin{aligned}
& \left(J + m_0 \varepsilon_0^2 + \sum_{i=1}^n J_i + m_i E^2 + m_i \varepsilon_i^2 + 2E m_i \varepsilon_i \cos(\gamma - \varphi_i) \right) \ddot{\theta} \\
& + \left(\beta_0 + \sum_{i=1}^n 2E m_i \varepsilon_i \sin(\gamma - \varphi_i) \dot{\varphi}_i \right) \dot{\theta} = \\
& M_0 + \left(m_0 \varepsilon_0 \sin(\theta) + \sum_{i=1}^n m_i E \sin(\gamma + \theta) + m_i \varepsilon_i \sin(\theta + \varphi_i) \right) \ddot{x} \\
& - \left(m_0 \varepsilon_0 \cos(\theta) + \sum_{i=1}^n E m_i \cos(\gamma + \theta) + m_i \varepsilon_i \cos(\theta + \varphi_i) \right) \ddot{y} \\
& - \sum_{i=1}^n \left(E m_i \varepsilon_i \cos(\gamma - \varphi_i) - \frac{J_i \varepsilon_i}{r_i} + m_i \varepsilon_i^2 \right) \ddot{\varphi}_i + E m_i \varepsilon_i \sin(\gamma - \varphi_i) \dot{\varphi}_i^2,
\end{aligned} \tag{4.16}$$

$$\begin{aligned}
& \left(\frac{J_i \varepsilon_i^2}{r_i^2} + m_i \varepsilon_i^2 \right) \ddot{\varphi}_i + \beta_i \dot{\varphi}_i = \\
& m_i \varepsilon_i \left(E \sin(\gamma - \varphi_i) \dot{\theta}^2 + \sin(\theta + \varphi_i) \ddot{x} - \cos(\theta + \varphi_i) \ddot{y} \right) \\
& + \left(\frac{J_i \varepsilon_i}{r_i} - E m_i \varepsilon_i \cos(\gamma - \varphi_i) - m_i \varepsilon_i^2 \right) \ddot{\theta} \quad \forall i \in \{1, \dots, n\}. \tag{4.17}
\end{aligned}$$

4.1.1. Numerical Solutions

The solution of the system of ordinary differential equations (ODEs) (4.14)-(4.17) can be calculated numerically with a variety of well established schemes ([HNW08; Rac18; RN17]). If the driving torque M_0 is smooth, stiffness is not an issue of the ODE system. Therefore, high-order Runge-Kutta methods, i.e., Tsitouras 5th order method [Tsi11], are well suited. In fig. 4.2 and fig. 4.3 verification simulations compared to planar oscillator models presented in [Ryz+01] and [BK18] are shown. As can be seen, the effect of sub-synchronous

4.1. Equations of motion

motion of the balancing balls, presented in section 4.2.2, and the influence of raceway eccentricity, described in section 4.2.4, can be identified.

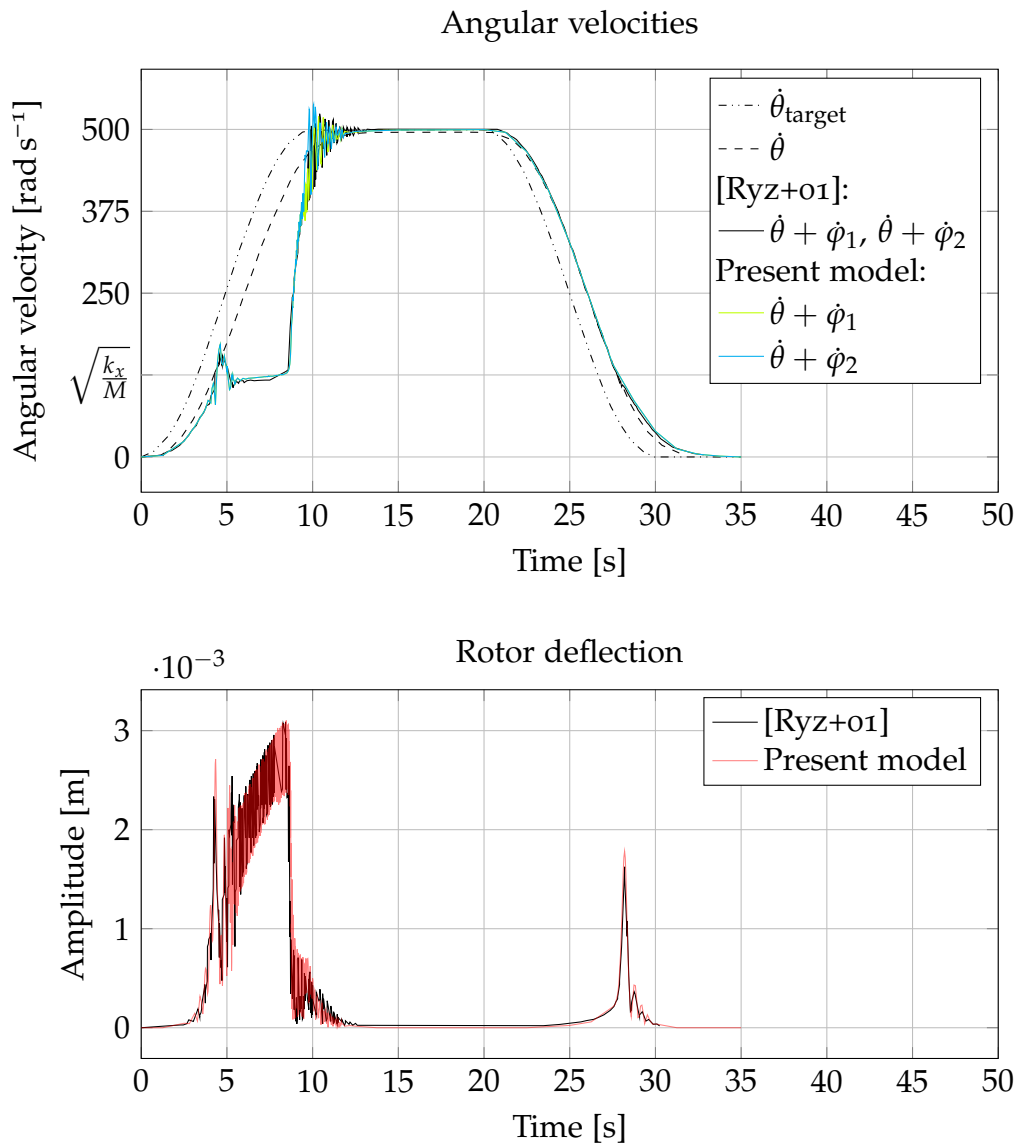
In [Ryz+01] a rotor with two balancing balls is driven by an external torque from rest to an angular velocity of 500 rad s^{-1} , followed by a short stationary phase and a deceleration to rest in an overall time of 35 s. The torque in this case is defined by $M_0 = \beta_0 \dot{\theta}_{\text{target}}$ with a given rated rotor speed $\dot{\theta}_{\text{target}}$. Since no further information on $\dot{\theta}_{\text{target}}$ is given, the data is digitized from the respective figure in the publication. As a result, minor deviations in the results occur. The effect of non-synchronous motion is visible in the range from 5 s to 8 s where the balancing balls, viewed from the inertial system, orbit with the critical velocity of the system while the rotor is accelerating further. Only when the rotor exceeds the threshold velocity for stable balancing, which in this example is approximately 383 rad s^{-1} , are the balls accelerated towards the rotor speed and rotate synchronously again. In the time between 15 s and 20 s, the balls come to rest at their ideal orbit position relative to the rotor and counteract the unbalance. The rotor deflection is eliminated.

The model in [BK18] includes an eccentricity of the balancing ball raceway and, consequently, shows residual vibration amplitudes. The initial conditions consist of a constant rotor angular velocity of $593.13 \text{ rad s}^{-1}$, a rotor deflection of zero and the orbit positions of the two balls being -0.2 rad and -0.4 rad , respectively. Due to the de-dimensioning, which was carried out in the reference implementation, minor deviations in the parameterization are present. Therefore, no equality but a good agreement of the transient ball positions and rotor amplitudes can be ascertained.

4.1.2. Averaged approximate analysis

Several aspects of orthotropic planar oscillators with ABBs can be studied by solving the equations of motion approximately based on the averaging principle. The objectives of such analyses cover the determination of critical and unstable operating frequencies. The question of stability is concerned with the attainment and retention of the stationary orbital positions of the balls, which is mandatory for the ABB to yield the desired effect. Even

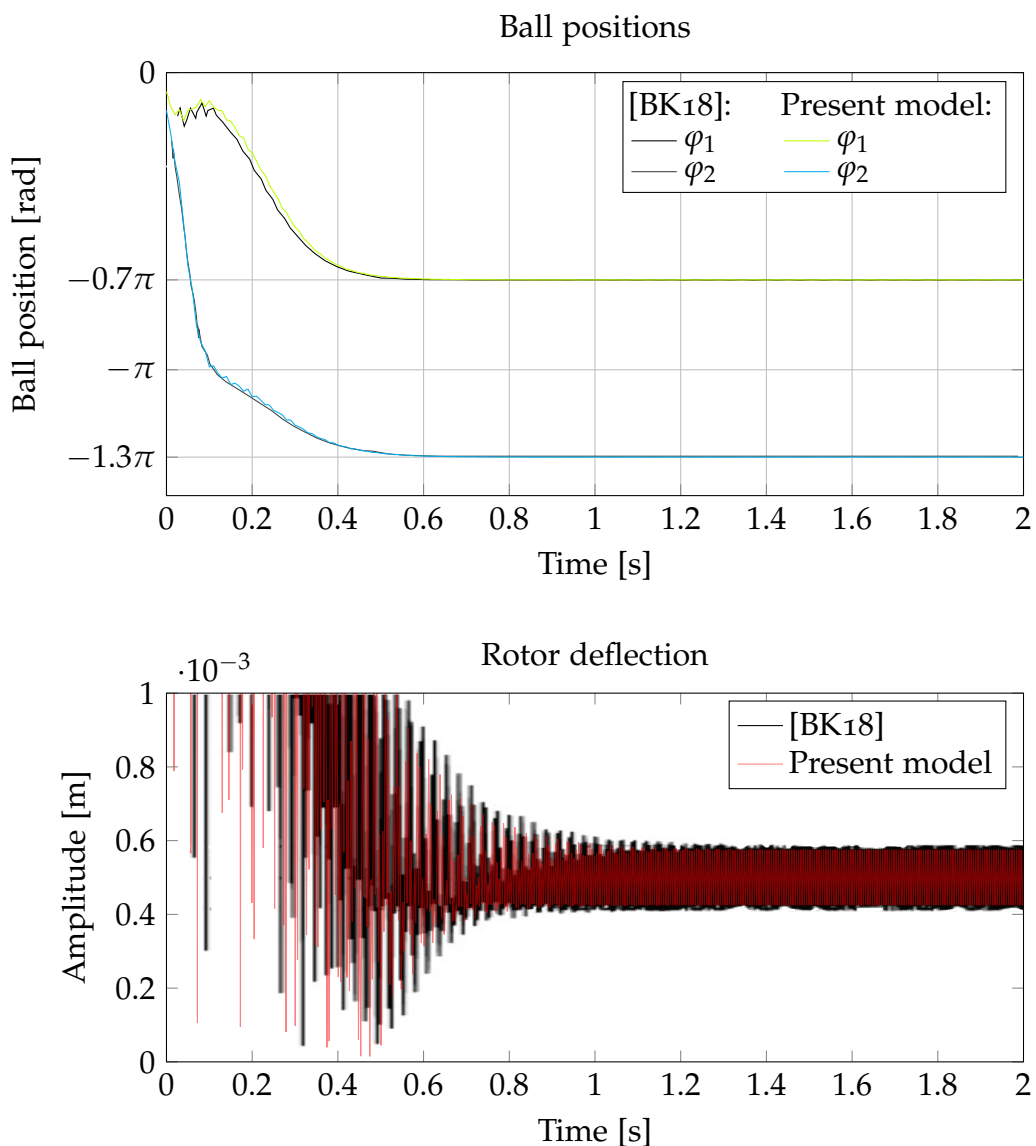
4. Translational oscillator model



Parameter	m_0	ε_0	k_x, k_y	b_x, b_y	m	J	β_0	
Value	5	65	15830	15	1.0	5.4	0.005	
Unit	g	mm	N m^{-1}	N s m^{-1}	kg	g m^2	N m s rad^{-1}	
Parameter	n	m_i	J_i	ε_i	r_i	γ	E	β_i
Value	2	2.5	0	65	5	0	0	0.000025
Unit	-	g	kg m^2	mm	mm	rad	mm	N m s rad^{-1}

Figure 4.2.: Comparison of numerical integration results for the model presented in [Ryz+01].

4.1. Equations of motion



Parameter	m_0	ε_0	k_x	k_y	m	J	J_i	β_0	β_i
Value	60	51.66	50	150	1.14	0	0	0	0.1
Unit	g	mm	kN m^{-1}		kg	g m^2		N m s rad^{-1}	
Parameter	n	m_i	b_x	b_y	ε_i	r_i	γ	E	$\dot{\theta}$
Value	2	37	80	20	60.05	0	0	0.5	593.13
Unit	-	g	N s m^{-1}		mm	mm	rad	mm	rad s^{-1}

Figure 4.3.: Comparison of numerical integration results for the model presented in [BK18].

4. Translational oscillator model

though rotating machinery can show unstable behaviour past a certain angular velocity, depending on factors such as internal and external damping and resulting in increasing deflection amplitudes, these stability borders are not kept in perspective in the following analysis, since those are not induced by ABBs.

Following the solution provided by [Kov16; BK18] the system (4.14)-(4.17) can be transformed using the Krylov-Bogoliubov-Mitropolsky (KBM) method ([KB47; Oli17]). The generalized coordinates are replaced by

$$\tilde{x} = A_x \cos(\theta) - B_x \sin(\theta), \quad \tilde{y} = A_y \sin(\theta) + B_y \cos(\theta), \quad (4.18)$$

$$\dot{\tilde{x}} = -\dot{\theta} A_x \sin(\theta) - \dot{\theta} B_x \cos(\theta), \quad \dot{\tilde{y}} = \dot{\theta} A_y \cos(\theta) - \dot{\theta} B_y \sin(\theta), \quad (4.19)$$

$$\ddot{\tilde{x}} = \frac{\partial \dot{\tilde{x}}}{\partial t} = (\dot{\theta}^2 B_x - \dot{\theta} \dot{A}_x) \sin(\theta) + (-\dot{\theta}^2 A_x - \dot{\theta} \dot{B}_x) \cos(\theta), \quad (4.20)$$

$$\ddot{\tilde{y}} = \frac{\partial \dot{\tilde{y}}}{\partial t} = (-\dot{\theta}^2 A_y - \dot{\theta} \dot{B}_y) \sin(\theta) + (-\dot{\theta}^2 B_y + \dot{\theta} \dot{A}_y) \cos(\theta). \quad (4.21)$$

Differentiation of (4.18) and comparison to (4.19) yields

$$\dot{A}_x = \dot{B}_x \frac{\sin(\dot{\theta}t)}{\cos(\dot{\theta}t)}, \quad \dot{A}_y = -\dot{B}_y \frac{\cos(\dot{\theta}t)}{\sin(\dot{\theta}t)}. \quad (4.22)$$

By inserting equations (4.18)-(4.21) in equations (4.14)-(4.15) under the assumption of constant angular velocity $\dot{\theta} = \Omega$ and using the substitutions in (4.22) one gains four expressions for \dot{A}_x , \dot{B}_x , \dot{A}_y and \dot{B}_y in terms of A_x , B_x , A_y , B_y and the system parameters.

Since the change in deflection amplitude during one rotation of the rotor is considered small, these expressions are approximated by their integral mean

4.1. Equations of motion

over one period,

$$\begin{aligned} \dot{A}_x &\approx \frac{1}{2\pi} \int_0^{2\pi} \dot{A}_x \, d\Omega t, & \dot{A}_y &\approx \frac{1}{2\pi} \int_0^{2\pi} \dot{A}_y \, d\Omega t, \\ \dot{B}_x &\approx \frac{1}{2\pi} \int_0^{2\pi} \dot{B}_x \, d\Omega t, & \dot{B}_y &\approx \frac{1}{2\pi} \int_0^{2\pi} \dot{B}_y \, d\Omega t, \end{aligned} \quad (4.23)$$

removing the trigonometric functions in $\theta = \Omega t$ from the equations. Proceeding similarly with equation (4.17) leads to

$$\begin{aligned} &\left(\frac{J_i \varepsilon_i^2}{r_i^2} + m_i \varepsilon_i^2 \right) \ddot{\varphi}_i + \beta_i \dot{\varphi}_i = m_i \varepsilon_i E \Omega^2 \sin(\gamma - \varphi_i) \\ &+ \frac{m_i \varepsilon_i \Omega}{2} ((\dot{B}_x + \dot{B}_y + \Omega(A_x + A_y)) \sin(\varphi_i) \\ &+ (\dot{A}_x + \dot{A}_y - \Omega(B_x + B_y)) \cos(\varphi_i)) \quad \forall i \in \{1, \dots, n\} \end{aligned} \quad (4.24)$$

Dismissing the temporal derivatives, provided by the consideration of the steady state, yields

$$\begin{aligned} \dot{A}_x &= \left(\frac{\Omega}{2} - \frac{k_x}{2M\Omega} \right) B_{0x} - \frac{b_x A_{0x}}{2M} \\ &+ \frac{\Omega}{2M} \sum_{i=1}^n E m_i \sin(\gamma) + \varepsilon_i m_i \sin(\varphi_{0i}) \end{aligned} \quad (4.25)$$

$$\begin{aligned} \dot{B}_x &= \left(-\frac{\Omega}{2} + \frac{k_x}{2M\Omega} \right) A_{0x} - \frac{b_x B_{0x}}{2M} - \frac{m_0 \Omega \varepsilon_0}{2M} \\ &- \frac{\Omega}{2M} \sum_{i=1}^n E m_i \cos(\gamma) + \varepsilon_i m_i \cos(\varphi_{0i}) \end{aligned} \quad (4.26)$$

4. Translational oscillator model

$$\begin{aligned} \dot{A}_y &= \left(\frac{\Omega}{2} - \frac{k_y}{2M\Omega} \right) B_{0y} - \frac{b_y A_{0y}}{2M} \\ &\quad + \frac{\Omega}{2M} \sum_{i=1}^n E m_i \sin(\gamma) + \varepsilon_i m_i \sin(\varphi_{0i}) \end{aligned} \quad (4.27)$$

$$\begin{aligned} \dot{B}_y &= \left(-\frac{\Omega}{2} + \frac{k_y}{2M\Omega} \right) A_{0y} - \frac{b_y B_{0y}}{2M} - \frac{m_0 \Omega \varepsilon_0}{2M} \\ &\quad - \frac{\Omega}{2M} \sum_{i=1}^n E m_i \cos(\gamma) + \varepsilon_i m_i \cos(\varphi_{0i}). \end{aligned} \quad (4.28)$$

Accordingly, the left-hand sides of the equations above are set to zero and the steady values of A_x , A_y , B_x , B_y , φ_i are designated A_{0x} , A_{0y} , B_{0x} , B_{0y} , φ_{0i} , respectively. Proceeding similarly with equation (4.24) leads to

$$\begin{aligned} 0 &= \frac{\Omega^2}{2} \left((A_{0x} + A_{0y}) \sin(\varphi_{0i}) - (B_{0x} + B_{0y}) \cos(\varphi_{0i}) \right) \\ &\quad - E \Omega^2 \sin(\gamma - \varphi_{0i}) \quad \forall i \in \{1, \dots, n\}. \end{aligned} \quad (4.29)$$

Ideal balancing of an ABB with eccentricity

Under the assumption that the rotor is perfectly balanced, meaning $A_{0x} = A_{0y} = B_{0x} = B_{0y} = 0$, either one of the equations (4.26) and (4.28) leads to equation (4.30), either one of the equations (4.25) and (4.27) leads to equation (4.31) and equation (4.29) results in (4.32)

$$\sum_{i=1}^n \varepsilon_i m_i \cos(\varphi_{0i}) = -m_0 \varepsilon_0 - E \cos(\gamma) \sum_{i=1}^n m_i, \quad (4.30)$$

$$\sum_{i=1}^n \varepsilon_i m_i \sin(\varphi_{0i}) = -E \sin(\gamma) \sum_{i=1}^n m_i, \quad (4.31)$$

$$\sin(\gamma - \varphi_{0i}) = 0 \quad \forall i \in \{1, \dots, n\}. \quad (4.32)$$

4.1. Equations of motion

Multiplying equation (4.30) with $\sin(\gamma)$, equation (4.31) with $\cos(\gamma)$ and subtracting from another yields

$$\sum_{i=1}^n \varepsilon_i m_i \sin(\gamma - \varphi_{0i}) = -m_0 \varepsilon_0 \sin(\gamma) \quad (4.33)$$

and in combination with equation (4.32)

$$\sin(\gamma) = 0 \rightsquigarrow \gamma = \{0, \pi\}, \quad (4.34)$$

as well as

$$\sin(\varphi_{0i}) = 0 \rightsquigarrow \varphi_{0i} = \{0, \pi\} \quad \forall i \in \{1, \dots, n\}. \quad (4.35)$$

The ideal balancing therefore requires the eccentricity and the balls to be positioned in the direction of the primary imbalance. Additionally, the primary imbalance needs to be counteracted exactly, stipulated by equation (4.30) yielding

$$m_0 \varepsilon_0 + \sum_{i=1}^n \varepsilon_i m_i \cos(\varphi_{0i}) \pm E \sum_{i=1}^n m_i = 0. \quad (4.36)$$

This is a condition that is not found in reality, so that perfect balancing cannot be achieved with the eccentricity present.

Stationary operation

Multiplication of equations (4.25) and (4.27) with $i = \sqrt{-1}$ and addition to equations (4.26) and (4.28), respectively, yields in combination with Euler's formula $\cos(x) + i \sin(x) = e^{ix}$

$$(A_x - i B_x) \left(\frac{k_x}{2M\Omega} - \frac{\Omega}{2} - i \frac{b_x}{2M} \right) = \frac{m_0 \varepsilon_0 \Omega}{2M} - \frac{\Omega}{2M} \sum_{i=1}^n E m_i e^{-i\gamma} + \varepsilon_i m_i e^{-i\varphi_i} \quad (4.37)$$

4. Translational oscillator model

and

$$(A_y - i B_y) \left(\frac{k_y}{2M\Omega} - \frac{\Omega}{2} - i \frac{b_y}{2M} \right) = \frac{m_0 \varepsilon_0 \Omega}{2M} - \frac{\Omega}{2M} \sum_{i=1}^n E m_i e^{-i\gamma} + \varepsilon_i m_i e^{-i\phi_i}. \quad (4.38)$$

As the right hand sides are identical, the amplitude ratio can be formulated as

$$\frac{A_x - i B_x}{A_y - i B_y} = \frac{M\Omega^2 - k_y + i b_y \Omega}{M\Omega^2 - k_x + i b_x \Omega} = \frac{R_x e^{i\phi_x}}{R_y e^{i\phi_y}} = \frac{R_x}{R_y} e^{i(\phi_x - \phi_y)} \quad (4.39)$$

with R_x, R_y, ϕ_x, ϕ_y being the magnitudes of the deflections in x and y direction and the arguments of the complex amplitudes, respectively. The ratio of magnitudes results in

$$\frac{R_x}{R_y} = \frac{\sqrt{b_y^2 \Omega^2 + (M\Omega^2 - k_y)^2}}{\sqrt{b_x^2 \Omega^2 + (M\Omega^2 - k_x)^2}}. \quad (4.40)$$

The two critical angular velocities $\Omega = \omega_{\text{crit}}$ of the system arise from the extrema of equation (4.40), yielding

$$\omega_{\text{crit}}^2 = \frac{(k_x - k_y)(k_x + k_y)}{2Mk_x - 2Mk_y - b_x^2 + b_y^2} \mp \frac{\sqrt{(M(k_x - k_y)^2 + b_x^2 k_y + b_y^2 k_x)^2 - (b_x b_y (k_x + k_y))^2}}{M(2M(k_y - k_x) + b_x^2 - b_y^2)}, \quad (4.41)$$

which is the known solution of the Jeffcott rotor in orthotropic bearings [Gas06; Gen05], showing no dependence on the eccentricity E of the ABB. The balancing masses only affect the total mass M .

4.1. Equations of motion

Evaluating (4.29) for two arbitrary compensation balls $i = \{j, k\}$ yields

$$0 = \frac{\Omega^2}{2} ((A_{0x} + A_{0y}) \sin(\varphi_{0j}) - (B_{0x} + B_{0y}) \cos(\varphi_{0j})) - E\Omega^2 \sin(\gamma - \varphi_{0j}), \quad (4.42)$$

$$0 = \frac{\Omega^2}{2} ((A_{0x} + A_{0y}) \sin(\varphi_{0k}) - (B_{0x} + B_{0y}) \cos(\varphi_{0k})) - E\Omega^2 \sin(\gamma - \varphi_{0k}). \quad (4.43)$$

Multiplication of equation (4.42) with either $\sin(\varphi_{0k})$ or $\cos(\varphi_{0k})$ and equation (4.43) with either $\sin(\varphi_{0j})$ or $\cos(\varphi_{0j})$, respectively, yields after subsequent subtraction

$$0 = \Omega^2 \left(E \cos(\gamma) + \frac{A_{0x} + A_{0y}}{2} \right) \sin(\varphi_{0j} - \varphi_{0k}) \quad (4.44)$$

and

$$0 = \Omega^2 \left(E \sin(\gamma) + \frac{B_{0x} + B_{0y}}{2} \right) \sin(\varphi_{0j} - \varphi_{0k}). \quad (4.45)$$

Therefore, stationary operation can be established under the condition

$$\varphi_{0j} = \varphi_{0k} \quad \vee \quad \varphi_{0j} = \varphi_{0k} + \pi, \quad (4.46)$$

meaning that the balancing balls are positioned diametrically on the orbit or at the same location. As shown by [BK18], this state can be achieved in simulations, but does not represent the general case of the two balancing balls counteracting the initial rotor unbalance. Consequently, stationary operation requires

$$\frac{A_{0x} + A_{0y}}{2} = -E \cos(\gamma) \quad (4.47)$$

$$\frac{B_{0x} + B_{0y}}{2} = -E \sin(\gamma), \quad (4.48)$$

4. Translational oscillator model

which yields, using the Pythagorean trigonometric identity,

$$E = \sqrt{\left(\frac{A_{0x} + A_{0y}}{2}\right)^2 + \left(\frac{B_{0x} + B_{0y}}{2}\right)^2}. \quad (4.49)$$

As a result, an eccentric ABB is incapable of ideally balancing the rotor, but the stationary operation in orthotropic bearings shows an average rotor deflection equal to the raceway eccentricity E . From equations (4.39), (4.47) and (4.48) it is easy to see that for the isotropic case $A_{0x} = A_{0y}$ and $B_{0x} = B_{0y}$ and thus the stationary rotor deflection is equal to the ABB eccentricity E .

From the first two representations of equation (4.39) and transformation of equations (4.47) and (4.48) to

$$(A_{0x} - i B_{0x}) + (A_{0y} - i B_{0y}) = -2E(\cos(\gamma) + i \sin(\gamma)), \quad (4.50)$$

a linear complex-valued system of equations

$$\begin{bmatrix} M\Omega^2 - k_x + i b_x \Omega & -M\Omega^2 + k_y - i b_y \Omega \\ 1 & 1 \end{bmatrix} \left(\begin{bmatrix} A_{0x} \\ A_{0y} \end{bmatrix} - i \begin{bmatrix} B_{0x} \\ B_{0y} \end{bmatrix} \right) = -2E \left(\begin{bmatrix} 0 \\ \cos(\gamma) \end{bmatrix} + i \begin{bmatrix} 0 \\ \sin(\gamma) \end{bmatrix} \right) \quad (4.51)$$

can be established. The solution results in

$$A_{0x} = -2E(P_{xy} \sin(\gamma) + Q_{xy} \cos(\gamma))S^{-1} \quad (4.52)$$

$$A_{0y} = -2E(P_{yx} \sin(\gamma) + Q_{yx} \cos(\gamma))S^{-1} \quad (4.53)$$

$$B_{0x} = -2E(Q_{xy} \sin(\gamma) + P_{yx} \cos(\gamma))S^{-1} \quad (4.54)$$

$$B_{0y} = -2E(Q_{yx} \sin(\gamma) + P_{xy} \cos(\gamma))S^{-1} \quad (4.55)$$

4.1. Equations of motion

with the abbreviations

$$P_{xy} = \Omega^3 M(b_y - b_x) + \Omega(b_x k_y - b_y k_x) \quad (4.56)$$

$$P_{yx} = \Omega^3 M(b_x - b_y) + \Omega(b_y k_x - b_x k_y) \quad (4.57)$$

$$Q_{xy} = 2M^2\Omega^4 - M\Omega^2(k_x + 3k_y) + k_x k_y + k_y^2 + \Omega^2(b_x b_y + b_y^2) \quad (4.58)$$

$$Q_{yx} = 2M^2\Omega^4 - M\Omega^2(k_y + 3k_x) + k_x k_y + k_x^2 + \Omega^2(b_x b_y + b_x^2) \quad (4.59)$$

$$S = \Omega^2 (b_x + b_y)^2 + \left(2M\Omega^2 - k_x - k_y\right)^2. \quad (4.60)$$

Since an ABB with more than two balancing balls has infinite combinations of ideal ball orbit positions, the following considerations are limited to ABBs with two balls. To simplify further, identical balls on the same orbit are presumed and the assumptions can be summarized as follows:

- Two identical balls share the same orbit: $m_1 = m_2 = m_b$, $\varepsilon_1 = \varepsilon_2 = \varepsilon$, $\beta_1 = \beta_2 = \beta$
- The rotor velocity is constant: $\ddot{\theta} = 0$, $\theta = \Omega t$
- The system is stationary: $\dot{A}_x = \dot{A}_y = \dot{B}_x = \dot{B}_y = 0$, $\dot{\varphi}_1 = \dot{\varphi}_2 = 0$

Inserting the solutions (4.52)–(4.55) into equations (4.25) and (4.26) on page 39 and evaluating with the simplifications stated above, yields

$$\begin{aligned} \chi_s &\equiv \sin(\varphi_{01}) + \sin(\varphi_{02}) \\ &= \frac{b_x}{\varepsilon m_b \Omega} A_{0x} + \frac{1}{\varepsilon m_b} \left(\frac{k_x}{\Omega^2} - M \right) B_{0x} - 2 \frac{E}{\varepsilon} \sin(\gamma), \end{aligned} \quad (4.61)$$

$$\begin{aligned} \chi_c &\equiv \cos(\varphi_{01}) + \cos(\varphi_{02}) \\ &= -\frac{b_x}{\varepsilon m_b \Omega} B_{0x} + \frac{1}{\varepsilon m_b} \left(\frac{k_x}{\Omega^2} - M \right) A_{0x} - 2 \frac{E}{\varepsilon} \cos(\gamma) - \frac{m_0 \varepsilon_0}{m_b \varepsilon}. \end{aligned} \quad (4.62)$$

4. Translational oscillator model

From the trigonometric identities

$$\frac{\chi_s}{\chi_c} = \tan\left(\frac{\varphi_{01} + \varphi_{02}}{2}\right), \quad \chi_s^2 + \chi_c^2 = 2(1 + \cos(\varphi_{01} - \varphi_{02})) \quad (4.63)$$

follows

$$\varphi_{01} + \varphi_{02} = 2 \arctan\left(\frac{\chi_s}{\chi_c}\right), \quad \varphi_{01} - \varphi_{02} = \arccos\left(\frac{\chi_s^2 + \chi_c^2}{2} - 1\right), \quad (4.64)$$

and therefore

$$\varphi_{01} = \arctan\left(\frac{\chi_s}{\chi_c}\right) + \frac{1}{2} \arccos\left(\frac{\chi_s^2 + \chi_c^2}{2} - 1\right), \quad (4.65)$$

$$\varphi_{02} = \arctan\left(\frac{\chi_s}{\chi_c}\right) - \frac{1}{2} \arccos\left(\frac{\chi_s^2 + \chi_c^2}{2} - 1\right) \quad (4.66)$$

can be used to determine the resting positions of the balancing balls if

$$\chi_s^2 + \chi_c^2 \leq 4 \quad (4.67)$$

holds true. For the eccentricity free ABB, equation (4.67) is violated if the masses of the balancing balls are insufficient to counteract the initial imbalance.

Stability

The stability of stationary operation of an ABB with two balancing balls can be assessed by a linear perturbation analysis of the system (4.23) and (4.24) on page 39, defining

$$A_x = A_{0x} + \Delta A_x, \quad B_x = B_{0x} + \Delta B_x, \quad \varphi_1 = \varphi_{01} + \Delta\varphi_1,$$

$$A_y = A_{0y} + \Delta A_y, \quad B_y = B_{0y} + \Delta B_y, \quad \varphi_2 = \varphi_{02} + \Delta\varphi_2.$$

Following the substitution, time derivatives of second order and powers of first-order time derivatives are neglected. Subsequently, time derivatives of the

4.1. Equations of motion

stationary parts $A_{0x}, B_{0x}, A_{0y}, B_{0y}, \varphi_{01}, \varphi_{02}$ are set to zero. The trigonometric functions are expanded according to

$$\sin(\varphi_{0i} + \Delta\varphi_i) = \sin(\varphi_{0i}) \cos(\Delta\varphi_i) + \cos(\varphi_{0i}) \sin(\Delta\varphi_i),$$

$$\cos(\varphi_{0i} + \Delta\varphi_i) = \cos(\varphi_{0i}) \cos(\Delta\varphi_i) - \sin(\varphi_{0i}) \sin(\Delta\varphi_i) \quad \forall i \in \{1, 2\}$$

and $\sin(\Delta\varphi_1), \cos(\Delta\varphi_1), \sin(\Delta\varphi_2), \cos(\Delta\varphi_2)$ replaced by linear series expansions. Ultimately, one obtains the system of linear ODEs of first order

$$\underline{A} \frac{d}{dt} \begin{bmatrix} \Delta A_x \\ \Delta B_x \\ \Delta A_y \\ \Delta B_y \\ \Delta\varphi_1 \\ \Delta\varphi_2 \end{bmatrix} + \underline{B} \begin{bmatrix} \Delta A_x \\ \Delta B_x \\ \Delta A_y \\ \Delta B_y \\ \Delta\varphi_1 \\ \Delta\varphi_2 \end{bmatrix} = \underline{0}. \quad (4.68)$$

48

With $\underline{\underline{A}}$ and $\underline{\underline{B}}$ being

$$\underline{\underline{A}} = \begin{bmatrix} -1 & 0 & 0 & 0 & \frac{m_b \varepsilon \sin(\varphi_{01})}{M} & \frac{m_b \varepsilon \sin(\varphi_{02})}{M} \\ 0 & -1 & 0 & 0 & -\frac{m_b \varepsilon \cos(\varphi_{01})}{M} & -\frac{m_b \varepsilon \cos(\varphi_{02})}{M} \\ 0 & 0 & -1 & 0 & \frac{m_b \varepsilon \sin(\varphi_{01})}{M} & \frac{m_b \varepsilon \sin(\varphi_{02})}{M} \\ 0 & 0 & 0 & -1 & -\frac{m_b \varepsilon \cos(\varphi_{01})}{M} & -\frac{m_b \varepsilon \cos(\varphi_{02})}{M} \\ \frac{\Omega \cos(\varphi_{01})}{2} & \frac{\Omega \sin(\varphi_{01})}{2} & \frac{\Omega \cos(\varphi_{01})}{2} & \frac{\Omega \sin(\varphi_{01})}{2} & \frac{\beta}{m_b \varepsilon} & 0 \\ \frac{\Omega \cos(\varphi_{02})}{2} & \frac{\Omega \sin(\varphi_{02})}{2} & \frac{\Omega \cos(\varphi_{02})}{2} & \frac{\Omega \sin(\varphi_{02})}{2} & 0 & \frac{\beta}{m_b \varepsilon} \end{bmatrix}$$

and

$$\underline{\underline{B}} = \begin{bmatrix} -\frac{b_x}{2M} & \frac{\Omega}{2} - \frac{k_x}{2M\Omega} & 0 & 0 & \frac{m_b \Omega \varepsilon \cos(\varphi_{01})}{2M} & \frac{m_b \Omega \varepsilon \cos(\varphi_{02})}{2M} \\ -\frac{\Omega}{2} + \frac{k_x}{2M\Omega} & -\frac{b_x}{2M} & 0 & 0 & \frac{m_b \Omega \varepsilon \sin(\varphi_{01})}{2M} & \frac{m_b \Omega \varepsilon \sin(\varphi_{02})}{2M} \\ 0 & 0 & -\frac{b_y}{2M} & \frac{\Omega}{2} - \frac{k_y}{2M\Omega} & \frac{m_b \Omega \varepsilon \cos(\varphi_{01})}{2M} & \frac{m_b \Omega \varepsilon \cos(\varphi_{02})}{2M} \\ 0 & 0 & -\frac{\Omega}{2} + \frac{k_y}{2M\Omega} & -\frac{b_y}{2M} & \frac{m_b \Omega \varepsilon \sin(\varphi_{01})}{2M} & \frac{m_b \Omega \varepsilon \sin(\varphi_{02})}{2M} \\ \frac{\Omega^2 \sin(\varphi_{01})}{2} & -\frac{\Omega^2 \cos(\varphi_{01})}{2} & \frac{\Omega^2 \sin(\varphi_{01})}{2} & -\frac{\Omega^2 \cos(\varphi_{01})}{2} & 0 & 0 \\ \frac{\Omega^2 \sin(\varphi_{02})}{2} & -\frac{\Omega^2 \cos(\varphi_{02})}{2} & \frac{\Omega^2 \sin(\varphi_{02})}{2} & -\frac{\Omega^2 \cos(\varphi_{02})}{2} & 0 & 0 \end{bmatrix}$$

4.2. Influences on the ABB operation

and the stationary orbit positions φ_{01} , φ_{02} being calculated utilizing equations (4.52)–(4.60), (4.65) and (4.66). By solving the eigenvalue problem (EVP) of the system

$$(\underline{B} + \lambda \underline{A}) \underline{v} = \underline{0} \quad (4.69)$$

and determining if all six eigenvalues λ have negative real parts

$$\Re(\lambda) < 0 \quad \forall \lambda, \quad (4.70)$$

the stability of the system can be obtained for a given angular frequency Ω of the rotor. Alternatively, the sixth order characteristic polynomial of eq. (4.69) can be tested with the Routh–Hurwitz stability criterion [Pop62]. The numerical evaluation of the stability encounters a badly conditioned matrix \underline{A} for configurations with small eccentricity, low viscous damping β and primary imbalance magnitudes, which can just be compensated by the balls, with the latter yielding $\varphi_{01} = -\varphi_{02} \approx \pi$. In combination, the last two rows and columns in \underline{A} become nearly congruent. Since stable behaviour at sub-critical speeds result in an increase in the total rotor imbalance, the focus lies on the stable balancing operation at supercritical speeds.

4.2. Influences on the ABB operation

Conclusions from the considerations presented in the previous section can be drawn to determine a suitable design for the balancing unit. In the following subsections, several aspects are described separately, even though interdependencies are often present.

4.2.1. Orthotropic supports

Implied in the functional principle described in chapter 1, the phase lag between excitation forces due to initial imbalance and the rotor deflection is mandatory to achieve the desired behaviour of counterbalancing and the

4. Translational oscillator model

reduction of imbalance loads. Considering orthotropic support, the translatory oscillator holds two resonance frequencies dividing the operating range in four intervals, see fig. 4.4. Without loss of generality, it is assumed that $\omega_x < \omega_y$ and

$$\omega_r = \sqrt{\frac{k_x + k_y}{2M}} = \sqrt{\frac{\omega_x^2 + \omega_y^2}{2}} \quad (4.71)$$

describes the angular velocity at which the deflection amplitudes in both directions are equal, resulting in a circular orbit of the rotor [Nes84]. The feasible operating ranges can be easily discussed using the unbalance response in complex polar form of the undamped Jeffcott rotor in orthotropic bearings [Gen05]

$$x + iy = m_0 \varepsilon_0 \Omega^2 \left(\frac{(\omega_r^2 - \Omega^2)}{(\omega_x^2 - \Omega^2)(\omega_y^2 - \Omega^2)} e^{i\Omega t} - \frac{(k_x - k_y)(2M)^{-1}}{(\omega_x^2 - \Omega^2)(\omega_y^2 - \Omega^2)} e^{-i\Omega t} \right) \quad (4.72)$$

with

$$(\omega_r^2 - \Omega^2) \left[(\omega_x^2 - \Omega^2)(\omega_y^2 - \Omega^2) \right]^{-1}$$

determining the phase shift regarding the imbalance excitation. Only in the speed ranges $\omega_x < \Omega < \omega_r$ and $\omega_y < \Omega$ this quotient is negative and describes a phase lag of 180° . Agafonov et al. used significant orthotropic supports of a grinding wheel in order to operate an ABB reliably in the former range [AB85; AB86]. The backward whirling component is not relevant for passive automatic balancing, as the effects on the balls cancel each other out during one revolution of the rotor. Therefore, 'auto-balancing device(s) can efficiently perform both in the case of isotropic and anisotropic supports.' ([RSD04b])

4.2. Influences on the ABB operation

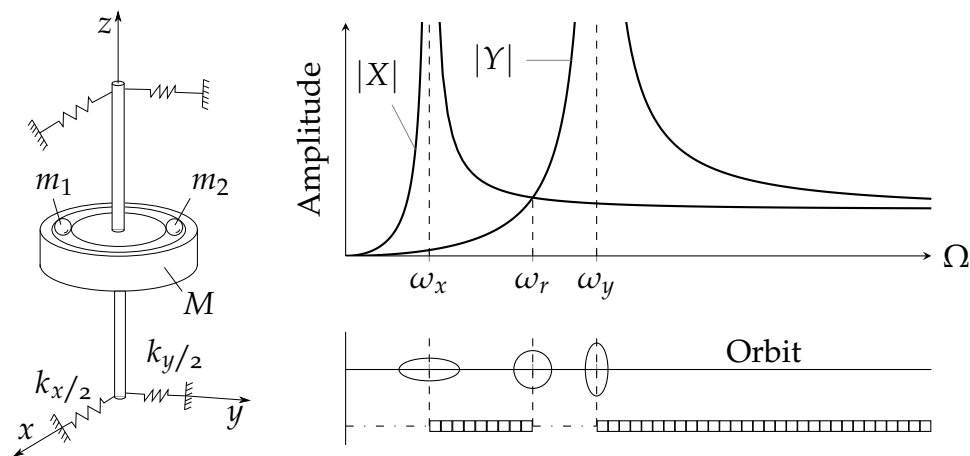


Figure 4.4.: Feasible operating ranges for automatic balancers in anisotropic supports.
 Automatic balancing possible. [Kel87]

4.2.2. Non-synchronous vibrations

The effect of non-synchronous vibrations occurs in the speed range above critical frequencies and is characterized by the orbiting of balancing balls with the critical angular frequency regarding the inertial system while the rotor is rotating at a higher frequency, i.e., $\dot{\theta} + \dot{\varphi} = \omega_{crit}$. See fig. 4.2 on page 36 for an ABB configuration showing this effect. For the test rig presented in section 6.1 the effect is also analysed experimentally and by simulation. Due to its relation to the capture of shafts at resonances, when the drive power is dissipated by the vibrational deformation [Dim+97], this phenomenon in automatic balancing is also called 'Sommerfeld effect' [Ryz+01; RSD04a]. Also, the terms 'limit cycle state' [Hai18] and 'self-excitation' [IIN12] in the context of ABBs are common. As the system passes a critical speed two of the complex conjugate eigenvalues, cf. (4.69), can cross into the right half plane of positive real parts, depending on the choices of system parameters. This results in a Hopf bifurcation [Str18] with two possible characteristics. In the case of a supercritical bifurcation the balancing balls oscillate around its former stable location on the raceway resulting in a limit cycle and minor increase in the vibration amplitude. The behaviour of circulating spheres within the annulus

4. Translational oscillator model

identified in experiments and simulations, however, is a subcritical Hopf bifurcation [Ado97].

Therefore, in addition to the mandatory supercritical operation, a subsequent border frequency Ω_{bo} just above the critical speed needs to be surpassed, to avoid the Sommerfeld effect that not only prevents automatic balancing but also induces non-synchronous excitation. While the primary imbalance of the rotor induces synchronous excitation with the angular frequency Ω , the balancing balls induce a sub-synchronous excitation with an angular frequency of ω_{crit} . To identify said border frequency, equations (4.69) and (4.70) can be made subject to a root finding procedure regarding the stability transition, see [Spa20a]. It must be noted that increasing the number of balls changes the underlying eigenvalue problem and thus changes the necessary border frequency.

To gain more insight into the dependencies, Ryzhik et al. used an approximate solution based on the method of direct separation of motion [Ryz+01], yielding

$$\frac{\Omega_{bo}}{\omega_{\text{crit}}} = 1 + 2 \frac{(m_b \varepsilon \omega_{\text{crit}})^2}{b \beta} \quad (4.73)$$

for the determination of the border frequency of an eccentricity-free ABB with two balls in isotropic supports. However, the used approximation approach assumes that the difference between rotor speed and critical speed is small, indicating inaccuracies when considering systems with larger areas of instability.

Recently, the explicit stability criterion

$$\beta \geq \frac{(m_b \varepsilon)^2 \omega_{\text{crit}}^2}{b} \frac{\Omega^2 + \omega_{\text{crit}}^2}{\Omega^2 - \omega_{\text{crit}}^2} \quad (4.74)$$

for the isotropic, eccentricity-free ABB with two balls was proposed in [SW20a]. It emerges from factorization of the characteristic equation of eq. (4.69) and utilization of the Routh-Hurwitz criterion¹ with details presented in ap-

¹However, a Laurent series expansion of eq. (4.74) does not lead exactly to eq. (4.73). The cause is suspected to be the different calculation methods.

4.2. Influences on the ABB operation

pendix A.1. The frequency band of unstable operation thus enlarges with increasing ball mass m_b and orbit radius ε and reduces with increasing external damping b and viscous damping β due to the fluid inside the ABB. From equation (4.74) follows also the minimum viscous damping

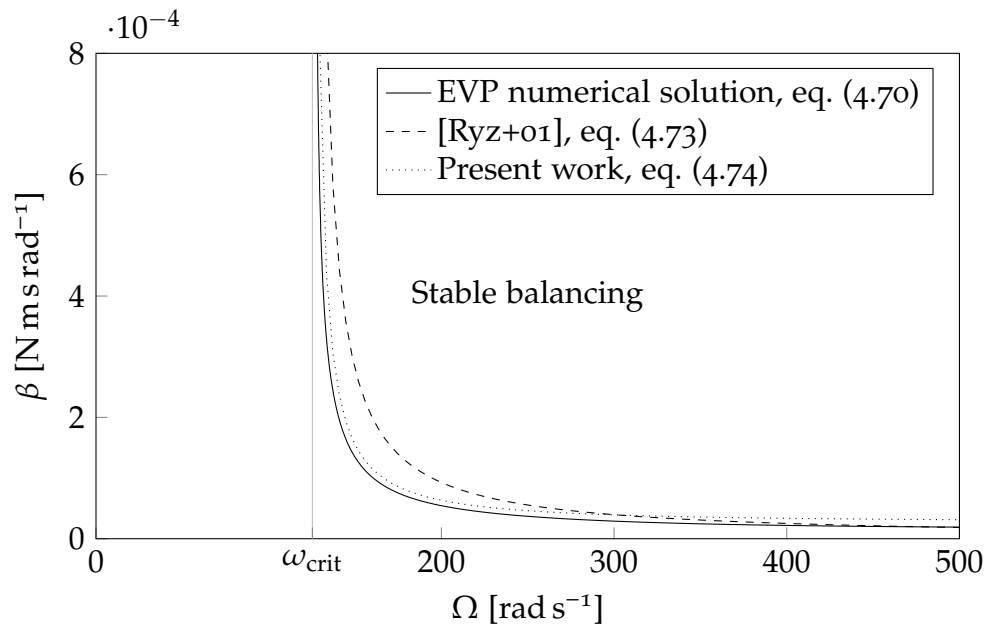
$$\beta_{min} = \lim_{\Omega \rightarrow \infty} \beta = \frac{(m_b \varepsilon)^2 \omega_{crit}^2}{b} \quad (4.75)$$

required, to be able to surpass the Sommerfeld region. Hence, the increase in fluid viscosity is common practice to reduce the Sommerfeld effect. To assist in the selection of appropriate fluid damping to prevent unstable behaviour at operating speed, stability maps are generated showing the stability border based on the criterion from equation (4.70), (4.73) or (4.75) depending on the viscous damping parameter β . Based on the system parameters from fig. 4.2 and fig. 4.3, such diagrams are shown in fig. 4.5. Since the isotropic example from fig. 4.2 presents ideal balancing with $\varphi_{01} = \varphi_{02} = \pi$, the condition of the matrices in equation (4.69) is insufficient, and the initial imbalance mass was reduced by ten percent to $m_0 = 4.5$ g.

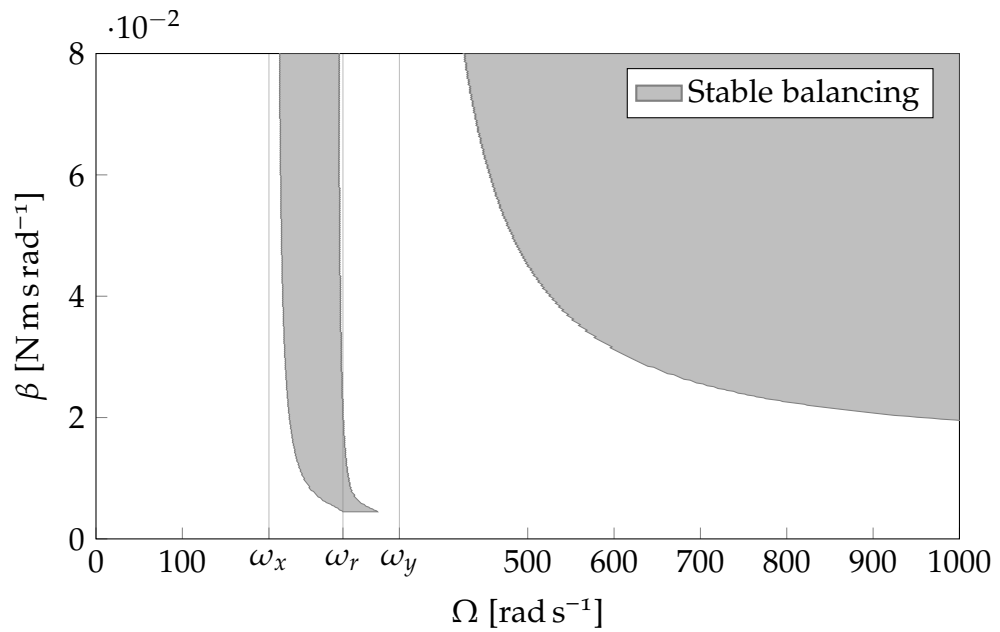
4.2.3. Influence of friction and adherence

Due to the persistent contact between the balancing balls and the raceway, the orbital movement of the balls is affected by adherence and friction throughout the operation. Adherence affects the balls when they come to rest with respect to the raceway, meaning that the orbital angular velocity relative to the rotor as well as the tangential velocity in the contact point is zero. Subsequent relative movement is hindered as long as the forces acting on the ball do not overcome the adherence. Considering stationary operation of the rotor, with the balancing balls still moving towards their resting positions, adherence will cause mispositioning near the ideal resting positions [CSC12]. Due to inertial effects in the orbital movement, the balancing balls will not come to an immediate rest at the point where the normal force, imposed by the raceway, is directed towards the centre of rotation. Rather, oscillations around these positions occur, which are damped by the viscous fluid, friction, and rolling

4. Translational oscillator model



(a) Stability map of the isotropic configuration presented in fig. 4.2 comparing the stability criteria from equations (4.70), (4.73) and (4.74).



(b) Stability map of the orthotropic configuration presented in fig. 4.3 using the stability criterion from equation (4.70).

Figure 4.5.: Stability maps for example ABB units with isotropic and orthotropic bearings.

4.2. Influences on the ABB operation

resistance. Therefore, the condition of zero contact velocity and adherence is fulfilled recurrently. The resulting positions of the balancing balls depend on the initial conditions and the run-up process, but the expansion of stable resting areas reduces with decreasing maximum adherence.

In addition, adherence also provides stable stationary orbital positions near the current location of collective imbalance due to the acute angle formed by the normal force and the connecting lines of the ball with \mathcal{O}_R , see fig. 4.6. This means that the adherence has to contribute only a modest amount in the azimuthal direction to achieve the centripetal force required for a stable position. In [Wou+05] a planar oscillator model with adherence is investigated and the areas of stable orbit positions depending on the friction coefficient and the rotor speed is presented. It is confirmed that in the case of extensive friction, the misalignments can lead to a deterioration of the imbalance situation even in supercritical operation, compared to the original system without an ABB. In [Vel+20b; Vel+20a], experimental and simulative examinations show, that the scatter of actual resting positions around the ideal positions can be reduced by altering the run-up profile of the rotor, in particular by reducing the speed again after the critical frequency was surpassed. This is due to the increase in rotor deflection and the associated increase in inertial effects near critical speeds. Regarding the influence of friction during the system run-up, an equivalent effect to damping can be acknowledged, including reduced lag regarding orbital velocities compared to the raceway.

Considering operation in the Sommerfeld region, cf. section 4.2.2, the dissipative effect of rolling friction reduces the speed range prone to non-synchronous vibration, leading to increased stability. For applications with ABBs restricted to gases inside the cavity, the fluid induced damping is negligible and unfavourable slow attenuating oscillations near the final resting positions may occur. Furthermore, the speed range of sub-synchronous vibration, see eq. (4.75), may not be surpassed. For these cases, as presented by [Yan+05] for CD-ROM drives, a certain amount of friction is necessary in order to gain feasible operating conditions.

Due to the shared nature of causes, adherence and rolling friction cannot be

4. Translational oscillator model

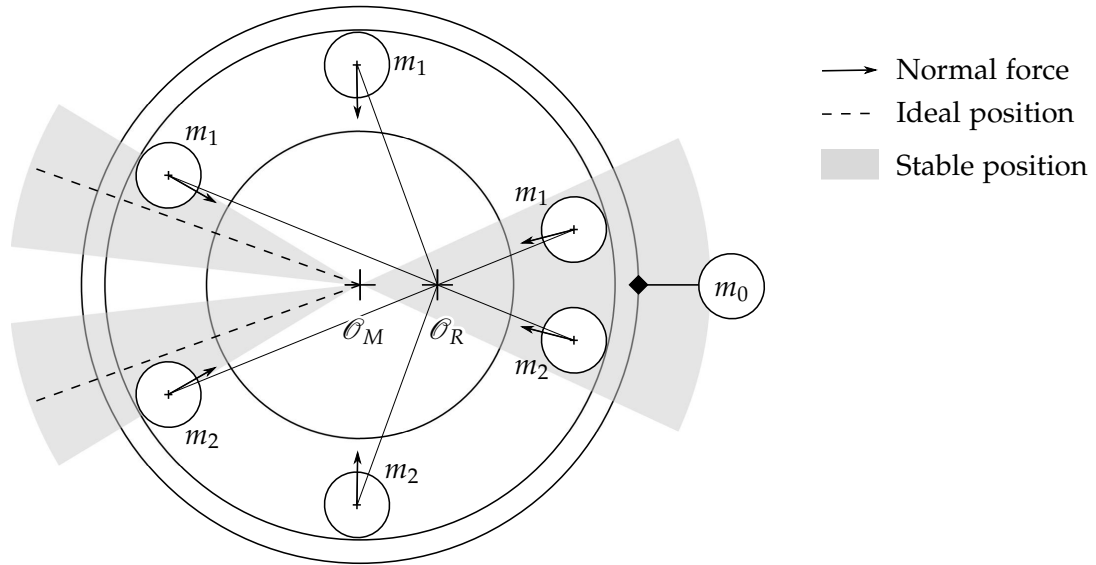


Figure 4.6.: Possible stable stationary positions of two balls in an ABB at supercritical speed under the influence of friction.

influenced separately and the negative aspects of adherence usually outweigh the assessment process. The adherence and friction in ABBs should therefore be minimized in order to maximize counterbalancing efficiency. This can be achieved with the use of high-quality surfaces and unyielding material for the raceway and balls, since friction increases with a larger contact area due to deformation [HFF05]. Ishida et al. conducted an experimental study with balls of different sizes but the same balancing capability, showing 'that larger balls are less affected by friction; in other words, larger balls improve balancing' ([IMZ12]).

4.2.4. Influence of runway imperfections

Deviations from the ideal circular centric raceway, due to manufacturing and assembly tolerances, prevent an ideal balancing of the system. Eccentricity of the raceway is considered in the oscillator model presented in section 4.1, showing that the average residual deflection of the rotor is equal to the eccentricity. As pointed out by Olsson, 'this result can also be arrived at by a simpler reasoning. It reflects the simple fact that this is the only possibility for the balls to be at rest.' ([Olso4]) Isotropic as well as orthotropic supported

4.2. Influences on the ABB operation

automatic balancers with eccentricity are investigated in several previous studies [AB86; Maj88; Olso4; BK14; BK15; BK18], with consistent conclusions. As mentioned in [Olso4] and investigated in detail in [BK19b], also ellipticity hinders ideal balancing of the system and leads to non-ideal resting positions of the balancing masses. As a general conclusion, perfect balancing cannot be reached without a perfect circular and centric orbit, and the met tolerances must be weighed against the reduced achievable compensation effect. In contrast to eccentricity and ellipticity which still yield unique resting positions for ABBs with two balancing masses, the resulting impact of more complex deviations from the ideal geometry, e.g., waviness, depends on the initial conditions and is to be investigated numerically.

4.2.5. Influence of fluid properties

Utilized fluids in ABBs range from air [CSC12; Hai18] to machine oils with a wide range in densities ρ_{fl} and kinematic viscosities ν , ultimately influencing the damping forces acting on the balancing masses and therefore altering the efficiency [RSD03]. As mentioned in section 4.2.2, the choice of fluid has a direct impact on the stability in stationary operation and so, if the necessary damping is not to be provided by frictional effects, a minimum viscosity must be provided. An increase in fluid damping also reduces the decay time of the oscillations the balls perform around their stationary resting positions.

Additionally, the resulting maximal magnitude of rotor deflection while passing a critical speed during run-up is an important objective. Even though high damping is beneficial to suppress sub-synchronous operation, it leads to less lag between the rotor speed and the orbiting speed of the balls during run-up. As a result, 'the balls move practically with the same speed as the rotor,' inducing 'rather high vibrations near the critical speed as a result of superposition.' ([RSD03]) In the case of low damping with significant difference in the rotational speeds, the effect of the superimposed ball imbalance cancels out over the respective number of rotations of the rotor.

These conflicting requirements for the fluid properties give rise to optimization potential, which can be exploited by parameter studies in simulations. If the

4. *Translational oscillator model*

ABU is also subject to temperature changes, the dependence of the fluid viscosity on these will need to be considered accordingly. In the conducted experiments, presented in chapter 6, silicone oils with different viscosities have been used to examine the referred influences.

In some applications of ABBs, however, the use of air as a fluid is mandatory since leakage of fluids is to be prevented [Wou+05] and appropriate sealing installation does not meet the economic constraints. As an alternative to the dedicated selection of fluid properties, multiple ABBs² in one plane and with different fluids can be used as a constructive measure, as suggested in [CJ17]. This measure causes different orbital velocities in the individual ABBs, which also results in alternating amplification and attenuation of the superimposed unbalances of the balls and the primary unbalance during run-up. In steady-state operation, the impact of diverse damping is minor as long as each ABB meets its stability criteria.

4.2.6. Influence of external excitation

Rotors with ABBs can be subject to external excitation from a variety of sources. They may result from nearby machinery, movement of the rotor system as part of a vehicle or work forces inherent to the machine operation, for example. Sung et al. [Sun+13] examined the influence of harmonic external forces on ABBs in optical disc drives and conclude that the ABB is only affected if the excitation frequency is equal to the rotation frequency of the rotor. In the case of synchronous excitation, the resting positions of the balls change depending on the amplitude and phase of the excitation to counteract not only the primary unbalance of the rotor but also the synchronous external excitation. This can be reasoned by the equivalent³ effect of both excitations on the rotor deflection and thus on the mechanism of the ABB. Therefore, a synchronously excited ABB exhibits residual unbalance [Maj88].

²This corresponds in principle to a special case of the design proposal in fig. 2.5g, in which several raceways of an ABB are sealed off from each other.

³An unidirectional harmonic excitation can be divided into the sum of a same and counter rotation excitation [Ish12]. As described above, counter rotation excitations have no effect on the ABB.

4.3. Extension to spatial rotordynamic models

The planar oscillator can only represent a limited part of the rotating machinery, whose unbalance excitation can be reduced by using ABBs. To support the application in more technically complex systems and to advance the use of ABBs, several authors have studied spatial rotors including ABBs.

In the case of a spatial rigid rotor, either in elastic bearings, cf. fig. 1.1 on page 2, or mounted to an elastic shaft in rigid bearings, cf. fig. 4.4 on page 51, the use of ABBs is generally possible with the statements on possible influences from section 4.2 still applicable. In addition to the balancing in one plane, a second ABB in a different plane can be utilized to counteract also the dynamic unbalance of the rotor [SRD01]. Due to the mandatory supercritical operation resulting in the required phase shift in the vibration response, ‘the rotor polar moment of inertia’ has to be ‘smaller than the transverse one, because only such rotors exhibit a critical speed.’ ([Spe+04])

The equations of motion with gyroscopic effects taken into account can be set up accordingly with Lagrange’s method formulated in generalised coordinates. This was done by [CR99], for example, analysing the stability of the stationary balanced state. As confirmed in [Rod+11] by experimental investigation on a spatially supported rotor with an ABB in elastic support, the functionality is provided.

For elastic rotors on the other hand, e.g., an elastic shaft with multiple discs, the profitability of using multiple ABBs depends on their position along the rotor axis. As derived in [Fil+17], a flexible rotor operated above the N -th critical speed needs N ABBs, mounted at the nodes of the $N + 1$ -th vibration mode of the rotor, for optimal performance.

5. ABB Multibody system force element

The fundamental rationale for ABBs lies in the modular application to rotating systems experiencing inadmissible unbalance excitations and are therefore often considered in the late stage of product design or after production to overcome problems that were only detected during operation. It is therefore appropriate to use the computer-aided modelling framework of Multi-body system (MBS) approaches to analyse rotating systems with ABBs. Due to the systematic modelling of interconnections of rigid and elastic bodies, this approach is particularly suitable to implement, analyse and optimise additional counterbalancing effects resulting from supplementation of ABBs to the system. In addition, the use of MBS software is common in the development and design of (rotating) machinery to determine feasible operating ranges, resonance frequencies and dynamic loads for example. Therefore, relevant models are often already present when residual problems of unbalance excitation are addressed.

Resulting from the resemblance of ABB designs to radial ball bearings, the relevant routines in MBS software, when available to the developer, can serve as a starting point to derive custom force elements. Details on rolling element bearing implementations can be found in [FBS09; Cen16] for MSC/ADAMS, in [Qia14] for SIMPACK and in [Dan13] for EMD¹. The latter was developed at the chair of Technical Dynamics of the University of Magdeburg [Wos13; Dan13; Nit17].

Despite the similarity to radial ball bearings, there are several differences

¹Due to the comprehensive access to the source code and readily available support of the main developers the implementation of an ABB force element in EMD is conducted. However, this does not impede an equivalent implementation in other MBS software.

in kinetic modelling and the associated numerical implementation, which are explained in this chapter. Generally, the ABB represents a radial ball bearing missing the cage together with a majority of the balls, showing distinct clearance between the balls and the inner ring to ensure unrestricted movements of the balls. Further, rolling element bearings are usually not fully filled with lubricant to reduce churning losses and increase efficiency. Since fluid damping is relevant to the dynamic behaviour of ABBs, it is modelled in more depth.

In contrast to the common usage in radial bearings, the load on the balls in ABBs is mainly resulting from gravitation, drag induced by the viscous fluid passing the balls and radial and tangential loads in the contact area with the outer ring. The radial load, directed to the bearing center, applies the centripetal force necessary to maintain orbital motion and the tangential loads result from contact friction and adherence. For moderate² rotational speeds, these loads are much lower than those in a radially loaded roller bearing and therefore typically neglected in the dimensioning with respect to mechanical robustness and approximated in their entirety to determine the power loss of the bearing.

The presented implementation of an ABB MBS force element is based on a planar radial ball bearing model calculating the reaction forces between the balancing masses and the raceway. In the use-case of automatic ball balancing the raceway, i.e., the outer ring, is tied to a rotor marker whose axial coordinate is located in the balancing plane. Hence, the deflection of the rotor can influence the contact condition. The sum of the raceway reaction forces with the balls is imposed on the marker of the rotor, representing the counterbalancing forces to reduce rotor unbalance excitation. The underlying sequence diagram of the rolling bearing force element is shown in fig. 5.1. The solution of the differential equation of motion in the time domain by an ODE solver yields the positions and velocities of all bodies. From the positions, the contact conditions between the rolling elements and the raceway can be

²In the case of super speed centrifuges and high-speed ball bearings the centripetal forces are distinct, accordingly.

5. ABB Multibody system force element

checked and consequently normal and tangential forces can be calculated, as described in the following section.

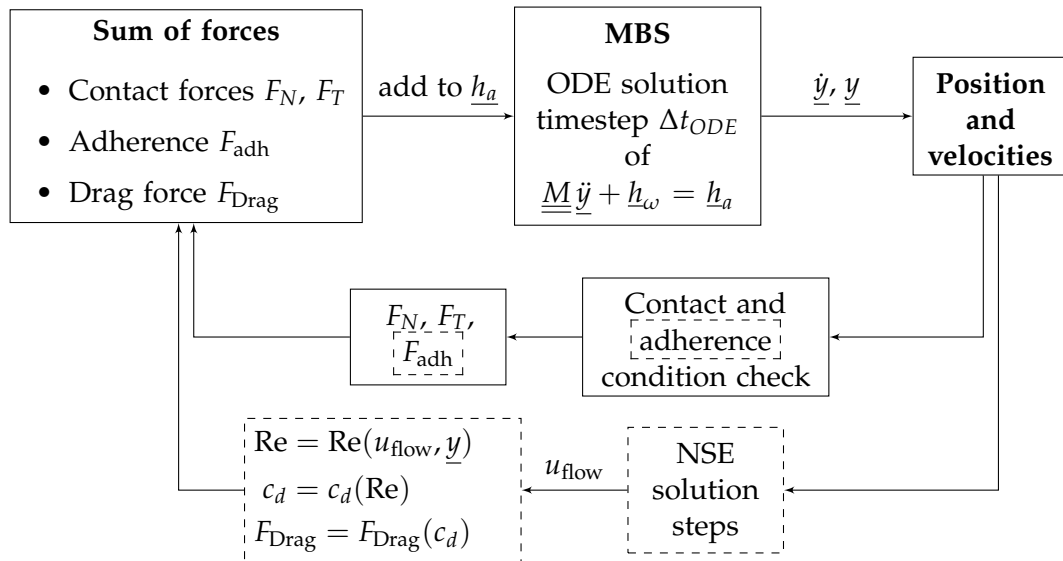


Figure 5.1.: Flowchart of the ABB force element based on a radial bearing force element. Expansions compared to the original routine are highlighted in dashed boxes.

As will be discussed further, the modelling of the adherence of the rolling elements is revised to reflect the potential misalignment in steady-state balancing. Since in regular rolling bearings a mostly uninterrupted orbital motion prevails due to the contact with inner and outer ring on both sides and possibly a cage, even if one of the two bearing rings is immobile with respect to the inertial system, the adherence is rather of secondary importance. In addition, the forces acting on the rolling elements in the orbital direction must be extended to include the flow resistance, as explained in section 5.2. Here, not only a non-linear damping characteristic is implemented by the flow velocity-dependent drag coefficient, but also the mass inertia of the fluid is represented, which has not yet been found in any published model on ABBs.

5.1. Modelling contact, friction, rolling resistance and adherence

5.1.1. Contact normal forces

The ABB force element is based on that of a 2D rolling element bearing [Dan13]. Therefore, the contact detection of the circular contours of the balls and the raceway by an analytical determination is efficient. It is assumed that the balls can have only a single point of contact with the raceway, be it a simple cylindrical geometry or the use of bearing outer rings with a groove to reduce rolling resistance. Contact with the raceway occurs when the distance of the ball center from the bearing center, calculated by the magnitude of the difference of the position vectors \underline{r}_b and \underline{r}_{or} , exceeds the nominal orbital radius ε , i.e., the indentation δ_c is given by

$$\delta_c = |\underline{r}_b - \underline{r}_{or}| - \varepsilon. \quad (5.1)$$

The indentation velocity relevant for modelling contact damping can then be determined by projecting the velocity difference in the direction of the contact point, i.e.,

$$\dot{\delta}_c = \frac{(\dot{\underline{r}}_b - \dot{\underline{r}}_{or}) \cdot (\underline{r}_b - \underline{r}_{or})}{|\underline{r}_b - \underline{r}_{or}|}. \quad (5.2)$$

The calculation of the contact normal force F_N can be performed subsequently by a linear spring-damper model

$$F_N = \begin{cases} \delta_c k_c + \dot{\delta}_c b_c & \text{if } \delta_c \geq 0 \\ 0 & \text{if } \delta_c < 0 \end{cases}. \quad (5.3)$$

In the dynamic rolling bearing simulation, the loads on the individual rolling elements are the primary target of the calculation, which are decisive for the bearing design. Due to the contour deformation of the bodies in contact, there is a strong non-linear relationship to the distribution of radial loads to be

5. ABB Multibody system force element

transmitted over the entire rolling elements. Thus, the determination of a suitable contact stiffness in eq. (5.3) is an essential part of the modelling. A common approach is to model according to the Hertz point contact, which results in a non-linear relationship between the flattening of the sphere, represented in the model by the indentation δ_c , and the normal force F_N [Teu05; Dan13; Kie17]. In this approach, the Youngs moduli, contour radii and Poisson's ratios of the contact bodies are thus included in the calculation. Therefore, only geometrical quantities as well as material parameters are to be identified and no estimation of integral equivalent quantities. This modelling can also be found in ABB models in the literature, e.g., [CSL05], for the subsequent calculation of friction forces that depend on the normal forces.

For the ABB simulation, such detailed modelling is not necessary, since the loading of the individual ball does not affect that of the others. In fact, underestimating the contact stiffness can improve the numerical stability of the solution in the time domain, since the contact force builds up more smoothly at the beginning of the contact. For large contact forces during contact initialization, smaller time step sizes of the solver are needed to reflect the gradient in the required error bounds. Even with underestimation of the contact stiffness for the above reason, the resulting orbit radius will be, by relative measure, insignificantly different from the nominal orbit radius ε . The relative error in the resulting unbalance radii of the balancing masses is just as large. Since the calculation by the Hertzian approach is already available as a subroutine in the underlying MBS force element, however, it was utilized.

5.1.2. Friction and rolling resistance

The modelling of sliding friction, rolling resistance and adhesion has a great influence on the resulting dynamic behaviour of the simulation model with ABB, as these influence the positions of the correction masses and thus the resulting unbalance excitation during the transient phase of the run-up as well as the stationary operation.

According to Coulomb's law, the tangential force F_T is proportional to the

5.1. Modelling contact, friction, rolling resistance and adherence

normal force F_N in the contact point

$$F_T = F_N \mu, \quad (5.4)$$

with the friction coefficient μ . During sliding at the contact point, i.e. when slip occurs, with the tangential relative velocity u_t , tangential forces act on the balancing mass, where the direction is determined by the sign of the relative velocity, and thus

$$\mu = \mu(u_t) = \mu_{\text{kin}} \text{sign}(u_t). \quad (5.5)$$

Here μ_{kin} is the coefficient of kinetic friction.

Since the velocity u_t never exactly equals zero during the simulations, this leads to an oscillating force at low slip velocities. The associated large gradients would lead to very small time step sizes being required for the numerical solution of the equations of motion [Mar+16]. To avoid this problem, the functional relationship between kinetic friction coefficient and slip velocity is regularised. This can be done by the tangent hyperbolic function

$$\mu(u_t) = \mu_{\text{kin}} \tanh\left(\frac{u_t}{u_1^*}\right) < \mu_{\text{kin}}. \quad (5.6)$$

In order to approximate adhesion in the vicinity of $u_t = 0$, which allows a larger maximum value of the tangential force with the coefficient $\mu_{\text{adh}} > \mu_{\text{kin}}$, formulations of the form

$$\mu(u_t) = \left[\mu_{\text{kin}} + (1.0 - \mu_{\text{kin}}) \exp\left(-\frac{u_t}{u_2^*} \text{sign}(u_t)\right) \right] \tanh\left(\frac{u_t}{u_3^*}\right) \quad (5.7)$$

are common. In both cases, the quantities u^* can be adjusted to obtain the desired regularised progression, see fig. 5.2.

In rolling bearing calculations, the tangential load dependent on the sliding speed is of interest. On the one hand, this is important for the mechanical load of the rolling elements and, on the other hand, as a measure of the dissipated energy and thus the efficiency of the bearing. However, this is not sufficient for the simulation of automatic balancing units, since in the case

5. ABB Multibody system force element

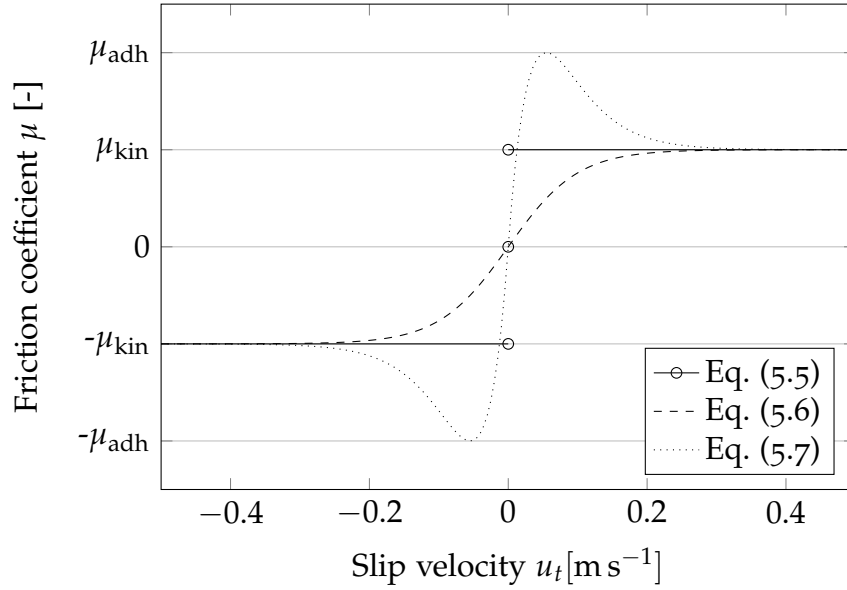


Figure 5.2.: Friction coefficient models depending on the slip velocity in the contact point.

of low tangential speeds, i.e. when the ideal rolling condition is fulfilled, no energy is dissipated. Especially in the positioning process of the balancing balls during stationary operation of the rotor, it can be assumed that the sliding speed at the contact point is close to zero.

A sphere rolling down an inclined plane, see fig. 5.3, would never reach a terminal velocity if only kinetic friction is considered. Therefore, the rolling resistance must be taken into account. The cause can be illustrated by the fact that there is a flattening in the contact surface which is not symmetrical. The normal force thus also exerts a moment on the ball via the length a , measured in the direction of the rolling motion. The evaluation of the equilibria according to the d'Alembert principle yields [Cro15]

$$m_b g \sin(\gamma) = m_b \ddot{x} + F_T \quad (5.8)$$

$$J \ddot{\kappa} + F_N a = F_T r_b \quad (5.9)$$

$$F_N = m_b g \cos(\zeta). \quad (5.10)$$

5.1. Modelling contact, friction, rolling resistance and adherence

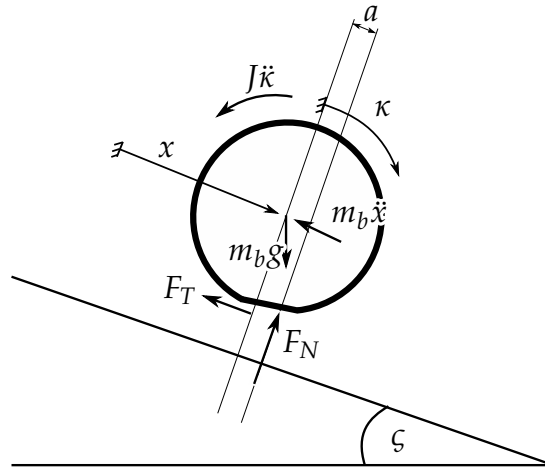


Figure 5.3.: Ball rolling down an inclined plane, influenced by friction and rolling resistance.

The combination of eq. (5.8) and eq. (5.9) after elimination of F_T yields

$$\ddot{x} + \frac{J}{m_b r_b^2} r_b \ddot{\kappa} = g \sin(\zeta) - \frac{F_N a}{m_b r_b}. \quad (5.11)$$

Together with eq. (5.10) this gives

$$\frac{r_b \ddot{\kappa}}{g} = \frac{\sin(\zeta) - \frac{a}{r} \cos(\zeta)}{\frac{\ddot{x}}{r_b \ddot{\kappa}} + \frac{J}{m_b r_b^2}}, \quad (5.12)$$

with $\frac{J}{m_b r_b^2} = 0.4$ for spheres. Division of eq. (5.9) by $F_N r_b$ then yields with eq. (5.12) the rolling resistance coefficient

$$\mu_R = \frac{F_T}{F_N} = \frac{\frac{J}{m_b r_b^2}}{\frac{J}{m_b r_b^2} + \frac{\ddot{x}}{r_b \ddot{\kappa}}} \tan(\zeta) + \frac{\frac{\ddot{x}}{r_b \ddot{\kappa}}}{\frac{J}{m_b r_b^2} + \frac{\ddot{x}}{r_b \ddot{\kappa}}} \frac{a}{r_b}. \quad (5.13)$$

This coefficient can take on at most the value of the kinetic coefficient of friction. For $\mu_{\text{kin}} = 0.05$ this is the case for inclination angles $\zeta > 10^\circ$. The right part in eq. (5.13) is of the order of 0.001 for hard surfaces [Cro15; Cro16] and can therefore be neglected for inclination angles $\zeta > 2^\circ$. However, for horizontal rolling without sliding, this is the only remaining resistance.

5. ABB Multibody system force element

In ABBs, as previously described, the normal force provides the necessary centripetal acceleration and the gravitational force is of minor relevance at the appropriate speed. In order to take the significant influence of the rolling resistance in the ABB into account during the positioning phase of the balancing masses as well as the stabilising effect when considering the Sommerfeld effect, eq. (5.5) is to be extended with

$$\mu = \mu_{\text{kin}} \text{sign}(u_t) + \frac{1}{1.4} \frac{a}{r_b} \text{sign}(u_{\text{orb}}), \quad (5.14)$$

where $u_{\text{orb}} = \varphi_b \varepsilon$ is the velocity of the balls centre on its orbit relative to the raceway. Again, the left part can be regularised according to eq. (5.6) or eq. (5.7). This is not the case for the right part.

5.1.3. Adherence regarding the orbital position

Although kinetic friction and rolling resistance influence the transient behaviour of the balancing masses, they have no influence on the final resting positions. These are 'determined by the static friction level and not by the friction model for nonzero velocities.' ([Wou+05]) And as mentioned, the adhesion should be as low as possible to keep the displacement regarding the optimal positions small.

In the model of [Bol10], which is based on minimal coordinates, the degree of freedom of the sphere position was locked when the adhesion condition was reached, i.e., the velocity of the sphere with respect to the raceway fell below a threshold velocity. For this purpose, the system of equations was adjusted during the numerical solution so that the acceleration of the relative orbit position is forced to zero. Such intervention in the solution routine should be avoided in the presented MBS approach and the limits of the force element as a subroutine in the MBS software should be respected. In addition, the degrees of freedom of the ball displacement are Cartesian and thus cannot be locked directly.

In the MBS force element the condition of adherence regarding the orbital position of each ball is met if the slip velocity u_t as well as the orbit velocity

5.1. Modelling contact, friction, rolling resistance and adherence

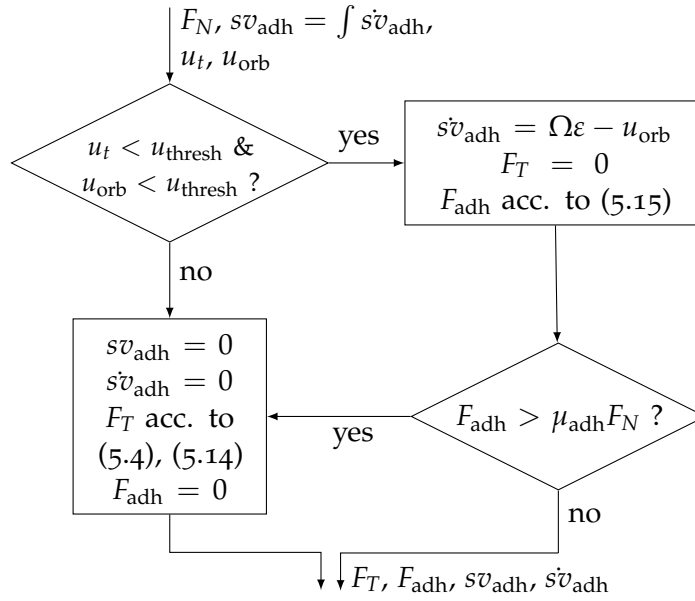


Figure 5.4.: Flow chart of adherence implementation.

u_{orb} relative to the raceway is below a predefined threshold u_{thres} , see fig. 5.4. An additional state variable sv_{adh} for each balancing ball was defined, which holds the deflection regarding the orbit position, at which the condition was met. The derivative of the state variable $s\dot{v}_{adh}$ is then calculated from the velocities of the raceway and the ball. Instead of a tangential force in the contact point, an adherence force

$$F_{adh} = k_{adh}sv_{adh} + b_{adh}s\dot{v}_{adh} \quad (5.15)$$

is calculated and imposed on the ball center. In this way, the ball is held at the position where adhesion was detected, in the manner of a spring-damper component. The stiffness and damping parameters are then selected in such a way that no high-frequency oscillations occur around this rest position. Since the driving forces in the orbit direction are small in general, a moderate stiffness of $k_{adh} = 1 \text{ N mm}^{-1}$ suffices.

If the resulting adherence force calculated from eq. (5.15) is larger than the maximum adherence force defined by the normal force and the maximum adherence coefficient μ_{adh} , the state variable is reset to zero and the regular

calculation of F_T in the contact point is reinstated. Through this implementation, oscillations around the rest position influenced by the adhesion are damped by the damping term in eq. (5.15) and small time step sizes are avoided.

5.2. Modelling drag forces

As explained in chapter 4, the damping effect of the fluid on the balancing balls is in most cases represented by a linear-viscous relationship, cf. eq. (4.11) on page 32. A sphere with the orbital radius ε is thus subjected to the force

$$F_{\text{Drag}} = \frac{\beta}{\varepsilon} \dot{\phi}_i, \quad (5.16)$$

proportional to the orbital angular velocity relative to the rotor, acting in the azimuthal direction. However, it must be criticised that β represents a parameter that is difficult to estimate quantitatively.

Although it is nowadays possible, with appropriate computing power, to configure a coupled simulation of the dynamics using MBS and the flow around the spheres in the cavity using computational fluid dynamics (CFD) software, this is still not practical. Due to the movement of two or more spheres in the domain, the adaptive meshing that this requires as a function of the sphere positions proves difficult. As a result, the required simulation time would increase by orders of magnitude compared to MBS without ABBs and corresponding CFD coupling. This is unacceptable in practice, especially if a large number of simulations are required due to parameter variation of the ABB design parameters. Thus, as is so often the case, a trade-off must be made between the modelling depth of the flow effects on the automatic balancing and the resulting increase in model setup time and simulation time. Therefore, an approach is pursued in which the flow-induced surface pressure on the sphere is represented by an effective drag force vector, see fig. 5.5.

5.2. Modelling drag forces

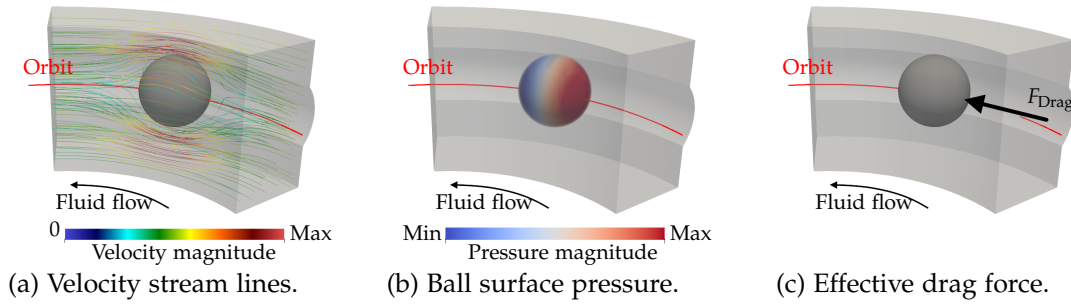


Figure 5.5.: Exemplary CFD results of laminar flow around a ball in the ABB annular cavity with reduction to an effective drag force tangential to the ball orbit.

As described in [Hua+02], the approach

$$F_{\text{Drag}} = \frac{1}{2} \rho_{\text{fl}} \bar{A} c_d u_{\text{rel}}^2 \text{sign}(u_{\text{rel}}), \quad (5.17)$$

commonly used in fluid dynamics to solve gas-particle flows [Hen76], can be used to concretise the modelling. Here, \bar{A} and u_{rel} describe the cross-sectional area of the ball and the velocity of the undisturbed flow relative to the ball. Huang et al., however, interpret the drag coefficient c_d as a constant parameter and u_{rel} is approximated by the relative velocity of the ball with respect to the cavity walls. Hence, the fluid is not modelled as a separate entity and its inertia is neglected. Further, as is well known from the literature on fluid dynamics [Mor13], the drag coefficient c_d depends on the geometry of the considered object, the flow velocity and the boundary effects of the fluid domain boundaries. As a result, especially in the transient phase of the operation of rotors with ABBs, significant non-linear correlations arise.

Prior to [SDW17], no published studies on a particle flow-based description with velocity dependent drag coefficients in the context of ABBs are known. But the idea of such an enhancement of the description of damping in the balancer cavity found approval in subsequent publications, [Hai18]. The implemented modelling of the mentioned aspects, namely the consideration of the fluid inertia, as was proposed later in [SDW18], and the velocity-dependent drag coefficient, are elaborated in the following subsections.

5. ABB Multibody system force element

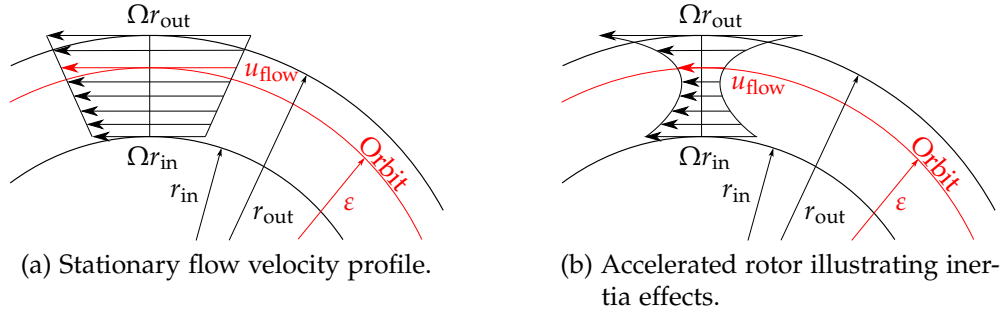


Figure 5.6.: Qualitative fluid velocity profiles in the ABB annulus under different conditions shown in the plane of the circular orbit of the balancing ball.

5.2.1. Solution of the transient fluid flow velocity profile

Due to the no-slip condition at the walls of the cavity, the fluid adopts the rotor speed. Considering the steady state of a rotating annular domain, a linear fluid velocity profile is established as shown in fig. 5.6a in a cross-sectional view. During acceleration of the rotor, however, the velocity profile changes, see fig. 5.6b. While the no-slip condition at the annulus boundaries still holds, the inertia of the fluid causes the flow velocity near the center of the annular cross-section to lag behind. The extent of which depends on the dimensions of the cross-section as well as the density and viscosity of the fluid.

Since the balls along the raceway disturb the rotational symmetry of the fluid domain, their retroaction is neglected in favour of a fast numerical solution of the flow profile. This assumption is thus a simplified representation whose inaccuracy increases with the number of balls in the ABB. However, for the ABB configurations with one or two spheres considered in this work, this is considered acceptable.

With this approach, the 2D angular momentum solution Γ based on the Navier-Stokes equations can be obtained efficiently for the rotationally symmetric problem according to the elaboration in chapter 3. The azimuthal fluid velocity required for the drag is then calculated from the angular momentum at the point where the centre of the sphere is located on the orbit, i.e.,

$$u_{\text{flow}} = \frac{1}{r} \Gamma \Big|_{r=\varepsilon, z=\frac{H}{2}}. \quad (5.18)$$

5.2. Modelling drag forces

The relative flow velocity u_{rel} is then calculated by subtracting the velocity of the balls centre of mass projected to the azimuthal direction.

To obtain a holistic solution method, the solution of the 2D flow velocity profile by finite differences is integrated into the routine of the ABB MBS force element utilizing the FISHPACK Fortran library, see chapter 3. However, the solution of the constructed systems of equations does not occur simultaneously with the solution of the equations of motion by the ODE solver, but is only updated after each valid time step Δt_{ODE} of the respective time integration.

It is to be noted that due to the CFL condition, eq. (3.20) on page 26, the maximum time step Δt_{NSE} of the solution of the Navier-Stokes equations is limited. In the case that $\Delta t_{NSE} < \Delta t_{ODE}$, the solution of the Navier-Stokes equations occurs in several consecutive time steps so that the two time axes are synchronous again. In the other case $\Delta t_{ODE} < \Delta t_{NSE}$, however, Δt_{NSE} is set equal to the current Δt_{ODE} .

If, during the solution of the MBS ODE, intermediate time steps are evaluated in the solution scheme, the ABB force element returns the drag force acting on each ball from the last valid time step from memory. This is considered permissible because the gradients of the flow resistance forces are comparatively small and are not subject to switching functions, as is the case with contact detection, for example, which requires iteration of the state variables.

5.2.2. Determination of the velocity dependent drag coefficient

The drag coefficient c_d used to calculate the drag force in eq. (5.17) is not constant. In addition to the shape of the body in the flow and the geometry of the fluid domain, it also represents the characteristics of the flow, i.e. whether it is laminar or turbulent. Since the flow regime changes depending on the flow velocity, the drag coefficient

$$c_d = c_d(\text{Re}) \tag{5.19}$$

5. ABB Multibody system force element

is a function of the dimensionless particle Reynolds number³

$$\text{Re} = \frac{u_{\text{rel}} d_b}{\nu}. \quad (5.20)$$

Analytical solutions to eq. (5.19) exist only for a few simple flow examples. One of them is the solution by Stokes for the problem of a sphere with laminar flow in the free field $c_d = 24/\text{Re}$, which applies for Reynolds numbers smaller than two [Mor13].

For technical relevant flows, e.g. that in ABBs, with more complicated boundary conditions and larger Reynolds numbers, empirically obtained approximate equations or numerical simulations using CFD must be resorted to. An investigation closer to the conditions in the ABB annulus is described in [JC97]. The authors investigated the terminal velocity of a sphere rolling down an inclined plane. The contact with a planar surface corresponds in a first approximation to the conditions in the ABB, where the ball is in constant contact with the raceway. The stated equation is [JC97]

$$c_d = \begin{cases} 322 \text{Re}^{-1} & \forall \text{Re} \leq 10 \\ 10^Y & \forall 10 < \text{Re} \leq 20000 \\ 0.74 & \forall \text{Re} > 20000, \end{cases} \quad (5.21)$$

with $Y = 3.02 - 1.89 \log(\text{Re}) + 0.411(\log(\text{Re}))^2 - 0.033(\log(\text{Re}))^3$.

However, the additional curvatures of the raceway are not taken into account here. This is, on the one hand, the curvature around the rotor axis and, on the other hand, due to the groove if the outer ring of a ball bearing is used for friction optimisation.

In [SW20b; Spa20b] the drag coefficient for the ABB annulus geometry of the rotor presented in section 6.1 in more detail was identified by CFD analysis for low Reynolds numbers, i.e., in the Stokes regime. By varying the ratios

³Reynolds numbers are also used for pipe flows and other applications with different definitions for the characteristic length. To emphasise the relation to the particle diameter as characteristic length, the designation of the particle Reynolds number is used. Since no additional Reynolds number is defined in this work, however, this emphasis is omitted in the following.

5.2. Modelling drag forces

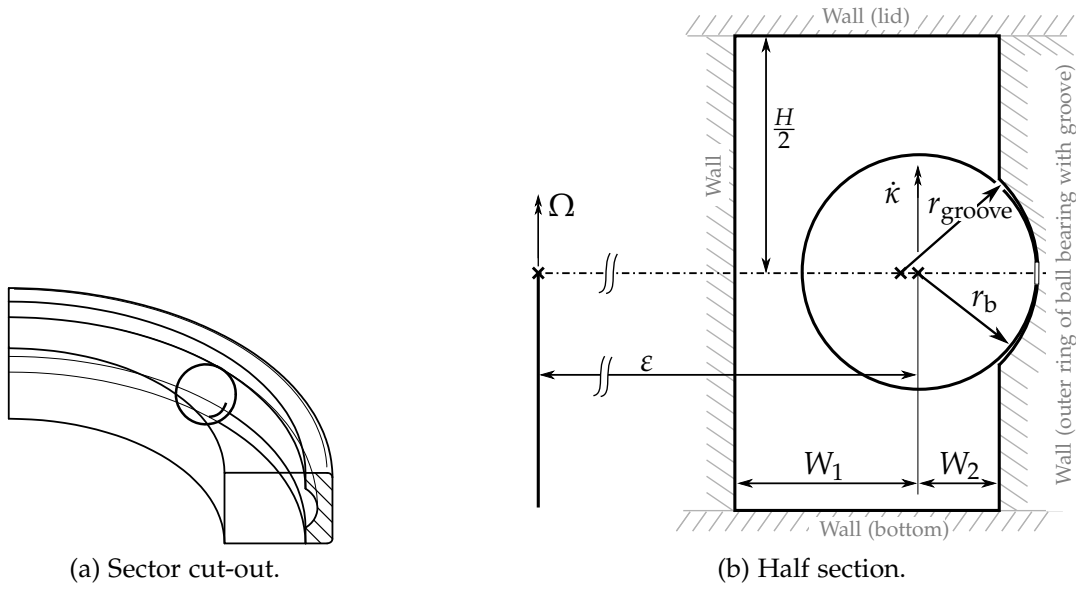


Figure 5.7.: Annulus inside an ABB with one ball and a rolling element bearing raceway.

of significant geometric parameters of the cross-section, see fig. 5.7b, the empirical relation [SW20b]

$$c_d = \left[248 \left(\frac{W_1}{r_b} \right)^{-11/8} + 245 + 813 \left(\frac{r_b}{\epsilon} - 0.08 \right) \right] \text{Re}^{-1} \quad \forall \text{Re} \leq 10 \quad (5.22)$$

is proposed.

5.2.3. Effect of virtual mass

Another aspect of fluid reaction forces is the added virtual mass, whose inertia is antagonising the acceleration of a rigid body in a fluid. Again, the appropriate coefficient is usually accessed empirically. No investigations were carried out on the ABB models, but for balls in contact with a flat surface, Jan and Chen [JC97] identified the coefficient empirically to be $c_{vm} = 2$. This was also applied in the same form to the ABB MBS simulations. Derived from their conclusions, the impact of the added mass effect is decreasing with an

5. ABB Multibody system force element

increasing ratio in the densities ρ_b/ρ_{fl} . The force of virtual mass equals

$$F_{vm} = \frac{\pi d_b^3}{6} \rho_{fl} c_{vm} \dot{u}_{rel}. \quad (5.23)$$

5.2.4. Slipstream effects

The modelling proposals from the previous subsections are based on the consideration of a single sphere in the flow. When using several balls in the ABB or even in the transient phase of an ABB with two balls, slipstream effects can occur with regard to the drag. If two bodies are in a tandem arrangement in the direction of flow, the body positioned downstream experiences less drag, as schematically shown in fig. 5.8.

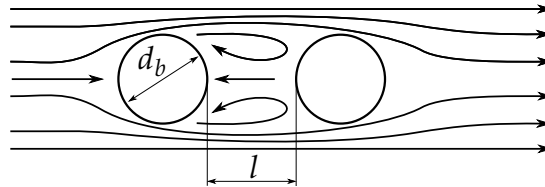


Figure 5.8.: Schematic of the interacting streamlines of a free flow around two spheres aligned in a tandem manner.

Depending on the distance l between two identical spheres in relation to their diameter d_b and the Reynolds number Re , a reduction of the drag coefficient c_d should be considered. This influence is also dependent on the geometric boundary conditions, but sufficient empirical data is only available in the literature for the free flow around two spheres.

The slipstream effect has been investigated experimentally and simulatively by various research groups [Tsu+03; YY07; Pra+07; PJR09; Lin11; BRS12]. Based on the data presented in these works, see fig. 5.9, a correction of the drag coefficient c_d in the range $Re = [0, 300]$ and $l/d_b = [0, 20]$ based on a polynomial fit is possible.

5.2. Modelling drag forces

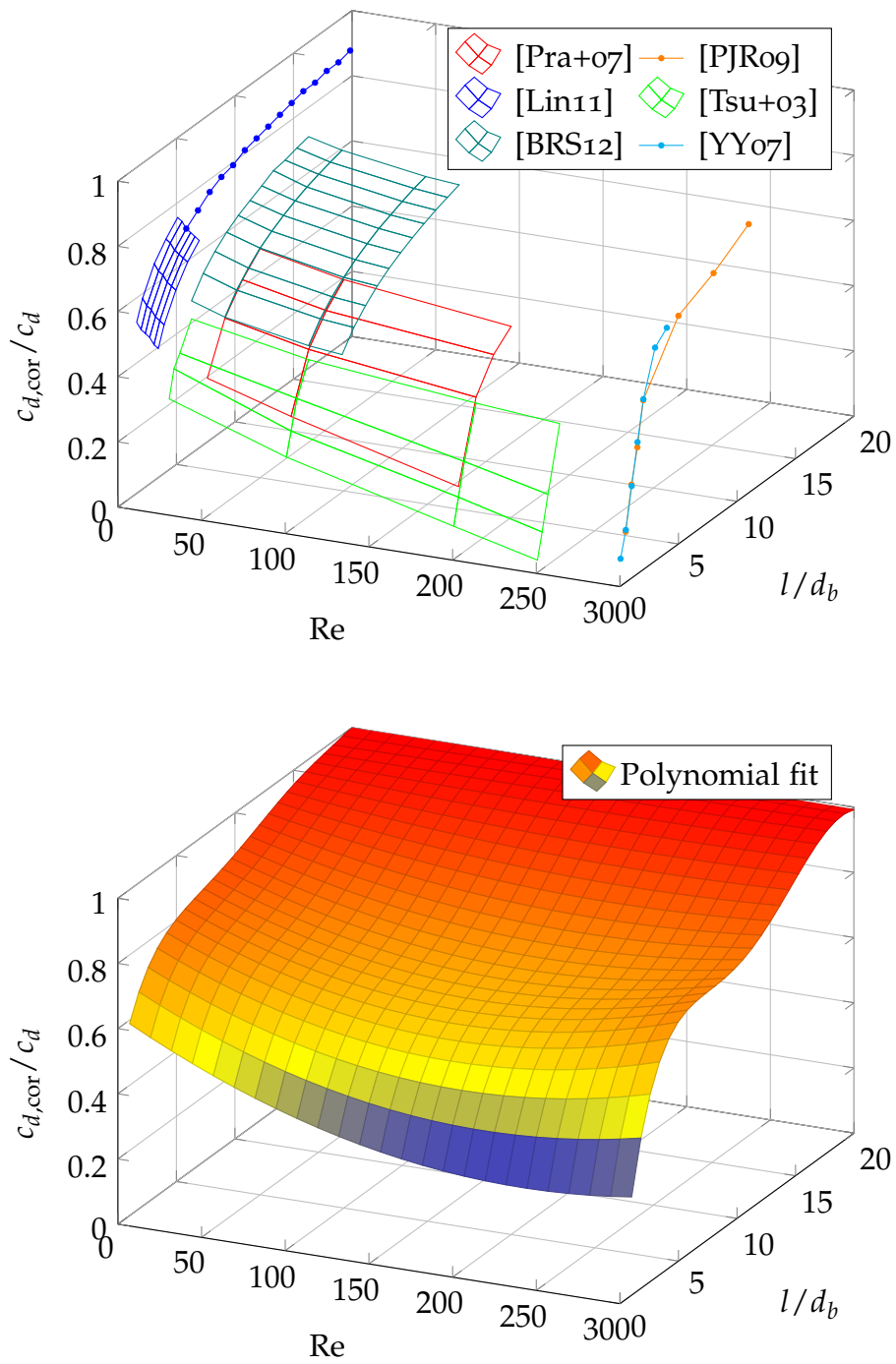


Figure 5.9.: Drag coefficient correction factors depending on Reynolds number and distance between spheres in tandem arrangement.

5. ABB Multibody system force element

The correction factor to obtain a corrected coefficient $c_{d,cor}$ yields

$$\frac{c_{d,cor}}{c_d} = \sum_{i=0}^2 \sum_{j=0}^5 p_{ij} \text{Re}^i \left(\frac{l}{d_b} \right)^j$$

with

$$\underline{\underline{p}} = \begin{bmatrix} 452\,100 & 164\,000 & -29\,690 & 2\,731 & -116.9 & 1.876 \\ -2937 & 321.9 & -55.15 & 4.918 & -0.1302 & 0 \\ 4.95 & 0.8646 & -0.1306 & 0.003\,754 & 0 & 0 \end{bmatrix}_{ij} \times 10^{-6}.$$

The sum of squared errors of the presented fit is 0.2422. It becomes clear that the drag decreases significantly when the balls are close to each other which reduces the ball acceleration during run-ups of ABB units as well as the viscous damping determining the presence and absence of sub-synchronous operation, due to the Sommerfeld effect, see section 4.2.2. As a disadvantageous consequence of the slipstream effect, the balls in the ABB will line up when operating in the Sommerfeld region and thus always cause the maximum sub-synchronous excitation.

Additional simulations were carried out by [MCV14] solving the Reynolds-averaged Navier–Stokes (RANS) equations to investigate the tandem effects at high Reynolds numbers ($\text{Re} = 45\,000$) in ball bearings. However, wall effects and the curvature of the bearing geometry were not considered for the sake of simplicity and computational effort.

Since the conducted experiments and according simulations presented in chapter 6 focus on a validation with one or two balls in the ABB unit, the correction of drag forces due to slipstream effects was not implemented. Based on the CFD model utilized to obtain the drag coefficient presented in eq. (5.22) on page 75, a more suitable slipstream correction specification may be established in future research.

5.2.5. Linear coefficient for stationary laminar flow

As stated above, the product of drag coefficient c_d and Reynolds number Re yields a constant in the laminar Stokes regime, meaning $Re \leq 10$. This relationship can be exploited to derive an equation for the linear viscous damping parameter β , which is difficult to assess otherwise, as described below. With this approach, published in [SW2ob; SW2oa], the multitude of available models in the literature, cf. section 1.1, can be applied even better to the explicit design of ABBs.

Assuming that the fluid is rotating stationary with the rotor angular velocity, the relative flow velocity equals

$$u_{\text{rel}} = \varepsilon \dot{\varphi}, \quad (5.24)$$

where φ describes the angular orbit position of the ball relative to the rotor, cf. section 4.1. Inserting equations (5.24) and (5.20) into eq. (5.17) yields

$$\begin{aligned} M_D &= F_{\text{Drag}} \varepsilon = \frac{1}{2} \rho_{\text{fl}} \bar{A} c_d(\text{Re}) u_{\text{rel}}^2 \varepsilon \text{sign}(u_{\text{rel}}) \\ &= c_d \text{Re} \frac{\pi}{4} \rho_{\text{fl}} \nu r_b \varepsilon^2 \dot{\varphi}. \end{aligned} \quad (5.25)$$

Hence, comparison with eq. (4.11) yields

$$\beta = c_d \text{Re} \frac{\pi}{4} \rho_{\text{fl}} \nu r_b \varepsilon^2. \quad (5.26)$$

The viscous parameter can thus be calculated on the basis of the orbital radius, the ball radius and the fluid properties. The product $c_d \text{Re}$ is a constant in this case and must be estimated for the ABB annulus geometry. In a first approximation, the empirical result $c_d \text{Re} = 322$ for the contact of a sphere with a plane surface from eq. (5.21) can be used. Alternatively, the result from the parameter study carried out by CFD analysis in eq. (5.22) is also available. Despite the fact that for transient simulations the flow resistance has a non-linear characteristic, eq. (5.26) is particularly useful for stability analyses, as the assumptions made at the beginning of this section apply.

6. Model validation with centrifuge test rigs

In order to check how accurate the multi-body system force element for ball balancers can replicate the dynamic behaviour of automatically balanced rotors, two test-rigs have been examined. To reduce friction and resulting mispositioning of the balancing balls, both rotors under consideration are equipped with outer rings of ball bearings, serving as raceways for the balls. The first system can be characterized as a rigid rotor mounted on rubber bushings with a discoidal rotor with an inbuilt ABB, section 6.1. The second system is a spatial centrifuge rotor, which was modified by attaching a modular ABB, mounted to an elastic shaft.

On the one hand, the transient rotor deflections and the stability limit of sub-synchronous operation, both important technical parameters to ensure safe operation, are compared. On the other hand, the test rotors are designed in such a way that the transient positions of the balls in the ABB can be recorded with a camera and compared to the results of the MBS. This provides a possibility to compare the dynamics resulting from the forces acting on the balls.

With the possibility to change the fluid inside the ABBs, the analysis of the influences of density and viscosity on the balancing process is made possible. For the purpose of the presented investigations, silicone oils with different nominal kinematic viscosities at room temperature are used. Silicone oils stand out with optical transparency, beneficial for the post processing of the video footage, good thermal robustness regarding their properties and are commercially available with nominal kinematic viscosities ranging from $0.65 \text{ mm}^2 \text{ s}^{-1}$ up to $2 \times 10^6 \text{ mm}^2 \text{ s}^{-1}$.

Table 6.1 lists properties of silicone oils with nominal viscosities from

Table 6.1.: Properties of silicone oils (Polydimethylsiloxane) [Mar99]

ν at 25 °C [mm ² s ⁻¹]	ρ_{fl} at 25 °C [g cm ⁻³]	Expansion coefficient [10 ⁻⁴ °C ⁻¹]	VTC [-]	P_1 acc. to eq. (6.1) [-]	P_2 [-]
1	0.820	-	0.370	6.839	-3.004
2	0.872	-	0.480	7.547	-3.191
3	0.900	-	0.510	7.106	-2.968
5	0.920	-	0.550	6.758	-2.778
10	0.945	10.0	0.560	5.514	-2.222
20	0.955	9.7	0.575	4.709	-1.855
50	0.960	9.5	0.590	3.920	-1.490
100	0.963	9.4	0.600	3.497	-1.291

1 mm² s⁻¹ to 100 mm² s⁻¹ relevant to automatic balancing and the comparison of available density and kinematic viscosity combinations is shown in fig. 6.1. The thermal stability of lubricants is often characterised by the viscosity-temperature coefficient

$$\text{VTC} = 1 - \frac{\nu(T = 372 \text{ K})}{\nu(T = 311 \text{ K})},$$

where lower coefficients represent better thermal robustness. As presented in [Seeo6], the logarithmic relation

$$\log_{10} \left(\log_{10} \left(\frac{\nu + 0.8 \text{ mm}^2 \text{ s}^{-1}}{1 \text{ mm}^2 \text{ s}^{-1}} \right) \right) = P_1 + P_2 \log_{10} \left(\frac{T}{1 \text{ K}} \right) \quad (6.1)$$

is suitable in order to describe the temperature dependence of low viscous lubricants. Based on the nominal viscosity at 25 °C and the VTC, the coefficients P_1 and P_2 can be derived and are appended in table 6.1. A diagram of the viscosity temperature relations is given in fig. 6.2, comparing the silicone oils to glycerol-water mixtures and ISO-VG machine oils.

6. Model validation with centrifuge test rigs

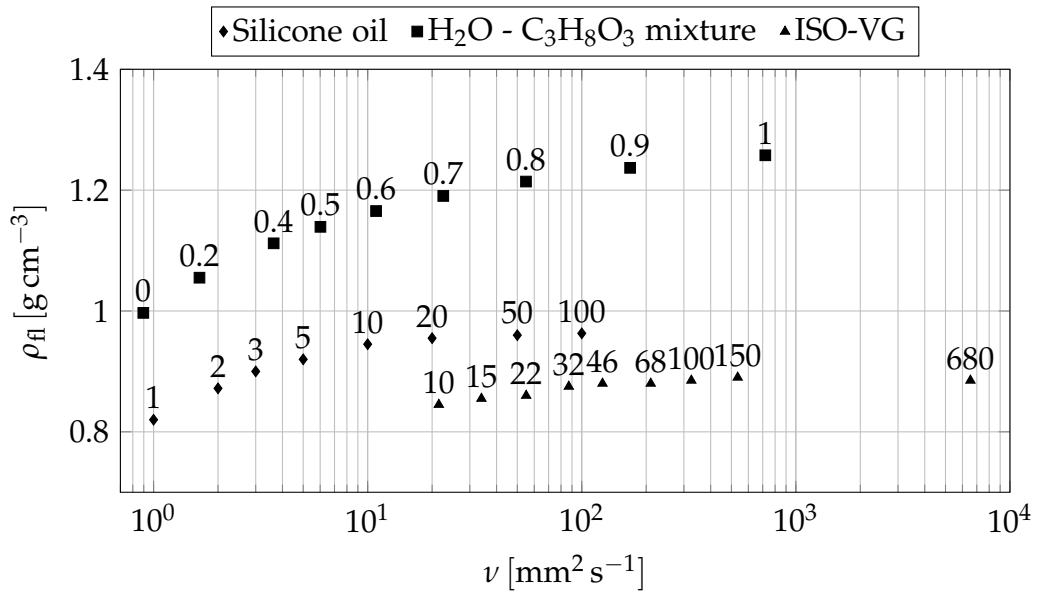


Figure 6.1.: Density-viscosity relations at room temperature for different lubricants. Indicators show the nominal viscosity for silicone oils, the viscosity grade for ISO-VG oils or the volume fraction of glycerol, respectively.

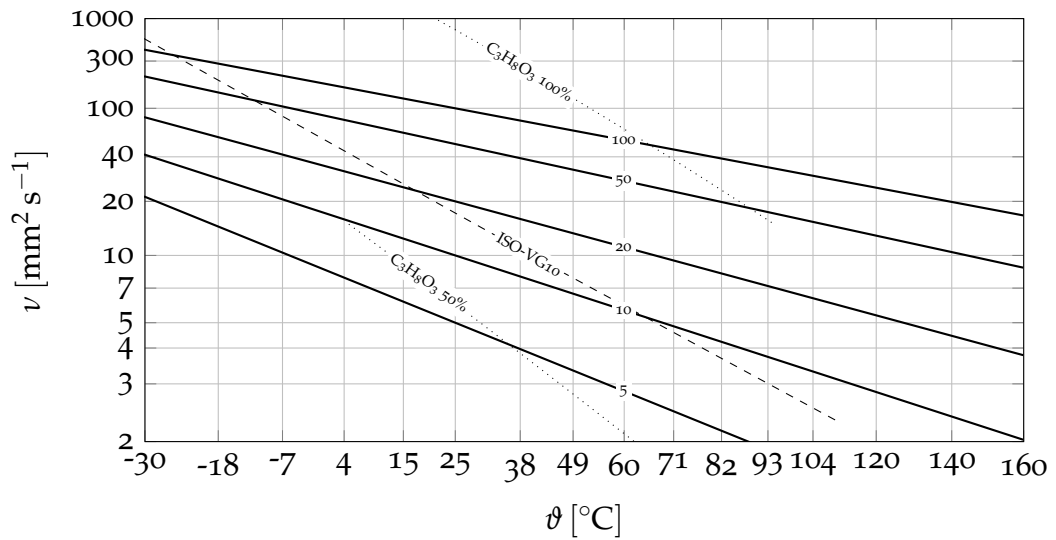


Figure 6.2.: Viscosity-temperature relation for low viscous silicone oils (solid lines). Indicators represent the nominal viscosity at 25°C in $\text{mm}^2 \text{s}^{-1}$. ISO-VG10 machine oil (dashed line) and glycerol-water mixtures with the indicated volume fraction of glycerol (dotted lines) for comparison.

6.1. Discoidal rotor

The drive¹ of a commercially available tabletop centrifuge is utilized for the conducted experiments with the discoidal ABB prototype. A cross-section of the system is given in fig. 6.3. The rotor shaft is mounted vertically with two ball bearings of the types 6204 and 6203 inside a tripartite stator assembly consisting of a covering lid, retaining the top bearing, the stator coil and a base body, retaining the bottom bearing. The base body is suspended by three equiangular positioned rubber bushings against a ground plate which is assumed to suit as the inertial system, see fig. 6.4. Defined unbalances can be placed in the top of the discoidal rotor, between the lid screws (3), by screwing them in provided threaded bores. Geometric and inertial details can be found in appendix B.1.

The entire experimental setup is placed on a vibration-isolated laboratory table and during the measurement runs the rotor is enclosed by a containment. A laser triangulation sensor (LTS) is used to measure the deflection of the shaft, component (8) in fig. 6.3, just above the lid. Due to the finer tolerances of the surface at this point compared to the circumferential surface of the discoidal rotor (5), a reduced influence of the surface waviness on the measurement signal is expected, even though the measured deflections are lower due to the reduced distance to the compliant rubber bushings.

6.1.1. Mechanical model

The structure presented can be regarded as a rigid machine, so that after rigidly connected components have been merged², the result is a oscillatory rotor system with two rigid assemblies, see fig. 6.5.

The two deep groove ball bearings, which support the shaft in relation to the stator, are represented by linear spring elements whose stiffnesses are defined

¹The installed motor is a Leroy[®] Somer D25/T typified as follows: 1.2 kW, 200 V, 4630 min⁻¹.

²As usual with MBS programmes, the calculation kernel handles the merging of the bodies.

6. Model validation with centrifuge test rigs

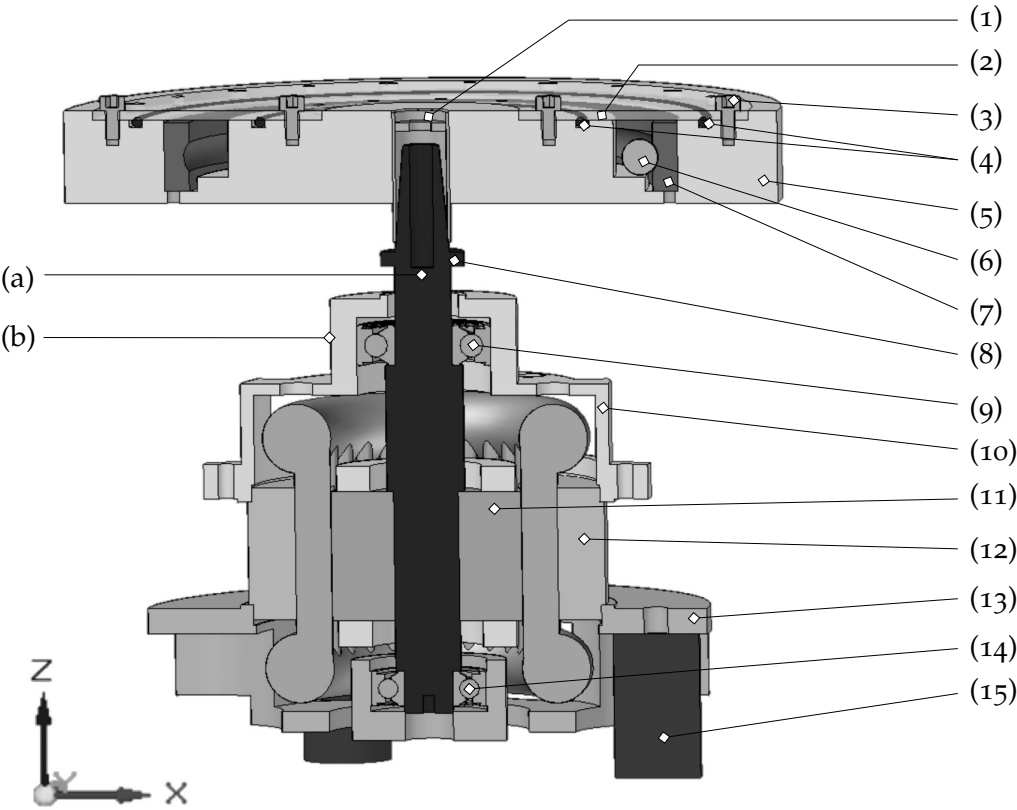


Figure 6.3.: Cross section of the test rig assembly for the discoidal rotor. (1) Clamping sleeve (2) transparent lid (3) screws fixating the lid (4) sealing rings (5) rotor body (6) ball from a 6926 ball bearing (7) outer ring from a 6926 ball bearing (8) rotor shaft (9) 6204Z ball bearing (10) motor cover (11) rotor ferrite (12) stator with copper coil (13) base (14) 6203Z ball bearing (15) rubber bushing. (a) LTS measuring point (b) acceleration sensor position.

6.1. Discoidal rotor

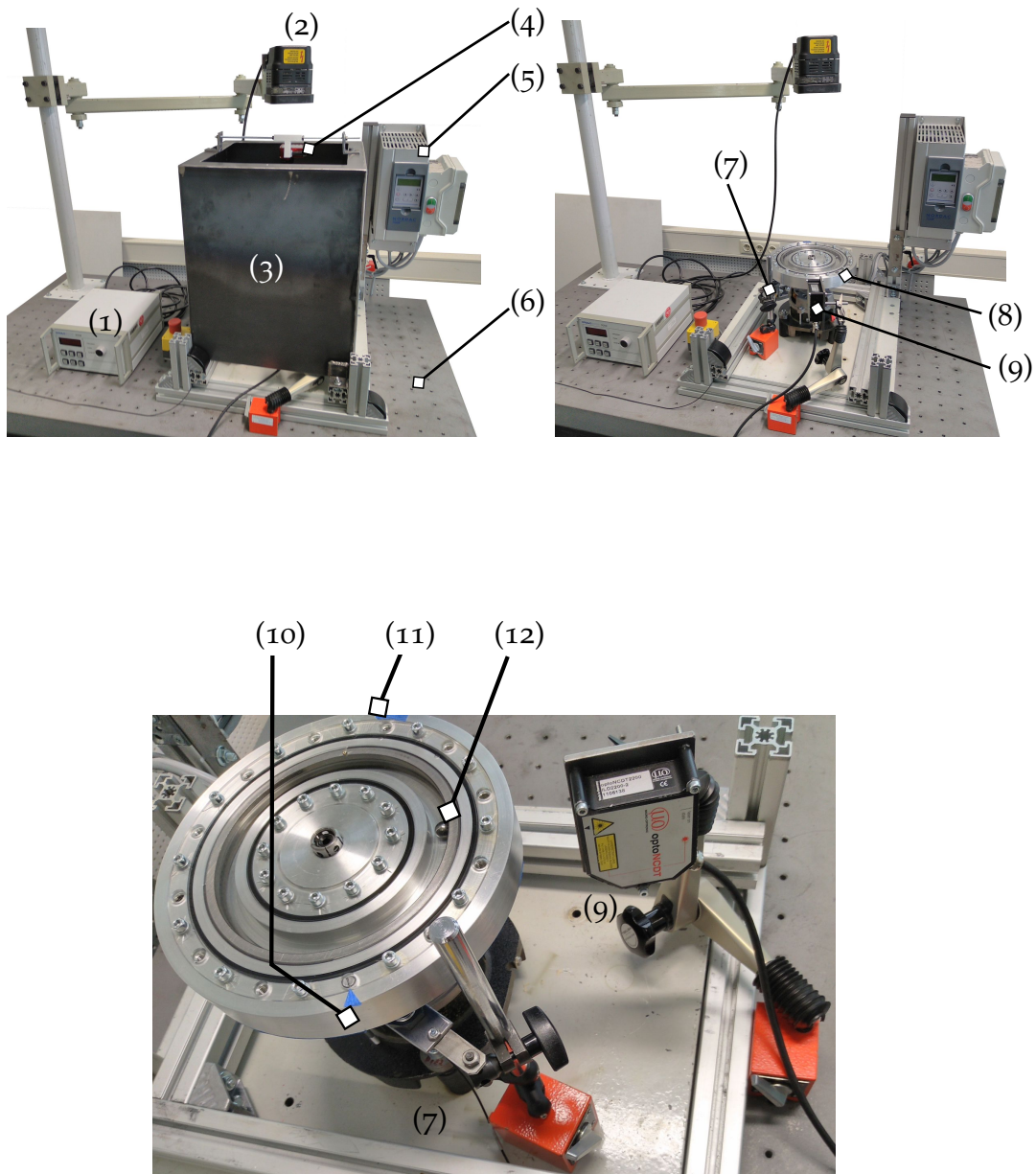


Figure 6.4.: Centrifuge test rig for the discoidal rotor with automatic balancing unit. (1) Strobe light controller (2) strobe light (3) containment (4) camera (5) motor control unit (6) vibration-isolated table (7) incremental encoder (8) rotor (9) laser triangulation sensor (10) rotor unbalance position (11) rotor optical zero marking (12) ball.

6. Model validation with centrifuge test rigs

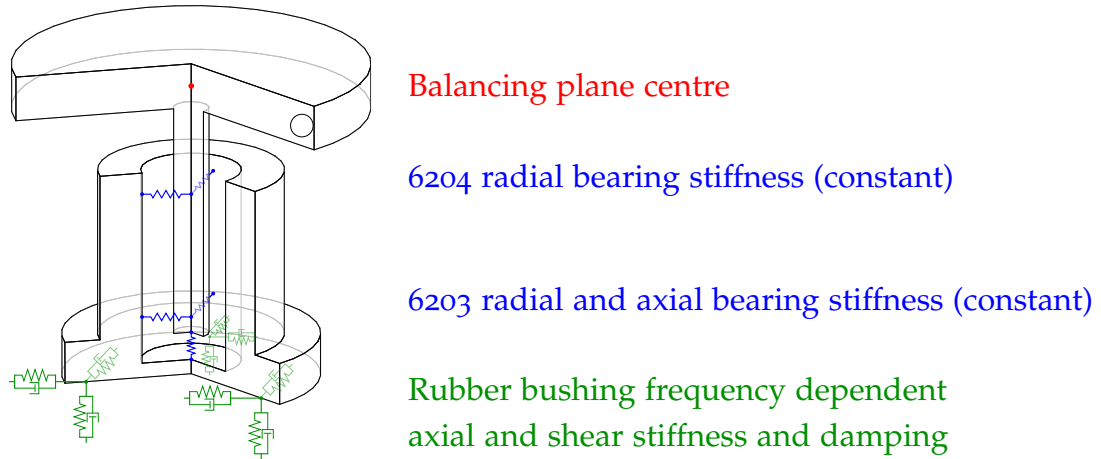


Figure 6.5.: 120 degree cut-out sketch of the reduced multi body model of the test rig with discoidal rotor.

according to an approximate equation from [Dre12]

$$k \approx (5 \dots 10) \times 10^3 \frac{d_{\text{bore}}}{\text{mm}} \frac{\text{N}}{\text{mm}},$$

with the inner bore diameter d_{bore} . The stiffnesses are configured as $250 \times 10^6 \text{ N m}^{-1}$ for the bearing of type 6204 and $150 \times 10^6 \text{ N m}^{-1}$ for the bearing of type 6203. The axial stiffness is estimated to be $1000 \times 10^6 \text{ N m}^{-1}$. This approximation is sufficient, since deviations in the bearing stiffnesses do not significantly influence the dynamics of the system in the considered speed range up to 1200 rpm.

The main compliance of the system is given by the three rubber bushings of diameter 30 mm and of length 50 mm, whose stiffness and damping influences depend on the operating condition. The amplitude- and frequency-dependent behaviour of the bushings is determined by measurements, described in the following subsection, in order to define corresponding spring-damper force elements in the MBS system. The selected force elements offer the look-up of tabled data, so that the frequency dependence can be realised in connection with the rotor speed. The rotor speed corresponds to the relevant part of the frequency spectrum of the bushing load.

6.1. Discoidal rotor

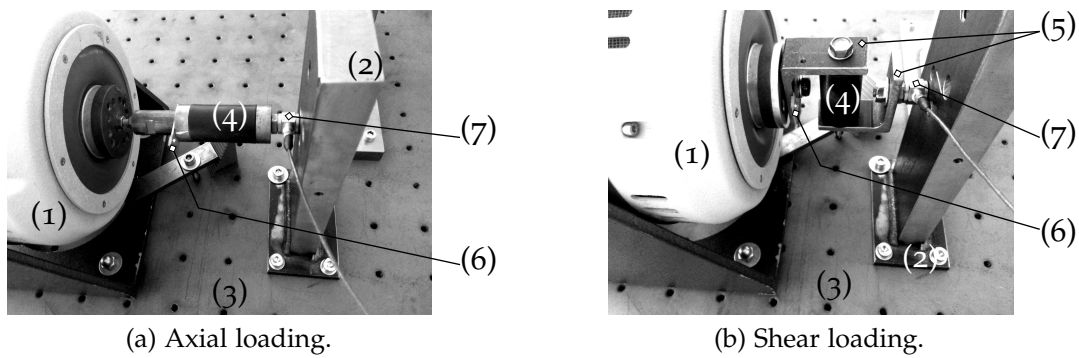


Figure 6.6.: Testing set-ups to determine the frequency dependent stiffness and damping of the centrifuge rubber bushings. (1) Shaker (2) bearing (3) vibration-isolated table (4) rubber bushing (5) steel adapter parts (6) LDV reflector (7) force sensor.

6.1.1.1. Rubber bushing properties

When measuring the frequency and amplitude dependent stiffnesses of the rubber buffers, they are mounted with a capacitive force sensor in series between a shaker and a steel bearing, as shown in fig. 6.6. The sensor³ is positioned on the bearing side so that the mechanics of the sensor are not exposed to its own inertial loads, which would falsify the measurement result and would require subsequent correction. For shear loading, two rigid steel angles are used and aligned in such a way that potential bending load on the bushing is minimised. Finally, a reflector is attached, which is used to measure the displacement of the shaker by means of a Laser-Doppler-Vibrometer (LDV).

Harmonic loads are applied to the bushing via the voltage signal transmitted to the shaker controller. By measuring the achieved displacement amplitude \hat{x} , the control voltage amplitude required for the nominal displacement is determined iteratively for each frequency considered. In order to reduce the influences of transients in the measurement results, each measurement procedure consists of a linear increase up to the target amplitude of the

³For shear loading a sensor of type 208Co1 with a rating of 45 N and a frequency range from 0.01 Hz to 36 kHz is used. For axial loading a sensor of type 208Co2 with a rating of 450 N and a frequency range from 0.001 Hz to 36 kHz is used. Both sensors are produced by PCB Piezotronics, Inc.

6. Model validation with centrifuge test rigs

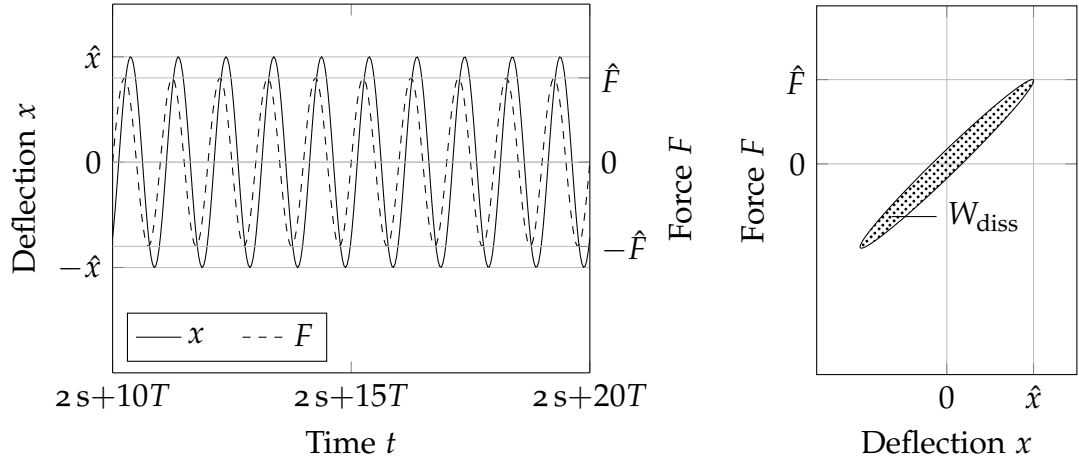


Figure 6.7.: Force and deflection measurement of the rubber bushing analysis.

displacement within 2 s followed by a holding period of 20 periods T of the respective frequency under consideration. Of these, only the last ten periods are used for the evaluation, so that a harmonic response

$$x(t) = \hat{x} \sin(2\pi ft + \Psi) \quad (6.2)$$

is obtained for the deflection signal, with Ψ being the phase angle with respect to the force signal, see fig. 6.7.

The stiffness

$$k = \frac{\hat{F}}{\hat{x}} \quad (6.3)$$

is calculated from the mean values of the 20 extrema for the force and the displacement. The hysteresis losses

$$W_{\text{diss}} = \frac{1}{10} \oint_{(10T)} F dx \quad (6.4)$$

result from the average circular integral, which is calculated for the measurement data of the ten periods using the trapezoidal rule. From the consideration

6.1. Discoidal rotor

of the single degree of freedom oscillator, the damping constant results in

$$b = \frac{W_{\text{diss}}}{2\pi^2 f \hat{x}^2}. \quad (6.5)$$

The results obtained for the three identical rubber bushings at displacement amplitudes of 0.25 mm, 0.5 mm and 1.0 mm and a frequency range of 2 to 35 Hz are shown in fig. 6.8. It can be seen that the damping constants show a frequency dependence known for carbon black rubber, but the dependence on the amplitude is negligible in comparison. The stiffnesses, on the other hand, show small increases with frequency but a distinct dynamic strain amplitude dependency, the so-called Payne-effect [Pay62].

The influence of constant pre-deformation was not determined, although other publications also attribute influence to it. For example in [WL13], an increase in stiffness of 25% at pre-strains of 10% were identified for carbon black rubber. It is noted that influence is dependent on the carbon percentage of the rubber bushings. The compound of the bushings utilized in the test-rig is unknown, unfortunately. Additionally, in the application of laboratory centrifuges, the pre-deformation due to the gravitational load of the centrifuge mass is smaller. From equilibrium estimates with the identified stiffness values the pre-strain is in the order of 1%.

In addition to the measured data, the table values stored in the MBS simulation model are also shown as solid curves in fig. 6.8. Adjustments due to comparison of the simulation results with the measured data on the vibration behaviour and the natural frequencies of the rotor system without balancing masses were made. This comparison is outlined in the following sections 6.1.2 and 6.1.3.

6.1.2. Eigenfrequency validation

For the experimental determination of the critical speeds of the rotor and thus an initial assessment of usable operating ranges for automatic balancing, the vibration responses to an impulse excitation at standstill and the run-up with initial unbalance, i.e., without added unbalance masses, were analyzed.

6. Model validation with centrifuge test rigs

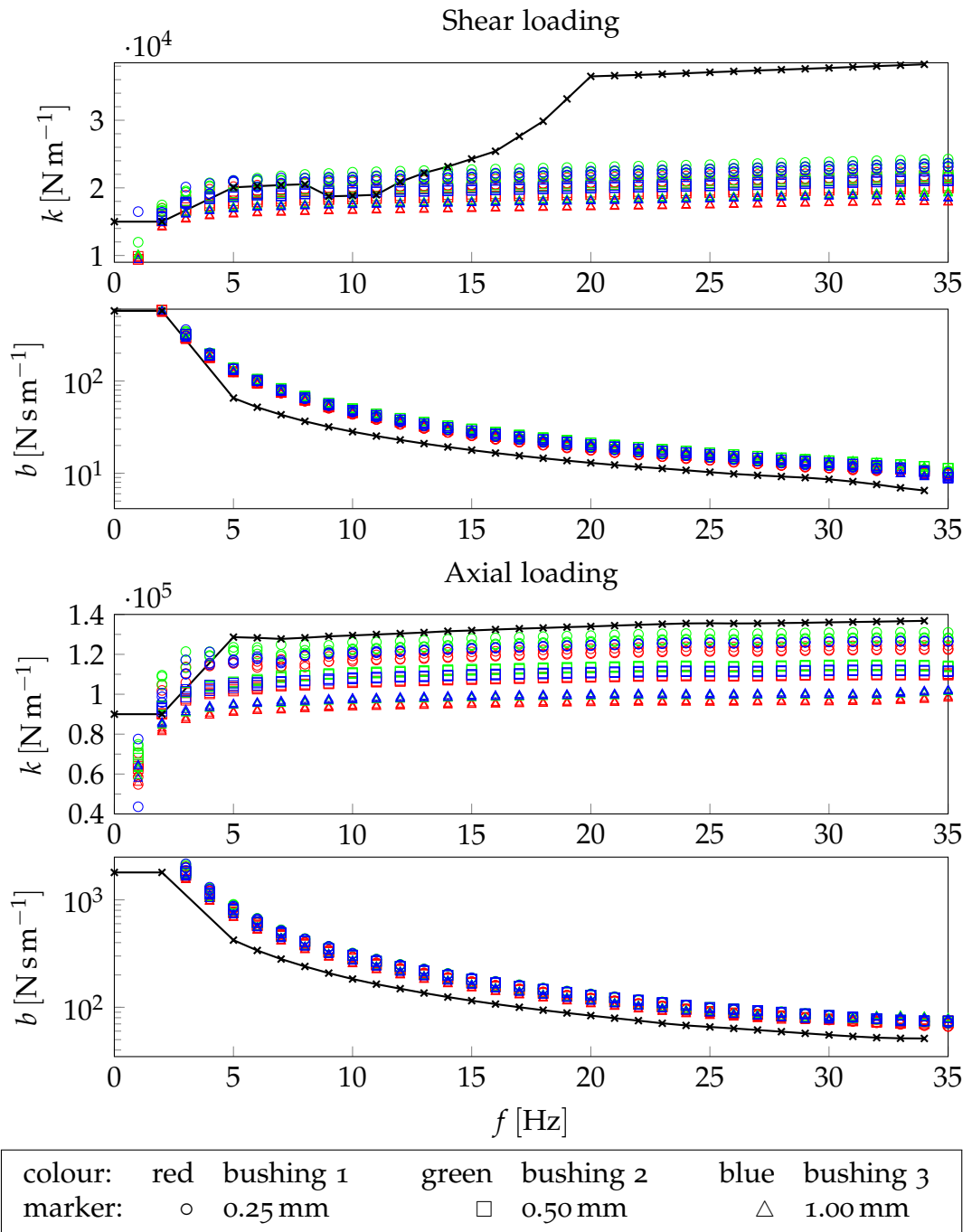


Figure 6.8.: Measurement of the rubber bushing stiffness and damping for different loading frequencies and amplitudes.

6.1. Discoidal rotor

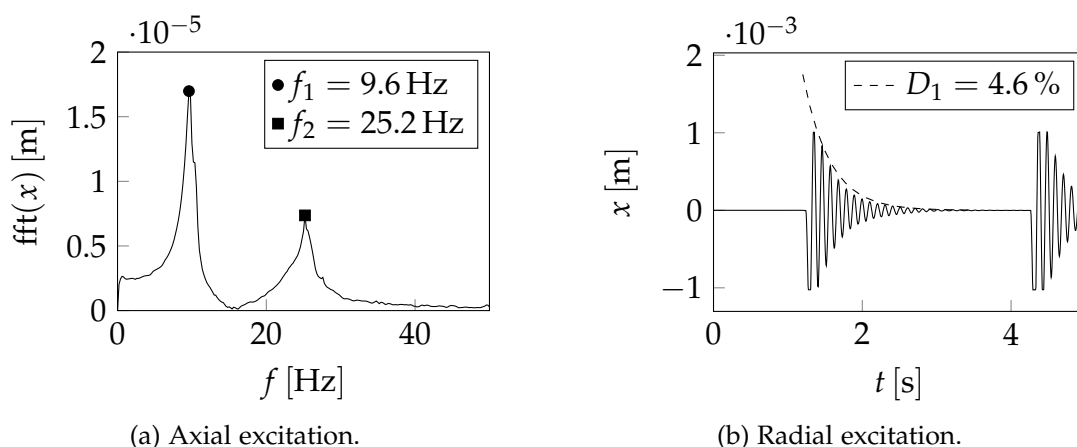


Figure 6.9.: Experimental determination of eigenfrequencies of the discoidal rotor at rest. a) FFT of the non rotating discoidal rotor oscillations excited by impulse. b) Decay of the first mode oscillation in the time domain.

During the impulse excitation, the rotor disc was excited with an impulse hammer in the axial direction at the top surface and in another measurement in the radial direction at the circumferential surface. The impulse in axial direction excited two eigenmodes of the rigid rotor system, as can be seen from the Fourier analysis of the recorded rotor deflection, fig. 6.9a. The first eigenmode responds with a frequency of 9.6 Hz and the second eigenmode with 25.2 Hz. Radial excitation, fig. 6.9b, showed that primarily the first eigenmode is excited. The recorded time signal mainly shows a response frequency of 9.6 Hz. By regression analysis of an exponential function on the decaying oscillation, the exponential decay rate can be calculated as 2.8 s^{-1} resulting in a damping factor of $D_1 = 4.6\%$.

For the transient tests, a nominal speed of 1200 rpm was specified in the frequency converter, which has to be carried out in a ramp-up time of 135 s. The resulting speed curve is shown in the figures for the vibration responses, as in the response to the run-up with initial rotor unbalance, fig. 6.10.

At the beginning of the run-up process, the rotor is accelerated significantly. In this phase, the frequency inverter checks the rotational inertia and then regulates the motor torque in such a way that the nominal speed is reached at

6. Model validation with centrifuge test rigs

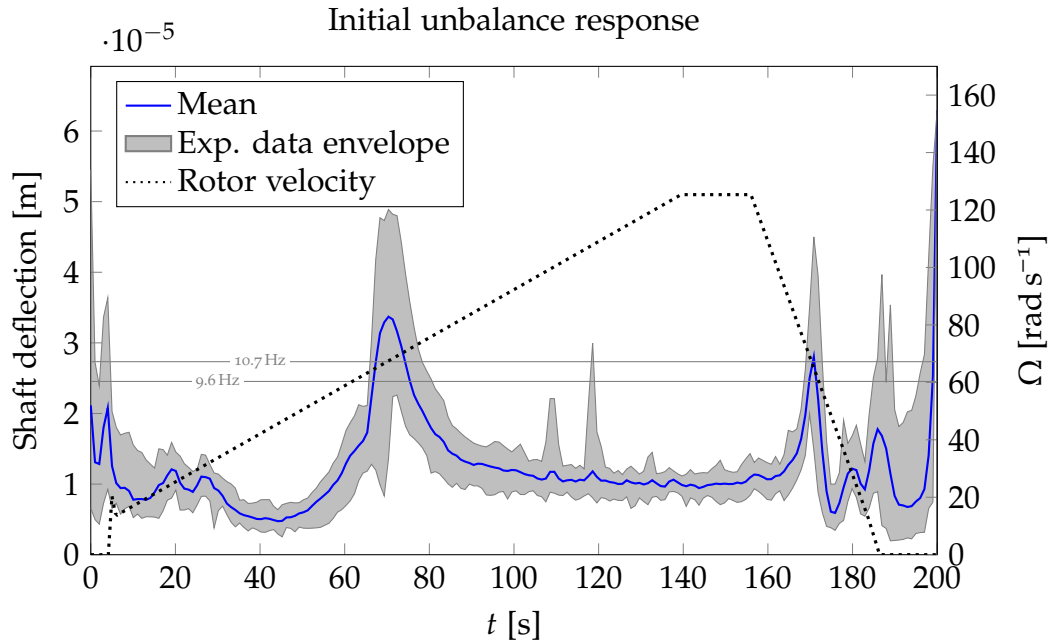


Figure 6.10.: Runup of the discoidal rotor in its initial configuration. Between each of the twelve run-ups the discoidal rotor was remounted with a different yaw angle.

the set time. This results in a linear increase of the speed with an acceleration of 0.837 rad s^{-2} in the main part of the run-up process.

The increased shaft deflection at $t = 70 \text{ s}$ indicates that the critical speed has been passed. At this point, the rotor has a rotational frequency of 10.7 Hz . Even though the rotor acceleration is small compared to the regular operation of this centrifuge assembly, the increase in deflection may have a time offset due to transient effects. However, the critical speed of synchronous unbalance excitation is thus below 10.7 Hz . It can be concluded that the gyroscopy of the rotor does not strongly influence this eigenmode in this operation range.

If the system of equations of motion of the multi-body simulation, after solving a linear run-up to 1200 rpm in the time domain, is linearised for several time points of this solution and subjected to an eigenvalue analysis, the Campbell diagram shown in fig. 6.11 can be generated.

In the frequency domain up to 30 Hz four modes can be identified. The first two modes correspond to the eigenfrequencies identified experimentally

6.1. Discoidal rotor

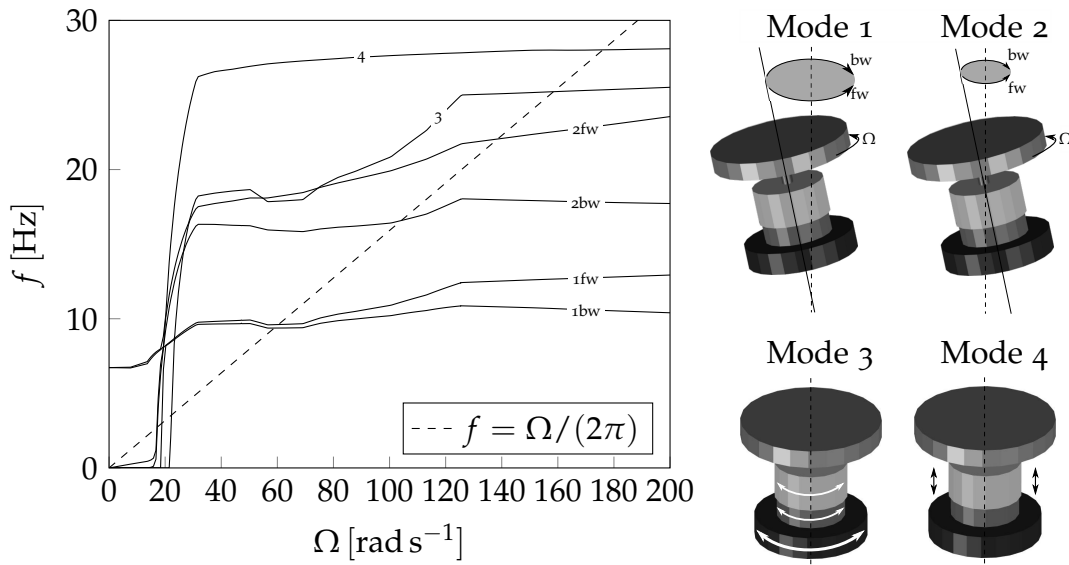


Figure 6.11.: Eigenfrequencies of the rotor system, calculated subsequently to a MBS solution of a run-up. The shapes of the four eigenmodes are depicted on the right side. Forward whirling and backward whirling motion is denoted with 'fw' and 'bw', respectively.

above. These modes have a conical shape in which the rubber bushings experience both shear and compression loading. However, shear deformation predominates in the first mode and axial loading in the second mode. This can be explained by the different axial position of the vibration node. The third mode is a pure rotation of the stator with pure shear load of the bushings and the fourth mode shows a pure axial load with translation of the entire assembly in axial direction. The last two modes are unimportant for the presented investigations and the automatic balancing of the rotor.

Since the load on the rubber bushings increases during resonance passage, there is a decrease in stiffness due to the Payne effect. The reduction in shear stiffness is particularly relevant for the location of the resonance frequency. Since the look-up tables for the bushing stiffness only act one-dimensionally with respect to the rotor speed, but not with respect to the current strain, an adjustment in the look-up table for shear stiffness is necessary. In the frequency range around the resonance frequency at 10 Hz the measured values for shear loads of 1 mm are used. In the speed range below that, the data row for an amplitude of 0.25 mm is used. In the case of the axial bushing stiffness,

6. Model validation with centrifuge test rigs

it was found that the deformations realised in the simulations were around 0.1 mm, but no measurement was made for its amplitude. Therefore, for each frequency in the experimental data of the amplitudes 0.25 mm, 0.5 mm and 1.0 mm, a stiffness for 0.1 mm amplitude was cubically extrapolated.

After an agreement of the critical speed was achieved, the bushing damping b of both load types was reduced by 30% in order to also achieve an agreement in the damping factor. Again, this would only have been necessary near resonance, but scaling the entire data row proved to be more practical. In the speed range outside the resonance, a change of the damping is not influential [Gen05]. The cause of the overestimation of the damping of the bushings derived from the measurement results could not be conclusively clarified. Through an experimental investigation of further eigenmodes, it may be possible to determine whether this deviation is specific to the first eigenmode or whether a systematic deviation is recognisable. A significant difference in running time between the signals of the force sensor and the LDV, which would directly affect the phase difference and thus W_{diss} , cf. eq. (6.4), was not found.

6.1.3. Unbalance response validation without ABB

To obtain a defined unbalance response of the rotor system before using the ABB, a threaded piece of mass $m_0 = 5.5$ g was screwed into the holes provided for this purpose. The radial position of these twelve holes distributed around the circumference is at $\varepsilon = 108$ mm, resulting in a primary unbalance of 594 g mm. One run-up for each of the twelve possible primary unbalance locations was conducted to assure the independence of the vibration response from the selected position. The resulting envelope of all measurement recordings is shown in section 6.1.3. It can be seen that there are only minor differences in the vibration amplitudes and the initial unbalance is negligible compared to the additional primary unbalance. The frequency converter was controlled manually and two inputs were necessary. One to start the run-up process and one to start the run-down process, which was scheduled at the time 145 s after the first input. The time variances between the indi-

6.1. Discoidal rotor

vidual run-ups caused by the manual operation could be compensated by the synchronisation based on the peak of the rotor speed in the start phase, positioned in the figures at $t = 5$ s. However, the time variance between the first and the second input cannot be compensated, so that the envelope is wider at the second resonance pass at run-down.

From the signal of the incremental encoder for determining the rotor speed and the displacement signal of the LTS, the angle of lag of the rotor deflection with respect to the unbalance excitation can be determined. The time progression is shown in the bottom diagram in fig. 6.12. For areas with low rotor deflection at the beginning and end of the recording, the measurement uncertainty is too large, but in the range between $t = 57$ s and 170 s the phase shift by 180° can be identified, which is a necessary condition for automatic balancing.

Since the angle of lag in supercritical operation remains at 180° even up to the nominal speed of 1200 rpm, it is shown that the influence of the next eigenmode is still too small to interfere with automatic balancing. For the planar oscillator in orthotropic bearings, cf. section 4.2.1 on page 49, an equation for the speed limits of balancing is given. In more complex systems, however, it is often only identifiable by simulation at which speed the subcritical orbit radius of the second eigenmode exceeds the orbit radius of the first eigenmode in the plane of the ABB.

In the progression of the vibration response between $t = 20$ s and 140 s, an asymmetry with respect to the resonance passage can be seen, which is, however, more pronounced than the one to be expected from self-centring. Since the MBS simulation initially delivered significantly smaller amplitudes in the time range $t = 80$ s to 140 s, the cause is assumed to be an underestimation of the rubber buffer stiffness, especially the shear stiffness. In order to achieve agreement between measurement results and MBS simulation, the deposited shear stiffness was increased for frequencies above 15 Hz, as shown in fig. 6.8.

The increase in shear stiffness thus also increases the critical speed for the respective operating frequency. Thus, the respective distance between rotor frequency and current critical speed increases more slowly than in the original

6. Model validation with centrifuge test rigs

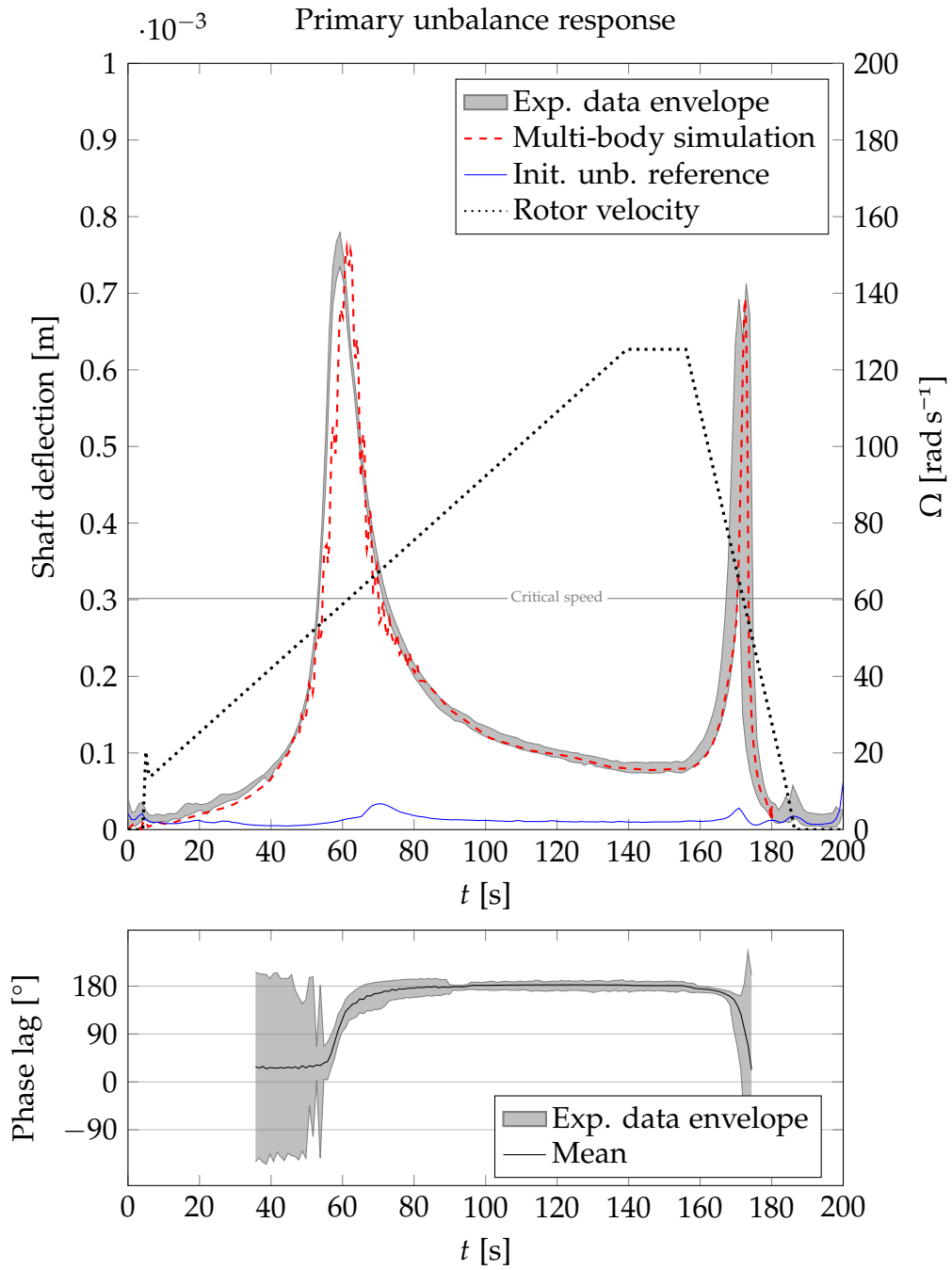


Figure 6.12.: Run-up of the discoidal rotor with an added (primary) unbalance but without balancing masses or fluid. One run-up for each of the twelve possible primary unbalance locations was conducted.

modelling. The vibration response, considered as a function of the rotor frequency, therefore decreases to a lesser extent.

6.1.4. Determination of the velocity dependent drag coefficient

As shown in section 5.2.2, the dependence of the drag coefficient on the flow profile, respectively the Reynolds number, is influenced by the geometrical boundary conditions. Due to the proportional influence in the damping force, which is one of the essential forces on the balls in the orbital direction, the modelling has a significant effect on the dynamics of the automatically balanced rotor. In order to concretise the relationship for the present rotor with an ABB and to derive a functional relationship that can be implemented in the MBS simulation, the flow was investigated empirically and by means of CFD analysis.

In the empirical study [SDW17], the rotor, whose essential annulus properties can be taken from table 6.2 and fig. 6.13, was mounted on a horizontal shaft with fluid and one ball. At a constant angular velocity Ω , equilibrium is thus established between gravity, friction and flow resistance, see fig. 6.14, and the equilibrium angle ζ with respect to the perpendicular can be determined optically in the steady state through the transparent lid.

Table 6.2.: Properties of the ball balancer in the discoidal rotor.

Description	Symbol	Dimension
Ball diameter	d_b	12.3 mm
Radius of the centroidal track	ε	76.95 mm
Height of the annulus cross-section	H	20 mm
Width of the annulus cross-section	W	13.8 mm

Experimental studies with a similar set-up have already been carried out by Muscă's research group [Mus03; Mus09; Sir+16; Sir+18b; Sir+18a]. However, the focus here was on the investigation of friction in rolling bearings and the flow resistance of the surrounding air was neglected.

6. Model validation with centrifuge test rigs

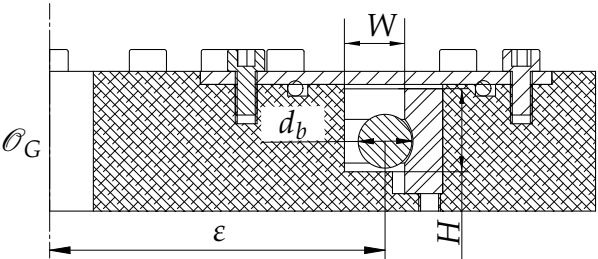


Figure 6.13.: Half-section of the discoidal rotor containing the outer ring of a ball-bearing.

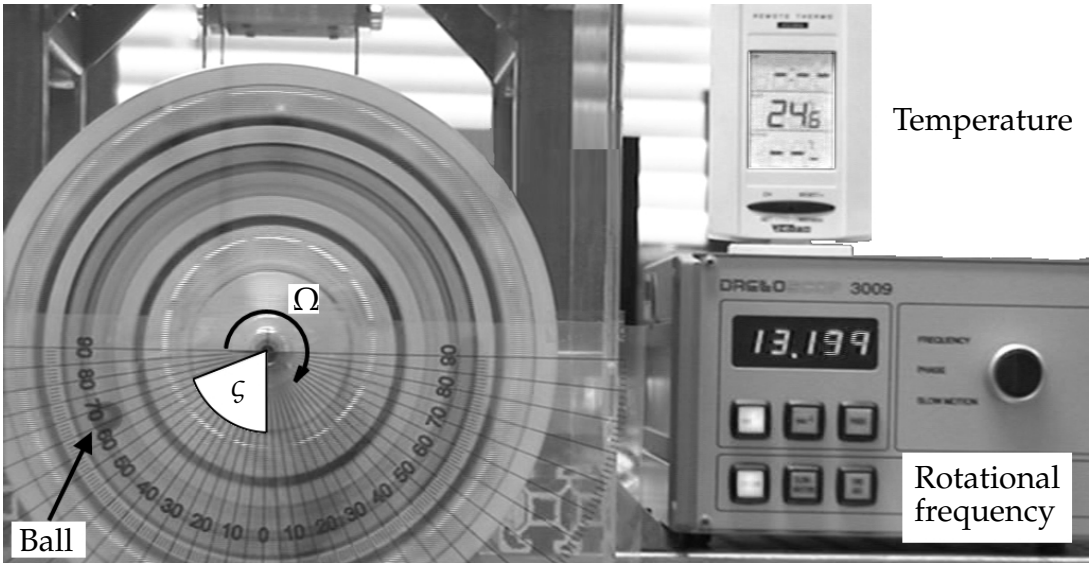


Figure 6.14.: Test rig setup for the verification of the drag coefficient relation for the discoidal rotor.

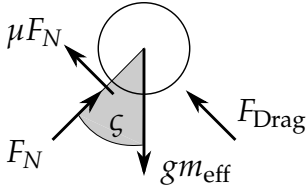


Figure 6.15.: Forces on the ball in equilibrium to access the drag coefficient.

6.1. Discoidal rotor

In the balance of forces acting on the sphere, see fig. 6.15 similar to the consideration in section 5.1.2, the buoyancy is taken into account by introducing the effective mass

$$m_{\text{eff}} = \frac{\pi}{6} d_b^3 (\rho_b - \rho_{\text{fl}}).$$

Evaluation of the balance of forces leads with eq. (5.17) to

$$c_d = \frac{2 m_{\text{eff}} g (\sin(\zeta) - \mu \cos(\zeta))}{\rho_{\text{fl}} \bar{A} \Omega^2 \varepsilon^2}, \quad (6.6)$$

where the equilibrium angle can only be evaluated up to 90° .

Using several fluids of different density and viscosity, the measurement range can be evaluated for a wide range of Reynolds numbers. The oils listed in table 6.3 were used for the experiment. Silicone oils of a specific viscosity can also be generated by mixing, as was done for the variants with $2 \text{ mm}^2 \text{ s}^{-1}$, $5 \text{ mm}^2 \text{ s}^{-1}$ and $10 \text{ mm}^2 \text{ s}^{-1}$. The necessary blending fractions w were derived from the Arrhenius equation for the viscosity of ideal binary mixtures [Zhm14]

$$\ln(\nu_{12}\rho_{12}) = w_1 \ln(\nu_1\rho_1) + (1 - w_1) \ln(\nu_2\rho_2). \quad (6.7)$$

With $\rho_{12} \approx (\rho_1 + \rho_2)/2$, the necessary blending fraction in order to obtain the desired kinematic viscosities yields

$$w_1 = \frac{\ln(\nu_{12} \frac{\rho_1 + \rho_2}{2}) - \ln(\nu_2\rho_2)}{\ln(\nu_1\rho_1) - \ln(\nu_2\rho_2)}. \quad (6.8)$$

If the data series determined in this way are compiled, fig. 6.16 follows, in which the already known progressions for the free flow [Mor13] and the flow around a sphere with one-sided planar contact [JC97] are given for reference. It can be seen that the flow resistance has increased in comparison. This is due to the more restricted flow cross-section in the ABB chamber.

Since the friction influence depends on the equilibrium angle, the coefficient of friction μ can be estimated from the collected series of measurements. The

6. Model validation with centrifuge test rigs

Table 6.3.: Properties of fluids used in the equilibrium experiments.

Fluid	ρ_{fl} [kg m ⁻³]	ν [mm ² s ⁻¹]	
Ravenol [®] 80W	886	214	nominal
ADDINOL [®] SD-Oil B 5W	836	31	nominal
Silicone oil 0.65 cSt	760	0.65	nominal
Silicone oil 50 cSt	950	50	nominal
Silicone oil 2 cSt	800	2	as of eq. (6.7)
Silicone oil 5 cSt	844	5	as of eq. (6.7)
Silicone oil 10 cSt	876	10	as of eq. (6.7)
Silicone oil 23 cSt	939	23	measured
Silicone oil 200 cSt [†]	953	298	measured
Silicone oil 400 cSt [†]	947	715	measured

[†] Silicone oils from a different supplier showing considerable deviations from nominal values.

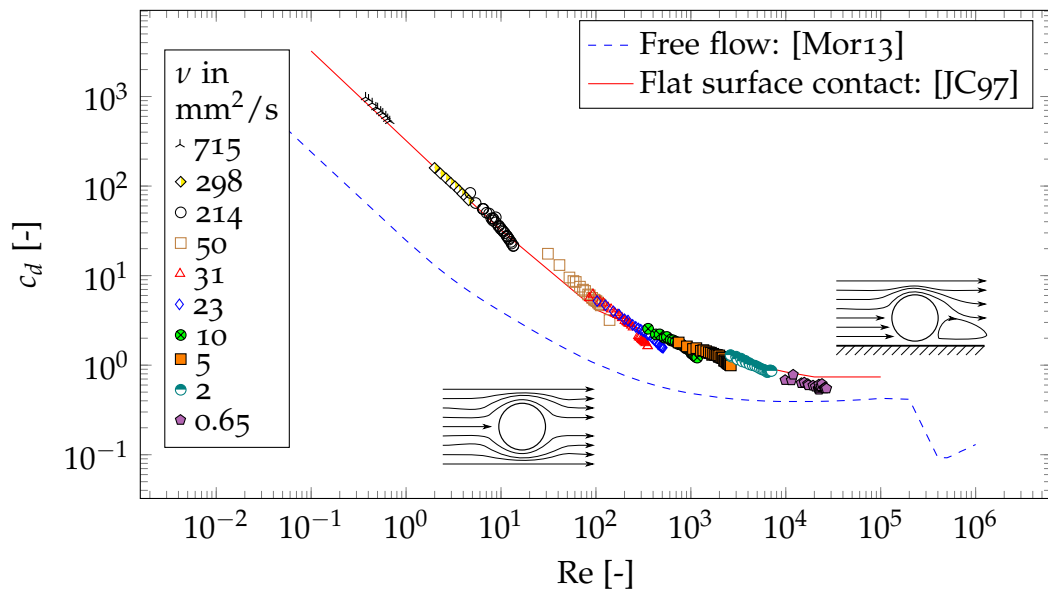


Figure 6.16.: Experimental validation of the drag coefficient for flow around a ball with different kinematic viscosities ν in an automatic ball balancer with a bearing raceway. The fitted rolling friction coefficient is $\mu = 0.05$.

6.1. Discoidal rotor

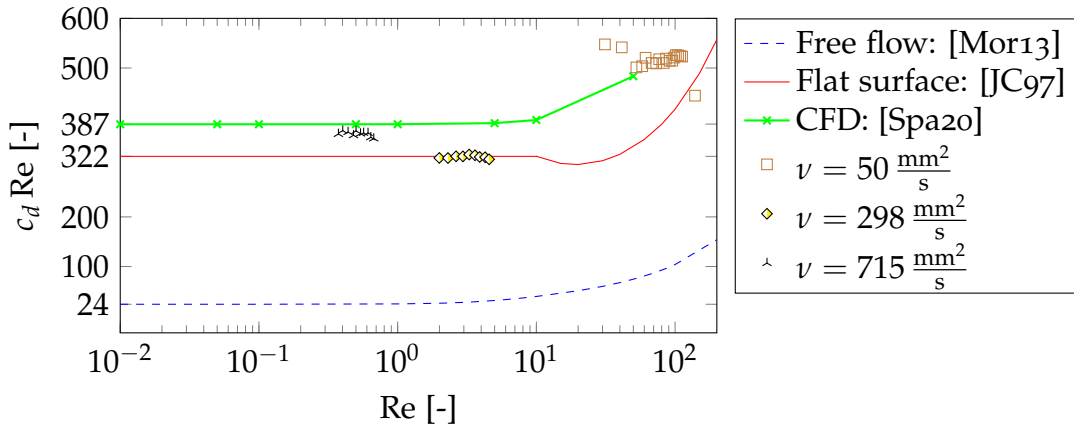


Figure 6.17.: Comparison of the product of drag coefficient and Reynolds number at low Reynolds numbers.

estimation follows from the requirement that overlapping measurement series in the diagram fig. 6.16 must be coincident for any given Reynolds number. The right points of a data series are marginally influenced by friction due to the large equilibrium angle, whereas the left points of the following data series are subject to large friction influence. For the lubricated frictional contact of a spherical rolling element with the outer rolling bearing ring, this results in a coefficient of $\mu = 0.05$.

A numerical determination of the progression of the drag coefficient by means of CFD analysis is also possible. Thus, with restriction to the Stokes regime for small Reynolds numbers, the comparatively simple steady state solution can be found with established solvers, as shown in [SW20b] for the annulus considered. For simulations with larger Reynolds numbers, a corresponding modelling of the turbulence is required, which was not pursued further in the present work. A comparison of the CFD results with the obtained measurement data in the range $Re = [0.1, 100]$ shows a good agreement. This is shown in fig. 6.17, where the ordinate represents the product $c_d Re$. This allows for better comparability in contrast to the otherwise usual logarithmic representation of c_d . Moreover, $c_d Re$ represents a constant in the Stokes regime, which is also of great importance especially for the established models of ABBs, as shown in section 5.2.5.

Using the results from the experiments and the CFD analysis, an empirical

6. Model validation with centrifuge test rigs

relation between c_d and Re similar to the equation presented in (5.21) can be expressed. Defining $c_d = 38.7$ and $c_d Re = 387$ for $Re = 10$ and a plateau of $c_d = 0.6$ for $Re > 2 \times 10^4$ the four coefficients in the exponential term can be determined, resulting in

$$c_d(Re) = \begin{cases} 387 Re^{-1} & \forall Re \leq 10 \\ 10^Y & \forall 10 < Re \leq 20000 \\ 0.6 & \forall Re > 20000, \end{cases} \quad (6.9)$$

with $Y = 2.72 - 1.25 \log(Re) + 0.121(\log(Re))^2 + 0.038(\log(Re))^3$.

6.1.4.1. Comparison of simulation results

In order to validate the implementation in the MBS force element, the experimental set-up is replicated in a model. However, the compliance of the structure is neglected and the rotor has only a rotational degree of freedom around the axis perpendicular to the gravitational acceleration. Different fluid properties from the measurement series are defined and the rotor is accelerated linearly to the respective maximum rotational speed at which the equilibrium angle yields 90° over a period of 300 seconds.

The resulting equilibrium angles, which occur when implementing eq. (6.9) in the simulation, are compared with the measured data in fig. 6.18. Only in the range of large equilibrium angles significant deviations can be seen. These are explained by the lift forces neglected in the model. At large equilibrium angles, these exceed the radially acting component of the gravitational force, so that the balls move radially inwards. The loss of contact with the raceway results in a flow cross-section with lower resistance. This contact loss was also observed in the experiments at equilibrium angles close to 90° . For the application of the model in ABB simulations, the neglect of lift forces does not pose a problem because, in contrast to this experiment, the balls are accelerated on a circular path and thus a permanent contact at the raceway is presumed.

6.1. Discoidal rotor

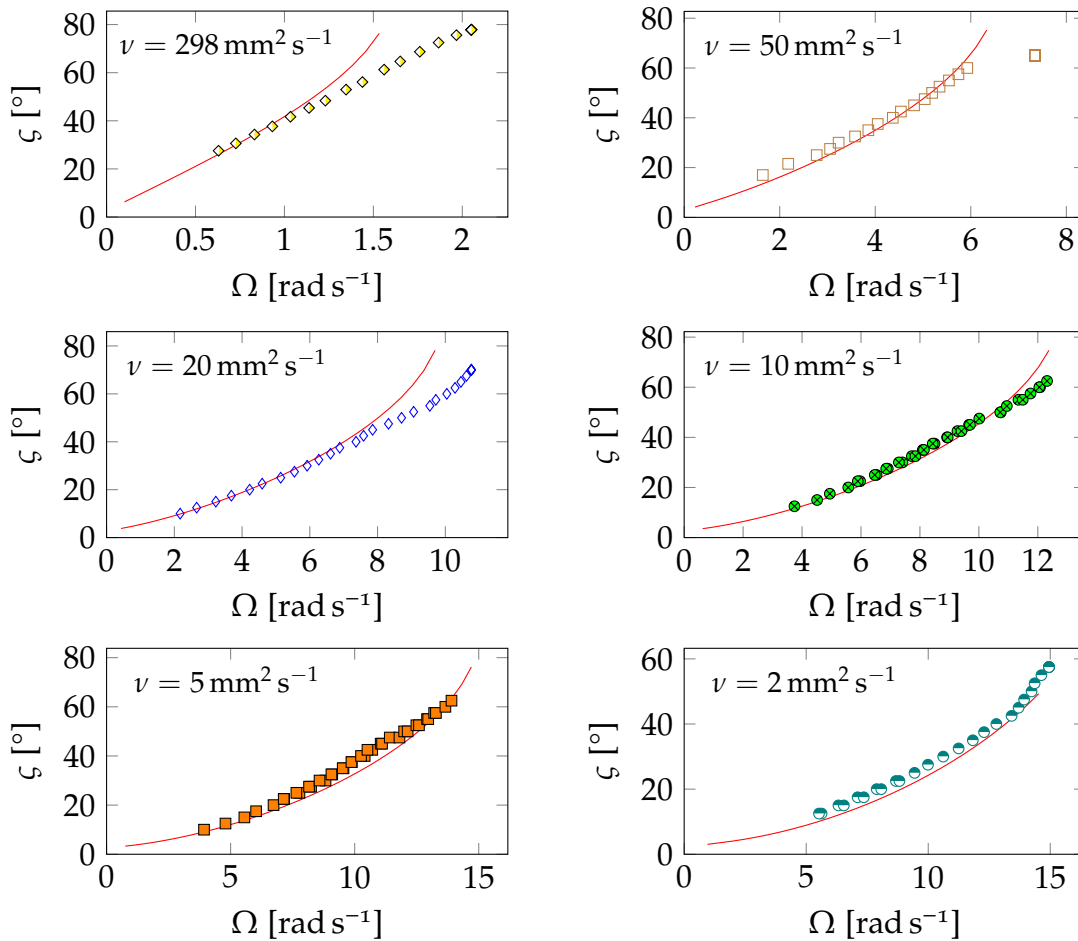


Figure 6.18.: Comparison of simulative results (solid lines) to the experiments (marker) used to determine the Reynolds number dependent drag coefficient. The rolling friction coefficient is set to $\mu = 0.05$.

6. Model validation with centrifuge test rigs



Figure 6.19.: Single frame of the 240 fps test bench recording at a momentary rotor speed of 1200 rpm. (1) Encoder stand (2) unbalance mass (3) laser triangulation sensor (4) ball (5) visual zero marking.

6.1.5. Capturing of balancing ball movement

In order to obtain a transient progression of the ball positions relative to the rotor, the rotors are covered with transparent lids. A video camera with a maximum frame rate of 240 fps was used to film the rotors. To achieve an exposure that would result in sharp snapshots in each video frame, a strobe was used, as seen in fig. 6.4 on page 85. The stroboscope's trigger was synchronised with the camera so that single-frame shots, as shown in fig. 6.19, are well suited for image evaluation even at maximum speed of 1200 rpm.

For the evaluation of the video material, the Computer Vision Toolbox™ in MATLAB® was used and the methods of foreground detection were applied [SG99; KB02].

6.1.6. Influence of raceway imprecision on the ball resting position

As shown in section 4.2.4, deviations of the raceway from a circular centric shape lead to mis-positioning of the balancing masses. In order to evaluate the influence of the existing deviations in the discoidal rotor on the ball positioning, the inner edge of the bearing ring was measured with respect to the

6.1. Discoidal rotor

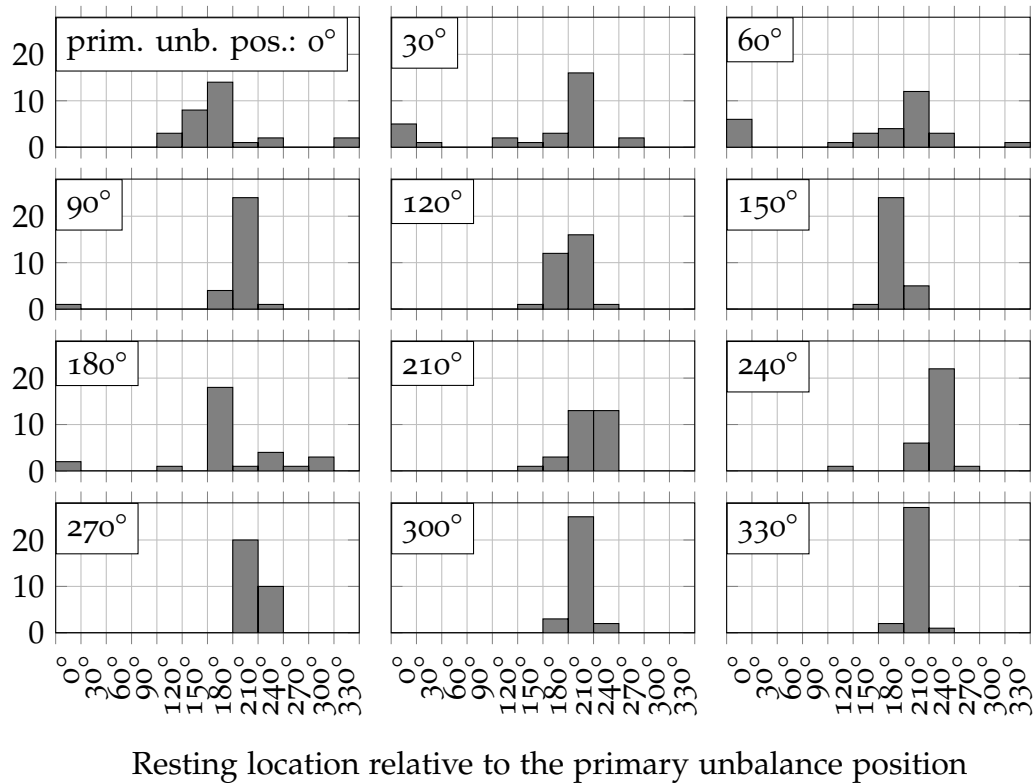


Figure 6.20.: Balancing ball resting position distributions for varied primary unbalance positions and 30 run-ups each. The labels indicate the center of the respective 30° wide bin.

centric bore of the rotor using a coordinate measuring machine. Subsequently, the rotor was equipped with a primary imbalance of 594 g mm, a silicone oil of viscosity $\nu = 20 \text{ mm}^2$ and one balancing ball. The balancing potential of the ball is $m_{\text{eff}} \varepsilon = 4.75 \text{ g} \times 77 \text{ mm} = 365.75 \text{ g mm}$ and could therefore compensate 62% of the primary unbalance.

The stable balancing position is opposing the primary unbalance and by varying the latter, the influence of the geometry deviation was measured. For each of the twelve possible primary unbalance positions, 30 run-ups were performed and the sector of the stationary ball position was determined. The histograms of the measurement results are compiled in fig. 6.20, where the abscissa describes the position corrected for the position of the primary unbalance, i.e., the ideal position for all diagrams is at 180°.

If the stable positions of all run-ups are evaluated together in a polar his-

6. Model validation with centrifuge test rigs

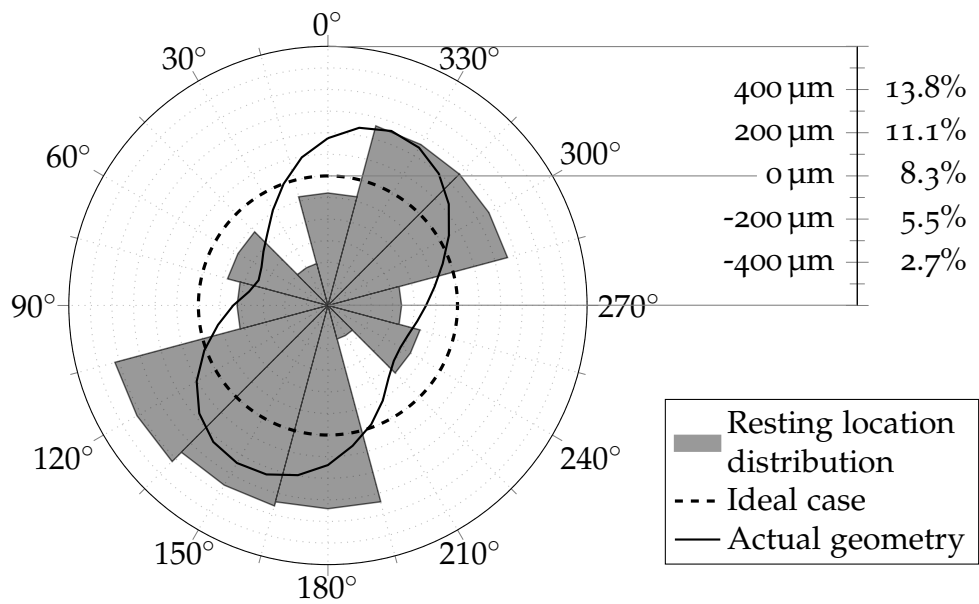


Figure 6.21.: Roundness deviations of the raceway after being pressed into the discoidal rotor and resulting resting position distribution.

togram, a bias with respect to two diametrically opposed positions can be detected, see fig. 6.21. The dashed line represents the ideal case of $1/12$ (8.3%), i.e., the balls are positioned opposing the primary unbalance for each of the twelve possible primary unbalance locations. Mispositioning caused by friction is evenly distributed and therefore does not influence the presented evaluation.

The solid line indicates the determined deformation of the raceway, which in simplified terms is an oval with expansions in the directions at 150° and 340° . Again, the ideal case of a circular raceway is indicated by the same dashed line, due to appropriate scaling. Thus, a correlation between the raceway deformation and the bias of the stationary ball positioning can be observed.

This must be taken into account when evaluating individual run-ups and the stationary ball position, and deviations in the stationary position cannot be attributed exclusively to friction. In the following investigations, the primary unbalance was left at the 0° position in order to keep this additional influence invariant.

6.1.7. Examination of the operating boundaries of stable balancing

Since the rubber bushings provide significant external damping to the rotor, the Sommerfeld effect of unstable balancing is not strongly pronounced for the ABB under consideration. When using two balls, sub-synchronous oscillations and orbiting of the balls could only be experimentally verified with the lowest viscosity silicone oil available and with air, as was presented in [SW21]. When using air, however, no transition to stable balancing could be detected in the operating range considered up to 1200 rpm.

Using the silicone oil with $\nu = 0.65 \text{ mm}^2 \text{ s}^{-1}$, the rotor was first accelerated to a rotational frequency of 48 rad s^{-1} and operated for 60 s to let transient influences decay. Subsequently, the rotor speed was incremented by 1 Hz and after a dwell time of 60 s the signal of the acceleration sensor, which is mounted to the lid of the stator as shown in fig. 6.4 on page 85, was recorded for 10 s. A subsequent FFT analysis provides the RMS acceleration amplitude in the frequency domain of the vibration response. The same process of speed increment followed by dwell and measurement time was repeated until a rotor speed of 700 rpm was reached. The resulting spectrogram is presented in fig. 6.22 and shows that in the rotor speed range from 57.5 rad s^{-1} to 64 rad s^{-1} sub-synchronous oscillations of the angular frequency 53 rad s^{-1} occur. For rotor speeds above 64 rad s^{-1} the sub-synchronous vibrations vanish and also the synchronous vibration amplitude gets reduced, showing that stable automatic balancing is in effect.

To determine the border frequency Ω_{bo} by means of the developed criterion eq. (4.74) on page 52 the rotor system is to be approximated with a planar oscillator. Based on the three-dimensional MBS model, the parameters for the planar oscillator model can be derived for small displacements. Starting from the results of a static force excitation of the ABB center, the stiffness k_x and k_y can be obtained. Concluding from the first critical speed and damping factor of the complex system a representative mass M of the rotor and suitable damping coefficients b_x, b_y can be derived. The obtained parameters are

6. Model validation with centrifuge test rigs

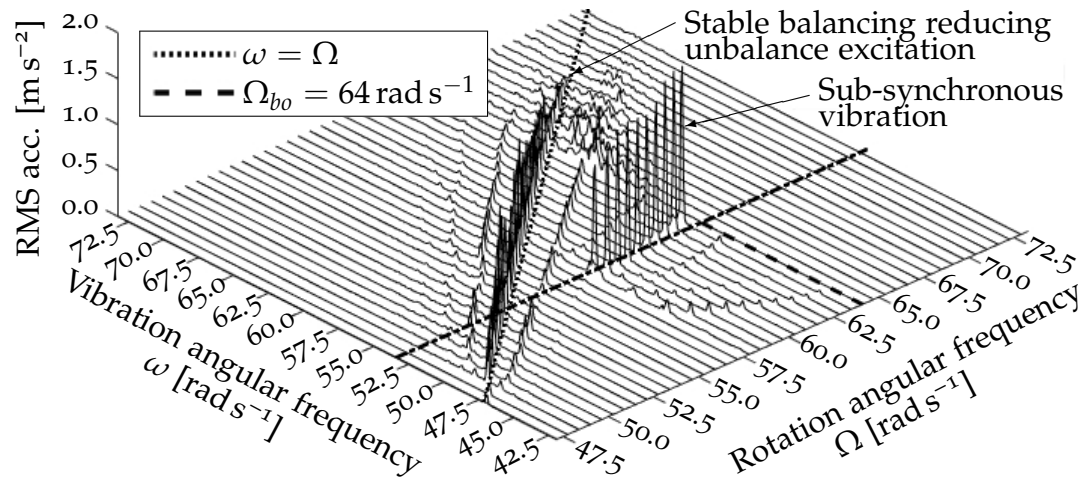


Figure 6.22.: FFT of the centrifuge stator acceleration for different rotation speeds of the ABB filled with silicone oil ($\nu = 0.65 \text{ mm}^2 \text{ s}^{-1}$) and two balancing balls. The intended reduction of unbalance excitation only occurs for rotor speeds $\Omega > \Omega_{b0} = 64 \text{ rad s}^{-1}$.

summarized in table 6.4. Utilizing eq. (4.74) in combination with eq. (5.26) from page 79, the solid line in the stability map, fig. 6.24, is obtained.

It can be seen that the measurement result from fig. 6.22 does not lie on the solid line, but shows stable balancing at a lower frequency. In fact, the limit consideration of eq. (4.75) shows that no stable balancing is possible with this fluid. This can be explained by the neglected friction, whose dissipative character stabilises the balancing. By dividing the right-hand side of eq. (4.74) by a factor of 50, e.g. by artificially increasing the external damping b_x and b_y by this same factor, the stability limit can be adjusted so that it corresponds better to the measurement results. This curve is shown dashed in the stability map.

The stability of the ABB can also be tested for individual fluids in a transient MBS simulation. The rotor acceleration near the critical speed is kept at 0.1 rad s^{-2} in this investigation to correspond to quasi-stationary operation and also coincides approximately with the incremental increase of 1 Hz min^{-1} described above. The limits of unstable operation can then be determined by evaluating one of the translational displacements in the balancing plane of one of the two balls. If this displacement is converted into a spectrogram

6.1. Discoidal rotor

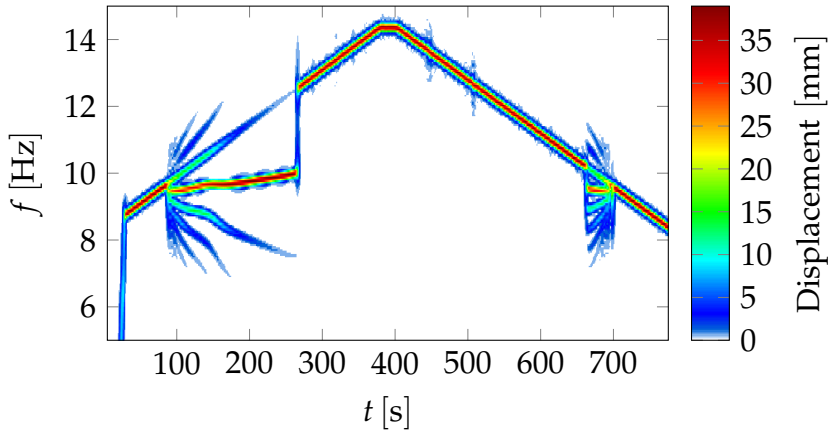


Figure 6.23.: Spectrogram of the inertial x position of one of the two balls inside the ABB during slow run-up and run-down simulation of the rotor system.

by an FFT, see fig. 6.23, the areas in which the ball does not rotate with the constantly accelerated rotor can be easily identified.

Table 6.4.: Planar oscillator model parameters for the centrifuge test rig with discoidal rotor.

Parameter	M	k_x	k_y	b_x	b_y	ε	m_b	r_b
Value	12.27	44.64		68.7		76.95	6.656	6.15
Unit	kg	kNm^{-1}		Ns m^{-1}		mm	g	mm

In contrast to the experimental investigation, the MBS simulation includes the run-up and the run-down. This results in two passes through the stability border in the time domain, which are drawn in the stability map in pairs. During the transition from the stable area to the unstable area, i.e. during the run-down, the balls are at rest relative to the rotor before passing the stability limit. On the other hand, during the transition from the unstable area to the stable area, i.e. during run-up, the balls have a relative speed to the raceway before passing the stability limit.

As can be seen from the spectrogram, the transition between the two operating states is quasi instantaneous. The ball accelerates abruptly to rotor speed at time $t = 264$ s. Just as suddenly, the subsynchronous state is resumed at $t = 662$ s. The difference in the stability limits is therefore not due to an

6. Model validation with centrifuge test rigs

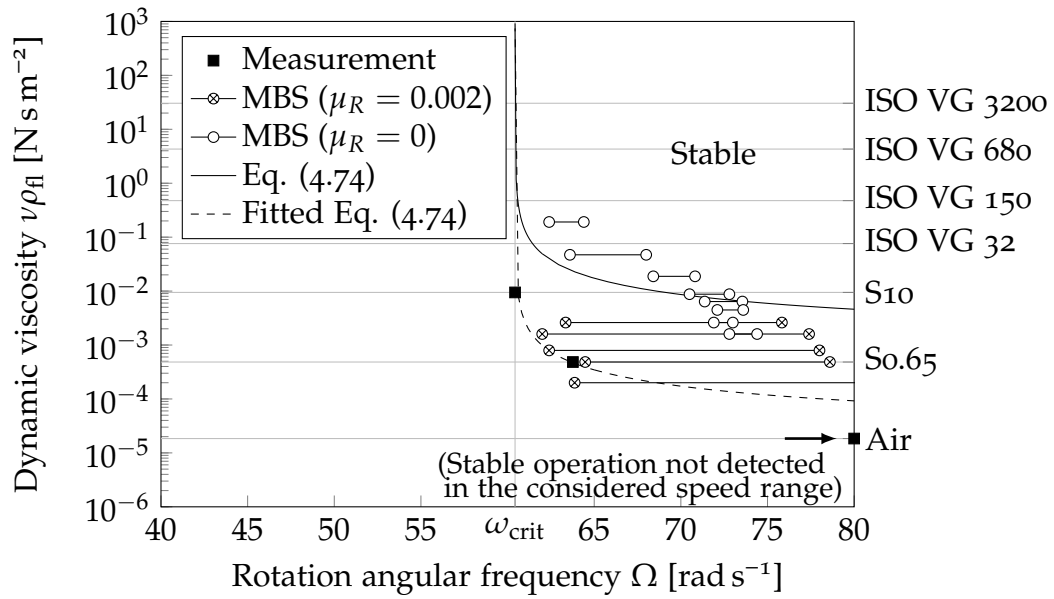


Figure 6.24.: Stability map of the centrifuge testrig. ISO VG viscosities at root temperature. So.65 and S10 indicate silicone oils with kinematic viscosities of $0.65 \text{ mm}^2 \text{ s}^{-1}$ and $10 \text{ mm}^2 \text{ s}^{-1}$ at room temperature, respectively.

inadmissibly high rotor acceleration for a quasi-static consideration. The maximum angular velocity difference, just before stability is achieved during run-up, is 2.6 Hz, which corresponds to a Reynolds number of 2.4×10^4 . This is in the range where the drag coefficient is almost constant at 0.6. The drag force is thus higher according to the modelling used, eq. (6.9), than according to the modelling with constant viscous parameter corresponding to eq. (5.26). One aspect that the current model cannot represent due to the way the rubber bushings are modelled is the difference in rotor deflection and the associated rubber bushing loads shortly before the stability borders are crossed. During run-up, the rubber bushings are more highly loaded before stability is reached than during run-down, where the rotor unbalance is compensated and the buffer load is minimal. This behaviour cannot be reproduced by purely frequency-dependent modelling of the rubber bushings.

It turns out that the simulated stability limits from the run-down are closer to the measured value. The reason for the discrepancy during run-up could not be conclusively narrowed down.

6.1.8. Unbalance response with ABB

In order to investigate the influence of fluid viscosity on the dynamic behaviour of the discoidal rotor with ABB, three different silicone oils of kinematic viscosities $5 \text{ mm}^2 \text{ s}^{-1}$, $20 \text{ mm}^2 \text{ s}^{-1}$ and $50 \text{ mm}^2 \text{ s}^{-1}$ were used. Similar to the investigation of the raceway inaccuracy, the rotor was equipped with a primary unbalance of 594 g mm and a balancing ball of mass $m_b = 5.4 \text{ g}$. The balancing potential of the ball now depends on the density of the fluid used, see table 6.3.

In the figures 6.25, 6.26 and 6.27 the rotor deflection is shown in the top axis and the ball position relative to the primary unbalance location is shown in the bottom axis. With each fluid ten run-ups were conducted with the envelopes of all runs combined shown with the gray shading. As can be seen for all three measurements, the mean deflection, shown in green, is reduced compared to the deflection of the rotor when no balancing ball is present, shown in red. In comparison to the configuration with the fluid of $20 \text{ mm}^2 \text{ s}^{-1}$ kinematic viscosity, the other two configurations show a larger variance in the ball positioning and ultimately in the resulting rotor deflection.

The simulation results, however, show poor agreement with the experimental data in the shaft deflection as well as in the transient ball position. In the starting phase, when the ball is touching the bottom of the annulus and no contact is made with the raceway, an additional force in the orbital direction was added to model friction with the annulus wall. But as the subsequent progress of the ball position shows, a distinct deviation starts to occur at the point where the ball changes its orbital movement direction relative to the raceway. This indicates a fault in the implemented adherence condition which is also evident from the fact that for the configurations with $5 \text{ mm}^2 \text{ s}^{-1}$ and $20 \text{ mm}^2 \text{ s}^{-1}$ the ball position is constant in the time window between $t = 10 \text{ s}$ and $t = 50 \text{ s}$.

6. Model validation with centrifuge test rigs

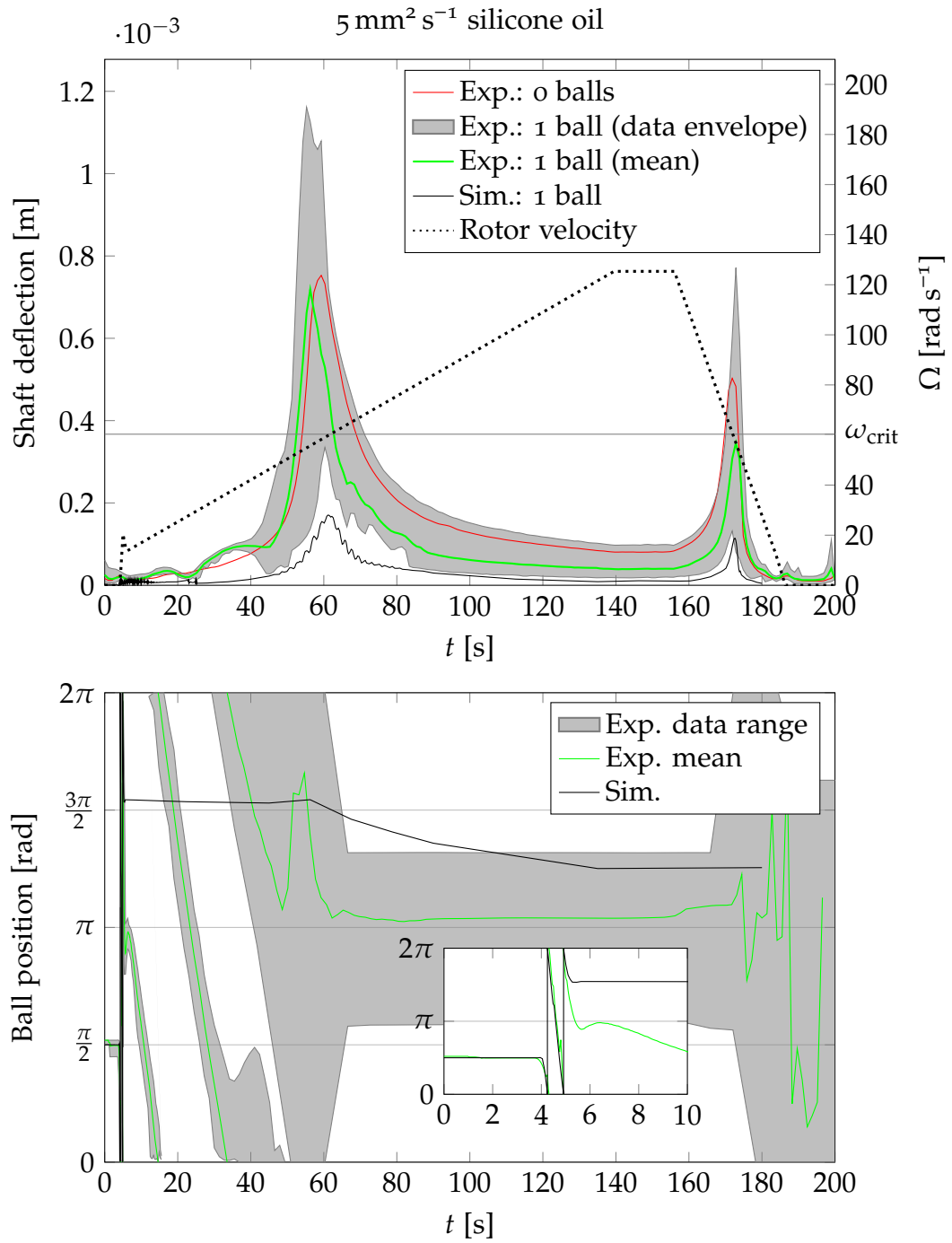


Figure 6.25.: Run-up of the discoidal rotor with primary unbalance, one balancing ball and silicone oil of viscosity $\nu = 5 \text{ mm}^2 \text{ s}^{-1}$.

6.1. Discoidal rotor

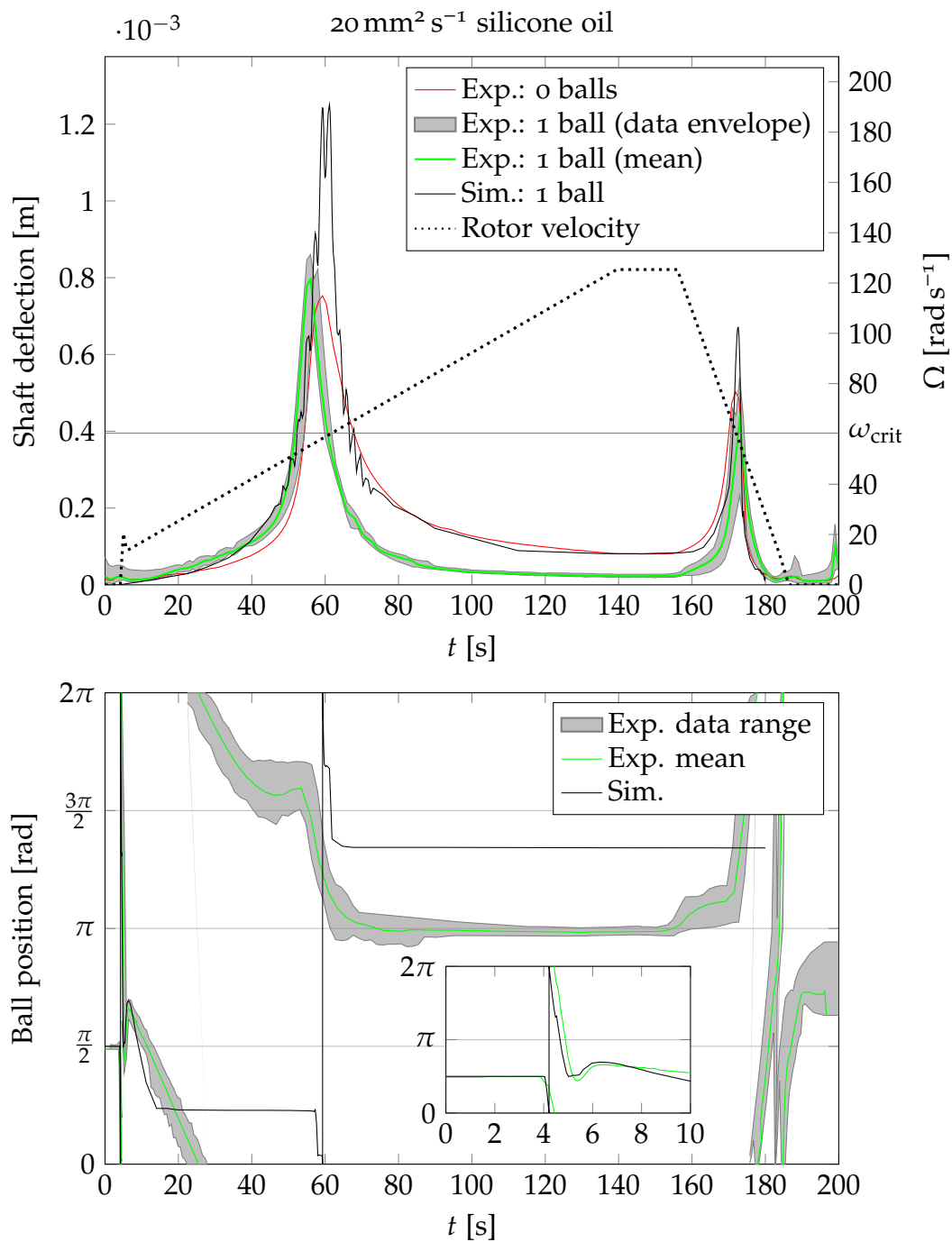


Figure 6.26.: Run-up of the discoidal rotor with primary unbalance, one balancing ball and silicone oil of viscosity $\nu = 20 \text{ mm}^2 \text{ s}^{-1}$.

6. Model validation with centrifuge test rigs

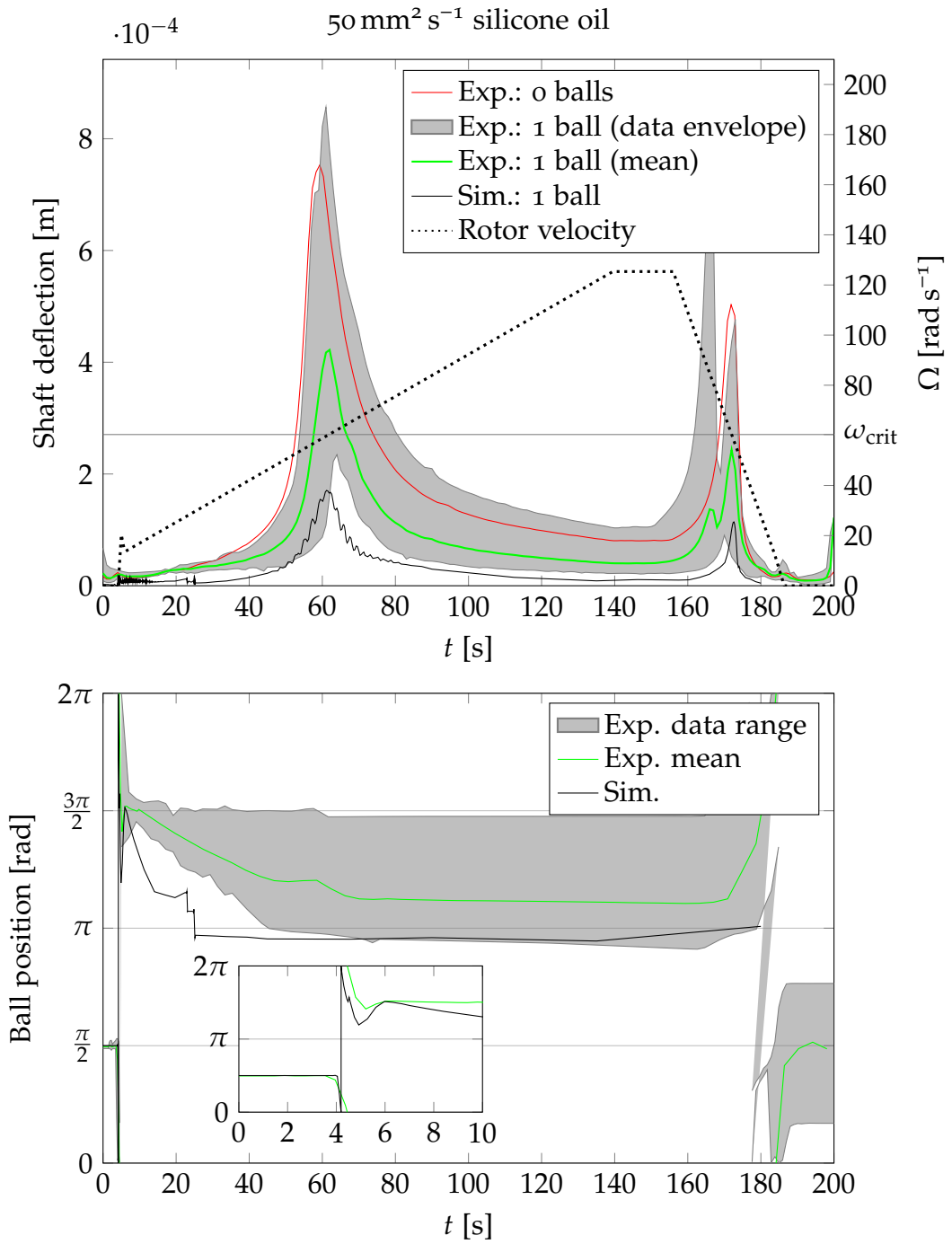


Figure 6.27.: Run-up of the discoidal rotor with primary unbalance, one balancing ball and silicone oil of viscosity $\nu = 50 \text{ mm}^2 \text{ s}^{-1}$.

6.1.9. Summary of the discoidal rotor test rig

The test rig with the discoidal rotor, mounted on a drive unit of a laboratory centrifuge, was initially investigated without ABB to validate a basic MBS model. Since the rotor is rigid, the main difficulty was to characterise the rubber feet on which the assembly is mounted. The measurement and subsequent modelling of the frequency-dependent stiffness and damping characteristics initially showed good agreement in the eigenvalue analyses.

However, since amplitude-dependent modelling was not available in the force elements used, adjustments were made to the data in the look-up table near the critical speeds. The adjustment of the transient rotor vibrations up to a speed of 1200 rpm showed that the non-linear behaviour of the rubber bushing after passing the critical speed was not sufficiently represented. By modelling additional frequency-dependent stiffening of the rubber bushing stiffness, an agreement of the vibration response could finally be achieved. However, this adjustment is linked to the selected rotor unbalance and a change in the primary unbalance or the rotor acceleration rate, both having impact on the resulting vibration response near the critical speed, may require a new adjustment. For future investigations, it is therefore recommended to investigate other modelling possibilities than a pure frequency-dependent mapping solution for the rubber bushings.

Experimental and simulative studies were carried out on the flow conditions in the discoidal rotor using CFD analysis and the MBS force element. For creeping flows, good agreement was achieved between the flow resistance determined by experiment and CFD analysis. A model of the presented experiment with the MBS force element, in which the empirical findings of the experiment are stored, could show that the implementation of the steady-state flow simulation in the MBS force element was successful.

Regarding stability, it could be shown that the MBS model is able to represent the unstable operation of the ABB and to take into account the frictional influence, which has a stabilising effect. However, since the rubber feet show strong damping, only few experimental data points could be obtained in the presented stability map. Also, the distance between the stability limit

6. Model validation with centrifuge test rigs

and the critical speed is only a few Hertz, which makes this area difficult to evaluate. In order to examine the quality of the mapping accuracy of the ABB force element for the determination of the stability limits more precisely, a weakly damped rotor test rig should be used, which has a more pronounced instability range.

When comparing the run-ups with a balance ball, the influence of the different fluids was shown both in the experiment and in the simulation. The number of rotations of the ball relative to the unbalance can be influenced by the choice of fluid for the run-up scenario presented. However, it also became apparent that several aspects at the beginning of the run-up process cannot yet be represented by the model. For example, the contact of the ball with the raceway is not yet given at the beginning, but frictional influences due to the bottom of the rotor are still present. Even after adjusting the frictional forces in this time frame up to the contact with the raceway, there was no good agreement in the further progression. This may be due to the neglected raceway deviations that the real rotor exhibits. However, the early settling of the ball with respect to the raceway additionally indicates an overestimation of the friction and adherence influences. In order to analyse these problems in more detail, instead of the outer ring of a radial bearing, the outer ring of a thrust bearing could be used to check the modelling in the MBS force element without the influence of the non-linear rubber bushing in an experimental comparison of a set-up similar to those in [Cro16].

6.2. CFRP centrifuge rotor

The second rotor considered is a CFRP rotor intended for use in laboratory centrifuges. A modular ABU was placed in the free space at the bottom to compensate for the imbalances caused by the different filling of sample containers in the 14 holders. A cross-sectional view of the design and a photo of the assembled rotor are shown in fig. 6.28 and geometric details are provided in appendix B.2. However, due to the assembly of the ABB on the underside, this prototype does not qualify for equivalent testing to the discoidal rotor on the test rig in section 6.1.

6.2. CFRP centrifuge rotor

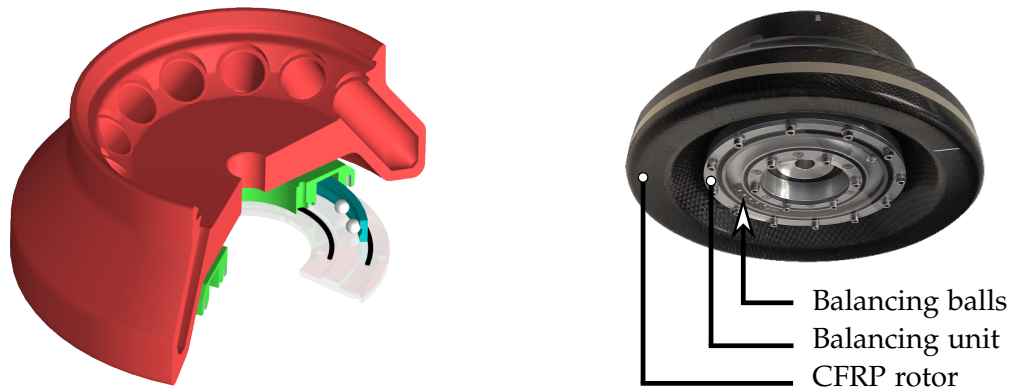


Figure 6.28.: CFRP rotor with attached ABB prototype.

The rotor was therefore examined in another test rig in which it is suspended from an elastic spring steel shaft, see fig. 6.29. In this orientation, the stroboscope and camera can be pointed at the ABB from below. The elastic shaft of diameter 6 mm is inserted into a drive shaft of diameter 20 mm on the side far from the rotor. This results in a length of 150 mm of the flexible section of the shaft. The drive shaft is supported by two roller bearings with respect to the aluminium profile frame of the test rig. The system is driven by a belt drive and the positioning and rotational speed is measured at the pulley by an incremental encoder.

To introduce external damping into the system for safe operation, two piston dampers are connected via threaded rods to a sleeve mounted over the elastic shaft. The sleeve is in turn supported by two roller bearings relative to the elastic shaft. Since the bushing offers a non-rotating but reflecting and sufficiently large surface, the displacement is measured on it via an LTS.

6.2.1. Mechanical model

The comparatively simple mounting via an elastic shaft of constant cross-section reduces the modelling extent. The elastic shaft of diameter 6 mm is modelled by finite elements of the Timoshenko beam theory. Since the elastic shaft below the lower bearing is inserted and clamped in a shaft of diameter 20 mm, which is considered rigid, a nearly rigid constraint is assumed at this point. The modelled bushing force element is modelled

6. Model validation with centrifuge test rigs

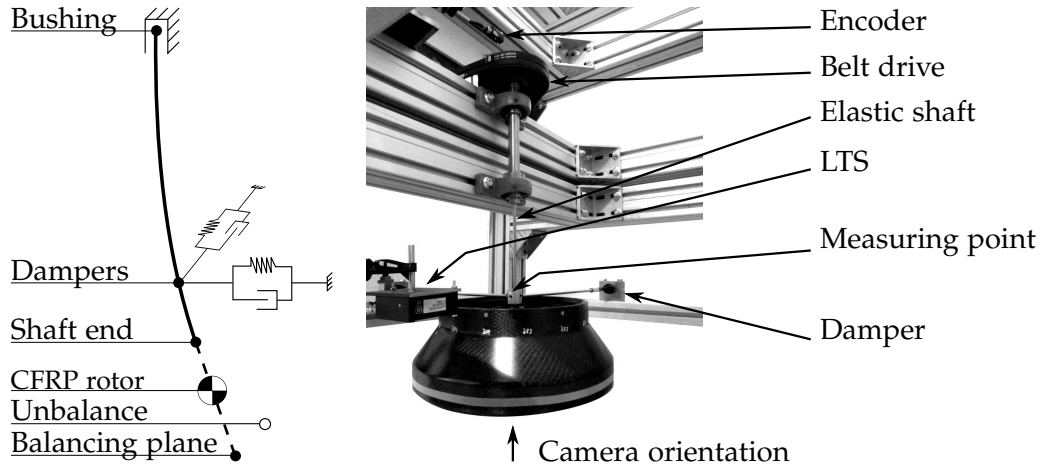


Figure 6.29.: Testrig for the CFRP rotor with mechanical model.

with translational spring stiffnesses of $250 \times 10^6 \text{ N m}^{-1}$ and rotational spring stiffnesses of $1 \times 10^4 \text{ N m rad}^{-1}$. The elastic shaft modelled hereafter has a total length of 180 mm, which extends to the top of the mounting clutch, see fig. B.7 in the appendix on page 152.

The segmentation of the finite element beam into several elements is only necessary due to the connection of the force elements for the piston dampers and the ABB. The reference marker of the ABB force element requires a shaft node in the balancing plane, but the shaft ends above the centre of gravity of the CFRP rotor. Therefore, a shaft section with increased modulus of elasticity and reduced density is defined, shown dashed in fig. 6.29, to realise the required rigid extension. The mass and the mass moments of inertia of the CFRP rotor are imposed as lumped mass with offset on the node of the shaft end.

6.2.2. Eigenfrequency validation

Due to the significant mass moments of inertia of the CFRP rotor and the overhung bearing on a flexible shaft, a pronounced gyroscopy and the associated speed dependence of the critical speeds are to be expected. For the calibration of the eigenbehaviour, the system was first excited at standstill by a remotely activated pulse hammer, see fig. 6.30. An impulse excitation at the widest

6.2. CFRP centrifuge rotor

point of the CFRP rotor in radial direction resulted in a vibration response containing primarily the first natural frequency of 3.4 Hz, see fig. 6.31a. An excitation at the lower rolling bearing resulted in a vibration response dominated by the second natural frequency of 21.2 Hz, see fig. 6.31b. The connection of the piston dampers had only a small influence on the natural frequencies, but from the comparison of the decay behaviour with and without dampers, the damping coefficient of the piston dampers could be approximated with $b = 57 \text{ N s m}^{-1}$.

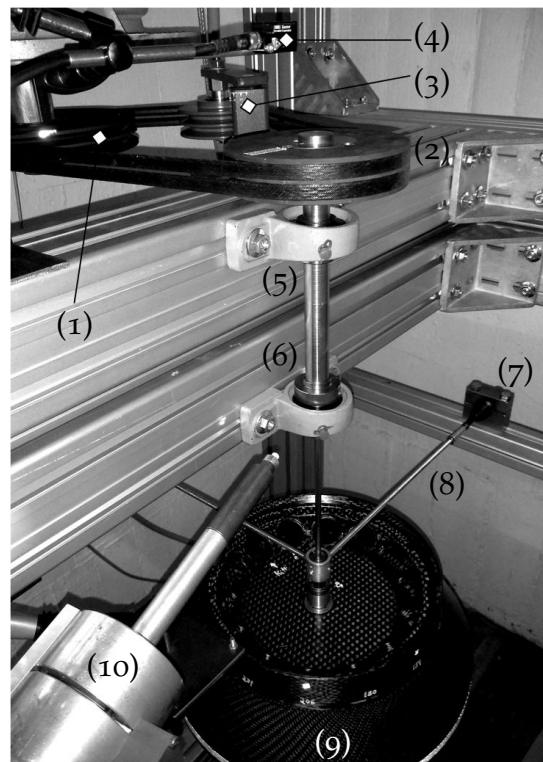
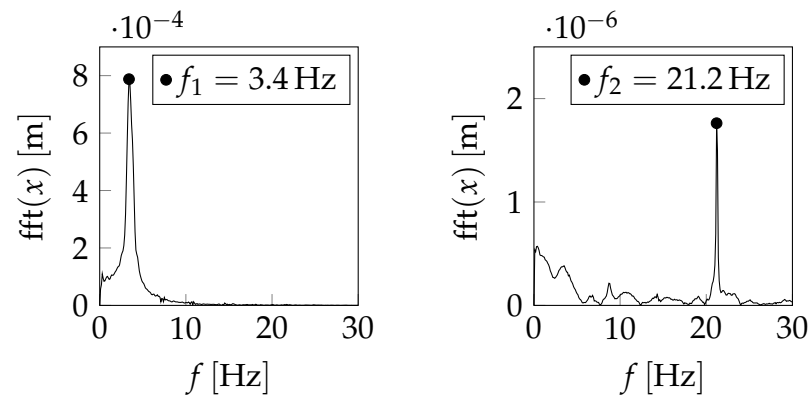


Figure 6.30.: Impulse excitation of the CFRP rotor in the test rig. (1) Motor pulley (2) rotor pulley (3) belt tensioner (4) incremental encoder (5) upper bearing (6) lower bearing (7) squeeze damper (8) connection rod (9) CFRP rotor (10) impulse device.

Subsequently, the impulse-excited vibration responses were measured in rotating operation. It was initially determined that the CFRP rotor in the assembled position exhibited a strong initial dynamic imbalance and required conventional balancing in order to safely pass through the first critical speed. In the two balancing planes, one at the top near the openings where the

6. Model validation with centrifuge test rigs



(a) Excitation of the first eigenfrequency.

(b) Excitation of the second eigenfrequency.

Figure 6.31.: FFT of the non rotating CFRP oscillations excited by impulse. a) Excitation of the CFRP rotor with dominant first eigenfrequency. b) Excitation of the lower axis bearing with dominant second eigenfrequency.

specimen holders are usually inserted and one in the plane of the specimen gap bottoms, additional masses of 70 g and 35 g at radii of 111 mm and 153 mm, respectively, were necessary.

With the sleeve to which the piston dampers are attached, only one non-rotating measuring point with significant deflection was available. The use of acceleration sensors on the bearing blocks proved to be unsuitable due to the superimposed rolling element excitation. Even when using eddy current sensors for contactless detection of the shaft deflection, the variance in the balancing runs could not be reduced to such an extent as to achieve complete compensation of the dynamic imbalance of the rotor.

Thus, although the first critical speed could be passed, the speed-synchronous vibration response to the unbalance excitation and its harmonics remained dominant. In order to capture the change in natural frequencies caused by the gyroscopy and to match it with the eigenvalue analysis of the MBS model, only isolated speeds were thus available at which the natural frequencies had a sufficient distance to the synchronous response and its harmonics.

Figure 6.32 shows the spectrogram of the rotor deflection during steady-state operation at 15 rad s^{-1} . By impulse excitation, vibration responses of the

6.2. CFRP centrifuge rotor

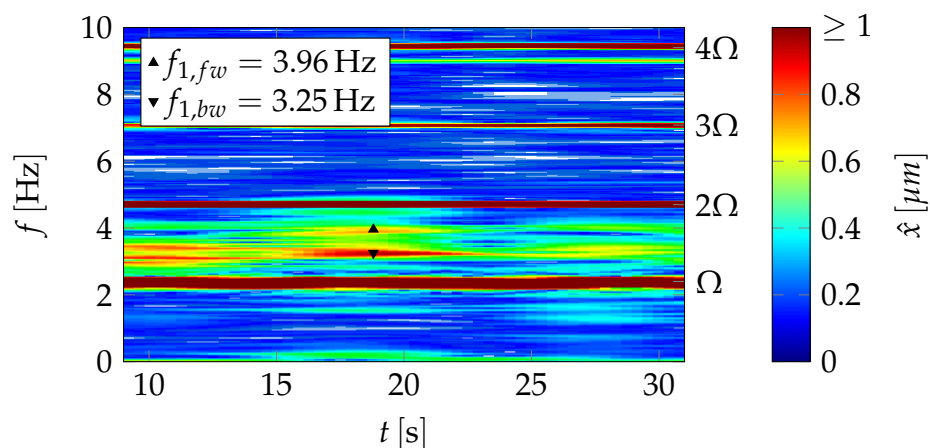


Figure 6.32.: Spectrogram of the CFRP rotor deflection in the time domain at constant rotational velocity $\Omega = 15 \text{ rad s}^{-1}$. The system was excited with an impulse device several times during the measurement.

backward whirl and the forward whirl of the first natural frequency at 3.25 Hz and 3.96 Hz can be identified. Furthermore, the steady-state operation at 40 rad s^{-1} and 50 rad s^{-1} was suitable to determine the position of natural frequencies, see fig. 6.33. The comparison of the determined frequencies is listed in table 6.5. It can be seen that a good agreement of the two considered natural frequency curves obtained from the MBS model could be achieved.

Table 6.5.: Comparison of experimentally and simulatively determined eigenfrequencies.

Ω [rad s ⁻¹]	$f_{1,bw}$ [Hz]		$f_{1, fw}$ [Hz]		$f_{2,bw}$ [Hz]		$f_{2, fw}$ [Hz]	
	Sim.	Exp.	Sim.	Exp.	Sim.	Exp.	Sim.	Exp.
0	3.50	3.4	3.50	3.4	22.39	21.2	22.39	21.2
15	3.06	3.25	3.97	3.96	20.84	-	24.21	-
40	2.44	2.38	4.80	4.61	18.7	-	27.9	-
50	2.23	-	5.12	5.0	18.1	17.9	29.6	30.0

6. Model validation with centrifuge test rigs

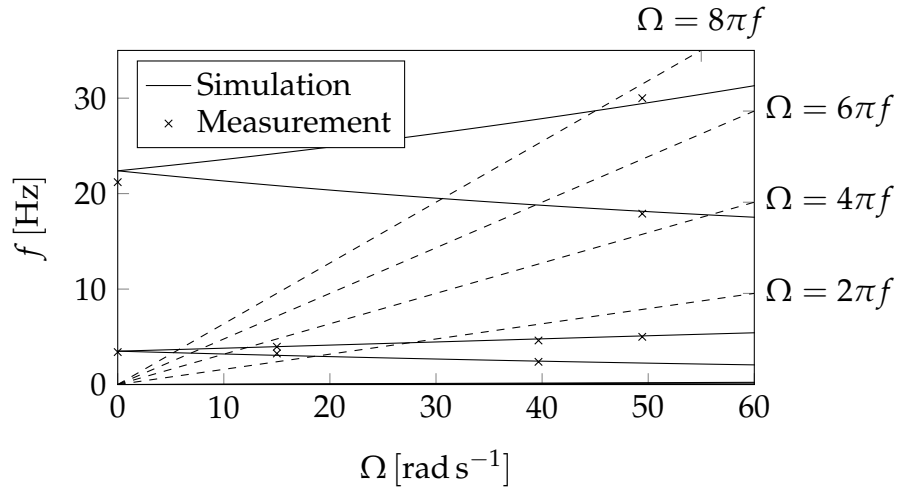


Figure 6.33.: Comparison of the CFRP rotor eigenvalues.

6.2.3. Planar oscillator model

The MBS model was again used to approximately parameterise an equivalent planar oscillator⁴, in the same procedure as for the centrifuge assembly on page 108. Utilizing the presented empirical approximation eq. (5.22) for ABB designs with raceways from roller bearings, the linear damping coefficient is calculated. With $W_1/r_b = 2.10$ and $r_b/\varepsilon = 0.07$, eq. (5.22) yields $c_d \text{Re} = 327$ and in combination with eq. (5.26) the parameter β as well as the stability map, see fig. 6.34, can be obtained. As before, friction is not considered in this stability map, yet a conservative design of minimum fluid viscosity for stable operation can be made.

6.2.4. Summary of the CFRP test rig

Compared to the discoidal rotor on the centrifuge assembly, the design of the CFRP test rig is free of non-linear components due to the vertically running drive shaft. This was reflected in the good agreement when matching the natural frequency responses. However, this set-up had problems that did not allow a similar analysis regarding the influence of different fluids and the

⁴By simply considering the deflection curve of the unilaterally clamped shaft, this would also be possible.

6.2. CFRP centrifuge rotor

Table 6.6.: Planar oscillator model parameters for the CRP rotor test rig.

With attached piston dampers:								
Property	M	k_x	k_y	b_x	b_y	ε	m_b	r_b
Value	5.573	2543		12.8		73.55	4.4	5.15
Unit	kg	N m^{-1}		N s m^{-1}		mm	kg	mm

Without attached piston dampers:								
Property	M	k_x	k_y	b_x	b_y	ε	m_b	r_b
Value	5.573	2543		0.7		73.55	4.4	5.15
Unit	kg	N m^{-1}		N s m^{-1}		mm	kg	mm

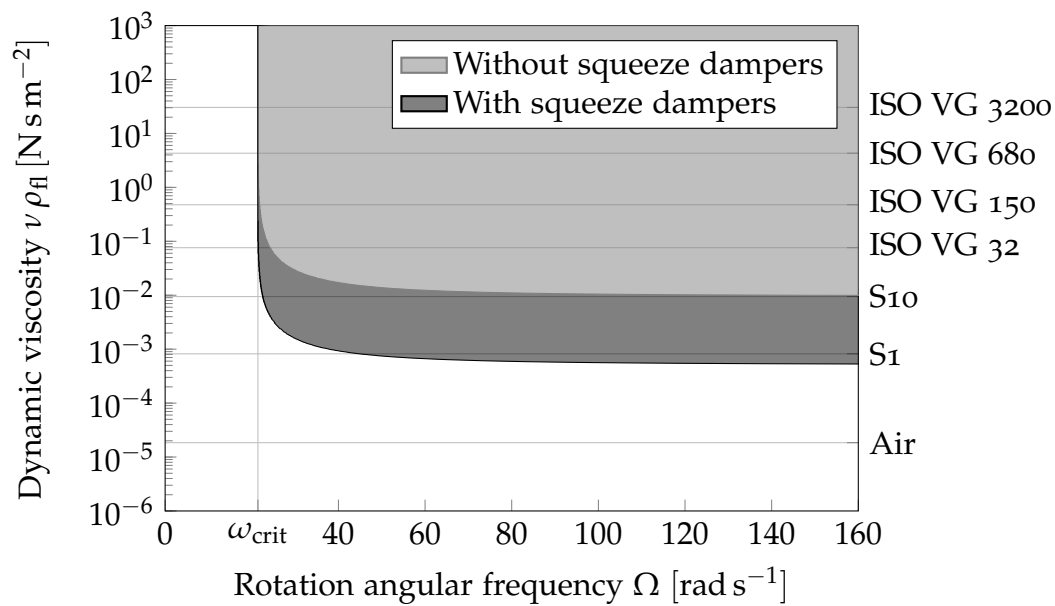


Figure 6.34.: Stability map of the CFRP testrig. The shaded areas indicate stable balancing. ISO VG viscosities are indicated at root temperature. S1 and S10 indicate silicone oils with kinematic viscosities of $1 \text{ mm}^2 \text{ s}^{-1}$ and $10 \text{ mm}^2 \text{ s}^{-1}$ at room temperature, respectively.

6. Model validation with centrifuge test rigs

vibration response during unbalance excitation with and without balancing masses. For example, the initial unbalance of the rotor had a significant magnitude and residual unbalance remained even after conventional balancing. In an analysis of the ABB influence with few balls, the influence would be small and could be lost in the natural measurement uncertainty. The main problem lies in the overhead arrangement of the ABB in connection with the mounting of the rotor on the drive shaft. Remounting the Rotor to the clutch resulted in a different unbalance state due to slightly different misalignments during assembly. It has been shown that for a variation of the fluid or the number of balls a disassembly of the rotor is necessary, because in the mounted position the chamber in the ABB could not be completely filled with fluid. Residual air always remained in the system, so that the ball in the ABB is influenced by a two-phase flow. However, this type of flow is not considered in the current modelling and significant deviations in the transient behaviour of the system are to be expected.

This problem clearly shows the limits of the potential of ABBs. The rotor system should be balanced in the base configuration so that the balancing masses only have to compensate for the variable imbalances. This is particularly relevant for massive rotors, such as the CFRP rotor presented.

7. Summary

The contents presented in this thesis can be roughly divided into two areas. First, the model of the planar oscillator with an ABB, which is widely used in the literature, was described, the equations of motion were analysed and the solutions were discussed. In the process, novel aspects of parameterisation and stability analysis were also brought out. For example, a proposal was made on how the parameter of the linear viscous modelled fluid damping can be quantitatively determined for an ABB. This parameter was previously difficult to estimate, even in its order of magnitude, if no empirical data were available. In this context, it could also be shown that a simple steady-state CFD analysis can be helpful to perform the mentioned quantification in more detail.

For the isotropic planar oscillator with two balancing masses, a novel stability criterion was also derived, which for an ABB configuration also provides the minimum dynamic viscosity of the fluid required for stable balancing. Even if the stabilising effect of friction is neglected, this can still be used as a criterion for a conservative design.

In the second part, the development of an MBS force element for modelling ABBs was presented. The basis for this development was a roller bearing force element, which, due to the similarity of the two systems, was expected to have the potential for code reuse. It turned out that the modelling of the radial rolling element load, which is relevant for the design of roller bearings, is not relevant for the ABB. On the other hand, the modelling of the rolling resistance in the slip-free state, which is neglected in the rolling bearing design, is of great importance for the dynamics of the ABB. Compared to the rolling bearing, the acting forces are orders of magnitude smaller.

For the transient nonlinear analysis of ABB simulation models, a particle

7. Summary

flow approach was presented. In the field of ABB analysis, this has not yet been implemented and investigated to the depth presented, especially the consideration of fluid inertia in the cavity. The metrological analysis of the presented test rigs showed that the presented particle flow approach is usable for ABBs and is especially suitable for configurations with few balls in the annulus. The analyses of the transient results of the simulation models, on the other hand, did not show very satisfactory agreements. On the one hand, this is due to initial conditions of the balls that cannot be determined in detail, especially the positioning in radial direction within the chamber. On the other hand, the implementation of the presented friction modelling shows deviations with respect to the expected behaviour.

Finally, the significance of transient simulations of the exact ball position must also be challenged by the fact that variable imbalances and initial conditions of the balancing masses are inherent to the application principle of ABBs. How far, for example, Monte Carlo analyses with the considered variance of the initial conditions and unbalance distributions can lead to better design decisions for ABBs is not certain.

In this context, however, the applications with impulse-like excitation should be emphasised, e.g. blade loss in turbines or ice shedding on rotor blades. In these cases, a balanced system is present before the sudden unbalance change, and the correction masses are therefore approximately symmetrically distributed. This initial condition is therefore easy to grasp in comparison. From the simulation of the sudden unbalance change, a suitable fluid can then be selected which achieves the most efficient balancing. Especially in the case of blade fractures, the ABB can act as a safety-relevant component. Thus, an extensive study for fluid selection can then be justified.

7.1. Outlook

For future work on the topic, the continuation of the validation of the MBS force element should be mentioned first. In contrast to the test rigs presented,

7.1. Outlook

a planar oscillator is also a suitable option. In addition, comparisons of the rolling resistance in non-rotating setups are worth investigating.

With regard to the progress achieved, further investigations can be made. For example, it seems possible with reasonable effort to extend the numerically evaluated stability criterion of the planar oscillator for more than two spheres. A similar assessment is made for the derivation of an explicit stability criterion of the orthotropically supported oscillator, similar to the equation presented in this work.

The implemented solution strategy for the determination of the flow profile based on finite differences is functional, but more efficient solution approaches exist. Since the retroaction of the balancing spheres is neglected, a smooth progression in the flow profile is obtained, which favours the application of spectral methods. Thus, it is assumed that the solution based on the Chebyshev polynomials [FP68; Boy01] leads to faster and more robust results. Possibly, the determination of the fluid velocity can thus also be transferred into a one-dimensional problem, since currently only the velocity value on the ball orbit is used for the calculation of the drag force.

For the rubber bushings installed in the centrifuge test rig, more detailed mechanical models should be compiled in the future in order to have the MBS simulation model of the basic drive ready to enable numerous rotordynamic investigations only by mounting the additional rotor.

In order to be able to compare different modelling depths of MBS ABB force elements, simpler implementations should also be implemented that are not based on the rolling bearing. Thus, the inertias of the balancing masses can also be modelled as pendulums and the presented non-linear influences due to flow and friction can be described as moments. This would eliminate the radial degree of freedom of the balancing masses, whose initial conditions are difficult to capture. Another possibility is the implementation of the equation of motion of the spheres presented in chapter 4, which only have one degree of freedom that describes the relative orbital position with respect to the rotor. Thus, the balancing masses would then no longer be explicit bodies in the MBS model, but would be described by state variables.

7. Summary

On the other hand, the described radial degree of freedom of the spheres may be necessary in acoustic investigations. In ABBs, especially with metallic components and the use of air in the chamber, a noise can be perceived when the balls repeatedly lose contact with the raceway. However, due to the high frequency of acoustic problems, investigations in this direction would cause a large increase in computation time.

If non-Newtonian fluids are also considered for the chamber filling, the changed properties can open up interesting areas of application and research. As an example, dilatant fluids exhibit a shear thickening behaviour. A review of various such fluids can be found in [Din+13]. More recently, in [BK19a] a constitutive model for the well-known Oobleck fluid, a mixture of water and corn starch, was presented. Especially for the application case of high-speed centrifuges, a pure fluid balancer with dilatant fluid represents an interesting concept, which may be able to mitigate the disadvantages of the regular fluid balancer, namely the lower balancing potential.

In conclusion to this paper, considering what has been said about the stable operation of ABBs, a fundamental design decision should be highlighted. The low prevalence of ABBs in technical systems is ultimately also due to economic aspects, since ABUs are not manufactured as a product in themselves, but are to be classified as an auxiliary measure. In the application example of the DVD-ROM drive presented in the introductory chapter, numerous balls were used in an air-filled chamber with a plastic raceway. Especially when an ABB with air is used, because the design of seals and manufacturing aspects are too costly, it is particularly vulnerable to unstable operation due to its low viscosity. With the use of a compliant raceway and the increased friction when using multiple balls, the dissipation created can allow for stable operation. Here, the associated susceptibility to misalignment due to the frictional effects is accepted. These types of low-cost ABBs thus require a deep understanding of the internal workings in order to ponder the aforementioned influences.

If, on the other hand, it is feasible to develop a fluid-filled ABB, then an ABB with multiple raceways should be chosen, where the individual radial sections are filled with fluids of different viscosities, as mentioned at the beginning, see fig. 2.5g. This is a robust variant to reduce the transient amplitudes of

7.1. Outlook

the rotor when passing the critical speed compared to the ABB with only one raceway.

A. Derivations of equations

A.1. Approximation of border frequencies of non-synchronous vibrations in isotropic, eccentricity-free ball balancers with two balls

Using the matrices $\underline{\underline{A}}$ and $\underline{\underline{B}}$ in equation (4.69) on page 49 and considering the isotropic case, i.e., $k_x = k_y = k$ and $b_x = b_y = b$, therefore substituting $k/M \equiv \omega_{\text{crit}}^2$, the determinant of the eigenvalue problem is calculated. Assuming no eccentricity of the ABB, the stationary positions of the two balls satisfy

$$\varphi_{02} = -\varphi_{01}, \quad \frac{\pi}{2} \leq \varphi_{01} \leq \pi \quad (\text{A.1})$$

and the characteristic equation can be written in a factorised form

$$\begin{aligned} 0 = & 16M^4(m_b\varepsilon)^2\Omega^4 \left[M^2 \left(\Omega^2 - \omega_{\text{crit}}^2 \right)^2 + \Omega^2 (2M\lambda + b)^2 \right] \\ & \left[4(m_b\varepsilon)^4 \left(\lambda^2\Omega^6 + \left(2\lambda^2\Omega^2 + \Omega^4 \right)^2 \right) \sin^2(\varphi_{01}) \cos^2(\varphi_{01}) \right. \\ & + \beta\lambda \left(2(m_b\varepsilon)^2\Omega^4 \left(M \left(\Omega^2 - \omega_{\text{crit}}^2 \right) + 3\lambda b \right) + M^2\beta\lambda \left(\Omega^2 - \omega_{\text{crit}}^2 \right)^2 \right. \\ & \left. \left. + 4M\lambda^2\Omega^2 \left((m_b\varepsilon)^2 \left(2\Omega^2 + \omega_{\text{crit}}^2 \right) + \beta(M\lambda + b) \right) + \beta\lambda\Omega^2 b^2 \right) \right]. \end{aligned}$$

A.1. Approximation of border frequencies of non-synchronous vibrations

From the first term in brackets follow the roots

$$\lambda = \left\{ -\frac{b}{2M} + i \frac{\omega_{\text{crit}}^2 - \Omega^2}{2\Omega}, -\frac{b}{2M} + i \frac{\omega_{\text{crit}}^2 + \Omega^2}{2\Omega} \right\}$$

with negative real parts. The second term in brackets is a fourth order polynomial $a_4\lambda^4 + a_3\lambda^3 + a_2\lambda^2 + a_1\lambda + a_0$ with the coefficients being rewritable as

$$a_4 = 4\Omega^2 \left(4(m_b\varepsilon)^4\Omega^2 \sin^2(\varphi_{01}) \cos^2(\varphi_{01}) + M^2\beta^2 \right)$$

$$a_3 = 4M\beta\Omega^2 \left(2(m_b\varepsilon)^2\Omega^2 + (m_b\varepsilon)^2\omega_{\text{crit}}^2 + \beta b \right)$$

$$a_2 = M^2\beta^2 \left(\Omega^2 - \omega_{\text{crit}}^2 \right)^2 + \Omega^2 \left(20(m_b\varepsilon)^4\Omega^4 \sin^2(\varphi_{01}) \cos^2(\varphi_{01}) \right. \\ \left. + 6(m_b\varepsilon)^2\beta\Omega^2 b + \beta^2 b^2 \right)$$

$$a_1 = 2(m_b\varepsilon)^2 M\beta\Omega^4 (\Omega - \omega_{\text{crit}}) (\Omega + \omega_{\text{crit}})$$

$$a_0 = 4(m_b\varepsilon)^4\Omega^8 \sin^2(\varphi_{01}) \cos^2(\varphi_{01}).$$

Since a_4 is positive, it is necessary and sufficient that $a_0 > 0$, $a_1 > 0$, $a_2 > 0$, $a_3 > 0$, i.e., the familiar condition $\Omega > \omega_{\text{crit}}$ for automatic balancing, and

$$0 < a_1(a_3a_2 - a_4a_1) - a_0a_3^2 \quad (\text{A.2})$$

to ensure stability of the system [Pop62]. Differentiation of the right hand side of equation (A.2) with respect to φ_{01} yields

$$\frac{d}{d\varphi_{01}} a_1(a_3a_2 - a_4a_1) - a_0a_3^2 = -K \sin(4\varphi_{01}) \quad (\text{A.3})$$

$$\frac{d^2}{d\varphi_{01}^2} a_1(a_3a_2 - a_4a_1) - a_0a_3^2 = -4K \cos(4\varphi_{01}) \quad (\text{A.4})$$

A. Derivations of equations

with

$$0 < K = 16(m_b \varepsilon)^4 M^2 \beta^2 \omega^{12} \left(\beta b \left(2\beta b + 3(m_b \varepsilon)^2 \omega^2 \right) + 9(m_b \varepsilon)^2 \omega_0^2 \left(\beta b + (m_b \varepsilon)^2 (\omega^2 + \omega_0^2) \right) \right).$$

Equation (A.3) delivers possible extrema of the stability criterion at

$$\varphi_{01} = j \frac{\pi}{4}, \quad j \in [2, 3, 4]$$

in the range defined in (A.1). Evaluation of the second derivative (A.4) shows that $\varphi_{01} = 3\pi/4$ is a minimum of the criterion, therefore the stability of the system is guaranteed if equation (A.2) holds true for $\varphi_{01} = 3\pi/4$, which reads after factorization

$$0 < 8(m_b \varepsilon)^2 M^2 \beta^2 \Omega^6 \left[\beta b (\Omega^2 - \omega_{\text{crit}}^2) - \omega_{\text{crit}}^2 (m_b \varepsilon)^2 (\Omega^2 + \omega_{\text{crit}}^2) \right] \left[M^2 \beta^2 (\Omega^2 - \omega_{\text{crit}}^2)^2 + (3(m_b \varepsilon)^2 \Omega^3 + \beta \Omega b)^2 \right].$$

Since the second bracketed term is always greater than zero, the criterion requires the first bracketed term to be positive and thus

$$\beta > \frac{(m_b \varepsilon)^2 \omega_{\text{crit}}^2}{b} \frac{\Omega^2 + \omega_{\text{crit}}^2}{\Omega^2 - \omega_{\text{crit}}^2}. \quad (\text{A.5})$$

From equation (A.5) the limit

$$\beta_{\text{min}} = \lim_{\Omega \rightarrow \infty} \beta = \frac{(m_b \varepsilon)^2 \omega_{\text{crit}}^2}{b} \quad (\text{A.6})$$

can be derived, describing a minimum required value for β in order to be able to pass the non-synchronous operation.

Equations (A.5) and (A.6) are applicable to an ABB with two balls. For an

A.2. Incompressible flow in cylindrical domains

ABB with only one ball, hence $\varphi_{01} = \pi$, similar reasoning leads to

$$\beta > \frac{(m_b \varepsilon)^2 \omega_{\text{crit}}^2}{2b} \frac{\Omega^2 + \omega_{\text{crit}}^2}{\Omega^2 - \omega_{\text{crit}}^2}, \quad (\text{A.7})$$

representing a lower limit. The reduction by half compared to an ABB with two balls is in accordance with the results of [Ryz+01]. Equation (A.7) is not relevant for the design of ABB devices, however, since a minimum of two balls is necessary to counteract variable unbalances.

A.2. Incompressible flow in cylindrical domains

The following section presents a detailed derivation of the Navier-Stokes equations in cylindrical coordinates starting from the Cauchy momentum equation, following the derivation provided by [Mic20].

Let

$$\underline{u}(r, \theta, z, t) = u_r(r, \theta, z, t) \underline{e}_r + u_\theta(r, \theta, z, t) \underline{e}_\theta + u_z(r, \theta, z, t) \underline{e}_z \quad (\text{A.8})$$

be the velocity vector of a fluid in a cylindrical domain. The Navier-Stokes equations can be derived by demanding mass conservation and evaluating the Cauchy momentum equation for Newtonian fluids.

A. Derivations of equations

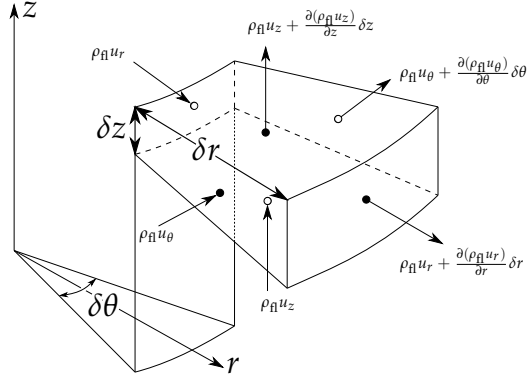


Figure A.1.: In- and outgoing mass fluxes of an infinitesimal volume in cylindrical coordinates.

Continuity equation

Summing the in- and outgoing mass flows on a reference volume in cylindrical coordinates, fig. A.1, and demanding mass conservation, yields

$$\begin{aligned}
 0 &= \rho_{fi} u_r r \delta \theta \delta z - \left(\rho_{fi} u_r + \frac{\partial(\rho_{fi} r)}{\partial r} \delta r \right) (r + \delta r) \delta \theta \delta z \\
 &+ \rho_{fi} u_\theta \delta r \delta z - \left(\rho_{fi} u_\theta + \frac{\partial(\rho_{fi} u_\theta)}{\partial \theta} \delta \theta \right) \delta r \delta z \\
 &+ \rho_{fi} u_z \left(r + \frac{\delta r}{2} \right) \delta r \delta \theta - \left(\rho_{fi} u_z + \frac{\partial(\rho_{fi} u_z)}{\partial z} \delta z \right) \left(r + \frac{\delta r}{2} \right) \delta r \delta \theta \\
 &= -\rho_{fi} u_r \delta r \delta \theta \delta z - \frac{\partial(\rho_{fi} u_r)}{\partial r} r \delta r \delta \theta \delta z - \frac{\partial(\rho_{fi} r)}{\partial r} \delta r^2 \delta \theta \delta z \\
 &\quad - \frac{\partial(\rho_{fi} u_\theta)}{\partial \theta} \delta r \delta \theta \delta z - \frac{\partial(\rho_{fi} u_z)}{\partial z} r \delta r \delta \theta \delta z - \frac{\partial(\rho_{fi} u_z)}{\partial z} \frac{\delta r^2}{2} \delta \theta \delta z.
 \end{aligned}$$

Dividing by the volume $r \delta r \delta \theta \delta z$ and letting $\delta r, \delta \theta, \delta z$ go to zero, yields

$$\frac{\rho_{fi}}{r} u_r + \frac{\partial(\rho_{fi} u_r)}{\partial r} + \frac{1}{r} \frac{\partial(\rho_{fi} u_\theta)}{\partial \theta} + \frac{\partial \rho_{fi} u_z}{\partial z} = 0,$$

A.2. Incompressible flow in cylindrical domains

which leads for incompressible fluids with constant density ρ_{fl} to

$$0 = \frac{1}{r}u_r + \frac{\partial u_r}{\partial r} + \frac{1}{r}\frac{\partial u_\theta}{\partial \theta} + \frac{\partial u_z}{\partial z} = \frac{1}{r}\frac{\partial(ru_r)}{\partial r} + \frac{1}{r}\frac{\partial u_\theta}{\partial \theta} + \frac{\partial u_z}{\partial z}. \quad (\text{A.9})$$

Momentum equation

The Cauchy momentum equation in convective form reads

$$\frac{Du}{Dt} = \frac{1}{\rho_{fl}}\nabla \cdot \underline{\underline{\sigma}} + \underline{g}, \quad (\text{A.10})$$

where $\underline{\underline{\sigma}}$ is the stress tensor and \underline{g} the vector of body forces.

The total differential on the left hand side expands to

$$\frac{Du}{Dt} = \frac{\partial u}{\partial t} + \frac{\partial u}{\partial r}\frac{dr}{dt} + \frac{\partial u}{\partial \theta}\frac{d\theta}{dt} + \frac{\partial u}{\partial z}\frac{dz}{dt}. \quad (\text{A.11})$$

While performing the derivatives of the velocity vector, the unit vectors must also be differentiated as they are not fixed in space:

$$\frac{\partial \underline{e}_r}{\partial r} = \frac{\partial \underline{e}_\theta}{\partial r} = \frac{\partial \underline{e}_z}{\partial r} = 0, \quad \frac{\partial \underline{e}_r}{\partial z} = \frac{\partial \underline{e}_\theta}{\partial z} = \frac{\partial \underline{e}_z}{\partial z} = 0 \quad (\text{A.12})$$

$$\frac{\partial \underline{e}_r}{\partial \theta} = \underline{e}_\theta, \quad \frac{\partial \underline{e}_\theta}{\partial \theta} = -\underline{e}_r, \quad \frac{\partial \underline{e}_z}{\partial \theta} = 0. \quad (\text{A.13})$$

The time derivative yields

$$\frac{\partial u}{\partial t} = \frac{\partial u_r}{\partial t}\underline{e}_r + \frac{\partial u_\theta}{\partial t}\underline{e}_\theta + \frac{\partial u_z}{\partial t}\underline{e}_z \quad (\text{A.14})$$

and by including the definition of the velocities $u_r = dr/dt$, $u_\theta/r = d\theta/dt$,

A. Derivations of equations

$u_z = dz/dt$, the remaining terms result in

$$\begin{aligned}
 \frac{dr}{dt} \frac{\partial u}{\partial r} &= u_r \frac{\partial u}{\partial r} \\
 &= u_r \left[\frac{\partial u_r}{\partial r} e_r + u_r \frac{\partial e_r}{\partial r} + \frac{\partial u_\theta}{\partial r} e_\theta + u_\theta \frac{\partial e_\theta}{\partial r} + \frac{\partial u_z}{\partial r} e_z + u_z \frac{\partial e_z}{\partial r} \right] \\
 &= u_r \left[\frac{\partial u_r}{\partial r} e_r + \frac{\partial u_\theta}{\partial r} e_\theta + \frac{\partial u_z}{\partial r} e_z \right] \tag{A.15}
 \end{aligned}$$

$$\begin{aligned}
 \frac{d\theta}{dt} \frac{\partial u}{\partial \theta} &= \frac{u_\theta}{r} \frac{\partial u}{\partial \theta} \\
 &= \frac{u_\theta}{r} \left[\frac{\partial u_r}{\partial \theta} e_r + u_r \frac{\partial e_r}{\partial \theta} + \frac{\partial u_\theta}{\partial \theta} e_\theta + u_\theta \frac{\partial e_\theta}{\partial \theta} + \frac{\partial u_z}{\partial \theta} e_z + u_z \frac{\partial e_z}{\partial \theta} \right] \\
 &= \frac{u_\theta}{r} \left[\frac{\partial u_r}{\partial \theta} e_r + u_r e_\theta + \frac{\partial u_\theta}{\partial \theta} e_\theta + u_\theta (-e_r) + \frac{\partial u_z}{\partial \theta} e_z \right] \\
 &= \frac{u_\theta}{r} \left[\left(\frac{\partial u_r}{\partial \theta} - u_\theta \right) e_r + \left(u_r + \frac{\partial u_\theta}{\partial \theta} \right) e_\theta + \frac{\partial u_z}{\partial \theta} e_z \right] \tag{A.16}
 \end{aligned}$$

$$\begin{aligned}
 \frac{dz}{dt} \frac{\partial u}{\partial z} &= u_z \frac{\partial u}{\partial z} \\
 &= u_z \left[\frac{\partial u_r}{\partial z} e_r + u_r \frac{\partial e_r}{\partial z} + \frac{\partial u_\theta}{\partial z} e_\theta + u_\theta \frac{\partial e_\theta}{\partial z} + \frac{\partial u_z}{\partial z} e_z + u_z \frac{\partial e_z}{\partial z} \right] \\
 &= u_z \left[\frac{\partial u_r}{\partial z} e_r + \frac{\partial u_\theta}{\partial z} e_\theta + \frac{\partial u_z}{\partial z} e_z \right] \tag{A.17}
 \end{aligned}$$

A.2. Incompressible flow in cylindrical domains

and therefore

$$\begin{aligned}
 \frac{Du}{Dt} = & \left[\frac{\partial u_r}{\partial t} + u_r \frac{\partial u_r}{\partial r} + \frac{u_\theta}{r} \frac{\partial u_r}{\partial \theta} - \frac{u_\theta^2}{r} + u_z \frac{\partial u_r}{\partial z} \right] \underline{e}_r \\
 & + \left[\frac{\partial u_\theta}{\partial t} + u_r \frac{\partial u_\theta}{\partial r} + \frac{u_\theta}{r} \frac{\partial u_\theta}{\partial \theta} + \frac{u_\theta u_r}{r} + u_z \frac{\partial u_\theta}{\partial z} \right] \underline{e}_\theta \\
 & + \left[\frac{\partial u_z}{\partial t} + u_r \frac{\partial u_z}{\partial r} + \frac{u_\theta}{r} \frac{\partial u_z}{\partial \theta} + u_z \frac{\partial u_z}{\partial z} \right] \underline{e}_z.
 \end{aligned} \tag{A.18}$$

Stress tensor

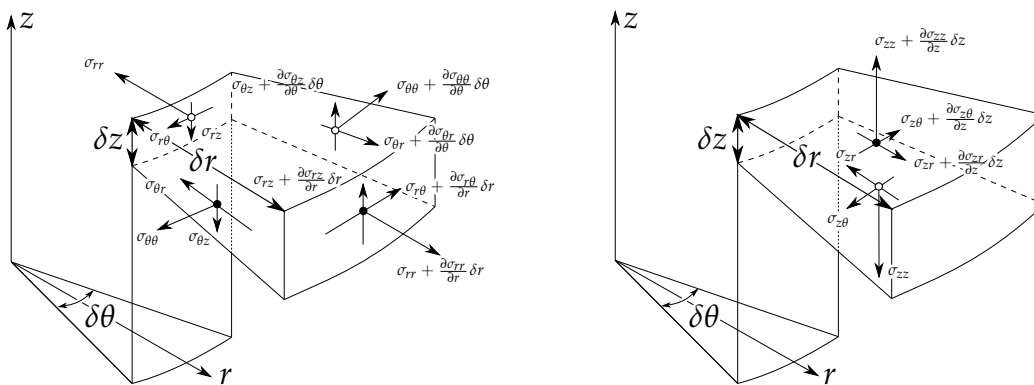


Figure A.2.: Stresses on an infinitesimal volume in cylindrical coordinates.

Summing up the forces acting on the reference volume, fig. A.2, referring them to the volume $r\delta r\delta\theta\delta z$ and letting δr , $\delta\theta$, δz go to zero while taking the symmetry

$$\sigma_{r\theta} = \sigma_{\theta r}, \quad \sigma_{rz} = \sigma_{zr}, \quad \sigma_{\theta z} = \sigma_{z\theta} \tag{A.19}$$

A. Derivations of equations

into account, yields for the r direction

$$\begin{aligned}
& \left(\sigma_{rr} + \frac{\partial \sigma_{rr}}{\partial r} \delta r \right) (r + \delta r) \delta \theta \delta z - \sigma_{rr} r \delta \theta \delta z \\
& + \left(\sigma_{\theta r} + \frac{\partial \sigma_{\theta r}}{\partial \theta} \delta \theta \right) \delta r \delta z \cos \left(\frac{\delta \theta}{2} \right) - \sigma_{\theta r} \delta r \delta z \cos \left(\frac{\delta \theta}{2} \right) \\
& + \left(\sigma_{zr} + \frac{\partial \sigma_{zr}}{\partial z} \delta z \right) \left(r + \frac{\delta r}{2} \right) \delta r \delta \theta - \sigma_{zr} \left(r + \frac{\delta r}{2} \right) \delta r \delta \theta \\
& - \left(\sigma_{\theta \theta} + \frac{\partial \sigma_{\theta \theta}}{\partial \theta} \delta \theta \right) \delta r \delta z \sin \left(\frac{\delta \theta}{2} \right) - \sigma_{\theta \theta} \delta r \delta z \sin \left(\frac{\delta \theta}{2} \right), \tag{A.20}
\end{aligned}$$

resulting in

$$\frac{\sigma_{rr}}{r} + \frac{\partial \sigma_{rr}}{\partial r} + \frac{1}{r} \frac{\partial \sigma_{r\theta}}{\partial \theta} + \frac{\partial \sigma_{rz}}{\partial z} - \frac{\sigma_{\theta \theta}}{r}, \tag{A.21}$$

and for the θ direction

$$\begin{aligned}
& \left(\sigma_{r\theta} + \frac{\partial \sigma_{r\theta}}{\partial r} \delta r \right) (r + \delta r) \delta \theta \delta z - \sigma_{r\theta} r \delta \theta \delta z \\
& + \left(\sigma_{\theta \theta} + \frac{\partial \sigma_{\theta \theta}}{\partial \theta} \delta \theta \right) \delta r \delta z \cos \left(\frac{\delta \theta}{2} \right) - \sigma_{\theta \theta} \delta r \delta z \cos \left(\frac{\delta \theta}{2} \right) \\
& + \left(\sigma_{\theta r} + \frac{\partial \sigma_{\theta r}}{\partial \theta} \delta \theta \right) \delta r \delta z \sin \left(\frac{\delta \theta}{2} \right) + \sigma_{\theta r} \delta r \delta z \sin \left(\frac{\delta \theta}{2} \right) \\
& + \left(\sigma_{z\theta} + \frac{\partial \sigma_{z\theta}}{\partial z} \delta z \right) \left(r + \frac{\delta r}{2} \right) \delta r \delta \theta - \sigma_{z\theta} \left(r + \frac{\delta r}{2} \right) \delta r \delta \theta, \tag{A.22}
\end{aligned}$$

resulting in

$$\frac{2}{r} \sigma_{r\theta} + \frac{\partial \sigma_{r\theta}}{\partial r} + \frac{1}{r} \frac{\partial \sigma_{\theta \theta}}{\partial \theta} + \frac{\partial \sigma_{\theta z}}{\partial z}, \tag{A.23}$$

A.2. Incompressible flow in cylindrical domains

and for the z direction

$$\begin{aligned}
 & \left(\sigma_{rz} + \frac{\partial \sigma_{rz}}{\partial r} \delta r \right) (r + \delta r) \delta \theta \delta z - \sigma_{rz} r \delta \theta \delta z \\
 & + \left(\sigma_{\theta z} + \frac{\partial \sigma_{\theta z}}{\partial \theta} \delta \theta \right) \delta r \delta z - \sigma_{\theta z} \delta r \delta z \\
 & + \left(\sigma_{zz} + \frac{\partial \sigma_{zz}}{\partial z} \delta z \right) \left(r + \frac{\delta r}{2} \right) \delta r \delta \theta - \sigma_{zz} \left(r + \frac{\delta r}{2} \right) \delta r \delta \theta,
 \end{aligned} \tag{A.24}$$

resulting in

$$\frac{1}{r} \sigma_{rz} + \frac{\partial \sigma_{rz}}{\partial r} + \frac{1}{r} \frac{\partial \sigma_{\theta z}}{\partial \theta} + \frac{\partial \sigma_{zz}}{\partial z}. \tag{A.25}$$

Thus, the gradient of the stress tensor yields

$$\begin{aligned}
 \nabla \cdot \underline{\underline{\sigma}} &= \left(\frac{\sigma_{rr}}{r} + \frac{\partial \sigma_{rr}}{\partial r} + \frac{1}{r} \frac{\partial \sigma_{r\theta}}{\partial \theta} + \frac{\partial \sigma_{rz}}{\partial z} - \frac{\sigma_{\theta\theta}}{r} \right) \underline{e}_r \\
 &+ \left(\frac{2}{r} \sigma_{r\theta} + \frac{\partial \sigma_{r\theta}}{\partial r} + \frac{1}{r} \frac{\partial \sigma_{\theta\theta}}{\partial \theta} + \frac{\partial \sigma_{\theta z}}{\partial z} \right) \underline{e}_\theta \\
 &+ \left(\frac{1}{r} \sigma_{rz} + \frac{\partial \sigma_{rz}}{\partial r} + \frac{1}{r} \frac{\partial \sigma_{\theta z}}{\partial \theta} + \frac{\partial \sigma_{zz}}{\partial z} \right) \underline{e}_z.
 \end{aligned} \tag{A.26}$$

Stress-strain

The Cauchy stress tensor can be separated in an isotropic part, giving the normal stresses, and an anisotropic part, describing the shear stresses

$$\underline{\underline{\sigma}} = -p \underline{\underline{I}} + \underline{\underline{\tau}}, \tag{A.27}$$

where $\underline{\underline{I}}$ is the identity matrix in the space considered, multiplied by the pressure p , and $\underline{\underline{\tau}}$ is the shear stress tensor. For incompressible fluids with constant viscosities, i.e. Newtonian fluids, the shear tensor is represented

A. Derivations of equations

by

$$\underline{\underline{\tau}} = \nu\rho_{\text{fl}} \left(\nabla \underline{u} + \nabla \underline{u}^T \right), \quad (\text{A.28})$$

while the gradient of the velocity vector equals

$$\nabla \underline{u} = \underline{u} \otimes \nabla = (u_r \underline{e}_r + u_\theta \underline{e}_\theta + u_z \underline{e}_z) \otimes \left(\underline{e}_r \frac{\partial}{\partial r} + \underline{e}_\theta \frac{1}{r} \frac{\partial}{\partial \theta} + \underline{e}_z \frac{\partial}{\partial z} \right) \quad (\text{A.29})$$

$$\nabla \underline{u} = \begin{bmatrix} \frac{\partial u_r}{\partial r} & \frac{1}{r} \frac{\partial u_r}{\partial \theta} - \frac{u_\theta}{r} & \frac{\partial u_r}{\partial z} \\ \frac{\partial u_\theta}{\partial r} & \frac{1}{r} \frac{\partial u_\theta}{\partial \theta} + \frac{u_r}{r} & \frac{\partial u_\theta}{\partial z} \\ \frac{\partial u_z}{\partial r} & \frac{1}{r} \frac{\partial u_z}{\partial \theta} & \frac{\partial u_z}{\partial z} \end{bmatrix}. \quad (\text{A.30})$$

This leads to the following components of the stress tensor

$$\begin{aligned} \sigma_{rr} &= -p + 2\nu\rho_{\text{fl}} \frac{\partial u_r}{\partial r}, & \sigma_{r\theta} &= \sigma_{\theta r} = \nu\rho_{\text{fl}} \left(\frac{1}{r} \frac{\partial u_r}{\partial \theta} + \frac{\partial u_\theta}{\partial r} - \frac{u_\theta}{r} \right), \\ \sigma_{\theta\theta} &= -p + 2\nu\rho_{\text{fl}} \left(\frac{1}{r} \frac{\partial u_\theta}{\partial \theta} + \frac{u_r}{r} \right), & \sigma_{rz} &= \sigma_{zr} = \nu\rho_{\text{fl}} \left(\frac{\partial u_r}{\partial z} + \frac{\partial u_z}{\partial r} \right), \\ \sigma_{zz} &= -p + 2\nu\rho_{\text{fl}} \frac{\partial u_z}{\partial z}, & \sigma_{\theta z} &= \sigma_{z\theta} = \nu\rho_{\text{fl}} \left(\frac{1}{r} \frac{\partial u_z}{\partial \theta} + \frac{\partial u_\theta}{\partial z} \right), \end{aligned}$$

which are substituted in the Cauchy momentum equation (A.10) yielding three equations for the components in \underline{e}_r , \underline{e}_θ and \underline{e}_z , respectively.

A.2. Incompressible flow in cylindrical domains

Radial component

$$\left[\frac{\partial u_r}{\partial t} + u_r \frac{\partial u_r}{\partial r} + \frac{u_\theta}{r} \frac{\partial u_r}{\partial \theta} - \frac{u_\theta^2}{r} + u_z \frac{\partial u_r}{\partial z} \right] e_r =$$

$$\left[-\frac{1}{\rho_{fl}} \frac{\partial p}{\partial r} + \nu \left\{ \frac{2}{r} \frac{\partial u_r}{\partial r} + 2 \frac{\partial^2 u_r}{\partial r^2} + \frac{1}{r} \frac{\partial^2 u_\theta}{\partial r \partial \theta} + \right. \right.$$

$$\left. \frac{1}{r^2} \frac{\partial^2 u_r}{\partial \theta^2} - \frac{1}{r^2} \frac{\partial u_\theta}{\partial \theta} + \frac{\partial^2 u_r}{\partial z^2} + \frac{\partial^2 u_z}{\partial r \partial z} - \frac{2}{r^2} \frac{\partial u_\theta}{\partial \theta} - \frac{2}{r^2} u_r \right\} + g_r \right] e_r$$

Rewriting the following terms as

$$\frac{2}{r} \frac{\partial u_r}{\partial r} + 2 \frac{\partial^2 u_r}{\partial r^2} = \frac{1}{r} \frac{\partial}{\partial r} \left(r \frac{\partial u_r}{\partial r} \right) + \frac{1}{r} \frac{\partial u_r}{\partial r} + \frac{\partial^2 u_r}{\partial r^2}$$

$$= \frac{1}{r} \frac{\partial}{\partial r} \left(r \frac{\partial u_r}{\partial r} \right) + \frac{u_r}{r^2} + \frac{\partial}{\partial r} \left(\frac{1}{r} \frac{\partial (r u_r)}{\partial r} \right)$$

$$\frac{1}{r} \frac{\partial^2 u_\theta}{\partial r \partial \theta} = \frac{\partial}{\partial r} \left(\frac{1}{r} \frac{\partial u_\theta}{\partial \theta} \right) + \frac{1}{r^2} \frac{\partial u_\theta}{\partial \theta},$$

leads to

$$\left[\frac{\partial u_r}{\partial t} + u_r \frac{\partial u_r}{\partial r} + \frac{u_\theta}{r} \frac{\partial u_r}{\partial \theta} - \frac{u_\theta^2}{r} + u_z \frac{\partial u_r}{\partial z} \right] e_r =$$

$$\left[-\frac{1}{\rho_{fl}} \frac{\partial p}{\partial r} + \nu \left\{ \frac{1}{r} \frac{\partial}{\partial r} \left(r \frac{\partial u_r}{\partial r} \right) + \frac{1}{r^2} \frac{\partial^2 u_r}{\partial \theta^2} + \frac{\partial^2 u_r}{\partial z^2} - \frac{u_r}{r^2} - \frac{2}{r^2} \frac{\partial u_\theta}{\partial \theta} \right. \right.$$

$$\left. \left. + \frac{\partial}{\partial r} \left[\frac{1}{r} \frac{\partial (r u_r)}{\partial r} + \frac{1}{r} \frac{\partial u_\theta}{\partial \theta} + \frac{\partial^2 u_z}{\partial r \partial z} \right] \right\} + g_r \right] e_r,$$

where the inner square bracket in the third line equals zero for incompressible fluids due to the continuity equation (A.9). Thus, the radial component of the

A. Derivations of equations

Navier-Stokes equations reads

$$\rho_{fl} \left(\frac{\partial u_r}{\partial t} + u_r \frac{\partial u_r}{\partial r} + \frac{u_\theta}{r} \frac{\partial u_r}{\partial \theta} + u_z \frac{\partial u_r}{\partial z} - \frac{u_\theta^2}{r} \right) = -\frac{\partial p}{\partial r} + \rho_{fl} g_r$$

$$+ \nu \rho_{fl} \left(\frac{1}{r} \frac{\partial}{\partial r} \left(r \frac{\partial u_r}{\partial r} \right) + \frac{1}{r^2} \frac{\partial^2 u_r}{\partial \theta^2} + \frac{\partial^2 u_r}{\partial z^2} - \frac{u_r}{r^2} - \frac{2}{r^2} \frac{\partial u_\theta}{\partial \theta} \right).$$

Angular component

$$\left[\frac{\partial u_\theta}{\partial t} + u_r \frac{\partial u_\theta}{\partial r} + \frac{u_\theta}{r} \frac{\partial u_\theta}{\partial \theta} + u_z \frac{\partial u_\theta}{\partial z} + \frac{u_r u_\theta}{r} \right] \underline{e}_\theta =$$

$$\left[-\frac{1}{\rho_{fl} r} \frac{\partial p}{\partial \theta} + \nu \left\{ -\frac{u_\theta}{r^2} + \frac{\partial^2 u_\theta}{\partial z^2} + \frac{1}{r} \frac{\partial u_\theta}{\partial r} + \frac{\partial^2 u_\theta}{\partial r^2} \right. \right.$$

$$\left. \left. + \frac{3}{r^2} \frac{\partial u_r}{\partial \theta} + \frac{2}{r^2} \frac{\partial^2 u_\theta}{\partial \theta^2} + \frac{1}{r} \frac{\partial^2 u_r}{\partial r \partial \theta} + \frac{1}{r} \frac{\partial^2 u_z}{\partial \theta \partial z} \right\} + g_\theta \right] \underline{e}_\theta$$

Rewriting the following term as

$$\frac{1}{r} \frac{\partial u_\theta}{\partial r} + \frac{\partial^2 u_\theta}{\partial r^2} = \frac{1}{r} \frac{\partial}{\partial r} \left(\frac{\partial u_\theta}{\partial r} \right)$$

and cancelling

$$\frac{1}{r^2} \frac{\partial u_r}{\partial \theta} + \frac{1}{r^2} \frac{\partial^2 u_\theta}{\partial \theta^2} + \frac{1}{r} \frac{\partial^2 u_r}{\partial r \partial \theta} + \frac{1}{r} \frac{\partial^2 u_z}{\partial \theta \partial z} = \frac{1}{r} \frac{\partial}{\partial \theta} \left[\frac{1}{r} u_r + \frac{1}{r} \frac{\partial u_\theta}{\partial \theta} + \frac{\partial u_r}{\partial r} + \frac{\partial u_z}{\partial z} \right]$$

due to the continuity equation, leads to the azimuthal component of the Navier-Stokes equations

$$\rho_{fl} \left(\frac{\partial u_\theta}{\partial t} + u_r \frac{\partial u_\theta}{\partial r} + \frac{u_\theta}{r} \frac{\partial u_\theta}{\partial \theta} + u_z \frac{\partial u_\theta}{\partial z} + \frac{u_r u_\theta}{r} \right) = -\frac{1}{r} \frac{\partial p}{\partial \theta} + \rho_{fl} g_\theta$$

$$+ \nu \rho_{fl} \left(\frac{1}{r} \frac{\partial}{\partial r} \left(r \frac{\partial u_\theta}{\partial r} \right) + \frac{1}{r^2} \frac{\partial^2 u_\theta}{\partial \theta^2} + \frac{\partial^2 u_\theta}{\partial z^2} + \frac{2}{r^2} \frac{\partial u_r}{\partial \theta} - \frac{u_\theta}{r^2} \right).$$

A.3. Vorticity-stream function formulation in axisymmetric cylindrical domains

Axial component

$$\left[\frac{\partial u_z}{\partial t} + u_r \frac{\partial u_z}{\partial r} + \frac{u_\theta}{r} \frac{\partial u_z}{\partial \theta} + u_z \frac{\partial u_z}{\partial z} \right] \underline{e}_z =$$

$$\left[-\frac{1}{\rho_{fl}} \frac{\partial p}{\partial z} + \nu \left\{ \frac{1}{r} \frac{\partial u_z}{\partial r} + \frac{\partial^2 u_z}{\partial r^2} + \frac{1}{r^2} \frac{\partial^2 u_z}{\partial \theta^2} \right. \right.$$

$$\left. \left. + \frac{1}{r} \frac{\partial u_r}{\partial z} + \frac{\partial^2 u_r}{\partial r \partial z} + \frac{1}{r} \frac{\partial^2 u_\theta}{\partial \theta \partial z} + 2 \frac{\partial^2 u_z}{\partial z^2} \right\} + g_z \right] \underline{e}_z$$

By rewriting the following term as

$$\frac{1}{r} \frac{\partial u_z}{\partial r} + \frac{\partial^2 u_z}{\partial r^2} = \frac{1}{r} \frac{\partial}{\partial r} \left(r \frac{\partial u_z}{\partial r} \right)$$

and cancelling

$$\frac{1}{r} \frac{\partial u_r}{\partial z} + \frac{\partial^2 u_r}{\partial r \partial z} + \frac{1}{r} \frac{\partial^2 u_\theta}{\partial \theta \partial z} + 1 \frac{\partial^2 u_z}{\partial z^2} = \frac{\partial}{\partial z} \left[\frac{1}{r} u_r + \frac{\partial u_r}{\partial r} + \frac{1}{r} \frac{\partial u_\theta}{\partial \theta} + \frac{\partial u_z}{\partial z} \right]$$

due to the continuity equation, one obtains the axial component of the Navier-Stokes equations

$$\rho_{fl} \left(\frac{\partial u_z}{\partial t} + u_r \frac{\partial u_z}{\partial r} + \frac{u_\theta}{r} \frac{\partial u_z}{\partial \theta} + u_z \frac{\partial u_z}{\partial z} \right) = -\frac{\partial p}{\partial z} + \rho_{fl} g_z$$

$$+ \nu \rho_{fl} \left(\frac{1}{r} \frac{\partial}{\partial r} \left(r \frac{\partial u_z}{\partial r} \right) + \frac{1}{r^2} \frac{\partial^2 u_z}{\partial \theta^2} + \frac{\partial^2 u_z}{\partial z^2} \right).$$

A.3. Vorticity-stream function formulation in axisymmetric cylindrical domains

To solve the Navier-Stokes equations in a axisymmetric cylindrical domain efficiently with a finite difference scheme, the Navier-Stokes equations are transformed to the vorticity-stream function formulation, as outlined in [LS98].

A. Derivations of equations

From the momentum equations on a control volume in a cylindrical coordinate system yield the Navier-Stokes equations expressed in the variables r, θ, z with the velocity vector $\underline{u} = (u_r, u_\theta, u_z)^T$, see appendix A.2.

$$\begin{aligned} \rho_{\text{fl}} \left(\frac{\partial u_r}{\partial t} + u_r \frac{\partial u_r}{\partial r} + \frac{u_\theta}{r} \frac{\partial u_r}{\partial \theta} + u_z \frac{\partial u_r}{\partial z} - \frac{u_\theta^2}{r} \right) &= -\frac{\partial p}{\partial r} + \rho_{\text{fl}} g_r \\ &+ \nu \rho_{\text{fl}} \left(\frac{1}{r} \frac{\partial}{\partial r} \left(r \frac{\partial u_r}{\partial r} \right) + \frac{1}{r^2} \frac{\partial^2 u_r}{\partial \theta^2} + \frac{\partial^2 u_r}{\partial z^2} - \frac{u_r}{r^2} - \frac{2}{r^2} \frac{\partial u_\theta}{\partial \theta} \right) \end{aligned} \quad (\text{A.31})$$

$$\begin{aligned} \rho_{\text{fl}} \left(\frac{\partial u_\theta}{\partial t} + u_r \frac{\partial u_\theta}{\partial r} + \frac{u_\theta}{r} \frac{\partial u_\theta}{\partial \theta} + u_z \frac{\partial u_\theta}{\partial z} + \frac{u_r u_\theta}{r} \right) &= -\frac{1}{r} \frac{\partial p}{\partial \theta} + \rho_{\text{fl}} g_\theta \\ &+ \nu \rho_{\text{fl}} \left(\frac{1}{r} \frac{\partial}{\partial r} \left(r \frac{\partial u_\theta}{\partial r} \right) + \frac{1}{r^2} \frac{\partial^2 u_\theta}{\partial \theta^2} + \frac{\partial^2 u_\theta}{\partial z^2} + \frac{2}{r^2} \frac{\partial u_r}{\partial \theta} - \frac{u_\theta}{r^2} \right) \end{aligned} \quad (\text{A.32})$$

$$\begin{aligned} \rho_{\text{fl}} \left(\frac{\partial u_z}{\partial t} + u_r \frac{\partial u_z}{\partial r} + \frac{u_\theta}{r} \frac{\partial u_z}{\partial \theta} + u_z \frac{\partial u_z}{\partial z} \right) &= -\frac{\partial p}{\partial z} + \rho_{\text{fl}} g_z \\ &+ \nu \rho_{\text{fl}} \left(\frac{1}{r} \frac{\partial}{\partial r} \left(r \frac{\partial u_z}{\partial r} \right) + \frac{1}{r^2} \frac{\partial^2 u_z}{\partial \theta^2} + \frac{\partial^2 u_z}{\partial z^2} \right) \end{aligned} \quad (\text{A.33})$$

It is assumed that the gravity components g_r, g_θ, g_z are zero or counteracted by pressure fields and therefore negligible from the equations. The continuity equation for incompressible fluids reads

$$\frac{\partial \rho_{\text{fl}}}{\partial t} + \frac{1}{r} \frac{\partial}{\partial r} (\rho_{\text{fl}} r u_r) + \frac{1}{r} \frac{\partial}{\partial \theta} (\rho_{\text{fl}} u_\theta) + \frac{\partial}{\partial z} (\rho_{\text{fl}} u_z) = 0. \quad (\text{A.34})$$

By introducing the Stokes stream function ψ and the angular momentum Γ according to

$$\underline{u} = -\frac{1}{r} \frac{\partial \psi}{\partial z} \underline{e}_r + \frac{1}{r} \Gamma \underline{e}_\theta + \frac{1}{r} \frac{\partial \psi}{\partial r} \underline{e}_z, \quad (\text{A.35})$$

the continuity equation is fulfilled automatically for incompressible flows.

A.3. Vorticity-stream function formulation in axisymmetric cylindrical domains

With the differential operator $\underline{\nabla} = \left(\frac{\partial}{\partial r}, \frac{\partial}{\partial \theta}, \frac{\partial}{\partial z} \right)^T$ the vorticity of the flow field yields

$$\underline{\nabla} \times \underline{u} = (\xi, \eta, \zeta)^T. \quad (\text{A.36})$$

In the axisymmetric case all partial derivatives with respect to θ equal zero and the vorticity components yield

$$\xi = -\frac{1}{r} \frac{\partial \Gamma}{\partial z}, \quad (\text{A.37})$$

$$\eta = -\frac{1}{r} \nabla^2 \psi, \quad (\text{A.38})$$

$$\zeta = \frac{1}{r} \frac{\partial \Gamma}{\partial r}, \quad (\text{A.39})$$

with $\nabla^2 = \frac{\partial^2}{\partial r^2} - \frac{1}{r} \frac{\partial}{\partial r} + \frac{\partial^2}{\partial z^2}$. By cross-differentiation of eq. (A.31) and eq. (A.33) and subtraction, the pressure p is eliminated yielding¹

$$D \left(\frac{\eta}{r} \right) = \nu \left[\nabla^2 \left(\frac{\eta}{r} \right) + \frac{4}{r} \frac{\partial}{\partial r} \left(\frac{\eta}{r} \right) \right] + \frac{\partial}{\partial z} \left(\frac{\Gamma^2}{r^4} \right) \quad (\text{A.40})$$

where

$$D = \frac{\partial}{\partial t} - \frac{1}{r} \frac{\partial \psi}{\partial z} \frac{\partial}{\partial r} + \frac{1}{r} \frac{\partial \psi}{\partial r} \frac{\partial}{\partial z}.$$

From eq. (A.32) follows

$$D\Gamma = \nu \nabla^2 \Gamma. \quad (\text{A.41})$$

Equations (A.38), (A.40) and (A.41) form a system of equations which are separated in one elliptic PDE of the Poisson type in ψ and two parabolic PDEs

¹The equations published in the appendix of [LS98] hold a typing error at this point.

A. Derivations of equations

in η and Γ , respectively, reading

$$\frac{\partial \Gamma}{\partial t} = \frac{1}{r} \frac{\partial \Gamma}{\partial r} \frac{\partial \psi}{\partial z} - \frac{1}{r} \frac{\partial \Gamma}{\partial z} \frac{\partial \psi}{\partial r} + \nu \left(\frac{\partial^2 \Gamma}{\partial r^2} - \frac{1}{r} \frac{\partial \Gamma}{\partial r} + \frac{\partial^2 \Gamma}{\partial z^2} \right) \quad (\text{A.42})$$

$$\begin{aligned} \frac{\partial \eta}{\partial t} = & -\frac{1}{r} \frac{\partial \psi}{\partial r} \frac{\partial \eta}{\partial z} + \frac{1}{r} \frac{\partial \psi}{\partial z} \frac{\partial \eta}{\partial r} - \frac{1}{r^2} \eta \frac{\partial \psi}{\partial z} + \frac{2}{r^3} \Gamma \frac{\partial \Gamma}{\partial z} \\ & + \nu \left(\frac{\partial^2 \eta}{\partial r^2} + \frac{\partial^2 \eta}{\partial z^2} + \frac{1}{r} \frac{\partial \eta}{\partial r} - \frac{1}{r^2} \eta \right) \end{aligned} \quad (\text{A.43})$$

$$-r\eta = \frac{\partial^2 \psi}{\partial r^2} - \frac{1}{r} \frac{\partial \psi}{\partial r} + \frac{\partial^2 \psi}{\partial z^2}. \quad (\text{A.44})$$

B. Test rig details

B.1. Discoidal rotor

Table B.1.: Inertial properties of the test rig assembly parts.

Part	Mass [kg]	Moments of inertia [g m ²]	
		$J_{xx} = J_{yy}$	J_{zz}
Discoidal rotor	4.142	16.92	33.15
Rotor shaft	1.502	2.00	0.64
Cover lid	0.333	0.54	0.77
Stator winding	3.720	6.80	9.00
Base	3.192	9.27	17.21

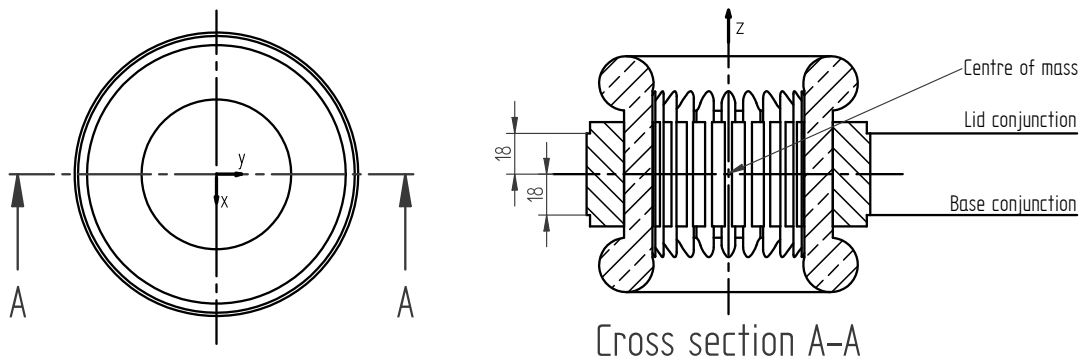


Figure B.1.: Properties of the stator of the motor unit.

B. Test rig details

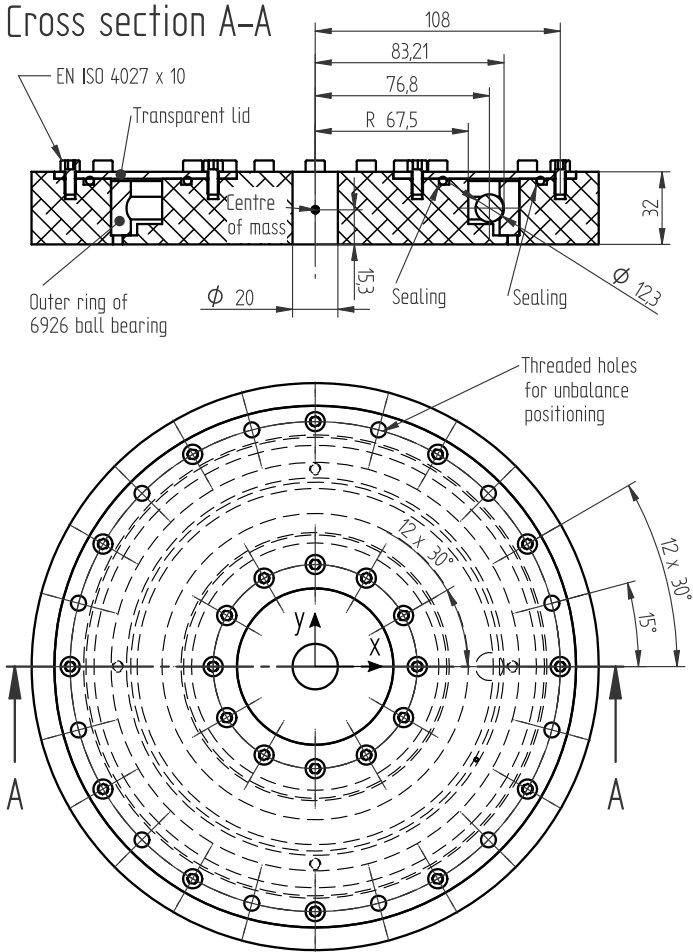


Figure B.2.: Mass properties of the discoidal rotor with included ball balancer.

B.1. Discoidal rotor

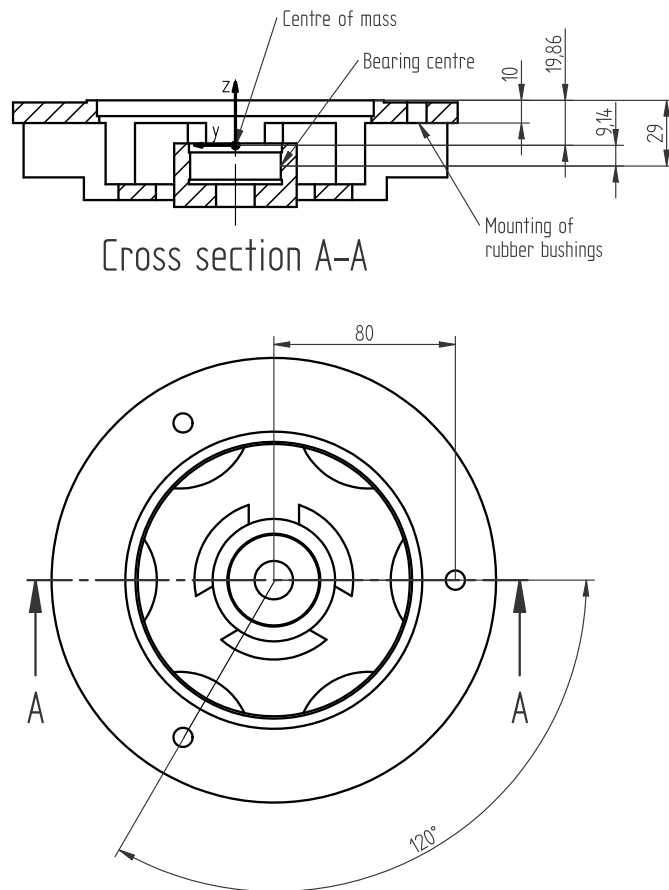


Figure B.3.: Properties of the base of the motor unit.

B. Test rig details

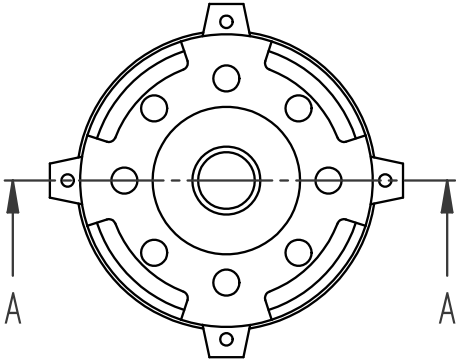
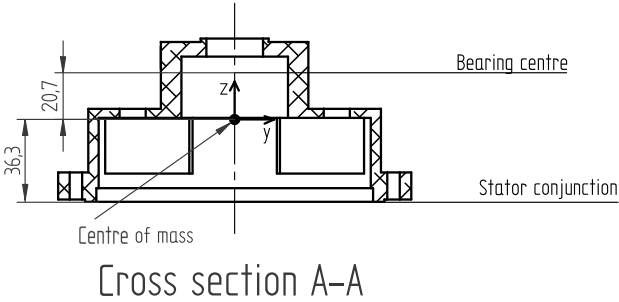


Figure B.4.: Properties of the lid of the motor unit.

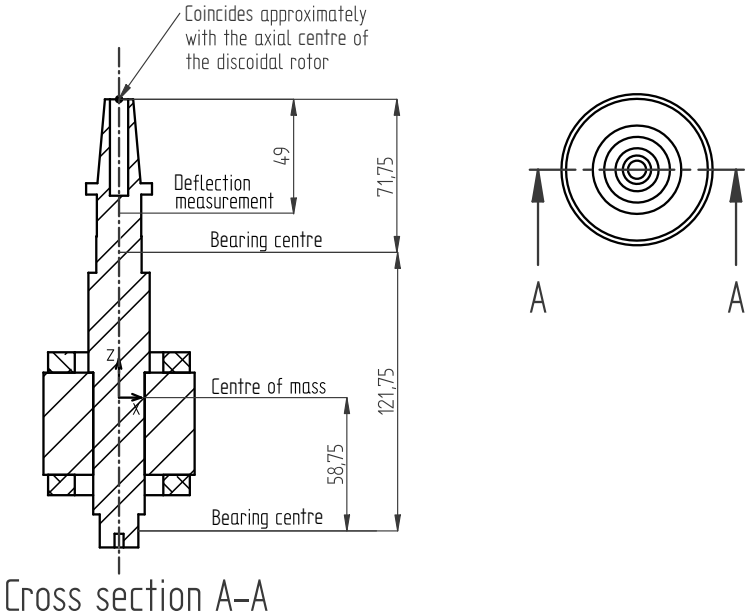


Figure B.5.: Properties of the shaft of the motor unit.

B.2. CFRP rotor

Table B.2.: Inertial properties of the CFRP rotor assembly.

Part	Mass [kg]	Moments of inertia [g m ²]	
		$J_{xx} = J_{yy}$	J_{zz}
CFRP rotor assembly	6.775	46.95	84.19

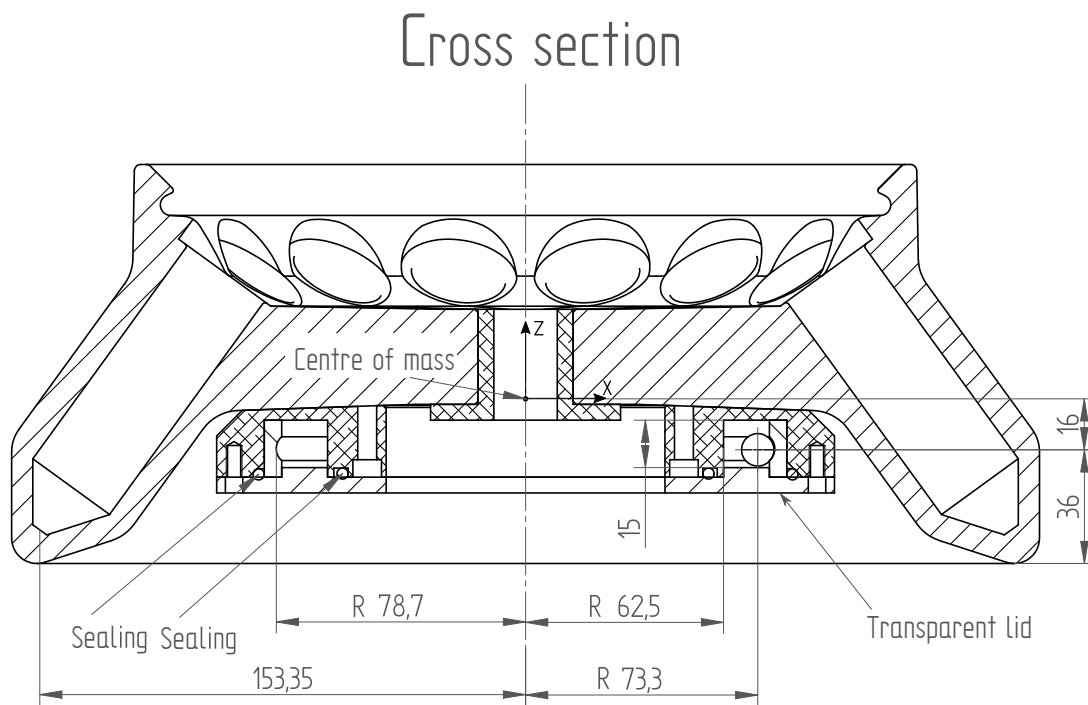


Figure B.6.: Important geometrical properties of the CFRP rotor with attached ball balancer. With courtesy of carbonic GmbH.

B. Test rig details

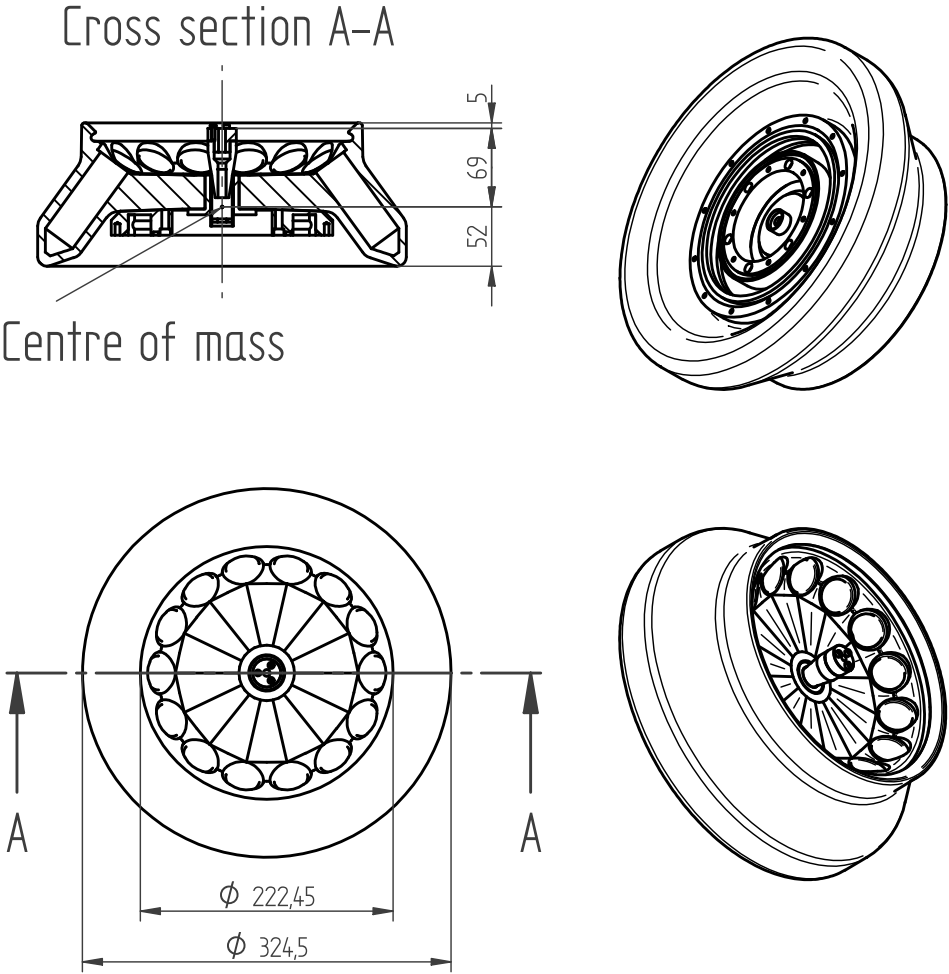


Figure B.7.: Terminal dimensions of the CFRP rotor with attached ball balancer and test-rig clutch. With courtesy of carbonic GmbH.

C. Useful dimensions of ball bearings for automatic balancing

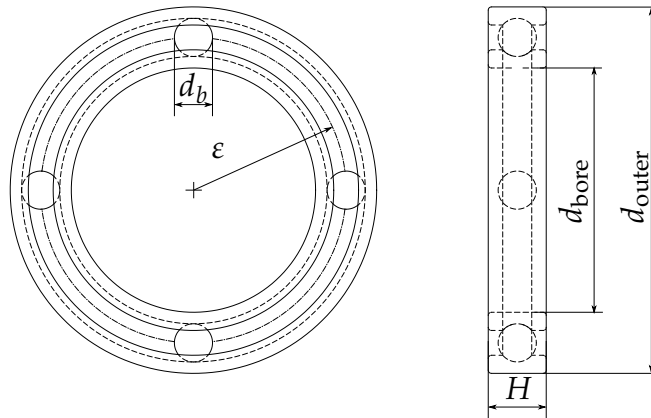


Table C.1.: Dimensions of deep groove ball bearings for automatic balancing. Data was taken from the SKF website [SKF18].

d_{bore} [mm]	d_{outer} [mm]	H [mm]	Designation	ϵ [mm]	d_b [mm]	Max. compensation [†] [g mm]
3	10	4	623	3.175	1.588	2.09×10^{-1}
4	9	2.5	618/4	3.175	1.588	2.09×10^{-1}
4	11	4	619/4	3.733	1.984	4.40×10^{-1}
4	12	4	604	3.755	2	4.53×10^{-1}
4	13	5	624	4.375	2.381	8.76×10^{-1}
4	16	5	634	5.1	2.381	1.20
5	11	3	618/5	4	1.588	3.27×10^{-1}
5	13	4	619/5	4.608	1.984	6.87×10^{-1}
5	16	5	625	5.1	2.381	1.20
5	19	6	635	6.5	3	3.08
6	13	3.5	618/6	4.76	1.984	7.30×10^{-1}
6	15	5	619/6	5.25	2.381	1.26
6	19	6	626	6.5	3	3.08
7	14	3.5	618/7	5.255	1.984	8.93×10^{-1}
7	17	5	619/7	6.01	2.778	2.26
7	19	6	607	6.5	3	3.08
7	22	7	627	7.35	3.969	6.86

C. Useful dimensions of ball bearings for automatic balancing

Continuation

d_{bore} [mm]	d_{outer} [mm]	H [mm]	Designation	ε [mm]	d_b [mm]	Max. compensation [†] [g mm]
8	16	4	618/8	6	2.381	1.65
8	19	6	619/8	6.53	3.175	3.52
8	22	7	608	7.35	3.969	6.86
8	24	8	628	8.5	3.969	9.25
9	17	4	618/9	6.5	2.381	1.96
9	20	6	619/9	7.25	3.175	4.36
9	24	7	609	8.5	3.969	9.25
9	26	8	629	8.9	4.762	1.44 × 10 ¹
10	19	5	61800	7.25	2.381	2.44
10	22	6	61900	7.775	3.175	4.97
10	26	8	6000	8.9	4.762	1.44 × 10 ¹
10	28	8	16100	10	4.762	1.85 × 10 ¹
10	30	9	6200	10	4.762	1.85 × 10 ¹
10	35	11	6300	11.1	7.144	5.00 × 10 ¹
12	21	5	61801	8.25	2.381	3.15
12	24	6	61901	9	3.175	6.64
12	28	8	6001	10	4.762	1.85 × 10 ¹
12	30	8	16101	10	4.762	1.85 × 10 ¹
12	32	10	6201	11	6	3.52 × 10 ¹
12	37	12	6301	12.25	7.938	7.54 × 10 ¹
15	24	5	61802	9.75	2.381	4.41
15	28	7	61902	10.75	3.969	1.49 × 10 ¹
15	32	8	16002	11.75	4.762	2.55 × 10 ¹
15	32	9	6002	11.75	4.762	2.55 × 10 ¹
15	35	11	6202	12.63	6	4.69 × 10 ¹
15	42	13	6302	14.35	7.938	1.05 × 10 ²
17	26	5	61803	10.75	2.381	5.39
17	30	7	61903	11.75	3.969	1.79 × 10 ¹
17	35	8	16003	13	4.762	3.14 × 10 ¹
17	35	10	6003	13	4.762	3.14 × 10 ¹
17	40	12	6203	14.25	6.747	7.54 × 10 ¹
17	40	12	6203 ETN9	14.35	8	1.07 × 10 ²
17	47	14	6303	16	8.731	1.58 × 10 ²
17	62	17	6403	19.75	12.7	5.00 × 10 ²
20	32	7	61804	13	3.5	1.70 × 10 ¹
20	37	9	61904	14.25	4.762	3.78 × 10 ¹
20	42	8	16004	15.4	5	4.85 × 10 ¹
20	42	12	6004	15.5	6.35	7.91 × 10 ¹
20	47	14	6204	16.75	7.938	1.44 × 10 ²
20	47	14	6204 ETN9	16.95	9.525	2.12 × 10 ²
20	52	15	6304	18	9.525	2.35 × 10 ²
20	52	15	6304 ETN9	18.2	10.319	2.88 × 10 ²
20	72	19	6404	23	15.081	9.63 × 10 ²
22	50	14	62/22	18.5	7.938	1.77 × 10 ²
22	56	16	63/22	19.5	10.319	3.24 × 10 ²
25	37	7	61805	15.4	3.5	2.38 × 10 ¹
25	42	9	61905	16.75	4.762	5.24 × 10 ¹

Continuation

d_{bore} [mm]	d_{outer} [mm]	H [mm]	Designation	ϵ [mm]	d_b [mm]	Max. compensation [†] [g mm]
25	47	8	16005	18.45	5	6.98×10^1
25	47	12	6005	18	6.747	1.21×10^2
25	52	15	6205	19.52	7.938	1.96×10^2
25	52	15	6205 ETN9	19.4	9.525	2.80×10^2
25	62	17	6305	21.75	11.5	5.01×10^2
25	62	17	6305 ETN9	22	12.7	6.39×10^2
25	80	21	6405	27.083	15.081	1.36×10^3
28	58	16	62/28	21.5	8.731	2.87×10^2
28	68	18	63/28	24.3	11.5	6.37×10^2
30	42	7	61806	18	3.5	3.27×10^1
30	47	9	61906	19.25	4.762	6.89×10^1
30	55	9	16006	21.25	6.35	1.49×10^2
30	55	13	6006	21.25	7.144	1.89×10^2
30	62	16	6206	23	9.525	3.93×10^2
30	62	16	6206 ETN9	23.1	11.112	5.39×10^2
30	72	19	6306	26	12.303	8.34×10^2
30	72	19	6306 ETN9	25.5	14.2	1.07×10^3
30	90	23	6406	30	16.669	2.03×10^3
35	47	7	61807	20.5	3.5	4.23×10^1
35	55	10	61907	22.5	5.556	1.28×10^2
35	62	9	16007	24.25	6.35	1.94×10^2
35	62	14	6007	24.25	7.938	3.04×10^2
35	72	17	6207	26.75	11.112	7.23×10^2
35	72	17	6207 ETN9	26.95	13	1.00×10^3
35	80	21	6307	28.75	13.494	1.22×10^3
35	100	25	6407	34.247	19.05	3.46×10^3
40	52	7	61808	23	3.5	5.33×10^1
40	62	12	61908	25.5	6.747	2.42×10^2
40	68	9	16008	27	6.35	2.42×10^2
40	68	15	6008	27	7.938	3.76×10^2
40	80	18	6208	30	12.303	1.11×10^3
40	80	18	6208 ETN9	30.2	14	1.45×10^3
40	90	23	6308	32.5	15.081	1.95×10^3
40	110	27	6408	37.5	20.638	4.85×10^3
45	58	7	61809	25.75	3.969	8.59×10^1
45	68	12	61909	28.25	6.747	2.99×10^2
45	75	10	16009	30	7.144	3.78×10^2
45	75	16	6009	30	8.731	5.61×10^2
45	85	19	6209	32.5	12.303	1.31×10^3
45	100	25	6309	36.25	17.462	3.28×10^3
45	120	29	6409	41.25	23.019	7.33×10^3
50	65	7	61810	28.75	3.969	1.07×10^2
50	72	12	61910	30.5	6.747	3.48×10^2
50	80	10	16010	32.5	7.144	4.43×10^2
50	80	16	6010	32.5	8.731	6.60×10^2
50	90	20	6210	35	12.7	1.62×10^3
50	110	27	6310	40	19.05	4.74×10^3

C. Useful dimensions of ball bearings for automatic balancing

Continuation

d_{bore} [mm]	d_{outer} [mm]	H [mm]	Designation	ε [mm]	d_b [mm]	Max. compensation [†] [g mm]
50	130	31	6410	45	24.606	9.92×10^3
55	72	9	61811	31.75	4.762	1.88×10^2
55	80	13	61911	33.75	7.144	4.77×10^2
55	90	11	16011	36.25	7.938	6.81×10^2
55	90	18	6011	36.25	10.319	1.14×10^3
55	100	21	6211	38.75	14.288	2.51×10^3
55	120	29	6311	43.75	20.638	6.64×10^3
55	140	33	6411	48.75	26.988	1.40×10^4
60	78	10	61812	34.5	5.556	3.02×10^2
60	85	13	61912	36.25	7.144	5.50×10^2
60	95	11	16012	38.75	7.938	7.78×10^2
60	95	18	6012	38.75	10.319	1.31×10^3
60	110	22	6212	42.5	15.875	3.74×10^3
60	130	31	6312	47.5	22.225	9.06×10^3
60	150	35	6412	52.5	28.575	1.82×10^4
65	85	10	61813	37.5	5.556	3.57×10^2
65	90	13	61913	38.75	7.144	6.31×10^2
65	100	11	16013	41.25	7.938	8.82×10^2
65	100	18	6013	41.25	10.319	1.49×10^3
65	120	23	6213	46.4	15.875	4.46×10^3
65	140	33	6313	51.25	23.812	1.21×10^4
65	160	37	6413	56.25	30.162	2.32×10^4
70	90	10	61814	40	5.556	4.06×10^2
70	100	16	61914	42.5	8.731	1.13×10^3
70	110	13	16014	45	9.525	1.51×10^3
70	110	20	6014	45	11.906	2.35×10^3
70	125	24	6214	48.75	16.669	5.43×10^3
70	150	35	6314	55	25.4	1.58×10^4
70	180	42	6414	62.5	34.925	3.87×10^4
75	95	10	61815	42.5	5.556	4.59×10^2
75	105	16	61915	45	8.731	1.27×10^3
75	115	13	16015	47.5	9.525	1.68×10^3
75	115	20	6015	47.5	11.906	2.63×10^3
75	130	25	6215	51.25	17.462	6.59×10^3
75	160	37	6315	58.75	26.988	2.04×10^4
75	190	45	6415	66.25	36.512	4.74×10^4
80	100	10	61816	45	5.556	5.14×10^2
80	110	16	61916	47.5	8.731	1.42×10^3
80	125	14	16016	51.25	10.319	2.30×10^3
80	125	22	6016	51.25	13.494	3.91×10^3
80	140	26	6216	55.85	17.462	7.83×10^3
80	170	39	6316	62.5	28.575	2.58×10^4
80	200	48	6416	70	38.1	5.75×10^4
85	110	13	61817	48.75	7.144	9.98×10^2
85	120	18	61917	51.25	10.319	2.30×10^3
85	130	14	16017	53.75	10.319	2.53×10^3
85	130	22	6017	53.75	13.494	4.32×10^3

Continuation

d_{bore} [mm]	d_{outer} [mm]	H [mm]	Designation	ϵ [mm]	d_b [mm]	Max. compensation [†] [g mm]
85	150	28	6217	59	19.844	1.13×10^4
85	180	41	6317	66.25	30.162	3.23×10^4
85	210	52	6417	73.75	39.688	6.90×10^4
90	115	13	61818	51.25	7.144	1.10×10^3
90	125	18	61918	53.75	10.319	2.53×10^3
90	140	16	16018	57.5	11.906	3.86×10^3
90	140	24	6018	57.5	15.081	6.14×10^3
90	160	30	6218	62.65	21.431	1.48×10^4
90	190	43	6318	70	31.75	3.99×10^4
90	225	54	6418	78.75	41.275	8.44×10^4
95	120	13	61819	53.75	7.144	1.21×10^3
95	130	18	61919	56.25	10.319	2.77×10^3
95	145	16	16019	60	11.906	4.19×10^3
95	145	24	6019	60	15.081	6.73×10^3
95	170	32	6219	66.25	23.812	2.03×10^4
95	200	45	6319	73.75	33.338	4.87×10^4
100	125	13	61820	56.25	7.144	1.33×10^3
100	140	20	61920	60	11.906	4.19×10^3
100	150	16	16020	62.5	11.906	4.55×10^3
100	150	24	6020	62.5	15.081	7.26×10^3
100	180	34	6220	70	25.4	2.59×10^4
100	215	47	6320	78.75	36.512	6.71×10^4
105	130	13	61821	58.75	7.144	1.45×10^3
105	145	20	61921	62.5	11.906	4.55×10^3
105	160	18	16021	66.25	13.494	6.57×10^3
105	160	26	6021	66.25	16.669	1.00×10^4
105	190	36	6221	73.75	26.988	3.24×10^4
105	225	49	6321	82.5	38.1	8.01×10^4
110	140	16	61822	62.5	8.731	2.45×10^3
110	150	20	61922	65	11.906	4.93×10^3
110	170	19	16022	70	14.288	8.23×10^3
110	170	28	6022	70	18.256	1.34×10^4
110	200	38	6222	77.5	28.575	4.02×10^4
110	240	50	6322	87.5	41.275	1.06×10^5
120	150	16	61824	67.5	8.731	2.86×10^3
120	165	22	61924	71.25	13.494	7.60×10^3
120	180	19	16024	75	14.288	9.44×10^3
120	180	28	6024	75	18.256	1.53×10^4
120	215	40	6224	83.75	30.162	5.21×10^4
120	260	55	6324	95	41.275	1.26×10^5
130	165	18	61826	73.75	10.319	4.76×10^3
130	180	24	61926	77.5	15.081	1.12×10^4
130	200	22	16026	82.5	16.669	1.55×10^4
130	200	33	6026	82.5	20.638	2.38×10^4
130	230	40	6226	90	31.75	6.64×10^4
130	280	58	6326 M	102.5	44.45	1.71×10^5
140	175	18	61828	78.75	10.319	5.42×10^3

C. Useful dimensions of ball bearings for automatic balancing

Continuation

d_{bore} [mm]	d_{outer} [mm]	H [mm]	Designation	ε [mm]	d_b [mm]	Max. compensation [†] [g mm]
140	190	24	61928 MA	82.5	15.081	1.27×10^4
140	210	22	16028	87.5	16.669	1.75×10^4
140	210	33	6028	87.5	20.638	2.68×10^4
140	250	42	6228	97.5	31.75	7.85×10^4
140	300	62	6328 M	110	47.625	2.26×10^5
150	190	20	61830	85	11.906	8.43×10^3
150	210	28	61930 MA	90	18.256	2.22×10^4
150	225	24	16030	93.75	18.256	2.41×10^4
150	225	35	6030	93.75	22.225	3.57×10^4
150	270	45	6230	105	31.75	9.13×10^4
150	320	65	6330 M	117.5	47.625	2.55×10^5
160	200	20	61832	90	11.906	9.44×10^3
160	220	28	61932 MA	95	18.256	2.47×10^4
160	240	25	16032	100	19.05	2.98×10^4
160	240	38	6032	100	23.812	4.67×10^4
160	290	48	6232	112.5	31.75	1.05×10^5
160	340	68	6332 M	125	50.8	3.29×10^5
170	215	22	61834	96.25	13.494	1.39×10^4
170	230	28	61934 MA	100	18.256	2.74×10^4
170	260	28	16034	107.5	21.431	4.36×10^4
170	260	42	6034 M	107.5	26.988	6.91×10^4
170	310	52	6234 M	120	34.925	1.44×10^5
170	360	72	6334 M	132.5	55.562	4.44×10^5
180	225	22	61836	101.25	13.494	1.54×10^4
180	250	33	61936 MA	107.5	20.638	4.05×10^4
180	280	31	16036	115	23.812	6.17×10^4
180	280	46	6036 M	115	30.162	9.83×10^4
180	320	52	6236 M	125	38.1	1.87×10^5
180	380	75	6336 M	140	57.15	5.22×10^5
190	240	24	61838	107.5	15.081	2.16×10^4
190	260	33	61938 MA	112.5	20.638	4.44×10^4
190	290	31	16038	120	23.812	6.70×10^4
190	290	46	6038 M	120	30.162	1.08×10^5
190	340	55	6238 M	132.5	41.275	2.46×10^5
190	400	78	6338 M	147.5	58.738	6.09×10^5
200	250	24	61840	112.5	15.081	2.37×10^4
200	280	38	61940 MA	120	23.812	6.70×10^4
200	310	34	16040	127.5	26.194	9.18×10^4
200	310	51	6040 M	127.5	33.338	1.47×10^5
200	360	58	6240 M	140	41.275	2.74×10^5
220	270	24	61844	122.5	15.081	2.81×10^4
220	300	38	61944 MA	130	23.812	7.89×10^4
220	340	37	16044	140	26.988	1.17×10^5
220	340	56	6044 M	140	36.512	2.15×10^5
220	400	65	6244 M	155	44.45	3.87×10^5
240	300	28	61848	135	18.256	5.00×10^4
240	320	38	61948 MA	140	23.812	9.14×10^4

Continuation

d_{bore} [mm]	d_{outer} [mm]	H [mm]	Designation	ϵ [mm]	d_b [mm]	Max. compensation [†] [g mm]
240	360	37	16048 MA	150	28.575	1.51×10^5
240	360	56	6048 M	150	36.512	2.45×10^5
240	500	95	6348 M	185	63.5	1.14×10^6
260	320	28	61852	145	18.256	5.76×10^4
260	360	46	61952 MA	155	30.162	1.80×10^5
260	400	44	16052 MA	165	33.338	2.49×10^5
260	400	65	6052 M	165	41.275	3.81×10^5
280	350	33	61856	157.5	20.638	8.68×10^4
280	380	46	61956 MA	165	30.162	2.04×10^5
280	420	44	16056 MA	175	33.338	2.80×10^5
280	420	65	6056 M	175	41.275	4.29×10^5
300	380	38	61860 MA	170	23.812	1.35×10^5
300	420	56	61960 MA	180	36.512	3.55×10^5
300	540	85	6260 M	210	60.325	1.31×10^6
320	400	38	61864 MA	180	23.812	1.51×10^5
320	480	50	16064 MA	200	38.1	4.77×10^5
320	480	74	6064 M	200	47.625	7.47×10^5
340	420	38	61868 MA	190	23.812	1.68×10^5
340	520	57	16068 MA	215	44.45	7.52×10^5
340	520	82	6068 M	215	53.975	1.11×10^6
360	440	38	61872 MA	200	23.812	1.87×10^5
360	480	56	61972 MA	210	36.512	4.84×10^5
360	540	57	16072 MA	225	44.45	8.20×10^5
360	540	82	6072 M	225	53.975	1.21×10^6
380	480	46	61876 MA	215	30.162	3.46×10^5
380	520	65	61976 MA	225	41.275	7.10×10^5
380	560	57	16076 MA	235	44.45	8.97×10^5
380	560	82	6076 M	235	53.975	1.32×10^6
400	500	46	61880 MA	225	30.162	3.79×10^5
400	540	65	61980 MA	235	41.275	7.72×10^5
400	600	90	6080 M	250	60.325	1.86×10^6
420	520	46	61884 MA	235	30.162	4.13×10^5
420	560	65	61984 MA	245	41.275	8.40×10^5
420	620	90	6084 M	260	60.325	2.02×10^6
440	540	46	61888 MA	245	30.162	4.49×10^5
440	600	74	61988 MA	260	47.625	1.26×10^6
440	650	94	6088 M	272.5	63.5	2.46×10^6
460	580	56	61892 MA	260	36.512	7.41×10^5
460	620	74	61992 MA	270	47.625	1.36×10^6
460	680	100	6092 MB	285	60.325	2.42×10^6
480	600	56	61896 MA	270	36.512	8.00×10^5
480	650	78	61996 MA	282.5	50.8	1.69×10^6
480	700	100	6096 MB	295	60.325	2.60×10^6
500	620	56	618/500 MA	280	36.512	8.60×10^5
500	670	78	619/500 MA	292.5	50.8	1.82×10^6
500	720	100	60/500 NiMAS	305	66.675	3.40×10^6
530	650	56	618/530 MA	295	36.512	9.55×10^5

C. Useful dimensions of ball bearings for automatic balancing

Continuation

d_{bore} [mm]	d_{outer} [mm]	H [mm]	Designation	ϵ [mm]	d_b [mm]	Max. compensation [†] [g mm]
530	710	82	619/530 MA	310	53.975	2.30×10^6
530	780	112	60/530 NiMAS	327.5	69.85	4.29×10^6
560	680	56	618/560 MA	310	36.512	1.05×10^6
560	750	85	619/560 MA	327.5	53.975	2.57×10^6
560	820	115	60/560 NiMAS	345	69.85	4.77×10^6
600	730	60	618/600 MA	332.5	38.1	1.32×10^6
600	800	90	619/600 MA	350	60.325	3.67×10^6
630	780	69	618/630 MA	352.5	44.45	2.02×10^6
630	850	100	619/630 NiMA	370	63.5	4.54×10^6
630	920	128	60/630 NiMBS	387.5	82.55	8.40×10^6
670	820	69	618/670 MA	372.5	44.45	2.26×10^6
670	900	103	619/670 MA	392.5	66.675	5.63×10^6
670	980	136	60/670 NiMAS	412.5	88.9	1.10×10^7
710	870	74	618/710 MA	395	47.625	2.91×10^6
710	950	106	619/710 MA	415	66.675	6.30×10^6
710	1030	140	60/710 MA	435	95.25	1.41×10^7
750	920	78	618/750 MA	417.5	50.8	3.70×10^6
750	1000	112	619/750 MA	437.5	73.025	8.38×10^6
800	980	82	618/800 MA	445	53.975	4.74×10^6
800	1060	115	619/800 MA	465	76.2	1.03×10^7
800	1150	155	60/800 NiMAS	487.5	95.25	1.77×10^7
850	1030	82	618/850 MA	470	53.975	5.30×10^6
850	1120	118	619/850 MA	492.5	76.2	1.16×10^7
1000	1220	100	618/1000 MA	555	57.15	8.28×10^6
1060	1280	100	618/1060 MA	585	63.5	1.13×10^7
1120	1360	106	618/1120 MA	620	63.5	1.27×10^7
1180	1420	106	618/1180 MB	650	63.5	1.40×10^7

[†] Under the assumption that $\rho_b = 7860 \text{ kg m}^{-3}$ and $\rho_{\text{fl}} = 0 \text{ kg m}^{-3}$

Table C.2.: Dimensions of thin section bearings for automatic balancing. Data was taken from the Schaeffler catalogue 575[Sch14].

d_{bore} [mm]	d_{outer} [mm]	H [mm]	Designation	ϵ [mm]	d_b [mm]	Max. compensation [†] [g mm]
25.4	34.925	4.763	CSCAA 010 TN	15.081	2.381	1.06×10^1
38.1	47.625	4.763	CSCAA 015 TN	21.431	2.381	2.14×10^1
44.45	53.975	4.763	CSCAA 017 TN	24.606	2.381	2.82×10^1
50.8	63.5	6.35	CSCA 020	28.575	3.175	6.77×10^1
50.8	66.676	7.938	CSCB 020	29.369	3.969	1.12×10^2
63.5	76.2	6.35	CSCA 025	34.925	3.175	1.01×10^2
63.5	79.376	7.938	CSCB 025	35.719	3.969	1.65×10^2
76.2	88.9	6.35	CSCA 030	41.275	3.175	1.41×10^2
76.2	92.076	7.938	CSCB 030	42.069	3.969	2.29×10^2
88.9	101.6	6.35	CSCA 035	47.625	3.175	1.88×10^2

Continuation

d_{bore} [mm]	d_{outer} [mm]	H [mm]	Designation	ε [mm]	d_b [mm]	Max. compensation [†] [g mm]
88.9	104.776	7.938	CSCB 035	48.419	3.969	3.04×10^2
101.6	114.3	6.35	CSCA 040	53.975	3.175	2.42×10^2
101.6	117.476	7.938	CSCB 040	54.769	3.969	3.89×10^2
101.6	120.65	9.525	CSCC 040	56.356	4.763	5.93×10^2
101.6	127	12.7	CSCD 040	57.15	6.35	1.08×10^3
107.95	120.65	6.35	CSCA 042	57.15	3.175	2.71×10^2
107.95	123.826	7.938	CSCB 042	57.944	3.969	4.35×10^2
107.95	127	9.525	CSCC 042	59.531	4.763	6.62×10^2
114.3	127	6.35	CSCA 045	60.325	3.175	3.02×10^2
114.3	130.176	7.938	CSCB 045	61.119	3.969	4.84×10^2
114.3	133.35	9.525	CSCC 045	62.706	4.763	7.34×10^2
114.3	139.7	12.7	CSCD 045	63.5	6.35	1.34×10^3
120.65	133.35	6.35	CSCA 047	63.5	3.175	3.34×10^2
120.65	139.7	9.525	CSCC 047	65.881	4.763	8.10×10^2
127	139.7	6.35	CSCA 050	66.675	3.175	3.69×10^2
127	142.876	7.938	CSCB 050	67.469	3.969	5.90×10^2
127	146.05	9.525	CSCC 050	69.056	4.763	8.90×10^2
127	152.4	12.7	CSCD 050	69.85	6.35	1.62×10^3
127	165.1	19.05	CSCF 050	73.025	9.525	3.98×10^3
139.7	152.4	6.35	CSCA 055	73.025	3.175	4.42×10^2
139.7	158.75	9.525	CSCC 055	75.406	4.763	1.06×10^3
139.7	165.1	12.7	CSCD 055	76.2	6.35	1.93×10^3
139.7	177.8	19.05	CSCF 055	79.375	9.525	4.70×10^3
139.7	190.5	25.4	CSCG 055	82.55	12.7	9.04×10^3
152.4	165.1	6.35	CSCA 060	79.375	3.175	5.23×10^2
152.4	168.276	7.938	CSCB 060	80.169	3.969	8.33×10^2
152.4	171.45	9.525	CSCC 060	81.756	4.763	1.25×10^3
152.4	177.8	12.7	CSCD 060	82.55	6.35	2.26×10^3
152.4	190.5	19.05	CSCF 060	85.725	9.525	5.49×10^3
165.1	177.8	6.35	CSCA 065	85.725	3.175	6.10×10^2
165.1	180.976	7.938	CSCB 065	86.519	3.969	9.70×10^2
165.1	184.15	9.525	CSCC 065	88.106	4.763	1.45×10^3
165.1	190.5	12.7	CSCD 065	88.9	6.35	2.62×10^3
165.1	203.2	19.05	CSCF 065	92.075	9.525	6.33×10^3
165.1	215.9	25.4	CSCG 065	95.25	12.7	1.20×10^4
177.8	190.5	6.35	CSCA 070	92.075	3.175	7.03×10^2
177.8	193.676	7.938	CSCB 070	92.869	3.969	1.12×10^3
177.8	196.85	9.525	CSCC 070	94.456	4.763	1.67×10^3
177.8	203.2	12.7	CSCD 070	95.25	6.35	3.01×10^3
177.8	215.9	19.05	CSCF 070	98.425	9.525	7.23×10^3
177.8	228.6	25.4	CSCG 070	101.6	12.7	1.37×10^4
190.5	203.2	6.35	CSCA 075	98.425	3.175	8.04×10^2
190.5	209.55	9.525	CSCC 075	100.806	4.763	1.90×10^3
190.5	228.6	19.05	CSCF 075	104.775	9.525	8.19×10^3
190.5	241.3	25.4	CSCG 075	107.95	12.7	1.55×10^4
203.2	215.9	6.35	CSCA 080	104.775	3.175	9.11×10^2
203.2	219.076	7.938	CSCB 080	105.569	3.969	1.44×10^3

C. Useful dimensions of ball bearings for automatic balancing

Continuation

d_{bore} [mm]	d_{outer} [mm]	H [mm]	Designation	ϵ [mm]	d_b [mm]	Max. compensation [†] [g mm]
203.2	222.25	9.525	CSCC 080	107.156	4.763	2.14×10^3
203.2	228.6	12.7	CSCD 080	107.95	6.35	3.87×10^3
203.2	241.3	19.05	CSCF 080	111.125	9.525	9.22×10^3
203.2	254	25.4	CSCG 080	114.3	12.7	1.73×10^4
228.6	241.3	6.35	CSCA 090	117.475	3.175	1.14×10^3
228.6	254	12.7	CSCD 090	120.65	6.35	4.83×10^3
228.6	266.7	19.05	CSCF 090	123.825	9.525	1.14×10^4
228.6	279.4	25.4	CSCG 090	127	12.7	2.14×10^4
254	266.7	6.35	CSCA 100	130.175	3.175	1.41×10^3
254	273.05	9.525	CSCC 100	132.556	4.763	3.28×10^3
254	279.4	12.7	CSCD 100	133.35	6.35	5.90×10^3
254	292.1	19.05	CSCF 100	136.525	9.525	1.39×10^4
254	304.8	25.4	CSCG 100	139.7	12.7	2.59×10^4
279.4	298.45	9.525	CSCC 110	145.256	4.763	3.94×10^3
279.4	304.8	12.7	CSCD 110	146.05	6.35	7.08×10^3
279.4	317.5	19.05	CSCF 110	149.225	9.525	1.66×10^4
304.8	317.5	6.35	CSCA 120	155.575	3.175	2.01×10^3
304.8	323.85	9.525	CSCC 120	157.956	4.763	4.66×10^3
304.8	330.2	12.7	CSCD 120	158.75	6.35	8.36×10^3
304.8	342.9	19.05	CSCF 120	161.925	9.525	1.96×10^4
304.8	355.6	25.4	CSCG 120	165.1	12.7	3.62×10^4
355.6	381	12.7	CSCD 140	184.15	6.35	1.13×10^4
355.6	393.7	19.05	CSCF 140	187.325	9.525	2.62×10^4
355.6	406.4	25.4	CSCG 140	190.5	12.7	4.82×10^4
365	415.8	25.4	CSCG 250	195.2	12.7	5.06×10^4
406.4	431.8	12.7	CSCD 160	209.55	6.35	1.46×10^4
406.4	444.5	19.05	CSCF 160	212.725	9.525	3.38×10^4
406.4	457.2	25.4	CSCG 160	215.9	12.7	6.19×10^4
457.2	508	25.4	CSCG 180	241.3	12.7	7.73×10^4
508	558.8	25.4	CSCG 200	266.7	12.7	9.44×10^4

[†] Under the assumption that $\rho_b = 7860 \text{ kg m}^{-3}$ and $\rho_{\text{fl}} = 0 \text{ kg m}^{-3}$

References

- [AB85] Y. V. Agafonov and Y. V. Bazykin. ‘Study Of Stability of ball-type automatic Balancer of rotor system on anisotropic flexible supports’. In: *Soviet machine science* 1.5 (1985). Translated from *Mashinovedenie*, No. 5, 1985, pp. 110–112.
- [AB86] Y. V. Agafonov and Y. V. Bazykin. ‘An Investigation into the influence of eccentricity of the running track of an automatic ball balancer on the balancing quality’. In: *Soviet engineering research: combined selective translation* 6.8 (1986). Translated from *Vestnik Mashinostroeniya*, pp. 22–24. ISSN: 0144-6622.
- [Ach90] D. J. Acheson. *Elementary Fluid Dynamics*. Oxford University Press, 1990. 406 pp. ISBN: 0198596790.
- [Ado97] J. Adolfsson. *A Study of Stability in AutoBalancing Systems using multiple Correction Masses*. Tech. rep. 3. ISSN: 0348-467X. Royal Institute of Technology in Stockholm, 1997. URL: https://www.mech.kth.se/thesis/1997/lic/lic_1997_jesper_adolfsson.pdf.
- [Aga76] Y. V. Agafonov. ‘Automatic balancing device for hand grinders’. In: *Russian Engineering Journal* 56.9 (1976). Translated from *Vestnik Mashinostroeniya*, pp. 31–33. ISSN: 0042-4633.
- [BH86] P. Bövik and C. Högfors. ‘Autobalancing of rotors’. In: *Journal of Sound and Vibration* 111.3 (1986), pp. 429–440. ISSN: 0022-460X. DOI: 10.1016/S0022-460X(86)81402-X.
- [BK14] V. G. Bykov and A. S. Kovachev. ‘Dynamics of a rotor with an eccentric ball auto-balancing device’. In: *Vestnik St. Petersburg University: Mathematics* 47.4 (Oct. 2014), pp. 173–180. ISSN: 1934-7855. DOI: 10.3103/S1063454114040037.

References

- [BK15] V. G. Bykov and A. S. Kovachev. 'On stability of unbalanced steady-state motions of a rotor with eccentric ball autobalancing device'. In: *International Conference on Mechanics - Seventh Polyakhov's Reading*. Feb. 2015, pp. 1–4. DOI: 10/gmnqd2.
- [BK18] V. G. Bykov and A. S. Kovachev. 'Autobalancing of a rigid rotor in viscoelastic orthotropic supports considering eccentricity of the automatic ball balancer'. In: *AIP Conference Proceedings* 1959.1 (2018), p. 080011. DOI: 10.1063/1.5034728.
- [BK19a] A. S. Baumgarten and K. Kamrin. 'A general constitutive model for dense, fine-particle suspensions validated in many geometries'. In: *Proceedings of the National Academy of Sciences* 116.42 (Sept. 2019), pp. 20828–20836. DOI: 10.1073/pnas.1908065116.
- [BK19b] V. G. Bykov and A. S. Kovachev. 'Dynamics of a statically unbalanced rotor with an elliptic automatic ball balancer'. In: *Vestnik of Saint Petersburg University. Mathematics. Mechanics. Astronomy* 6.64 (2019). In Russian, pp. 452–462. DOI: 10/drzbz.
- [Ble64] I. Blekhman. 'The problem of synchronization of dynamical systems'. In: *Journal of Applied Mathematics and Mechanics* 28.2 (1964), pp. 239–265. DOI: 10.1016/0021-8928(64)90160-1.
- [Bol10] J. N. Bolton. 'Single- and Dual-Plane Automatic Balancing of an Elastically-Mounted Cylindrical Rotor with Considerations of Coulomb Friction and Gravity'. PhD thesis. Virginia Polytechnic Institute and State University, 2010. URL: <http://hdl.handle.net/10919/29946>.
- [Boy01] J. P. Boyd. *Chebyshev and Fourier spectral methods*. 2nd ed. DOVER Publications, 2001. ISBN: 9780486141923. URL: <http://www-personal.umich.edu/~jpboyd/>.
- [BRS12] S. Baz-Rodríguez, J. Ramírez-Muñoz and A. Soria. 'In-line interaction between two spherical particles due to a laminar wake effect'. In: *International Journal of Multiphase Flow* 39 (Mar. 2012), pp. 240–244. DOI: 10.1016/j.ijmultiphaseflow.2011.09.010.

References

- [BW01] C. Bucher and S.-C. Wu. ‘Balancing ring for a ceiling fan’. U.S. pat. 6213717. 2001.
- [CCA16] C. Clerc, A. Carbonelli and R. Augez. ‘An auto-balancer device to control a variable imbalance (application in EU LoWash Project)’. In: *VIRM 11 - vibrations in rotating machinery*. Institution of Mechanical Engineers. Manchester, United Kingdom, Sept. 2016, pp. 759–767.
- [Cen16] C. Cenci. ‘Implementation of a user-defined element simulating deep groove ball bearings in MSC Adams’. PhD thesis. Pisa University, 2016. URL: <https://core.ac.uk/display/79622948>.
- [CFL67] R. Courant, K. Friedrichs and H. Lewy. ‘On the Partial Difference Equations of Mathematical Physics’. In: *IBM Journal of Research and Development* 11.2 (1967), pp. 215–234. ISSN: 0018-8646. DOI: 10.1147/rd.112.0215.
- [Cha93] M. R. Chatelain. ‘Self balancing motor’. U.S. pat. 5256037. 1993.
- [CJ17] Y. Cho and G. Jang. ‘Automatic ball balancer using permanent magnets to reduce transient vibration’. In: *IEEE Transactions on Magnetics* 53.11 (2017), pp. 1–4. ISSN: 0018-9464. DOI: 10/gch4z3.
- [CJK14] J.-S. Cho, H.-Y. Jeong and K.-C. Kong. ‘Analysis of dynamic model of a top-loading laundry machine with a hydraulic balancer’. In: *International Journal of Precision Engineering and Manufacturing* 15.8 (2014), pp. 1615–1623. DOI: 10/gkxsnp.
- [Con94] D. C. Conrad. ‘The fundamentals of automatic washing machine design based upon dynamic constraints’. PhD thesis. USA: Purdue University, 1994. ISBN: 9780591345728. URL: <http://docs.lib.purdue.edu/dissertations/AAI9725673/>.
- [CR99] J. Chung and D. Ro. ‘Dynamic analysis of an automatic dynamic balancer for rotating mechanisms’. In: *Journal of Sound and Vibration* 228.5 (1999), pp. 1035–1056. DOI: 10.1006/jsvi.1999.2456.
- [Cro15] R. Cross. ‘Rolling to a stop down an inclined plane’. In: *European Journal of Physics* 36.6 (2015), p. 065047. DOI: 10/gfv5wn.

References

- [Cro16] R. Cross. ‘Coulomb’s law for rolling friction’. In: *American Journal of Physics* 84.3 (Mar. 2016), pp. 221–230. DOI: 10.1119/1.4938149.
- [CSC12] T.-C. Chan, C.-K. Sung and P. C.-P. Chao. ‘Friction effect on ball positioning of an automatic balancer in optical disk drives’. In: *Microsystem Technologies* 18.9-10 (2012), pp. 1343–1351. DOI: 10.1007/s00542-012-1540-y.
- [CSL05] P. C.-P. Chao, C.-K. Sung and H.-C. Leu. ‘Effects of Rolling Friction of the Balancing Balls on the Automatic Ball Balancer for Optical Disk Drives’. In: *Journal of Tribology* 127.4 (2005), pp. 845–856. DOI: 10.1115/1.2032992.
- [CZW15] H.-W. Chen, Q.-J. Zhang and X.-Q. Wu. ‘Stability and dynamic analyses of a horizontal axis washing machine with a ball balancer’. In: *Mechanism and Machine Theory* 87 (May 2015), pp. 131–149. DOI: 10.1016/j.mechmachtheory.2015.01.001.
- [Dan13] C. Daniel. ‘Simulation von gleit- und wälzgelagerten Systemen auf Basis eines Mehrkörpersystems für rotordynamische Anwendungen’. German. PhD thesis. Otto-von-Guericke-Universität Magdeburg, 2013. DOI: 10.25673/3986.
- [Ded16] G. A. Dedow. ‘The effects of ball interactions on the dynamic behavior of a ball balancer rotating at speeds above the translational resonant frequency of the system.’ MA thesis. University of Louisville, KY, 2016. URL: <http://ir.library.louisville.edu/etd/2447>.
- [Dim+97] M. F. Dimentberg et al. ‘Dynamics of an Unbalanced Shaft Interacting with a Limited Power Supply’. In: *Nonlinear Dynamics* 13.2 (1997), pp. 171–187. DOI: 10.1023/a:1008205012232.
- [Din+13] J. Ding et al. ‘Review on shear thickening fluids and applications’. In: *Textiles and Light Industrial Science and Technology* 2.4 (2013), pp. 161–173. URL: <https://ro.uow.edu.au/aiimpapers/1411/>.
- [Dre12] H. Dresig. *Maschinendynamik*. Ed. by F. Holzweißig. 11th ed. German. Berlin, Heidelberg: Springer, 2012. DOI: 10/gkxspk.

References

- [FA18] H. Funakoshi and Y. Akita. ‘Method for reducing vibration during dehydration, and washing machine using same’. U.S. pat. 0327956. 2018.
- [FBS09] F. Fritz, A. Basler and W. Seemann. ‘Simulation of High-Speed Ball Bearings with MSC/ADAMS’. In: *PAMM* 9.1 (2009), pp. 115–116. DOI: 10.1002/pamm.200910032.
- [Fil+17] G. Filimonikhin et al. ‘Methods of balancing of an axisymmetric flexible rotor by passive auto-balancers’. In: *Eastern-European Journal of Enterprise Technologies* 3.7 (87) (2017), pp. 22–27. DOI: 10.15587/1729-4061.2017.101832.
- [Fil+19] I. Filimonikhina et al. ‘Experimental study of the accuracy of balancing an axial fan by adjusting the masses and by passive auto-balancers’. In: *Eastern-European Journal of Enterprise Technologies* 6.1 (102) (2019), pp. 60–69. DOI: 10.15587/1729-4061.2019.184546.
- [Fil+20] G. Filimonikhin et al. ‘Synthesizing a resonance anti-phase two-mass vibratory machine whose operation is based on the Sommerfeld effect’. In: *Eastern-European Journal of Enterprise Technologies* 6.7 (2020), pp. 42–50. ISSN: 1729-4061. DOI: 10/gkxspm.
- [FP68] L. Fox and I. Parker. *Chebyshev Polynomials in Numerical Analysis*. Ed. by J. Crank and C. C. Ritchie. Oxford Mathematical Handbooks, 1968.
- [Gas06] R. Gasch. *Rotordynamik*. Ed. by R. Nordmann and H. Pfützner. 2nd ed. Berlin, Heidelberg: Springer-Verlag, 2006.
- [Geno5] G. Genta. *Dynamics of Rotating Systems*. Ed. by F. F. Ling. New York, NY: Springer Science+Business Media Inc, 2005. DOI: 10.1007/0-387-28687-X.
- [Gon+17a] V. Goncharov et al. ‘An increase of the balancing capacity of ball or roller-type auto-balancers with reduction of time of achieving auto-balancing’. In: *Eastern-European Journal of Enterprise Technologies* 1.7 (2017), pp. 15–24. ISSN: 1729-3774. DOI: 10/gkxspm.

References

- [Gon+17b] V. Goncharov et al. 'Parameter optimization of the centrifugal juicer with the ball auto-balancer under the impulse change of an unbalance by 3D modeling'. In: *Eastern-European Journal of Enterprise Technologies* 3.7 (87) (2017), pp. 50–58. DOI: 10/gkxspq.
- [Hai18] A. M. Haidar. 'Vibration Control of Shafts via Automatic Passive Balancing with Numerical Analysis and Experimental Verification'. PhD thesis. Pennsylvania, USA: Pennsylvania State University, 2018. URL: <https://etda.libraries.psu.edu/catalog/15708amh5766>.
- [HC99] C.-H. Hwang and J. Chung. 'Dynamic analysis of an automatic ball balancer with double races'. In: *JSME International Journal Series C Mechanical Systems, Machine Elements and Manufacturing* 42.2 (1999), pp. 265–272. DOI: 10.1299/jsmec.42.265.
- [Hen76] C. B. Henderson. 'Drag Coefficients of Spheres in Continuum and Rarefied Flows'. In: *AIAA Journal* 14.6 (1976), pp. 707–708. DOI: 10.2514/3.61409.
- [HFF05] R. Horvath, G. T. Flowers and J. Fausz. 'Influence of Nonidealities on the Performance of a Self-Balancing Rotor System'. In: *ASME 2005 International Mechanical Engineering Congress and Exposition*. American Society of Mechanical Engineers. ASME, Nov. 2005, pp. 233–242. DOI: 10.1115/IMECE2005-82279.
- [HNWo8] E. Hairer, S. P. Nørsett and G. Wanner. *Solving ordinary differential equations I*. Ed. by R. Bank et al. 2nd ed. Springer, 2008. ISBN: 9783642051630. DOI: 10.1007/978-3-540-78862-1.
- [HP16] A. Haidar and J. Palacios. 'Experimental Model Validation of a Passive Balancing Device for Supercritical Helicopter Drive-shafts'. In: *72nd American Helicopter Society International Annual Forum*. Vol. 4. American Helicopter Society. West Palm Beach, Florida, USA, 2016, pp. 3193–3206. ISBN: 9781510825062.
- [Hua+02] W. Huang et al. 'The application of ball-type balancers for radial vibration reduction of high-speed optic disk drives'. In: *Journal of Sound and Vibration* 250 (2002), pp. 415–430. DOI: 10/b4g748.

References

- [IAM67] J. Inoue, Y. Araki and S. Miyaura. ‘On the Self-Synchronization of Mechanical Vibrators : Part II. Rolling Mechanism with a Pair of Self-Synchronizing Vibrators and Automatic Balancer’. In: *Bulletin of JSME* 10.41 (1967), pp. 755–762. DOI: 10/bs6r5k.
- [IIN12] T. Inoue, Y. Ishida and H. Niimi. ‘Vibration Analysis of a Self-Excited Vibration in a Rotor System Caused by a Ball Balancer’. In: *J. Vib. Acoust.* 134.2 (2012), p. 021006. DOI: 10.1115/1.4005141.
- [IMZ12] Y. Ishida, T. Matsuura and X. L. Zhang. ‘Efficiency Improvement of an Automatic Ball Balancer’. In: *Journal of Vibration and Acoustics* 134.2 (2012), p. 021012. DOI: 10.1115/1.4005013.
- [Ish12] Y. Ishida. *Linear and nonlinear rotordynamics a modern treatment with applications*. Ed. by T. Yamamoto. 2nd ed. Wiley-VCH, 2012. ISBN: 9783527651924. DOI: 10.1002/9783527651894.
- [JC97] C.-D. Jan and J.-C. Chen. ‘Movements of a sphere rolling down an inclined plane’. In: *Journal of Hydraulic Research* 35.5 (1997), pp. 689–706. DOI: 10.1080/00221689709498402.
- [JKJ20] M.-G. Jeong, I.-Y. Kwak and H.-Y. Jeong. ‘Development of an active two degree-of-freedom balancer for top loading washing machines’. In: *Journal of Mechanical Science and Technology* 34.7 (July 2020), pp. 2933–2939. DOI: 10.1007/s12206-020-0625-2.
- [Jun20] D. Jung. ‘A Control Strategy of Actively Actuated Eccentric Mass System for Imbalance Rotor Vibration’. In: *Actuators* 9.3 (2020), p. 69. DOI: 10.3390/act9030069.
- [Kan+01] J.-R. Kang et al. ‘The dynamics of a ball-type balancer system equipped with a pair of free-moving balancing masses’. In: *Journal of vibration and acoustics* 123.4 (2001), pp. 456–465. DOI: 10.1115/1.1385203.
- [KBo2] P. KaewTraKulPong and R. Bowden. ‘An Improved Adaptive Background Mixture Model for Real-time Tracking with Shadow Detection’. In: *Video-Based Surveillance Systems*. Springer US, 2002. Chap. 11, pp. 135–144. DOI: 10.1007/978-1-4615-0913-4_11.

References

- [KB47] N. Kryloff and N. Bogoliubov. *Introduction to non-linear mechanics*. Ed. by E. Artin and M. Morse. Annals of Mathematics Studies. English translation. Princeton University Press, 1947.
- [Kel87] W. Kellenberger. *Elastisches Wuchten*. German. Springer-Verlag, 1987. ISBN: 9783642829314. DOI: 10.1007/978-3-642-82930-7.
- [Kie17] T. Kiekbusch. ‘Strategien zur dynamischen Simulation von Wälzlagern’. German. PhD thesis. Technische Universität Kaiserslautern, 2017. ISBN: 9783959740432. URL: <http://d-nb.info/1132259177>.
- [KN13] T. Kim and S. Na. ‘New automatic ball balancer design to reduce transient-response in rotor system’. In: *Mechanical Systems and Signal Processing* 37.1-2 (2013), pp. 265–275. DOI: 10/f43qks.
- [Kov16] A. Kovachev. ‘Dynamics of unbalanced rotors equipped with non-ideal autobalancing devices’. In Russian. PhD thesis. St. Petersburg: St. Petersburg State University, 2016. URL: <https://disser.spbu.ru/dis-list/details/14/824.html>.
- [KSG13] U. Klaeger, U. Schmucker and V. Galazky. ‘Development of a novel technology for rapidly rotating systems for medical technology’. In: *Management and Production Engineering Review* 4.4 (2013), pp. 28–34. DOI: 10.2478/mper-2013-0036.
- [Lin11] V. Lindqvist. ‘Simulation of drag reduction due to multi-aligned spheres’. MA thesis. Oregon State University, 2011. URL: <http://hdl.handle.net/1957/23606>.
- [Lin96] H. Lindell. ‘Vibration reduction on hand-held grinders by automatic balancing’. In: *Central European journal of public health* 4.1 (1996), pp. 43–45.
- [LS98] J. M. Lopez and J. Shen. ‘An Efficient Spectral-Projection Method for the Navier-Stokes Equations in Cylindrical Geometries’. In: *Journal of Computational Physics* 139.2 (1998), pp. 308–326. ISSN: 0021-9991. DOI: 10.1006/jcph.1997.5872.

References

- [LV96] J. Lee and W. Van Moorhem. ‘Analytical and Experimental Analysis of a Self-Compensating Dynamic Balancer in a Rotating Mechanism’. In: *Journal of Dynamic Systems, Measurement, and Control* 118.3 (1996), pp. 468–475. DOI: 10.1115/1.2801169.
- [LW11] C.-J. Lu and M.-C. Wang. ‘Stability analysis of a ball–rod–spring automatic balancer’. In: *International Journal of Mechanical Sciences* 53.10 (2011), pp. 846–854. DOI: 10.1016/j.ijmecsci.2011.07.005.
- [LWH09] C.-J. Lu, M.-C. Wang and S.-H. Huang. ‘Analytical study of the stability of a two-ball automatic balancer’. In: *Mechanical Systems and Signal Processing* 23.3 (Apr. 2009), pp. 884–896. DOI: 10.1016/j.ymsp.2008.06.008.
- [Lyn05] D. R. Lynch. *Numerical Partial Differential Equations for Environmental Scientists and Engineers. A First Practical Course*. Springer Science+Business Media, Inc., 2005. ISBN: 9780387236209.
- [Maj88] T. Majewski. ‘Position error occurrence in self balancers used on rigid rotors of rotating machinery’. In: *Mechanism and Machine Theory* 23.1 (1988), pp. 71–78. DOI: 10.1016/0094-114x(88)90011-0.
- [Mar+16] F. Marques et al. ‘A survey and comparison of several friction force models for dynamic analysis of multibody mechanical systems’. In: *Nonlinear Dynamics* 86.3 (2016), pp. 1407–1443. DOI: 10.1007/s11071-016-2999-3.
- [Mar99] J. Mark. *Polymer Data Handbook*. Ed. by J. Mark. Oxford University Press, 1999. ISBN: 9780195181012.
- [MCV14] Y. Marchesse, C. Changenet and F. Ville. ‘Numerical Investigations on Drag Coefficient of Balls in Rolling Element Bearing’. In: *Tribology Transactions* 57.5 (2014), pp. 778–785. DOI: 10/ggfwq4.
- [Mic20] M. d. Michieli Vitturi. *Navier-Stokes Equations in Cylindrical Coordinates. Derivation of the Equations*. Commit 3a78d37. Feb. 2020. URL: https://github.com/demichie/NS_cylindrical/.
- [Mor13] F. A. Morrison. *An introduction to fluid mechanics*. Cambridge University Press, 2013. ISBN: 9781107003538. DOI: 10/ggfwq5.

References

- [Mus03] I. Muscă. 'About rolling friction evaluation in a ring-ball contact'. In: *Proceedings of International Conference ROTRIB'03*. 2003, pp. 284–287.
- [Mus09] I. Muscă. 'Ball-Ring Friction at Low Rotating Speed'. In: *Tribology in Industry* 31.1&2 (2009), pp. 53–56. ISSN: 2217-7965.
- [Nes84] V. P. Nesterenko. 'Automatic Elimination of the static imbalance of a rotor with anisotropic supports'. In: *Soviet machine science* 1.1 (1984). Translated from *Mashinovedenie*, No. 1, pp. 24–25, 1984, pp. 21–23.
- [Nit17] S. Nitzschke. 'Instationäres Verhalten schwimmbuchsenlagerter Rotoren unter Berücksichtigung masseerhaltender Kavitation'. German. PhD thesis. Otto-von-Guericke-Universität Magdeburg, 2017. ISBN: 9783869485539.
- [Oli+17] L. Olijnichenko et al. 'Experimental study of the process of the static and dynamic balancing of the axial fan impeller by ball auto-balancers'. In: *Eastern-European Journal of Enterprise Technologies* 2.1 (86) (Apr. 2017), pp. 42–50. DOI: 10/czwwg.
- [Oli17] A. R. E. Oliveira. 'History of Krylov-Bogoliubov-Mitropolsky Methods of Nonlinear Oscillations'. In: *Advances in Historical Studies* 06.01 (2017), pp. 40–55. DOI: 10.4236/ahs.2017.61003.
- [Olso4] K.-O. Olsson. 'Limits for the Use of Auto-Balancing'. In: *International Journal of Rotating Machinery* 10.3 (2004), pp. 221–226. DOI: 10.1155/S1023621X04000235.
- [Pay62] A. R. Payne. 'The dynamic properties of carbon black-loaded natural rubber vulcanizates. Part I'. In: *Journal of Applied Polymer Science* 6.19 (Jan. 1962), pp. 57–63. DOI: 10.1002/app.1962.070061906.
- [PJR09] L. Prah, A. Jadoon and J. Revstedt. 'Interaction between two spheres placed in tandem arrangement in steady and pulsating flow'. In: *International Journal of Multiphase Flow* 35.10 (2009), pp. 963–969. DOI: 10.1016/j.ijmultiphaseflow.2009.05.001.

References

- [Pop62] E. P. Popov. *The Dynamics of Automatic Control Systems*. Pergamon Press, 1962. 776 pp.
- [Pra+07] L. Prahl et al. 'On the interaction between two fixed spherical particles'. In: *International journal of multiphase flow* 33.7 (2007), pp. 707–725. DOI: 10.1016/j.ijmultiphaseflow.2007.02.001.
- [PTA12] R. H. Pletcher, J. C. Tannehill and D. A. Anderson. *Computational Fluid Mechanics and Heat Transfer*. Ed. by W. J. Minkowycz and E. M. Sparrow. 3rd ed. Series in Computational and Physical Processes in Mechanics and Thermal Sciences. CRC Press, 2012. ISBN: 9781591690375.
- [Qia14] W. Qian. 'Dynamic simulation of cylindrical roller bearings'. PhD thesis. Rheinisch-Westfälische Technische Hochschule Aachen, 2014. URL: <https://nbn-resolving.org/urn:nbn:de:hbz:82-opus-49034>.
- [Rac18] C. Rackauckas. 'A Comparison Between Differential Equation Solver Suites In MATLAB, R, Julia, Python, C, Mathematica, Maple, and Fortran'. In: *The Winnower* (2018). DOI: 10/gkxsps.
- [RF15] M. Rezaee and R. Fathi. 'A new design for automatic ball balancer to improve its performance'. In: *Mechanism and Machine Theory* 94 (2015), pp. 165–176. ISSN: 0094-114X. DOI: 10/gkxspt.
- [RN17] C. Rackauckas and Q. Nie. 'Differentials.jl—a performant and feature-rich ecosystem for solving differential equations in Julia'. In: *Journal of Open Research Software* 5.1 (2017). DOI: 10.5334/jors.151.
- [Rod+11] D. Rodrigues et al. 'Experimental investigation of a single-plane automatic balancing mechanism for a rigid rotor'. In: *Journal of Sound and Vibration* 330.3 (Jan. 2011), pp. 385–403. DOI: 10/d53wbb.
- [RR98] C. Rajalingham and S. Rakheja. 'Whirl Suppression in Hand-held Power Tool Rotors Using Guided Rolling Balancers'. In: *Journal of Sound and Vibration* 217.3 (Oct. 1998), pp. 453–466. DOI: 10.1006/jsvi.1998.1780.

References

- [RSD03] B. Ryzhik, L. Sperling and H. Duckstein. ‘The Influence of Damping on the Efficiency of Autobalancing Devices for Rigid Rotors’. In: *Proceedings of The Second International Symposium on Stability Control of Rotating Machinery ISCORMA-2003*. Gdańsk, Poland: MAX MEDIA Sp. z o.o., 2003, pp. 104–113. ISBN: 8391302849.
- [RSD04a] B. Ryzhik, L. Sperling and H. Duckstein. ‘Non-synchronous motions near critical speeds in a single-plane auto-balancing device’. In: *Technische Mechanik* 24.1 (2004), pp. 25–36. ISSN: 2199-9244. URL: <https://www.ovgu.de/techmech/article/view/911>.
- [RSD04b] B. Ryzhik, L. Sperling and H. Duckstein. ‘Auto-balancing of anisotropically supported rigid rotors’. In: *Technische Mechanik* 24.1 (2004), pp. 37–50. URL: <https://www.ovgu.de/techmech/article/view/912>.
- [Ryz+01] B. Ryzhik et al. ‘Zum Sommerfeldeffekt beim selbsttätigen Auswuchten in einer Ebene’. In: *Technische Mechanik* 21.4 (2001), pp. 297–312. URL: <https://www.ovgu.de/techmech/article/view/1066>.
- [Sch14] Schaeffler Technologies GmbH & Co. KG. *Dünnringlager Katalog* 575. Online. German. Accessed 12 Aug. 2019. 2014.
- [SDW17] L. Spannan, C. Daniel and E. Woschke. ‘Experimental Study on the Velocity Dependent Drag Coefficient and Friction in an Automatic Ball Balancer’. In: *Technische Mechanik* 37.1 (2017), pp. 62–68. ISSN: 2199-9244. DOI: 10.24352/UB.OVGU-2017-082.
- [SDW18] L. Spannan, C. Daniel and E. Woschke. ‘Simulation of the Ball Kinetic in Ball-Type Automatic Balancing Devices by Solving the Axisymmetric Navier-Stokes Equations in Annular Cavities’. In: *Proceedings of the 10th International Conference on Rotor Dynamics - IFToMM*. Ed. by K. Cavalca and H. Weber. Vol. 63. Cham: Springer, 19th Aug. 2018, pp. 109–118. ISBN: 978-3-319-99272-3. DOI: 10.1007/978-3-319-99272-3_8.

References

- [Seeo6] C. J. Seeton. 'Viscosity–temperature correlation for liquids'. In: *Tribology Letters* 22.1 (2006), pp. 67–78. ISSN: 1573-2711. DOI: 10.1007/s11249-006-9071-2.
- [SG99] C. Stauffer and W. Grimson. 'Adaptive background mixture models for real-time tracking'. In: *1999 IEEE Computer Society Conference on Computer Vision and Pattern Recognition (Cat. No PR00149)*. Vol. 2. IEEE. 1999, pp. 246–252. DOI: 10/dch4ph.
- [Sha75] R. Sharp. 'An analysis of a self-balancing system for rigid rotors'. In: *Journal of Mechanical Engineering Science* 17.4 (1975), pp. 186–189. DOI: 10.1243/JMES_JOUR_1975_017_027_02.
- [Sir+16] S. Siretean et al. 'Hertzian Point Contact-sliding And Rolling Aspects'. In: *Bulletin of the Transilvania University of Brasov, Series I: Engineering Sciences* 9.2 (2016), pp. 259–266.
- [Sir+18a] S. T. Siretean et al. 'Determining the coefficient of rolling friction using hypocycloidal oscillations'. In: *IOP Conference Series: Materials Science and Engineering* 444.2 (2018), p. 022017. ISSN: 1757-899X. DOI: 10.1088/1757-899x/444/2/022017.
- [Sir+18b] S. T. Siretean et al. 'Use of Hypocycloidal Motion in the Study of Rolling Friction'. In: *New Advances in Mechanism and Machine Science*. Ed. by I. Doroftei et al. Mechanism and Machine Science. Proceedings of The 12th IFToMM International Symposium on Science of Mechanisms and Machines (SYROM 2017). Springer International Publishing, 2018, pp. 467–476. ISBN: 9783319791111. DOI: 10.1007/978-3-319-79111-1_46.
- [SKF18] SKF. *Rolling bearings catalogue*. online. Accessed 12 Aug. 2019. 2018. URL: <https://skf.com/go/17000>.
- [SMDoo] L. Sperling, F. Merten and H. Duckstein. 'Self-synchronization and Automatic Balancing in Rotor Dynamics'. In: *International Journal of Rotating Machinery* 6.4 (2000), pp. 275–285. DOI: 10/d25fj2.
- [Spa20a] L. Spannan. *Automatic Ball Balancer Stability Map Generator*. Online ressource. 2020. DOI: 10.5281/zenodo.3894373.

References

- [Spa20b] L. Spannan. *OpenFOAM case files for drag coefficient determination in automatic ball balancers*. Version 0.1.0. 2020. DOI: 10.5281/zenodo.3741868.
- [Spe+02] L. Sperling et al. 'Simulation of two-plane automatic balancing of a rigid rotor'. In: *Mathematics and computers in simulation* 58.4 (2002), pp. 351–365. DOI: 10.1016/S0378-4754(01)00377-9.
- [Spe+04] L. Sperling et al. 'Auto-Balancing of Rotors with a Rigid Bearing'. In: *Machine Dynamics Problems* 28.2 (2004), pp. 45–64. ISSN: 0239-7730.
- [SRD01] L. Sperling, B. Ryzhik and H. Duckstein. 'Two-plane automatic balancing'. In: *Machine Dynamics Problems* 25.3/4 (2001), pp. 139–152. ISSN: 0239-7730. URL: <https://www.infona.pl/resource/bwmeta1.element.baztech-article-BWA2-0005-0352>.
- [SS76] U. Schumann and R. A. Sweet. 'A direct method for the solution of poisson's equation with neumann boundary conditions on a staggered grid of arbitrary size'. In: *Journal of Computational Physics* 20.2 (Feb. 1976), pp. 171–182. DOI: 10/bp5mpd.
- [Str18] S. H. Strogatz. *Nonlinear Dynamics and Chaos*. 2nd ed. CRC Press, 2018. ISBN: 9780429399640. DOI: 10.1201/9780429399640.
- [Sun+13] C. Sung et al. 'Influence of external excitations on ball positioning of an automatic balancer'. In: *Mechanism and Machine Theory* 69 (2013), pp. 115–126. DOI: 10/gkxsp7.
- [SW20a] L. Spannan and E. Woschke. 'Approximating unstable operation speeds of automatic ball balancers based on design parameters'. In: *Advanced Problems in Mechanics II - Proceedings of the XLVIII International Summer School-Conference*. Ed. by D. Indeitsev and A. Krivtsov. Lecture Notes in Mechanical Engineering. Preprint. St. Petersburg, Russia: Springer International Publishing, 2020. DOI: 10.31224/osf.io/f4bvp.

References

- [SW20b] L. Spannan and E. Woschke. ‘Determination of drag coefficients in automatic ball balancers at low Reynolds numbers’. In: *Engineering Applications of Computational Fluid Mechanics* (2020). ISSN: 1997-003X. DOI: 10/fq9c.
- [SW21] L. Spannan and E. Woschke. ‘Investigating the influence of rolling friction on the stable operation of automatic balancing units’. In: *Proceedings of SIRM 2021 – The 14th International Conference on Dynamics of Rotating Machines*. Ed. by G. Żywica and T. Szolc. Institute of Fluid Flow Machinery, Polish Academy of Sciences. Gdańsk, Poland: IMP PAN Publishers, 2021, pp. 92–99. ISBN: 978-83-88237-98-0.
- [Teu05] R. Teutsch. ‘Kontaktmodelle und Strategien zur Simulation von Wälzlagern und Wälzführungen’. German. PhD thesis. Technische Universität Kaiserslautern, 2005. ISBN: 3936890730. URL: <http://d-nb.info/97492590X>.
- [The50] E. Thearle. ‘Automatic Dynamic Balancers’. In: *Machine Design* 22 (1950), pp. 103–106.
- [TS32] E. L. Thearle and N. Y. Schenectady. ‘A new type of dynamic balancing machine’. In: *Transactions of the American Society of Mechanical Engineers* 54.12 (1932), pp. 131–141.
- [Tsi11] C. Tsitouras. ‘Runge–Kutta pairs of order 5(4) satisfying only the first column simplifying assumption’. In: *Computers & Mathematics with Applications* 62.2 (2011). DOI: 10/d5p2zf.
- [Tsu+03] T. Tsuji et al. ‘Unsteady three-dimensional simulation of interactions between flow and two particles’. In: *International journal of multiphase flow* 29.9 (Sept. 2003), pp. 1431–1450. DOI: 10/b3xpnj.
- [Vel+20a] G. V. Velde et al. ‘Let’s Make Ball Balancing Great Again: Why You Should Use Temporary Speed Reduction’. In: *Machines* 8.4 (Nov. 2020), p. 74. DOI: 10.3390/machines8040074.
- [Vel+20b] G. V. Velde et al. ‘Reducing the statistical scatter of automatic ball balancers using temporary speed reduction’. In: *Journal of Sound and Vibration* (July 2020), p. 115582. DOI: 10/gkxsp9.

References

- [WL13] D. Wollscheid and A. Lion. 'Predeformation- and frequency-dependent material behaviour of filler-reinforced rubber: Experiments, constitutive modelling and parameter identification'. In: *International Journal of Solids and Structures* 50.9 (May 2013), pp. 1217–1225. DOI: 10.1016/j.ijsolstr.2012.12.015.
- [Wos13] E. Woschke. 'Simulation gleitgelagerter Systeme in Mehrkörperprogrammen unter Berücksichtigung mechanischer und thermischer Deformationen'. German. PhD thesis. Otto-von-Guericke-Universität Magdeburg, 2013. DOI: 10.25673/3946.
- [Wou+05] N. V. Wouw et al. 'Performance of an Automatic Ball Balancer with Dry Friction'. In: *International Journal of Bifurcation and Chaos* 15.01 (2005), pp. 65–82. DOI: 10.1142/s0218127405012016.
- [Yan+05] Q. Yang et al. 'Study on the influence of friction in an automatic ball balancing system'. In: *Journal of Sound and Vibration* 285.1-2 (July 2005), pp. 73–99. DOI: 10.1016/j.jsv.2004.08.009.
- [Yat+17] V. Yatsun et al. 'Experimental research of rectilinear translational vibrations of a screen box excited by a ball balancer'. In: *Eastern-European Journal of Enterprise Technologies* 3.1 (87) (2017), pp. 23–29. DOI: 10.15587/1729-4061.2017.101798.
- [Yat+18] V. Yatsun et al. 'On stability of the dual-frequency motion modes of a single-mass vibratory machine with a vibration exciter in the form of a passive auto-balancer'. In: *Eastern-European Journal of Enterprise Technologies* 2.7 (92) (Apr. 2018), pp. 59–67. DOI: 10.15587/1729-4061.2018.128265.
- [Yat+20] V. Yatsun et al. 'Searching for the twofrequency motion modes of a threemass vibratory machine with a vibration exciter in the form of a passive autobalancer'. In: *Eastern-European Journal of Enterprise Technologies* 4.7 (106) (Aug. 2020), pp. 103–111. DOI: 10.15587/1729-4061.2020.209269.
- [Yat20] V. Yatsun. 'Experimental Study of Resonance Vibrations of the Vibratory Machine Excited by a Ball Auto-Balancer'. In: *Eastern-*

References

- European Journal of Enterprise Technologies* 2.1 (2020), pp. 32–40. ISSN: 1729-3774. DOI: 10.15587/1729-4061.2020.201105.
- [YY07] D.-H. Yoon and K.-S. Yang. ‘Flow-induced forces on two nearby spheres’. In: *Physics of Fluids* 19.9 (2007), p. 098103. DOI: 10/fs3xvr.
- [Zhm14] B. Zhmud. ‘Viscosity Blending Equations’. In: *Lube-Tech* 121.93 (2014), pp. 22–27.
- [ZLZ18] X. Zhang, X. Liu and H. Zhao. ‘New Active Online Balancing Method for Grinding Wheel Using Liquid Injection and Free Dripping’. In: *Journal of Vibration and Acoustics* 140.3 (2018), p. 031001. DOI: 10.1115/1.4037955.

List of figures

1.1.	Example of a dynamically unbalanced Jeffcott rotor equipped with two automatic balancers	2
1.2.	Imbalance-excited vibration response of an undamped oscillator as a function of the circular frequency of excitation relative to the critical speed.	2
1.3.	Working principle of the ABB.	2
2.1.	Concept design of a tabletop centrifuge rotor with an integrated ABB.	10
2.2.	Partially disassembled HP SH-216 DVD Writer Drive	11
2.3.	Basic design parameters of an automatic ball balancer.	12
2.4.	Increase of the exploited ABB potential as a function of the sector occupied by the balls.	13
2.5.	Ball-balancer modifications to reduce unbalance increase at sub-critical speeds.	16
3.1.	In- and outgoing mass flows of an infinitesimal volume in cylindrical coordinates.	19
3.2.	Stresses on an infinitesimal volume in cylindrical coordinates.	21
3.3.	Boundary conditions for the rotating annulus problem in the stream function formulation.	23
3.4.	A staggered grid with 32×32 grid points.	27
3.5.	Finite difference grid points on a non-uniform mesh given exemplarily for the radial coordinate.	27
4.1.	Translational oscillator with primary unbalance and one counterbalancing mass of a balancer with an eccentricity.	29

List of figures

4.2.	Comparison of numerical integration results for the model presented in [Ryz+01].	36
4.3.	Comparison of numerical integration results for the model presented in [BK18].	37
4.4.	Feasible operating ranges for automatic balancers in anisotropic supports	51
4.5.	Stability maps for example ABB units with isotropic and orthotropic bearings.	54
4.6.	Possible stable stationary positions of two balls under the influence of friction.	56
5.1.	Flowchart of the ABB force element based on a radial bearing force element. Expansions compared to the original routine are highlighted in dashed boxes.	62
5.2.	Friction coefficient models depending on the slip velocity in the contact point.	66
5.3.	Ball rolling down an inclined plane, influenced by friction and rolling resistance.	67
5.4.	Flow chart of adherence implementation.	69
5.5.	Exemplatory CFD results of laminar flow around a ball in the ABB annular cavity with reduction to an effective drag force tangential to the ball orbit.	71
5.6.	Qualitative fluid velocity profiles in the ABB annulus under different conditions shown in the plane of the circular orbit of the balancing ball.	72
5.7.	Annulus inside an ABB with one ball and a rolling element bearing raceway.	75
5.8.	Schematic of the interacting streamlines of a free flow around two spheres aligned in a tandem manner.	76
5.9.	Drag coefficient correction factors depending on Reynolds number and distance between spheres in tandem arrangement. . .	77

List of figures

6.1. Density-viscosity relations at room temperature for different lubricants. Indicators show the nominal viscosity for silicone oils, the viscosity grade for ISO-VG oils or the volume fraction of glycerol, respectively.	82
6.2. Viscosity-temperature relation for low viscous silicone oils.	82
6.3. Cross section of the test rig assembly for the discoidal rotor	84
6.4. Centrifuge test rig for the discoidal rotor with automatic balancing unit.	85
6.5. 120 degree cut-out sketch of the reduced multi body model of the test rig with discoidal rotor.	86
6.6. Testing set-ups to determine the frequency dependent stiffness and damping of the centrifuge rubber bushings.	87
6.7. Force and deflection measurement of the rubber bushing analysis.	88
6.8. Measurement of the rubber bushing stiffness and damping for different loading frequencies and amplitudes.	90
6.9. Experimental determination of eigenfrequencies of the discoidal rotor at rest.	91
6.10. Runup of the discoidal rotor in its initial configuration.	92
6.11. Eigenfrequencies of the rotor system, calculated subsequently to a MBS solution of a run-up.	93
6.12. Run-up of the discoidal rotor with an added (primary) unbalance but without balancing masses or fluid. One run-up for each of the twelve possible primary unbalance locations was conducted.	96
6.13. Half-section of the discoidal rotor containing the outer ring of a ball-bearing.	98
6.14. Test rig setup for the verification of the drag coefficient relation for the discoidal rotor.	98
6.15. Forces on the ball in equilibrium to access the drag coefficient.	98
6.16. Experimental validation of the drag coefficient for flow around a ball with different kinematic viscosities in an automatic ball balancer with a bearing raceway	100

List of figures

6.17. Comparison of the product of drag coefficient and Reynolds number at low Reynolds numbers.	101
6.18. Comparison of simulative results to the experiments used to determine the Reynolds number dependent drag coefficient.	103
6.19. Single frame of the 240 fps test bench recording at a momentary rotor speed of 1200 rpm.	104
6.20. Balancing ball resting position distributions for varied primary unbalance positions.	105
6.21. Roundness deviations of the rotor raceway.	106
6.22. FFT of the centrifuge stator acceleration for different rotation speeds of the ABB filled with silicone oil ($\nu = 0.65 \text{ mm}^2 \text{ s}^{-1}$) and two balancing balls. The intended reduction of unbalance excitation only occurs for rotor speeds $\Omega > \Omega_{bo} = 64 \text{ rad s}^{-1}$	108
6.23. Spectrogram of the inertial x position of one of the two balls inside the ABB during slow run-up and run-down simulation of the rotor system.	109
6.24. Stability map of the centrifuge testrig.	110
6.25. Run-up of the discoidal rotor with primary unbalance, one balancing ball and silicone oil of viscosity $\nu = 5 \text{ mm}^2 \text{ s}^{-1}$	112
6.26. Run-up of the discoidal rotor with primary unbalance, one balancing ball and silicone oil of viscosity $\nu = 20 \text{ mm}^2 \text{ s}^{-1}$	113
6.27. Run-up of the discoidal rotor with primary unbalance, one balancing ball and silicone oil of viscosity $\nu = 50 \text{ mm}^2 \text{ s}^{-1}$	114
6.28. CFRP rotor with attached ABB prototype.	117
6.29. Testrig for the CFRP rotor with mechanical model.	118
6.30. Impulse excitation of the CFRP rotor in the test rig.	119
6.31. FFT of the non rotating CFRP oszillations excited by impulse	120
6.32. Spectrogram of the CFRP rotor deflection in the time domain at constant rotational velocity $\Omega = 15 \text{ rad s}^{-1}$	121
6.33. Comparison of the CFRP rotor eigenvalues	122
6.34. Stability map of the CFRP testrig.	123
A.1. In- and outgoing mass fluxes of an infinitesimal volume in cylindrical coordinates.	134

List of figures

A.2. Stresses on an infinitesimal volume in cylindrical coordinates.	137
B.1. Properties of the stator of the motor unit	147
B.2. Properties of the discoidal rotor with included ball balancer .	148
B.3. Properties of the base of the motor unit	149
B.4. Properties of the lid of the motor unit	150
B.5. Properties of the shaft of the motor unit	150
B.6. Important geometrical properties of the CFRP rotor	151
B.7. Terminal dimensions of the CFRP rotor with attached ball balancer	152

List of tables

3.1. Central finite difference coefficients for the first and second derivative on a non-uniform mesh.	26
6.1. Properties of silicone oils (Polydimethylsiloxane)	81
6.2. Properties of the ball balancer in the discoidal rotor.	97
6.3. Properties of fluids used in the equilibrium experiments.	100
6.4. Planar oscillator model parameters for the centrifuge test rig with discoidal rotor.	109
6.5. Comparison of experimentally and simulatively determined eigenfrequencies.	121
6.6. Planar oscillator model parameters for the CRP rotor test rig.	123
B.1. Inertial properties of the test rig assembly parts.	147
B.2. Inertial properties of the CFRP rotor assembly.	151
C.1. Dimensions of deep groove ball bearings for automatic balancing.	153
C.2. Dimensions of thin section bearings for automatic balancing.	160